



HAL
open science

Transition ductile-fragile des aciers pour gazoducs : Étude quantitative des ruptures fragiles hors plan et corrélation à l'anisotropie de microtexture

Franck Tankoua Yinga

► **To cite this version:**

Franck Tankoua Yinga. Transition ductile-fragile des aciers pour gazoducs: Étude quantitative des ruptures fragiles hors plan et corrélation à l'anisotropie de microtexture. Mécanique des matériaux [physics.class-ph]. Ecole Nationale Supérieure des Mines de Paris, 2015. Français. NNT: 2015ENMP0014 . tel-01212488

HAL Id: tel-01212488

<https://pastel.hal.science/tel-01212488>

Submitted on 6 Oct 2015

HAL is a multi-disciplinary open access archive for the deposit and dissemination of scientific research documents, whether they are published or not. The documents may come from teaching and research institutions in France or abroad, or from public or private research centers.

L'archive ouverte pluridisciplinaire **HAL**, est destinée au dépôt et à la diffusion de documents scientifiques de niveau recherche, publiés ou non, émanant des établissements d'enseignement et de recherche français ou étrangers, des laboratoires publics ou privés.

École doctorale n° 432 : Sciences des Métiers de l'Ingénieur

Doctorat ParisTech

THÈSE

pour obtenir le grade de docteur délivré par

l'École nationale supérieure des mines de Paris

Spécialité Sciences et Génie des matériaux

présentée et soutenue publiquement par

Franck TANKOUA

le 02 juillet 2015

Ductile to brittle transition in pipeline steels: Quantitative investigation of brittle out-of-plane cracking and correlation to microtexture anisotropy

Transition ductile-fragile des aciers pour gazoducs: Etude quantitative des ruptures fragiles hors plan et corrélation à l'anisotropie de microtexture

Directeurs de thèse : **Anne-Françoise GOURGUES-LORENZON, Jérôme CREPIN**

Jury

M. Jean Hubert SCHMITT, Professeur, Ecole Centrale des Arts et Manufactures de Paris
M. Benoît TANGUY, Ingénieur de Recherche, HDR, CEA Saclay DEN/DANS/DMN/SEMI
M. Javier GIL-SEVILLANO, Professeur, Université de Navarre
Mme Clotilde BERDIN, Professeur des Universités, ICMMO, Université Paris-Sud 11
M. Thomas PARDOEN, Professeur, Université Catholique de Louvain, Belgique
M. Yazid MADI, Chargé de recherche EPF-Ecole d'ingénieurs
Mme Anne-Françoise GOURGUES, Professeur, Centre des Matériaux, MINES ParisTech
M. Jérôme CREPIN, Directeur de Recherche, Centre des Matériaux, MINES ParisTech
M. Philippe THIBAUX, Ingénieur de Recherche, OCAS

Président
Rapporteur
Rapporteur
Examinateur
Examinateur
Examinateur
Examinateur
Examinateur
Invité

T
H
È
S
E

Pour toi Grand-Mère

Avant-propos

C'est toujours avec beaucoup d'émotions qu'on débute la rédaction de cette page d'avant-propos qui annonce la fin... Avec ces dernières lignes, qui pour le lecteur seront ses premières du manuscrit, je tiens à présenter mes remerciements à tous ceux qui ont contribué à l'aboutissement de cette étude.

Cette thèse est le fruit d'une collaboration entre le Centre des Matériaux de l'Ecole Nationale Supérieure des Mines de Paris et le Centre de Recherche OCAS d'ArcelorMittal à Gand. Chaque centre m'a donné le meilleur tant scientifique qu'humain.

Je souhaite tout d'abord remercier Philippe THIBAUX et Steven COOREMAN qui m'ont suivi à OCAS et qui tout le long de cette thèse ont apporté leur vision industrielle au projet. J'associe à ces remerciements, Nuria, Laura et toute l'équipe métallurgie d'OCAS. Je n'oublie pas tous les techniciens d'OCAS, en particulier Andries et Marteen qui ont réalisé les essais DWTT et Charpy.

Mes remerciements vont aussi à mes directeurs de thèse au Centre des Matériaux : Anne-Françoise GOURGUES et Jérôme CREPIN. Leurs qualités tant scientifiques qu'humaines ont été pour moi un soutien inestimable. Ils ont fait preuve d'une grande disponibilité et m'ont totalement fait confiance.

Je suis très reconnaissant envers Yazid MADI et Benoît TANGUY avec qui j'ai fait mes premiers pas dans le monde de la recherche au travers des stages au Centre des Matériaux et au CEA. Je leur remercie aussi d'avoir accepté de faire partie de mon jury en tant qu'examinateur et rapporteur. De même, je remercie aussi tous les autres membres du jury, Jean Hubert SCHMITT, Javier GIL-SEVILLANO, Clotilde BERDIN et Thomas PARDOEN, pour l'intérêt qu'ils ont porté à mon travail et leurs commentaires.

Tout au long de cette thèse, j'ai pu profiter des conseils des responsables scientifiques du Centre des Matériaux et en particulier André PINEAU et Jacques BESSON. Je vous exprime toute ma gratitude pour cette aide.

J'ai eu la chance de disposer de moyens expérimentaux de grande qualité au Centre des Matériaux. Mes remerciements vont d'abord à nos techniciens de l'atelier : René, Georges, Christophe, Jean-Pierre. Avec leur expérience, ils ont usiné avec une grande précision toutes les éprouvettes de cette étude, malgré la sévérité de certaines géométries. Je souhaite par la suite remercier Abdenour et Régis pour l'aide qu'ils m'ont apportée dans la réalisation des essais mécaniques. Je te remercie Anne pour ton aide avec les cartographies EBSD et je te souhaite du courage pour la suite. Je profite par la même occasion pour remercier toute l'équipe Microscopie et Analyse du laboratoire, et en particulier Fabrice, Brigitte, Maria, Lyn-thy pour leur formation en microscopie.

J'ai aussi eu la chance de profiter de moyens numériques performants et surtout de personnes prêtes à me débloquer en cas de soucis dans Zset, Abaqus ou Zmat. Je remercie Fifou, Farida, Djamel, NiKolay, Kaïs, Françoise, Lucien et Son pour cette aide.

Je remercie aussi toute l'équipe administrative qui s'occupe de la vie quotidienne du Centre des Matériaux et de l'équipe informatique avec Olivier et Gregory. Je remercie sincèrement Odile pour son aide précieuse dans mon étude bibliographique.

Pendant cette thèse, j'ai aussi pu développer mes talents footballistiques avec nos séances de foot du mercredi. Je remercie toute l'équipe de foot du Centre des Matériaux pour ces bons moments passés. De même, je remercie tout l'ensemble des doctorants, post-doctorants, permanents et stagiaires que j'ai pu rencontrer, et dont leur bonne humeur ou tout simplement leur sourire a rendu ces années de thèse agréables. Une pensée particulière pour mes amis du bureau B107 au Centre des Matériaux et du célèbre bureau « coralito » à OCAS.

Enfin je remercie tous ceux qui m'ont supporté pendant cette grande étape de ma vie : Mes parents, mes frères et sœurs et toute ma famille en générale.

Table of Contents

Introduction	3
Chapter I – Metallurgical characterization of as-received materials.....	5
I.1. General presentation and reference of the two steels.....	7
I.2. Chemical composition	7
I.3. Nature and distribution of inclusions.....	7
I.4. Hardness	9
I.5. Microstructure	9
I.6. Average texture	12
I.7. Summary and conclusion	13
Chapter II – Toughness characterization of as-received materials	15
II.1. Literature survey	18
II.1.1. Battelle drop weight tear tests (DWTT)	18
II.1.2. Brittle-out-of plane cracking during impact tests	23
II.2. Results of drop weight tear tests	24
II.2.1. Impact toughness of Steels A and B	24
II.2.2. Fracture modes during DWTT and effect on impact toughness	24
II.2.3. Effect of the loading direction	30
II.2.4. Summary	31
II.3. Results of Charpy tests	31
II.3.1. Charpy impact toughness of Steels A and B	32
II.3.2. Fracture mode and effect on impact toughness	33
II.3.3. Summary of Charpy results and comparison to DWTT results	39
II.4. Brittle out-of-plane cracking during fracture toughness tests	42
II.4.1. Brittle out-of-plane cracking during tests on pre-cracked CT specimens.....	43
II.4.2. Comparison with impact tests.....	43
II.5. Discussion and conclusions	44
Chapter III – Plastic flow and fracture anisotropy.....	45
III.1. Introduction and state-of-the-art	48
III.2. Experimental approach.....	50
III.3. Plastic anisotropy and elastic-plastic behavior	50
III.3.1. Strain anisotropy	50
III.3.2. Anisotropy in strength	51
III.3.3. Evolution of the plastic flow behavior with temperature	52
III.3.4. Summary on the plastic flow behavior.....	54
III.4. Fracture resistance of the rolling plane (tensile tests along ND).....	54
III.4.1. Fully ductile fracture mode	55
III.4.2. Mixed ductile-cleavage fracture mode.....	57
III.4.3. Full cleavage fracture mode	59
III.5. Fracture resistance of the θ -plane (tensile tests along BTD)	60
III.5.1. Fully ductile fracture mode	60
III.5.2. Mixed ductile-delamination-cleavage fracture mode	61
III.5.3. Full cleavage fracture mode	62
III.6. Fracture resistance of the TD-ND plane (tensile tests along RD)	63
III.6.1. Fully ductile fracture mode	63
III.6.2. Mixed ductile-delamination fracture mode.....	63
III.6.3. Full cleavage fracture mode	65
III.7. Fracture resistance of the RD-ND plane (tensile tests along TD)	66
III.7.1. Fully ductile fracture mode	66

III.7.2.	Mixed ductile-delamination fracture mode.....	67
III.7.3.	Mixed delamination-brittle out-of-plane fracture mode.....	67
III.7.4.	Full cleavage fracture mode.....	68
III.8.	Discussion and conclusions.....	69
Chapter IV – Quantitative study of cleavage stress anisotropy.....		71
IV.1.	Literature survey.....	73
IV.1.1.	Microstructural parameters controlling cleavage fracture in bcc steels.....	74
IV.1.2.	Local approach to fracture.....	76
IV.1.3.	Literature survey of physically-based cleavage fracture models.....	77
IV.2.	Anisotropy in potential cleavage facet distribution.....	83
IV.2.1.	The concept of potential cleavage facets.....	83
IV.2.2.	Analysis of potential cleavage facets for different planes of the plate.....	87
IV.3.	Anisotropy in critical cleavage stress, correlation with PCFs.....	91
IV.3.1.	Procedure.....	91
IV.3.2.	Critical cleavage stress along ND, BT, RD and TD.....	92
IV.3.3.	Correlation between PCF size and critical cleavage stress.....	93
IV.4.	Conclusions.....	94
Chapter V – Prediction of brittle out-of-plane cracking with a deterministic approach.....		95
V.1.	Introduction and state-of-the-art.....	97
V.2.	Prediction of the onset of brittle out-of-plane cracking during quasi-static tensile tests on notched specimens.....	98
V.2.1.	Application of the macroscopic critical stress criterion to the prediction of delamination..	99
V.2.2.	Effect of stress triaxiality.....	100
V.2.3.	Effect of the ductile crack on the stress state at the onset of delamination.....	101
V.2.4.	Effect of prior plastic deformation on critical cleavage stress.....	105
V.2.5.	Discussion of the criterion for numerical prediction of brittle out-of-plane cracking.....	106
V.3.	Prediction of brittle out-of-plane cracking occurrence during impact tests on Charpy specimens.....	107
V.4.	Conclusions.....	109
Chapter VI – Application: Study of delamination on pre-strained and on heat treated Steel B.....		111
VI.1.	Study of delamination on prestrained Steel B (20pct-steel).....	113
VI.1.1.	Metallurgical characterization of the 20pct-steel.....	113
VI.1.2.	Results of Charpy tests on 20pct-steel.....	115
VI.1.3.	Quantitative study of the cleavage sensitivity along (RD-TD) plane of the 20pct-steel ..	116
VI.2.	Sensitivity of Steel B to delamination after a heat-treatment.....	120
VI.2.1.	Metallurgical characterization of the heat-treated steel.....	120
VI.2.2.	Charpy impact behavior of the heat-treated steel.....	122
VI.2.3.	Tensile behavior in the ductile to brittle transition domain.....	122
VI.2.4.	Cleavage fracture behavior of the heat-treated steel.....	124
VI.3.	Conclusions.....	127
Conclusions and Outlook.....		129
A-	Interrupted DWTT and results of impact tests.....	133
B-	Design of NT2 geometry and results of tensile tests on smooth and notched specimens.....	141
C-	Elastic-plastic constitutive modelling for quasi-static tests.....	155
D-	Simulation of Charpy tests: Ductile crack advance modeling up to the onset of delamination ...	175
References.....		187

Introduction

To take the increasing natural gas demand all over the world during the past decades into account, the gas pressure inside pipelines has been increased. More and more resistant pipeline steels generally produced using thermomechanically controlled process (TMCP) routes are used. A good toughness of these pipeline steels at lower temperatures is required to avoid long brittle crack propagation.

In order to validate the toughness requirement, a first test so-called “full scale test” could be used. In this test, investigations are performed on a real linepipe after initiation of a brittle crack with explosive charge. The crack propagation distance before arrest is evaluated. In addition to being excessively expensive and time consuming, the full scale test could not be easily performed at very low temperatures. Therefore, in linepipe industry the drop weight tear test (DWTT) is the alternative test commonly used for impact toughness validation. In DWTT test, a three point bending specimen with the same thickness as the pipeline wall is impacted by a mass. The brittle area measured after DWTT should be lower than 15% of the total fracture area to consider the specimen as valid. Steels which fulfilled this requirement were found to also be validated according to full scale test.

The so-called Charpy test, the famous impact toughness test, is also used in pipeline industry. This test is especially convenient for new pipeline steel design, because of the small size of the specimen comparing to that for DWTT. A good correlation between DWTT and Charpy tests exists for lower pipeline steel grade (<X70). Unfortunately, this correlation is partly lost for modern pipeline steel grades generally obtained by TMCP.

The difference in experimental conditions between Charpy and DWTT tests might not be the major cause of the poor correlation, since for lower grades this correlation still exists. One plausible cause could be the difference in the criterion of validation. For Charpy tests, a minimal absorbed energy is required and for DWTT it is a maximal brittle area imposed. But, in modern pipeline steels, brittle out-of-plane cracks observed within the ductile to brittle transition domain could increase this brittle area and could also affect the impact toughness evaluation differently in Charpy and DWTT tests.

These brittle out-of-plane cracks (Figure 1) are mainly due to delamination, which propagates along the rolling plane, and to brittle tilted fracture (BTF), which propagates along so-called θ -planes (tilted by 40° around the rolling direction). This topic also raises the scientific problem of the anisotropy in brittle fracture, as BTF does not propagate in the usual Mode I. This study aims at answering the three

following questions: How does brittle out-of-plane cracking affect the ductile to brittle transition? Which are the origins of brittle out-of-plane cracks? How could we predict brittle out-of-plane cracking?

To this aim, the local approach to fracture was applied. As a result, the study started with the investigation of brittle out-of-plane cracking on impact specimens. Then, anisotropy of brittle fracture was characterized using tensile specimens, so that the planes associated to brittle out-of-plane crack propagation could be studied via mode I loading. From these tests, the origin of brittle out-of-plane cracks was investigated and criteria for their prediction were proposed. Hypotheses concerning physical mechanisms that control brittle out-of-plane fracture were proposed. Some of them were then tested by modifying the as-received material. This approach is closely followed in the following manuscript.

In chapter I, the two materials under investigation are presented.

In chapter II, brittle out-of-plane cracking is studied from two kinds of impact tests, namely, Charpy tests and Battelle drop weight tear tests (DWTTs). The effect of these cracks on the impact toughness is analyzed. The occurrence of these fracture modes is compared for Charpy and DWTT specimens. Further comparison is made with fracture of precracked compact tensile specimens tested in a quasi-static manner.

In chapter III, tensile tests are reported along different directions to study the anisotropy in brittle fracture and the sensitivity to cleavage along the rolling plane and along the θ -plane.

In chapter IV, a quantitative value is assigned to the sensitivity to cleavage fracture along each plane, via calculation of critical cleavage stresses. This criterion was derived from thorough mechanical analysis of tests on tensile specimens. The microtexture along each plane was quantified to correlate the anisotropy in critical cleavage stress to microtexture anisotropy.

In chapter V, going back to brittle out-of-plane fracture, a criterion is proposed to numerically predict the occurrence of delamination cracking on tensile and Charpy specimens. The effects of a ductile micro-crack and of plastic deformation have been taken into account.

In chapter VI, effects of plastic deformation and of initial microtexture anisotropy on critical cleavage stress are tentatively determined in more detail. To this aim, the as-received material was modified by prestraining or by a heat treatment, and the resulting sensitivity to delamination was studied using a simplified approach based on the above described methodology.

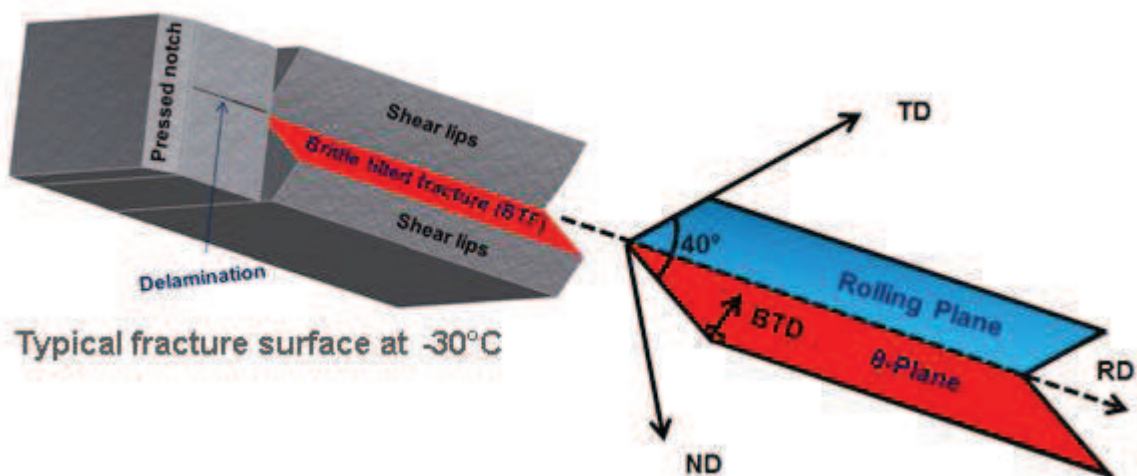


Figure 1: Schematic drawing of brittle out-of-plane cracking in DWTT specimens. Delamination propagates along the rolling plane and BTF propagates along θ -plane.

Chapter I – *Metallurgical characterization of as-received materials*

Table of Contents

I.1.	General presentation and reference of the two steels.....	7
I.2.	Chemical composition	7
I.3.	Nature and distribution of inclusions.....	7
I.4.	Hardness	9
I.5.	Microstructure	9
I.6.	Average texture	12
I.7.	Summary and conclusion	13

This first chapter focuses on the metallurgical characterization of the two as-received steels provided for this study. The chemical composition, inclusion distribution, hardness, microstructure and texture of both steels are presented.

Résumé

Dans ce chapitre, les deux aciers de nuance X70 de l'étude (aciers A et B) sont présentés. La composition chimique, la nature et distribution des inclusions, la microstructure et la dureté des aciers ont été étudiées dans l'état de réception.

La composition chimique des deux aciers est assez proche avec un bas niveau en soufre (<30 ppm) et des taux de carbone et nickel légèrement plus élevés pour l'acier A. Les inclusions majoritaires dans les deux aciers sont des MnS et d'autres complexes riches en aluminium, oxygène, magnésium et calcium. Des inclusions riches en titane ont aussi été observées pour l'acier B. Bien que les deux aciers aient des fractions inclusionnaires surfaciques très proches (2×10^{-4}), l'acier B possède plus de particules et donc une distance inter-particulaire plus faible. La dureté Vickers des deux aciers est aux environs de 210 et leur microstructure est essentiellement ferritique avec quelques colonies perlitiques. Des entités allongées suivant la direction de laminage, constituées de sous-grains, recouvrent toute la surface analysée. Le rôle de ces entités sur la rupture par clivage sera mis en évidence dans cette étude.

I.1. General presentation and reference of the two steels

The two steels of this study have been provided by ArcelorMittal. They have been taken from hot-rolled coils used for linepipe manufacturing, which were obtained after thermomechanical controlled processing. The first steel, referenced as *Steel A* hereafter, is 19.5-mm-thick and the second steel, referenced as *Steel B* hereafter, is 23-mm-thick. Both steels are X70 grade. The three principal directions of the plate are referenced as *RD* (rolling direction), *TD* (transverse direction) and *ND* (normal direction).

I.2. Chemical composition

The chemical composition of the steels is presented in Table I-1. Both are low alloy steels, with a slightly higher amount of carbon and nickel for Steel A. The level of manganese is higher for Steel B. The sulfur content, almost identical for both steels, is low.

	C	Mn	Si	P	Ni+Cr+Mo	Al	Ti+Nb	Cu	S
Steel A	0.047	1.18	0.24	0.013	0.640	0.018	0.083	0.31	0.0025
Steel B	0.031	1.7	0.21	0.013	0.403	0.05	0.138	0.28	0.0018

Table I-1: Chemical composition of Steel A and Steel B (wt. %)

I.3. Nature and distribution of inclusions

Analyzing the nature, size and distribution of inclusions is important for the study of ductile fracture. In fact, these inclusions are expected to generate void nucleation. Quantitative analysis of inclusions was performed on INCA equipment attached to the scanning electron microscope available at OCAS. The analysis was done on polished specimens in the (RD-ND) plane. A scanned area of $1.31 \times 10^6 \mu\text{m}^2$, divided into 276 elementary fields of $4.76 \times 10^3 \mu\text{m}^2$ each in area was considered for Steel A; the same elementary field area was also considered for Steel B but in that case only 142 fields have been scanned. The size of these scanned areas was chosen to obtain representative results.

The observed inclusions are: ((Al,Mg)-oxide + (Ca,Mn)-sulfide + Ti); ((Al,Mg)-oxide + (Ca,Mn)-sulfide); (Al,Mg)-oxide; Al-oxide; Ti-rich particles, and MnS sulfide. The aspect ratio for all these inclusions remains close to 1 and is slightly higher for Al-Oxide (sometimes higher than 2) in Steel A. This suggests an equiaxed shape of inclusions.

The size distribution of inclusions (equivalent circle diameter) in number is presented in Figure I-1. Steel A mostly contains MnS, ((Al,Mg)-oxide+ (Ca,Mn)-sulfide) and (Al,Mg)-oxide. Steel B also exhibits a large amount of MnS, and (Al,Mg)-oxide with additional Ti-rich particles. No obvious correlation has been found between the nature and the size of inclusions. The small size of MnS particles, especially for Steel A, highlighted the benefit role of calcium treatment. 76 inclusions have been counted for Steel A and only 55 inclusions counted for Steel B. Before dropping into any conclusion, it is important to normalize this number of inclusions by the total scanned area, since the scanned area was almost two times higher for Steel A. For an equivalent area, Steel B has 40% more inclusions than Steel A. Moreover, according to Figure I-1, the inclusion size is uniformly distributed in the range [1 – 4 μm] within Steel B. The inclusion size is more scattered for Steel A, with many inclusions lower than 1 μm and some inclusions which can reach 7 μm . The area-weighted size distribution of inclusions is presented in Figure I-2.

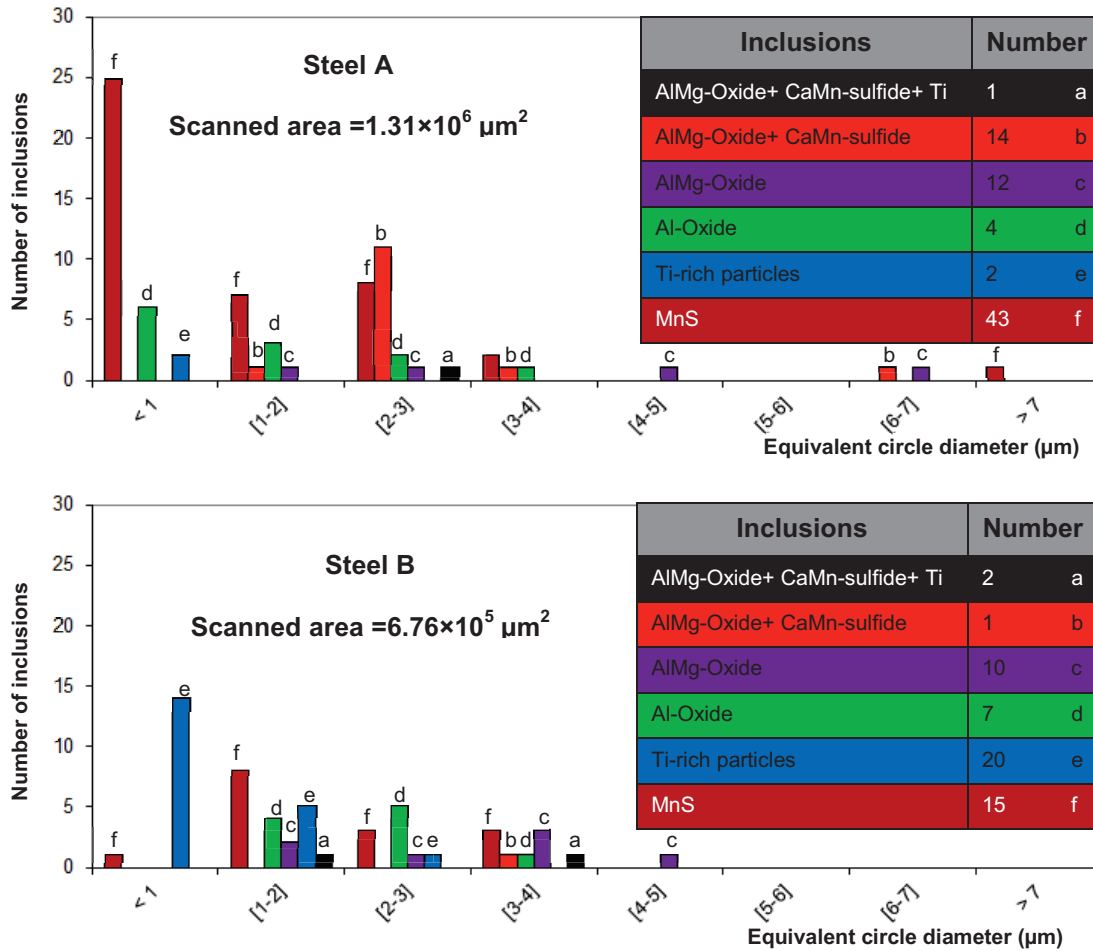


Figure I-1: Distribution in number of inclusions by equivalent circle diameter and total number of inclusions

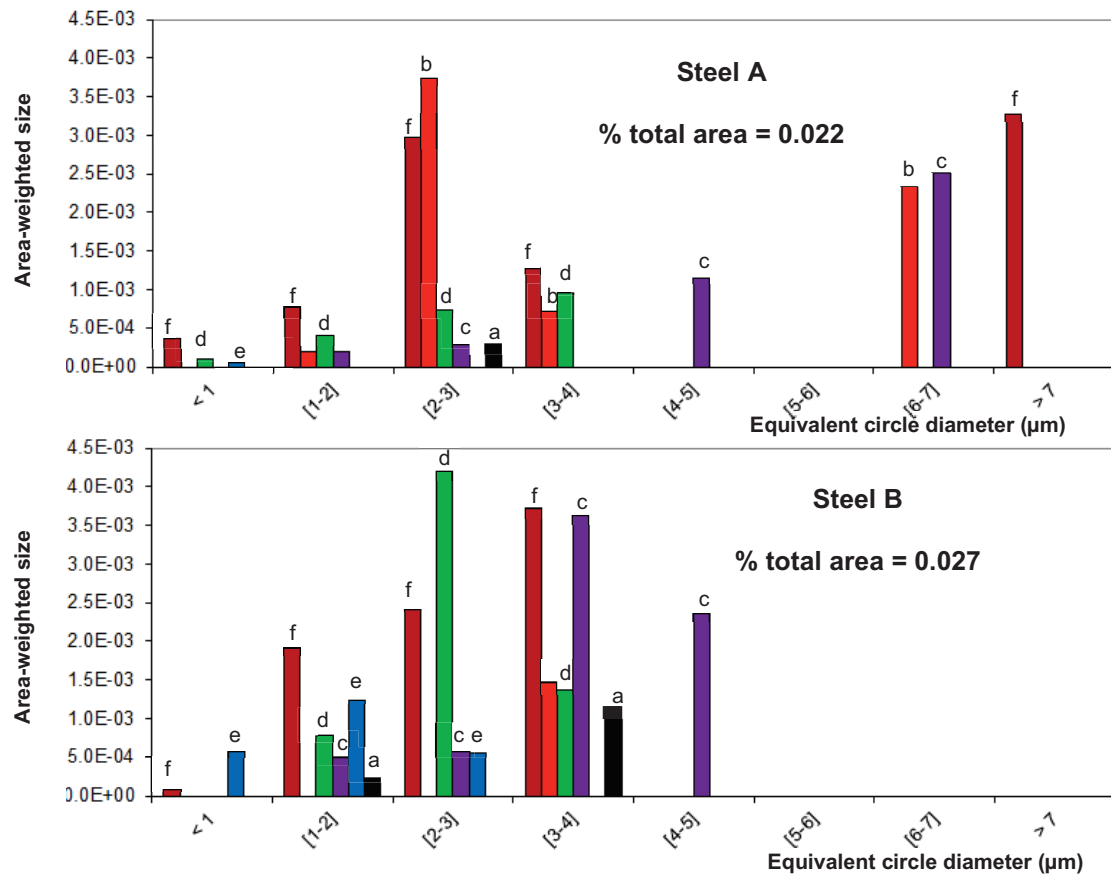


Figure I-2: Distribution in area-weighted size of inclusions by equivalent circle diameter

The total area fractions of inclusions are respectively 2.2×10^{-4} and 2.7×10^{-4} for steels A and B. Since these values are close for both steels and at the same time Steel B has a 40% higher number of inclusions, the average distance between inclusions is expected to be lower for Steel B than Steel A.

Investigations of ductile fracture reported in chapter III showed that the nature of particles from which voids nucleated was in good agreement with the inclusion analysis. The lower average distance between inclusions in Steel B facilitates void coalescence. Actually, the number density of voids is higher in Steel B than in Steel A.

I.4. Hardness

Hardness analysis was performed with two aims: characterizing the average steel hardness and investigating the heterogeneity within both steels. Vickers hardness measurements were performed on BUEHLER equipment with an indentation load of 300g and indentation duration of 10s per point. The hardness evolution across the thickness of the steel plates has been measured within the (RD-ND) plane. The distance between two indentation points was set to 0.5mm. Figure I-3 gives the results of this analysis. Taking the experimental uncertainty of hardness measurement (around 10 Vickers) into account, the hardness of Steel B could be considered as homogenous across the plate thickness. Concerning Steel A, the hardness measured close to the external skin is slightly higher than in the rest of the plate. This difference could probably result from slight hardening generated during hot coiling. Nevertheless, the discrepancy between the skin and mid-thickness is less than 10%, thus Steel A could be also considered as macroscopically homogenous across its thickness. The average values of hardness of steels A and B are respectively $HV_{0.3} = 210 \pm 10$ and $HV_{0.3} = 220 \pm 10$.

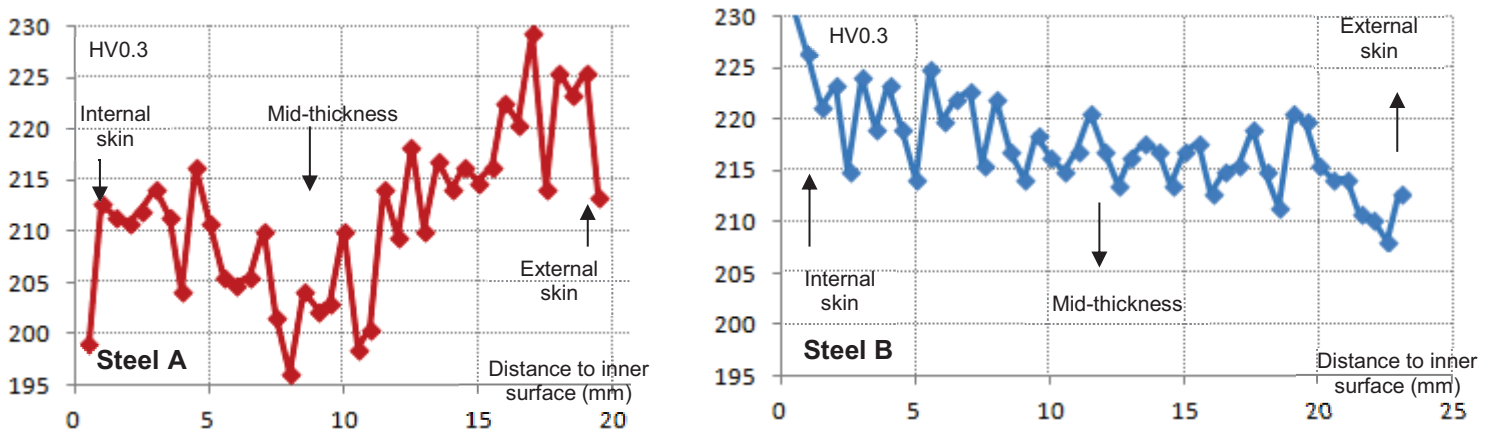
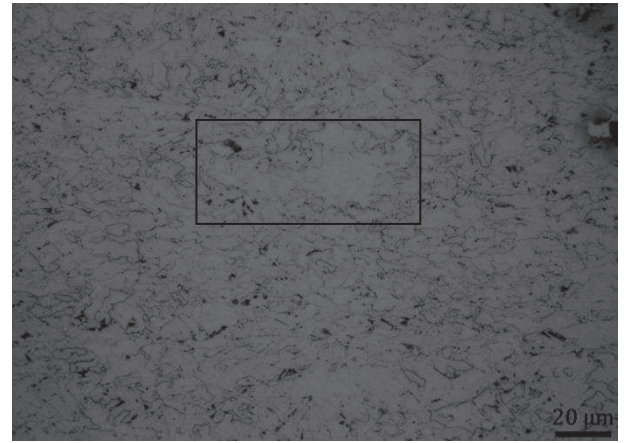


Figure I-3: Hardness evolution across the thickness of Steel A and Steel B

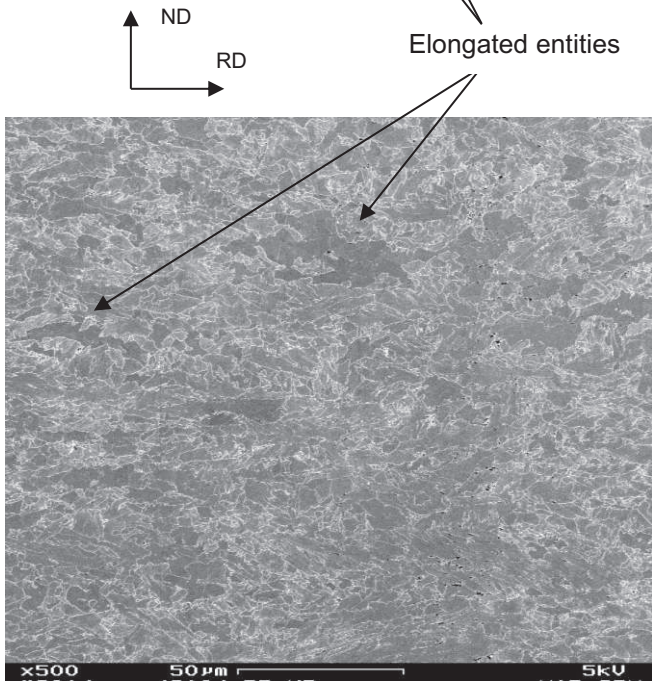
I.5. Microstructure

The microstructure was observed using light optical microscopy after Nital etching. SEM observations with backscattered electrons were also carried out to obtain images at higher magnifications. Preliminary observations performed at mid-thickness, quarter thickness and close to the outer surface confirmed the homogeneity of both steels along the thickness as suggested in the previous section. Consequently, quantitative observations were performed only around mid-thickness within the (RD-ND) plane.

Figure I-4 shows the results of optical and SEM observations on Steel A. The steel is essentially composed of ferrite grains with rare pearlite colonies observed at some grain boundaries (Figure I-5). No pronounced banded structure was observed, even if ferrite grains seem to be elongated along the rolling direction. Some elongated entities that are relatively dark in SEM images were found all over the observed region. Closer views of these entities revealed the presence of sub-grain boundaries. These entities with a typical length of $30 \mu\text{m}$ were surrounded by smaller equiaxed ferrite grains ($2 - 5 \mu\text{m}$) and rare elongated ferrite grains with a typical length of $10 \mu\text{m}$ along RD.

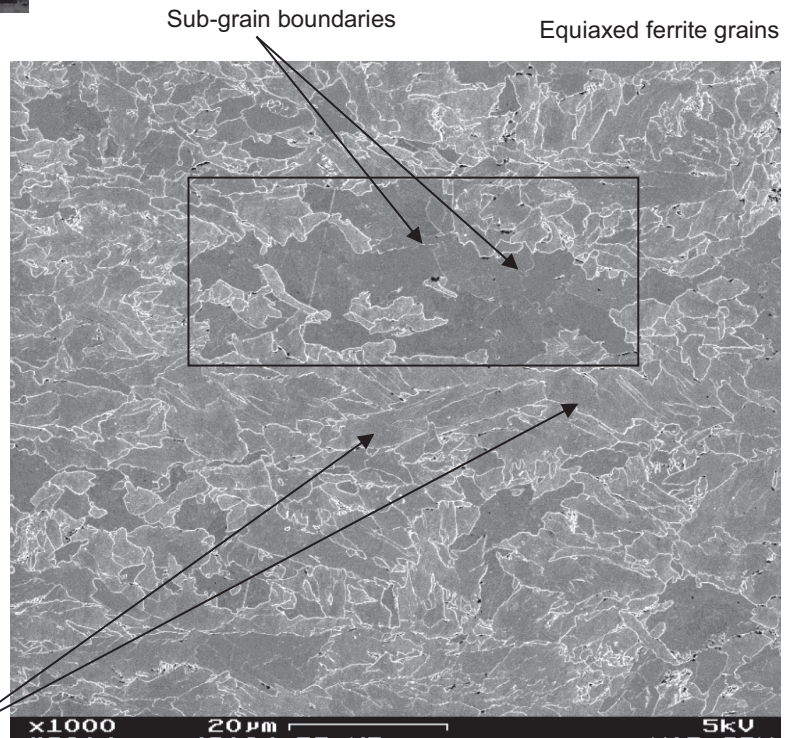


Zoom on the entity



Elongated entities

Elongated ferrite grains



Zoom on the entity

Figure I-4: Optical and SEM observations of Steel A microstructure: Elongated entity surrounded by small circular ferrite grains

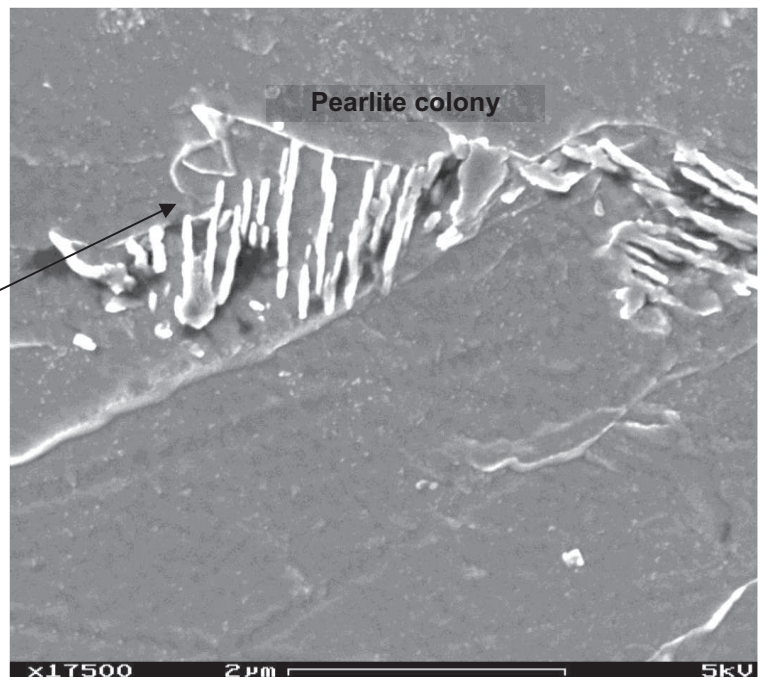
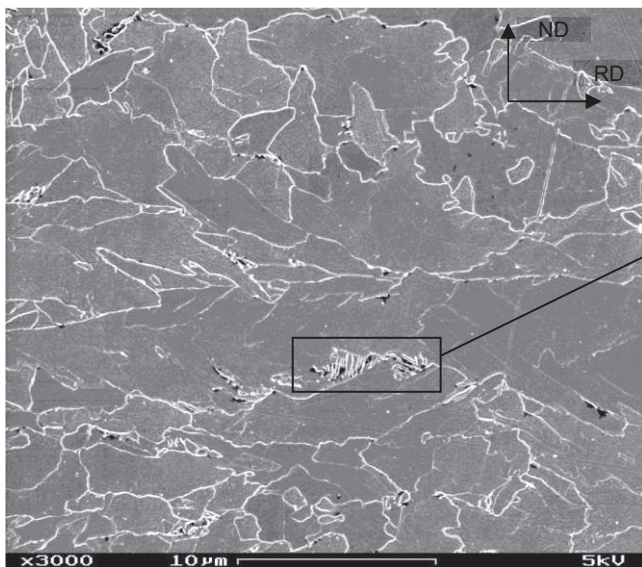


Figure I-5: Pearlite colony observed on grain boundaries (Steel A)

Figure I-6 shows the microstructure of Steel B. The microstructure as for Steel B is essentially ferritic, with no pronounced banded structure. The elongated entities observed in Steel A are also present in Steel B. These entities, which are thinner in Steel B, exhibited more pronounced sub-grain boundaries. Equiaxed ferrite grains (1 – 4 μm) were also observed.

Elongated entities observed within both steels have been characterized in more detail in chapter IV. At this step, we can keep memory that they are clusters of sub-grains that could be somewhat detrimental if well oriented for cleavage fracture. In that case, the higher density of these entities might lead to easier cleavage crack propagation.

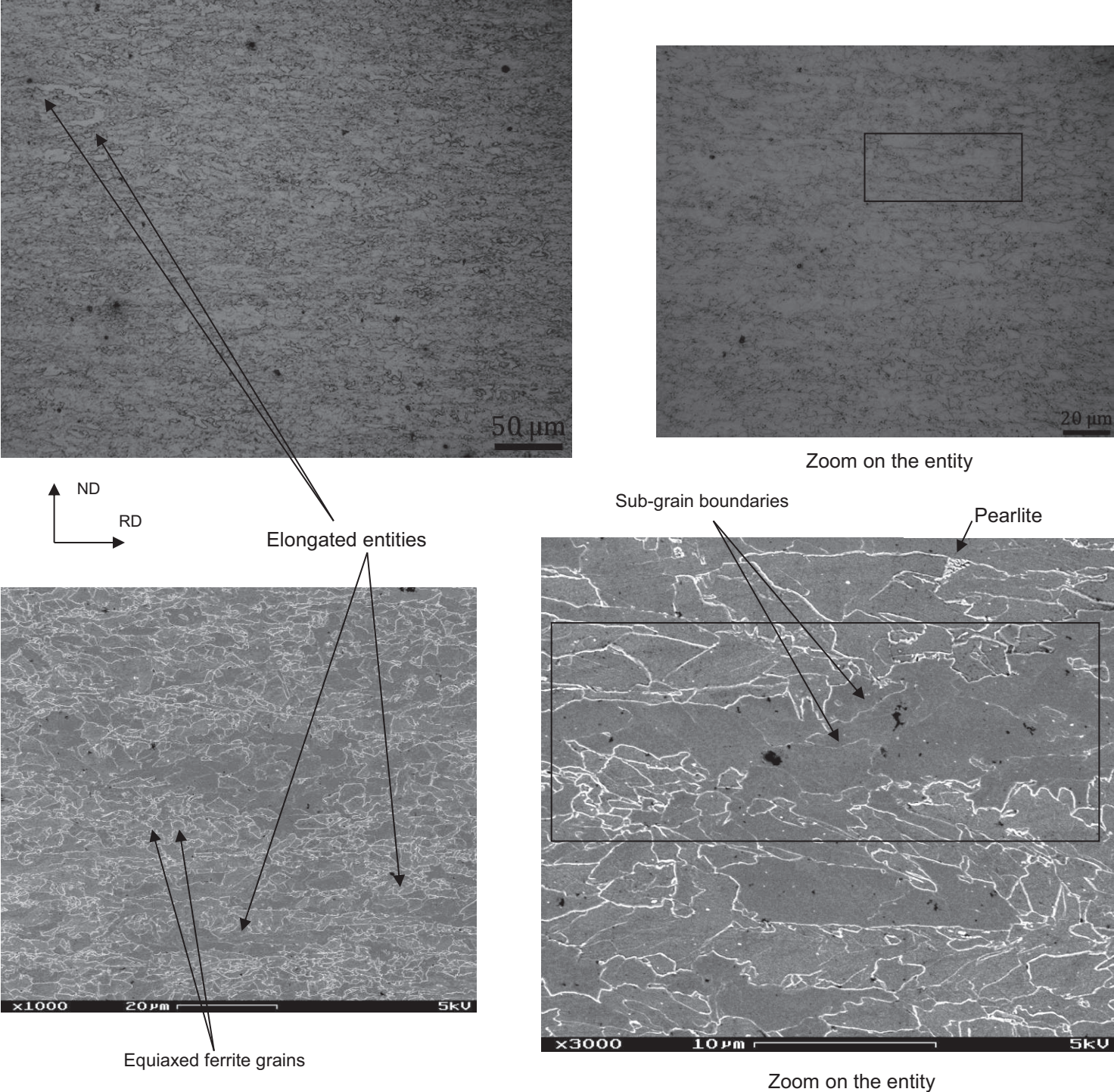


Figure I-6: Optical and SEM observations of Steel B microstructure: Elongated entity surrounded by small circular ferrite grains

I.6. Average texture

Texture analysis has been done to investigate the anisotropy in crystal orientation distribution in the two steels. The orientation distribution functions (ODF) sections at $\varphi_2 = 45^\circ$ (Bunge angle notation) have been determined by X-ray diffraction. After conventional cloth polishing down to 1 μm diamond paste, further polishing using OPS colloidal silica solution was carried out to remove superficial hardening and increase the surface quality of the sample. The analysis was performed along the (RD-TD) plane at mid-thickness.

The results of ODF sections at $\varphi_2 = 45^\circ$ are presented in Figure I-7 and Figure I-8 respectively for Steels A and B. Even if Steel A has a relatively stronger average texture than Steel B, no sharp texture has been observed in both steels. This suggests that the plastic anisotropy of these steels might be low, at least for small strains, i.e., before extensive crystal rotation induced by plastic deformation.

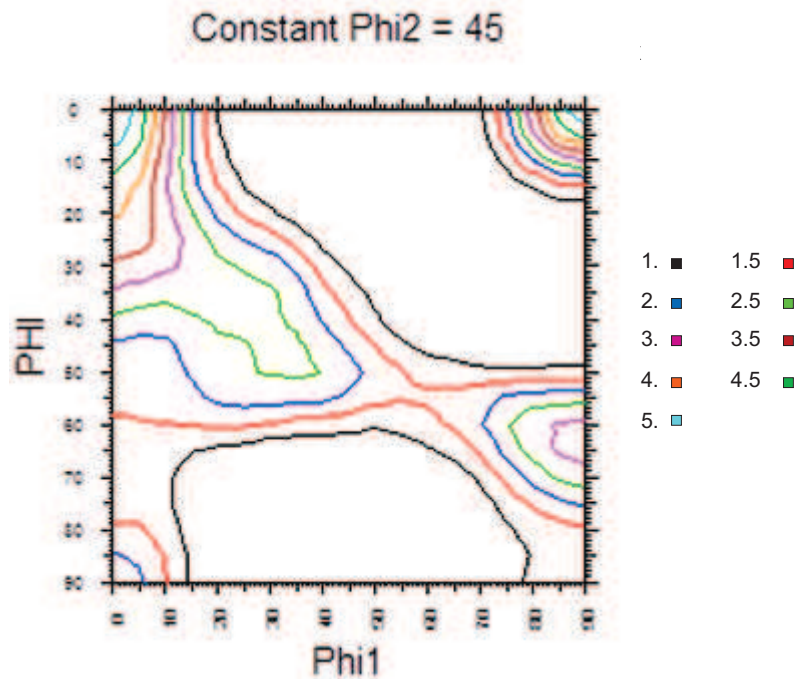


Figure I-7: ODF section ($\varphi_2 = 45^\circ$) of Steel A

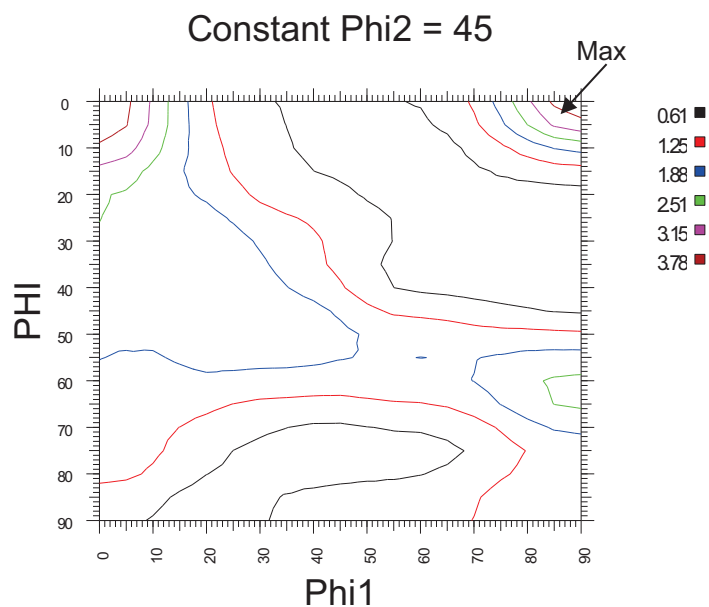


Figure I-8: ODF section ($\varphi_2 = 45^\circ$) of Steel B

I.7. Summary and conclusion

The two steels under study are API X70 grade used for linepipe manufacturing. The chemical compositions of both steels are close to each other, with slightly higher contents of carbon and nickel in Steel A; the level of sulfur is lower than 30 ppm. The observed inclusions are mainly MnS and some complex particles containing aluminum, oxygen, magnesium and calcium. Titanium-rich inclusions were also observed in Steel B. The volume fraction of inclusions, around 2×10^{-4} , is similar for both steels. However, the number of inclusions is 40% higher within Steel B, suggesting a lower inter-inclusion distance for this steel. The size distribution of inclusions is also more homogeneous in Steel B compared to Steel A, which contains both coarse and fine inclusions. This distribution of inclusions is to be correlated to the onset of coalescence during ductile fracture in chapter III. The average values of hardness of the two steels were found similar, around (210-220) $HV_{0.3}$ and no obvious evolution in hardness across the thickness was found. The microstructure of these steels is essentially ferritic. Some elongated entities wherein sub-grain boundaries were observed, covered all the volume of the steel. These entities which might be a problem for cleavage fracture are investigated in chapter IV. The average texture is rather weak for both steels.

Chapter II – *Toughness characterization of as-received materials*

Table of Contents

II.1.	Literature survey	18
II.1.1.	Battelle drop weight tear tests (DWTT)	18
II.1.2.	Brittle-out-of plane cracking during impact tests	23
II.2.	Results of drop weight tear tests	24
II.2.1.	Impact toughness of Steels A and B	24
II.2.2.	Fracture modes during DWTT and effect on impact toughness	24
II.2.3.	Effect of the loading direction	30
II.2.4.	Summary	31
II.3.	Results of Charpy tests	31
II.3.1.	Charpy impact toughness of Steels A and B	32
II.3.2.	Fracture mode and effect on impact toughness	33
II.3.3.	Summary of Charpy results and comparison to DWTT results	39
II.4.	Brittle out-of-plane cracking during fracture toughness tests	42
II.4.1.	Brittle out-of-plane cracking during tests on pre-cracked CT specimens	43
II.4.2.	Comparison with impact tests	43
II.5.	Discussion and conclusions	44

This chapter focuses on the toughness of the two as-received steels. Impact toughness was investigated with both Battelle drop weight tear tests (DWTTs) and Charpy tests. Fracture toughness was characterized by quasi-static tests on compact tensile (CT) specimens.

Before studying the fracture toughness of our steels, a literature survey on Battelle drop weight tear tests commonly used for pipeline steels characterization is reported. This literature survey also includes a study of brittle out-of-plane cracking observed after impact tests.

The results of Battelle drop weight tear tests and Charpy tests are then reported for Steels A and B. Detailed toughness values are reported in Appendix A. In this chapter, special attention has been paid to the fracture mode analysis and to the effect of brittle out-of-plane cracking on impact toughness.

Finally, fracture modes occurring during quasi-static tests on compact tensile specimens have been analyzed and compared to the ones exhibited in impact tests.

Résumé

La résilience et la ténacité de nos aciers sont à l'honneur dans ce deuxième chapitre. Les résultats d'essais de flexion par choc sur éprouvettes DWTT et Charpy des deux aciers sont analysés, de même pour les essais de ténacité qui ont été effectués sur des éprouvettes CT sous sollicitation quasi-statique.

Dans un premier temps, une étude bibliographique a été faite sur les essais DWTT et leur instrumentation. Cette étude a permis de mettre en évidence des ruptures fragiles hors-plan qui se manifestent pour les températures situées dans la transition ductile-fragile.

Une étude approfondie de ces modes de rupture fragile hors-plan après essais DWTT a été faite sur nos aciers. Les deux ruptures fragiles hors-plan généralement observées sont : Le délaminage qui se propage par clivage dans un plan parallèle au plan de laminage et la rupture fragile en biseau (BTF) qui se propage par clivage dans des plans θ reliés par de microfissures ductiles. Ces plans θ sont inclinés de 40° autour de l'axe RD par rapport au plan de laminage, contrairement à l'anti-plan θ qui est, lui, incliné de 40° autour de l'axe TD. Contrairement au délaminage qui n'est pas pris en compte lors de l'évaluation de la taille de la zone fragile après l'essai DWTT, le BTF est pris en compte et par conséquent affecte directement la résistance à l'impact de l'acier selon la norme API5L. Le BTF qui est observé après essais DWTT sur des éprouvettes prélevées dans la direction TD, ne l'est plus quand l'éprouvette est prélevée dans la direction RD. Ceci semble souligner le rôle important que jouerait la microstructure sur l'apparition du BTF, avec entre autres le rôle des plan θ . Pour une éprouvette prélevée dans la direction TD, le BTF se propage dans les plans θ ; par contre pour une éprouvette prélevée dans la direction RD, l'anti-plan θ remplace le plan θ et dans cette nouvelle configuration le BTF n'a pas été observé. Pour ce qui est du délaminage, l'amorçage peut se faire sur la zone ductile triangle ou le slant ductile. Pour certaines éprouvettes le délaminage a subi une rotation pour rejoindre le plan principal de sollicitation. Avec le slant ductile, le délaminage est l'un des sites d'amorçage du BTF.

L'analyse des ruptures fragiles hors-plan sur éprouvettes Charpy a aussi signalé la présence de délaminage et de BTF. Deux types de délaminage ont été identifiés : Le délaminage de type 1 qui amorce au niveau de l'entaille et sans avancée ductile, et le délaminage de type 2 où une avancée ductile est observée avant le délaminage. Le délaminage de type 1 observé aux basses températures (-100°C) est généralement le site d'amorçage d'autres ruptures

fragiles hors-plan qui se propagent dans l'ensemble de l'éprouvette étant donnée la petite taille du ligament. Le délaminage après une propagation dans le plan de laminage peut subir une rotation progressive pour rejoindre le plan principal de sollicitation. Une autre possibilité est de voir le BTF qui amorce sur une microfissure de délaminage.

Une comparaison entre les résultats d'essais Charpy et DWTT montre que les ruptures fragiles hors-plan sont visibles à de plus hautes températures pour l'essai Charpy, conduisant ainsi à une température de transition ductile-fragile plus élevée. La longueur du ligament des éprouvettes Charpy semblerait insuffisante pour une propagation du BTF après de grandes avancées ductiles comme c'est le cas pour les éprouvettes DWTT.

Les ruptures fragiles hors-plan ont aussi été mises en évidence sur éprouvettes de ténacité CT sollicitées en quasi-statique. Ceci montre que ces modes de rupture ne sont pas nécessairement liés aux phénomènes dynamiques. La compréhension de l'origine des ruptures fragiles hors-plan passera par l'analyse de l'anisotropie de la rupture par clivage avec une étude de la réponse des plans θ et de laminage aux sollicitations de traction en mode I.

II.1. Literature survey

This literature survey concerns Battelle drop weight tear tests and focuses on the brittle out-of-plane cracking observed during impact tests. Readers interested by a detailed literature survey of the Charpy test procedure could refer to [1].

II.1.1. Battelle drop weight tear tests (DWTT)

a) Introduction

Avoiding the propagation of long brittle cracks is one of the major issues in pipeline industry. To ensure the safety of linepipes, the test originally used was the so-called “Athens test”. It is a full-scale burst test on a section around 200 m in length, pressurized with natural gas (Figure II-1). From this test, it was possible to know whether a crack initiated in the linepipe would propagate or not in a catastrophic manner i.e. would arrest after only a long distance.

Burst tests are expensive and not convenient for experimental campaigns where many temperatures and materials are evaluated. Consequently, an alternative laboratory-scale test was needed, especially for alloy development and quality control. The work of Battelle Memorial Institute on this alternative laboratory-scale test resulted in the so-called drop weight tear test. The Battelle drop weight tear test (DWTT) has been adopted by the American Petroleum Institute in 1965 as recommended practice API 5L3.

Nowadays, DWTT is widely used to evaluate the impact toughness of pipeline steels within the ductile to brittle transition. As for Charpy tests, a notched three point bending specimen is impacted by a hammer. Since specimens are larger for DWTT, a steady-state propagation regime could more likely be reached than for Charpy tests. Thus, it gives a better prediction of pipeline burst test results than classical Charpy tests for linepipe applications [3]. A high number of papers have been published on DWTT [4-11].

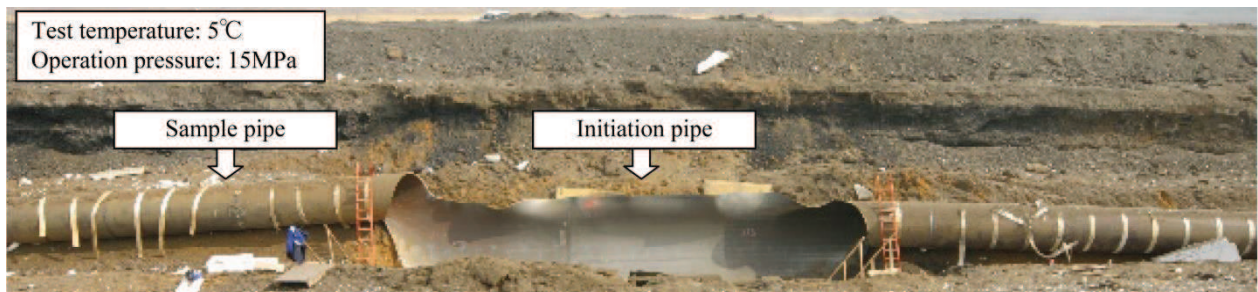


Figure II-1: Pipe fracture appearance after a full scale burst test (temperature 5°C, pressure 15 MPa) [2]

b) Procedure and typical experimental results

The experimental procedure of DWTT is available from API 5L3 standard [5]. The specimen is impacted with a hammer and the percent shear area is evaluated. As prescribed by the standard, the specimen thickness should be the same as that of the wall pipe unless the pipe thickness is higher than 19 mm. Specimens taken from pipe with wall thickness greater than 19mm shall be either: the full wall thickness or reduced in thickness down to 19mm with a reduction of the test temperature. Two kinds of notch geometry could be used for the specimen: Pressed notch (made by indentation) or Chevron notch (made by machining). Complete dimensions of the specimen are presented in Figure II-2. Since the specimen dimensions are much greater than those of a Charpy specimen, the impact energy that is necessary for this test is significantly higher than that for Charpy tests, and specific equipment (hammer attached to a falling weight) is used for this test (Figure II-3).

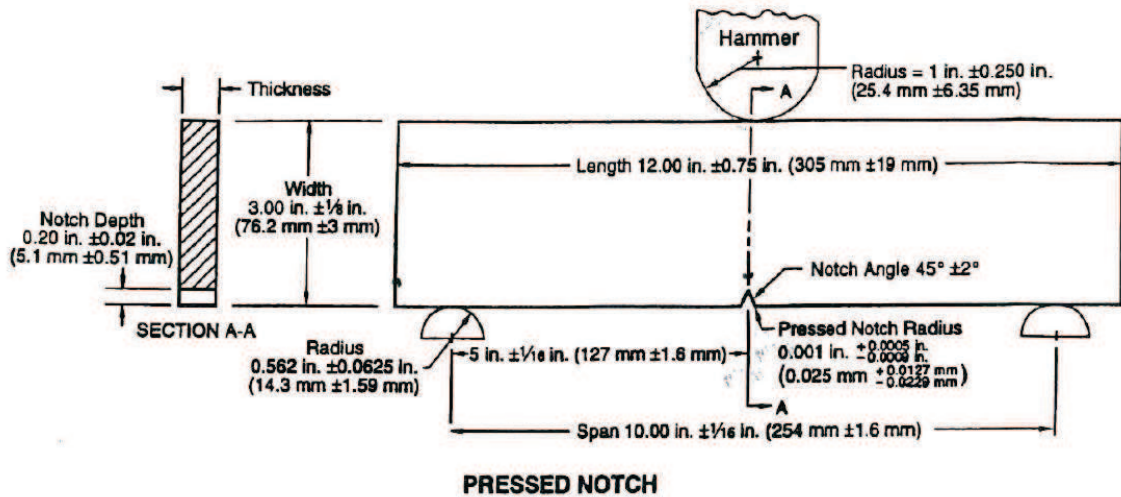


Figure II-2: Dimension of Battelle specimens, hammer and anvils according to API 5L3 standard [5]



Figure II-3: Battelle drop weight tear test equipment

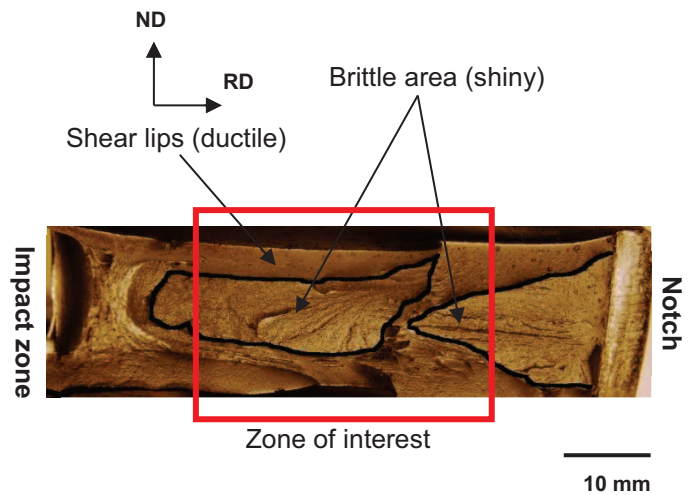


Figure II-4: Typical fracture surface of pipeline Steel A at -30°C , detailed study reported in the second part of the chapter

After DWTT, the fracture surface of the specimen is observed by eye and the percentage of shear area is measured. A minimal shear area percentage of 85% is required for the fulfillment of the API 5L3 standard requirement [5]. In fact, it has been assumed that for such values of shear area, the material is sufficiently tough to resist crack propagation in a full scale burst test [3]. As can be observed in Figure II-4, the brittle area could be easily identified by its shiny aspect. The area with a silky or dull aspect is shear (ductile) fracture. Due to boundary conditions (pressed notch and hammer impact zones), zones at both ends of the fracture surface are not taken into account for the evaluation of the percent shear area.

c) Instrumentation of Battelle drop weight tear tests

By using conventional DWTT equipment, the shear area percentage is the only measurement extracted from the test. But over the years, this measurement became no longer sufficient and more detailed information about the mechanical behavior of the steel seemed necessary, for instance the fracture energy and the crack propagation velocity.

- Fracture energy

A first way to measure the fracture energy from DWTT is to use a pendulum drop weight tear tester. The drawback of this method is that only global fracture energy could be extracted. There is no way to distinguish the energy consumed during crack initiation and the one consumed by crack propagation. For this reason, the energy absorbed during instrumented DWTT is more commonly extracted from load-displacement curves [6]. As observed in Figure II-5, before the maximum load all the area under the curve is associated to crack initiation. The complementary area corresponds to the energy that is necessary for crack propagation. Now, the issue is to find a method to measure the load and displacement values.

The load evolution is generally measured with sensors fixed on the hammer. In most cases, the value of displacement is generated from the load measurement using the second Newton's law. In fact, if neglecting all contact issues, the deceleration of the hammer is proportional to the applied load. From this deceleration, the velocity and then the displacement of the hammer could be extracted. This method is an indirect way to determine displacement and might lead to some inaccuracy. This explains why some authors as Wilkowski [7] used high-speed camera to measure the specimen displacement.

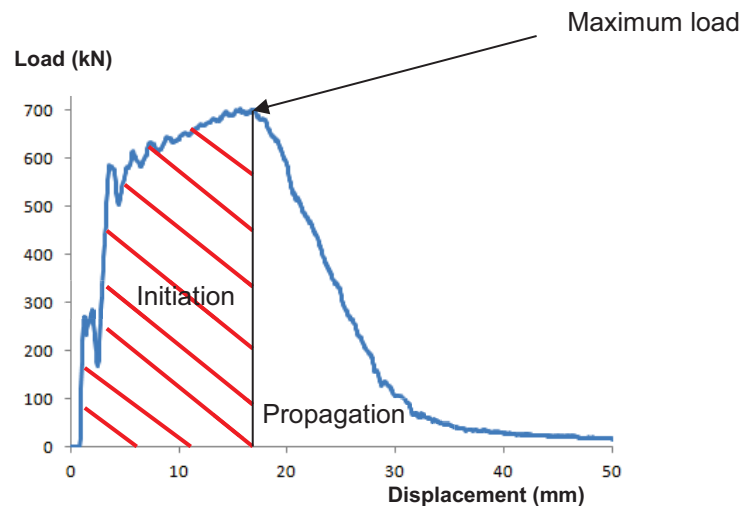


Figure II-5: Load-displacement curve at -20°C (Steel A) and data processing to extract fracture energy

- Crack propagation velocity

Measurement of the crack propagation velocity could be interesting, especially to compare the crack speeds observed during drop weight tear tests and during full scale burst tests. Two techniques could be used to measure this velocity: High speed camera or electrical wires (Figure II-6). Crack propagation is divided into three stages: Crack initiation, steady-state propagation and crack arrest (or deceleration). Figure II-7 shows the evolution of the crack length and crack tip opening angle (CTOA) of two specimens during drop weight tear tests. The three stages of crack propagation are well visible on the crack length evolution curve. Crack initiation is associated to a zero value crack speed; Steady-state propagation is associated to a constant value of the crack speed; Crack deceleration or arrest is associated to a decreasing value of the crack speed.

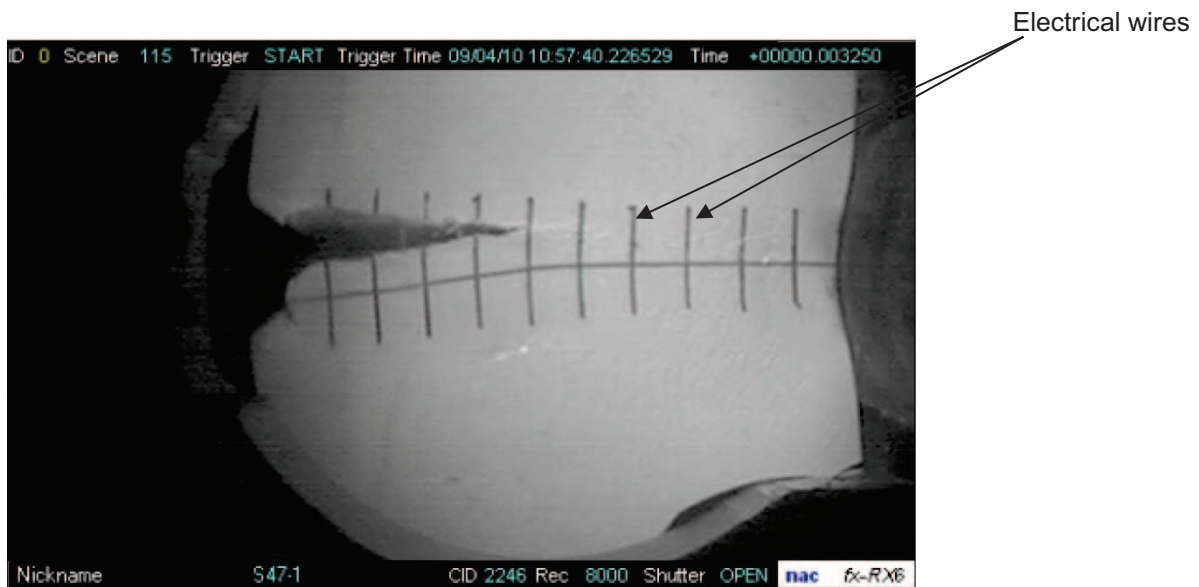


Figure II-6: Fracture crack velocity measured with electrical wires and high-speed camera [7]

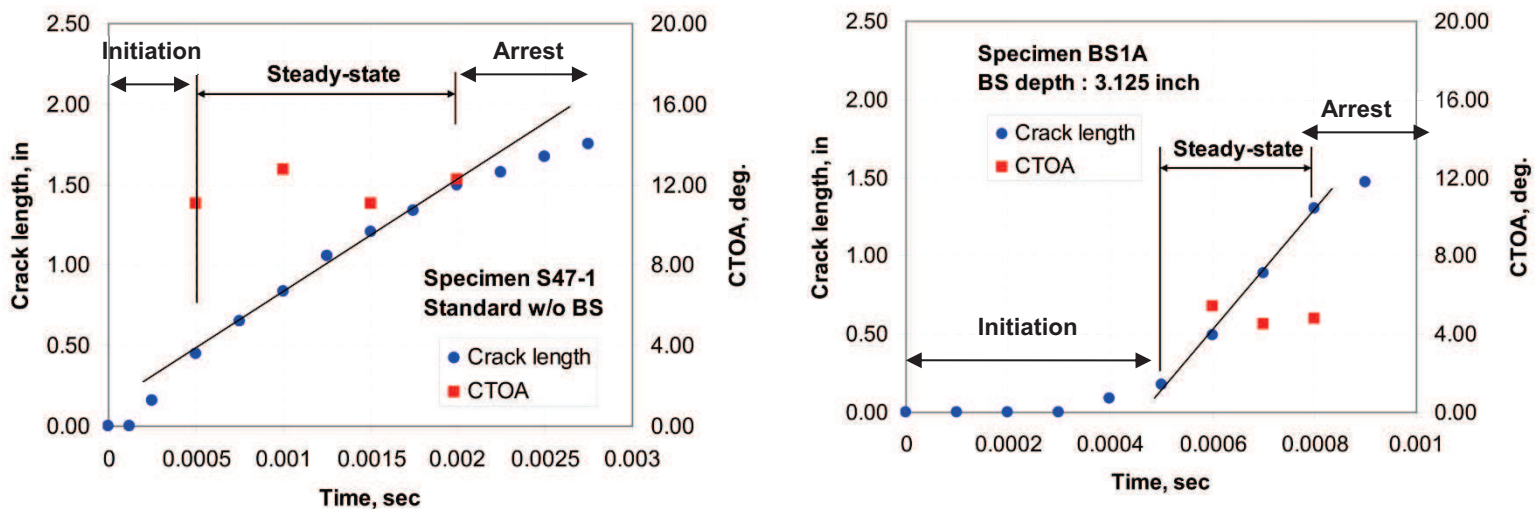


Figure II-7: Evolution of the crack length and CTOA of two specimens during drop weight tear tests [7]

Moreover, Figure II-7 shows that the CTOA value remains constant during steady-state propagation. There seems to exist a relationship between fracture speed and CTOA within the steady state propagation stage. Wilkowski et al. [7] showed that the higher the CTOA value, the lower the crack speed during the steady state stage (Figure II-8). Other authors [8] proposed a correlation between the CTOA at steady state and DWTT propagation energy (Figure II-9). For all these reasons, CTOA at steady state could be considered as an intrinsic parameter for impact toughness. Some authors as O'Donoghue et al [12], which worked on fracture propagation models for linepipes chose a crack arrest criterion based on the CTOA at steady state during DWTT. The crack propagating during full scale burst tests was assumed to be arrested as soon as the CTOA value predicted by the model becomes higher than the critical CTOA value extracted from DWTT.

d) Abnormal fracture appearance

According to the API 5L3 standard, for a DWTT test to be valid, the fracture surface should exhibit cleavage fracture under the notch tip, which will turn into ductile fracture during propagation of the crack, with the exception of specimens exhibiting complete ductile fracture. Every time when the ductile shear crack turns into a cleavage crack, it is considered as abnormal fracture appearance (AFA). Two types of AFA are generally observed: The first type occurs when the ductile shear crack is initiated from the notch root; the second type, so-called "inverse fracture", is similar to the first type, but in that case there is a cleavage crack close to the impacted region (Figure II-10).

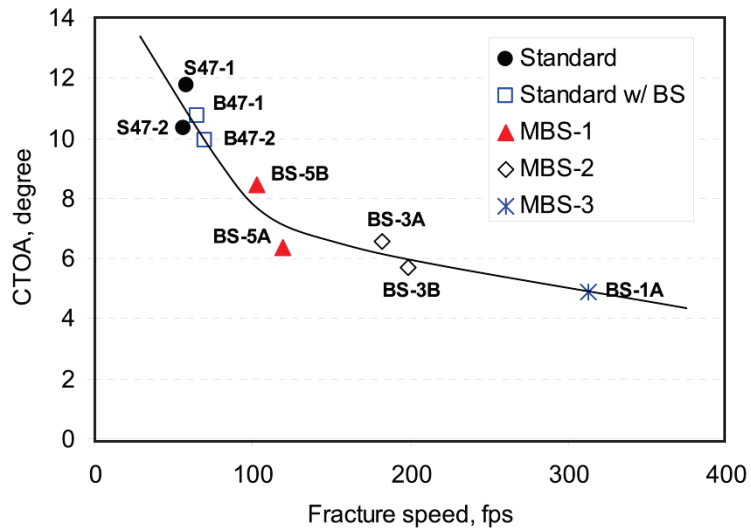


Figure II-8: CTOA vs. fracture speed (feet per second) during steady state propagation [7]

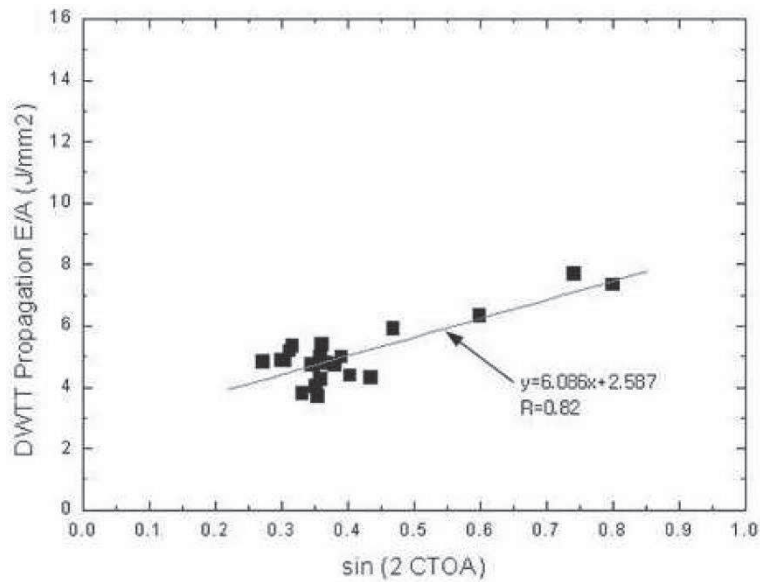


Figure II-9: Correlation between CTOA at the steady state and DWTT propagation energy [8]

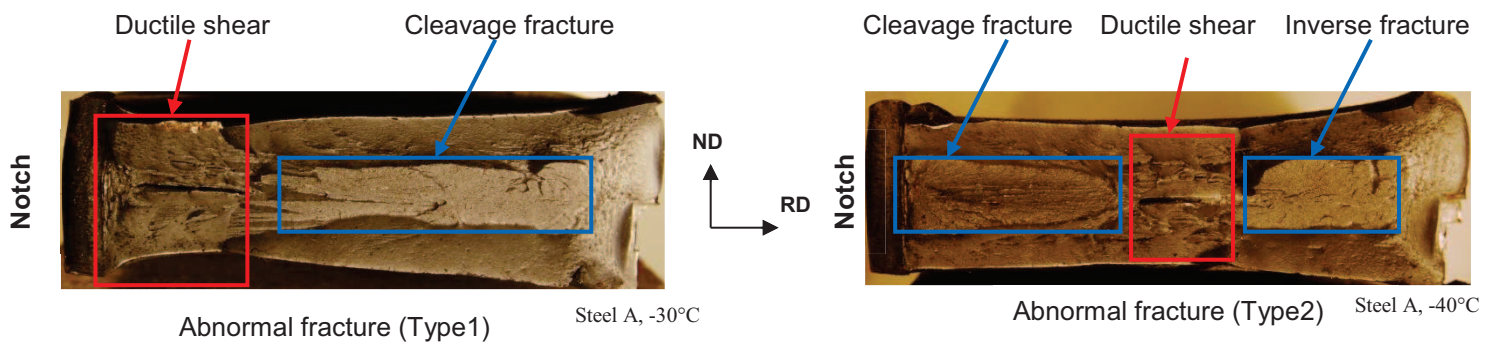


Figure II-10: Abnormal fracture appearance of pipeline steel tested at -40°C (Type 1 and type 2)

This abnormal fracture appearance is frequently observed on DWTT fracture surface of modern pipeline steels [8-9]. The first type can be partially solved by inserting a fatigue pre-crack or a chevron notch instead of a conventional pressed notch, so that cleavage fracture could more easily initiate from the notch root. Even if including a chevron notch enables one to reduce Type 1 abnormal fracture appearance, the machining cost is higher and the shear area percentage is generally 5-8% lower than for a pressed notch [8]. Type 2 abnormal fracture mode with inverse fracture is not removed by using chevron notches. According to [8-9], this fracture mode is mainly induced by the work hardening due to hammer impact. Consequently, the high plastic deformation introduced by hammer impact is claimed to play an important role during this inverse fracture. The shear area percentage is decreased by the presence of inverse fracture and thus toughness properties are deteriorated. A closer look on the inverse fracture surface yet shows that the brittle crack does not obviously initiate from the back of the specimens, and it propagates out of the main loading plane. It could be out-of-plane brittle cracking instead of inverse fracture, at least in some cases. Consequently, it seemed necessary to study brittle-out-of plane cracking.

II.1.2. Brittle-out-of plane cracking during impact tests

Brittle out-of-plane cracking is associated to all brittle cracks which propagate within a plane other than the main loading plane (i.e. the plane perpendicular to the direction of applied load). This phenomenon is more pronounced within the ductile to brittle transition. The most widely known and studied brittle out-of-plane cracking is delamination fracture [13-24]. This delamination fracture propagates within the rolling plane (Figure II-11). Another brittle out-of-plane cracking is the so-called brittle tilted fracture (BTF), also called brittle slant in some papers [2, 24]. The propagation plane of BTF is macroscopically tilted by an average angle of 40° around RD, with respect to the rolling plane [2,24].

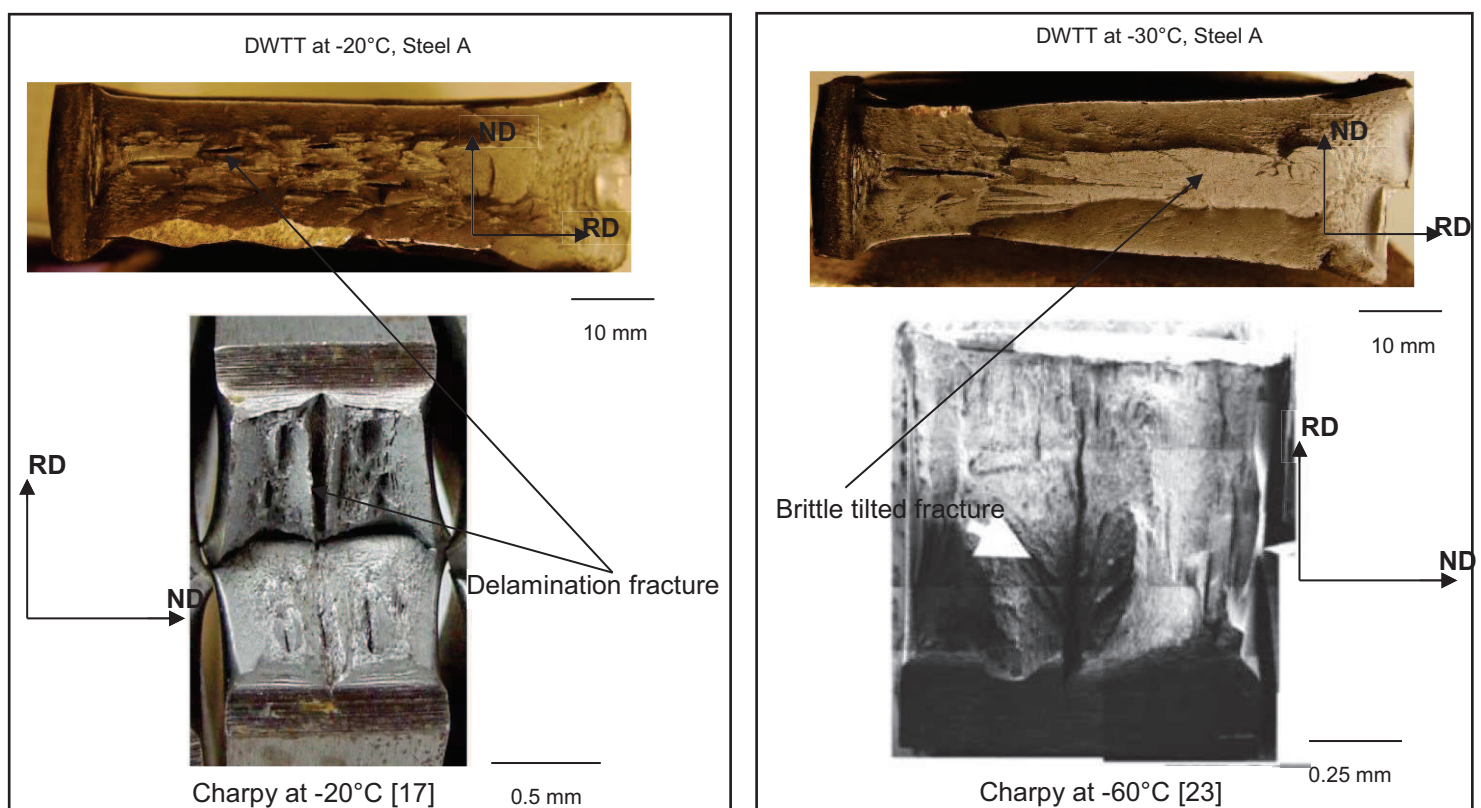


Figure II-11: Delamination (left) and brittle tilted fracture (right) of DWTT and Charpy specimens

a) Delamination cracking

Delamination cracking generally occurs by cleavage or by ductile fracture along MnS-rich bands. In some cases, cleavage fracture could be completed or replaced by intergranular fracture. Cleavage fracture initiates from interfaces between phases, or from intersections between {100} and {111}

planes, or from flat inclusion decohesion zones. Some authors as [14] observed delamination after large plastic deformation leading to uncommon cleavage facets. This fracture mode was called quasi-cleavage. Delamination fracture is sensitive to microstructure (banded structure, segregation and shape, dimensional anisotropy of grains), presence of inclusions (mainly MnS) and texture (average distribution of {100} planes) [16].

According to the API 5L3 standard, delamination cracks are not taken into account for the shear area percentage measurement. Even if some authors like [13] and [17] support that delamination cracks do not really deteriorate the impact toughness and sometimes could increase the fracture resistance of steels, the main tendency reported in literature is that delamination fracture decreases the upper shelf energy. According to Figure II-11, delamination cracks could rotate to join the main loading plane or could be the initiation point of other brittle cracks. This might suggest a negative effect of delamination on impact toughness.

b) Brittle tilted fracture

Brittle tilted fracture which occurs by cleavage might be influenced by the microstructure and texture (distribution of {100} planes) [2]. It is clearly detrimental to the fracture resistance of pipeline steels. In DWTT data processing, the brittle tilted area is taken into account for the measurement of the percent shear area and thus, reduces impact toughness. Hara [13] also showed that the presence of brittle tilted fracture drastically decreases the fracture energy of pre-cracked DWTT specimens. Finally, the presence of brittle tilted cracks may have further consequences on the propagation of the main crack.

Impact tests have been carried out on our as-received steels to investigate their impact toughness and to study brittle out-of-plane cracking. Special attention has been paid to analyze the effect of these brittle out-of-plane cracks on toughness properties. Occurrence of brittle out-of-plane cracking has also been investigated during quasi-static tests via CT tests, to assess the influence of dynamic loading conditions.

II.2. Results of drop weight tear tests

Battelle drop weight tear tests were performed on pressed notch specimens taken along the transverse direction TD, according to API 5L3 standard. Full thickness geometry was considered for Steel A (19.5 mm). For Steel B, the plate thickness was reduced from both sides from 23 mm to 19 mm. These tests were done on the instrumented DWTT equipment of OCAS, with a hammer of 985 kg hanging 2.19 meters above the specimen. The maximal energy provided by the hammer is 21 kJ and the speed at the impact is 6.5 m/s. Specimens were cooled down to various temperatures between 0°C and -100°C, after immersion into a batch of silicone solution for temperatures higher than -70°C or with a climatic chamber for temperatures lower than -70°C. Some interrupted tests (reported in appendix A) were performed on Steel B at -60°C to study the interaction between fracture modes. Finally, some specimens of Steel B taken along RD were tested after being flattened by four-point bending (because of the hot coil geometry), so that anisotropy issues on brittle out-of-plane cracking could be studied.

II.2.1. Impact toughness of Steels A and B

The evolutions of impact energy and shear area percentage with temperature are presented in Figure II-12 and Figure II-13 respectively for Steels A and B. The fracture appearance transition temperature (FATT) at 50% was found around -60°C for both steels. The temperature associated to 85% shear percentage (required by API 5L standard) was around -20°C for Steel A. This temperature seemed to be lower for Steel B, but there is not enough data at higher temperature to extract an accurate value. In a general tendency, the shear area percentage is slightly lower for Steel B than Steel A.

II.2.2. Fracture modes during DWTT and effect on impact toughness

The fracture surface of DWTT specimens generally exhibits many fracture modes which interact together. This section presents these fracture modes, their evolution with temperature and how they affect the impact toughness properties.

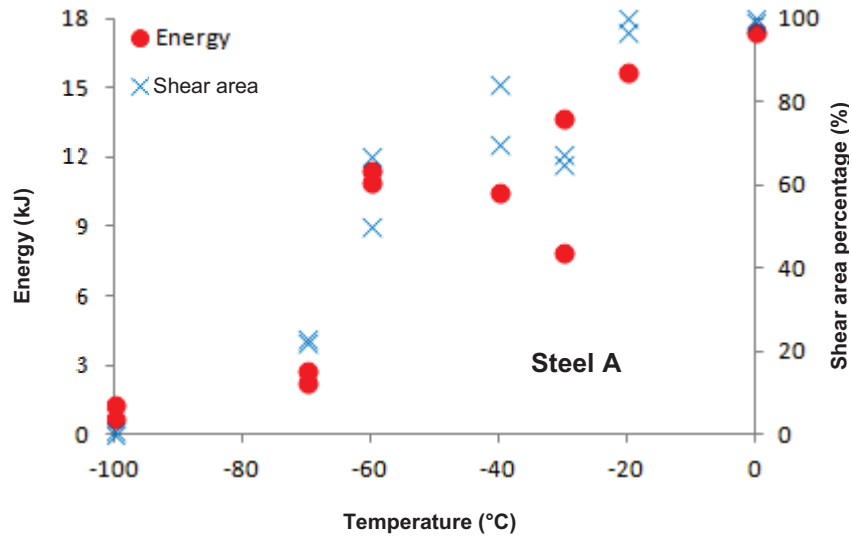


Figure II-12: Evolution of the impact energy and shear area percentage with temperature (Steel A)

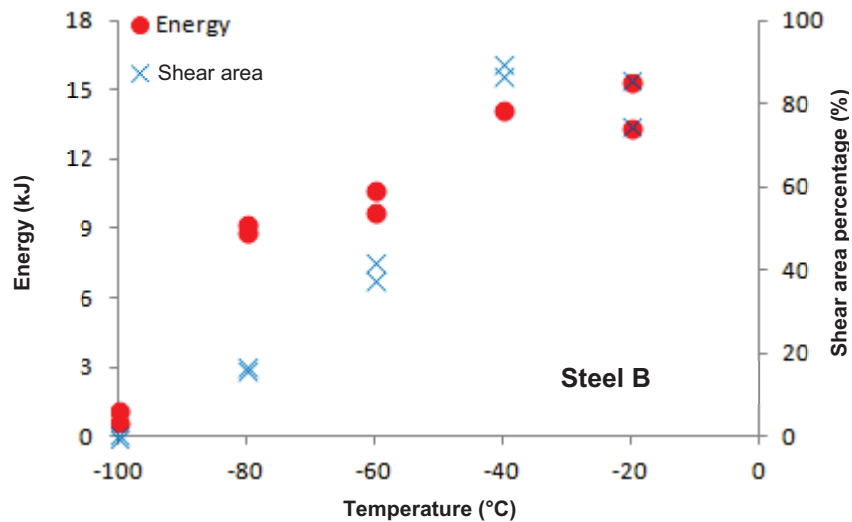


Figure II-13: Evolution of the impact energy and shear area percentage with temperature (Steel B)

a) Ductile slant and shear lips

Ductile slant is the desired fracture mode during drop weight tear tests. For both steels, this ductile slant was mixed with delamination even within the upper-shelf domain (Figure II-14). By decreasing the test temperature, brittle fracture modes appeared and the ductile slant fracture did no longer propagate over the entire thickness. This ductile slant propagated independently on both sides of the brittle area leading to shear lips (Figure II-14). These shear lips were also observed close to the impact area, possibly because the work hardening induced by the hammer did not enable ductile slant propagation. Ductile crack propagation is associated to a stable decrease in the load on the load-displacement curve (Figure II-15).

b) Triangular ductile crack advance

For almost all specimens, namely, for temperatures outside the lower shelf domain where full cleavage fracture occurred, a small ductile crack advance was observed at the notch root. This ductile advance with a triangular shape is presented in Figure II-16. A mid-thickness delamination was frequently initiated from this triangular ductile crack.

c) Flat brittle fracture

Within the ductile to brittle transition, it was rare to get specimen without triangular ductile crack advance at the notch root (this was only the case for two specimens of Steel A). In those two cases, a large flat brittle area replaced the triangular ductile crack advance (Figure II-17). According to the API 5L3 standard, all specimens in valid tests must exhibit brittle fracture at the notch root, which then turns into ductile slant. However, with the high ductility of modern pipeline steels, brittle fracture initiation at the notch is more difficult. The usage of a machined notch (chevron) or of a pre-cracked notch is the solution proposed in literature [8] but was not adopted here.

This flat brittle fracture could be followed by ductile slant, delamination and brittle tilted fracture, or could simply propagate along the entire ligament (Figure II-17). Presence of the flat brittle fracture is associated to an earlier drop of the load on the load vs. displacement curve (Figure II-18). When the brittle crack is followed by ductile slant, a stable decrease is observed on the curve (-30°C). In absence of ductile slant, the load abruptly drops to zero (-70°C and -100°C). As a consequence, the absorbed energy is lower when flat brittle crack initiates from the notch root.

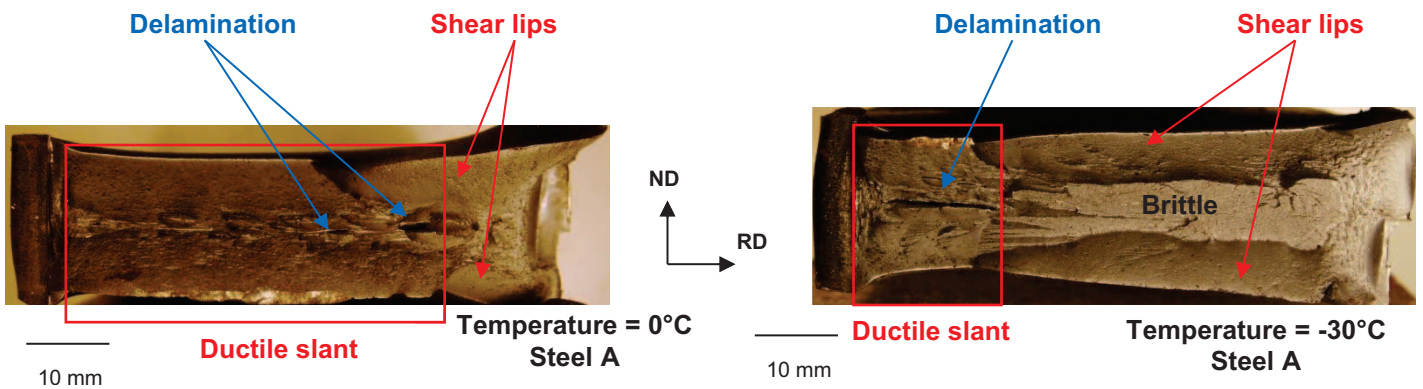


Figure II-14: Observation of ductile slant and shear lips after drop weight tear tests

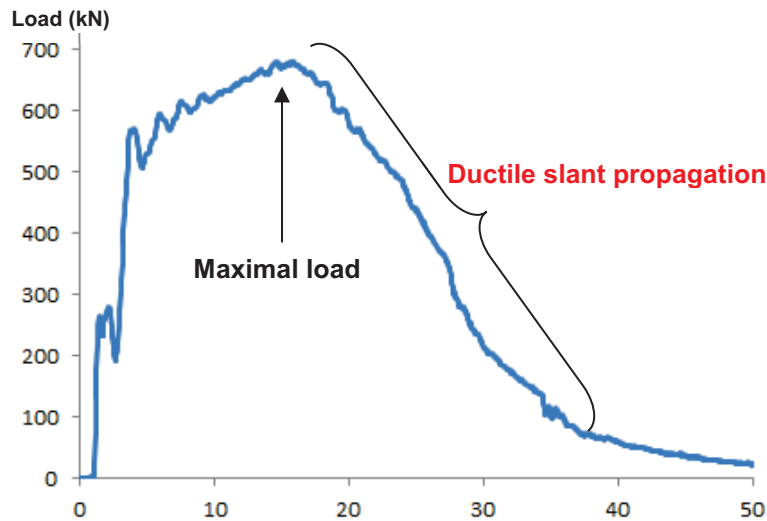


Figure II-15: Load displacement curve at -20°C, Steel A

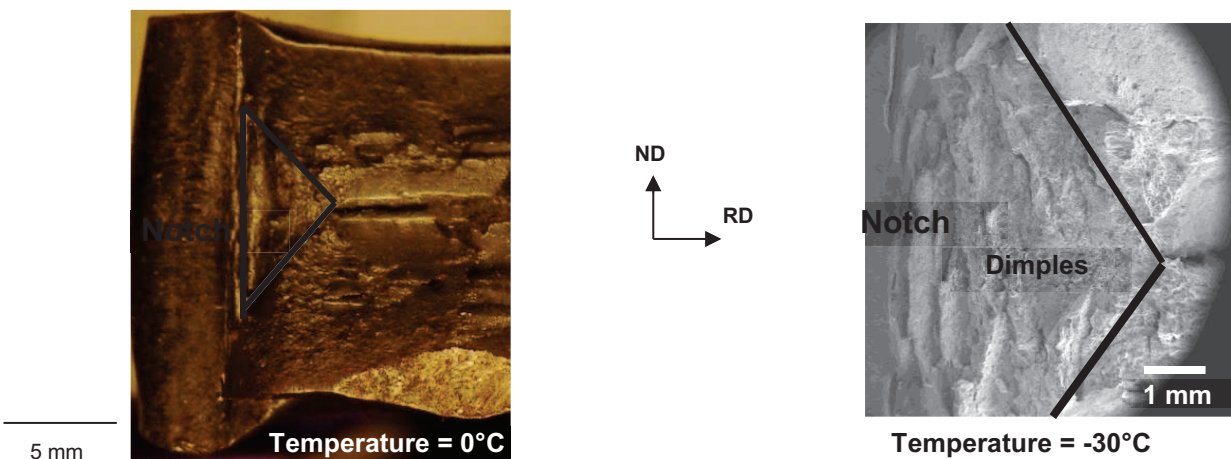


Figure II-16: Triangular ductile crack advance at the notch root, steel A

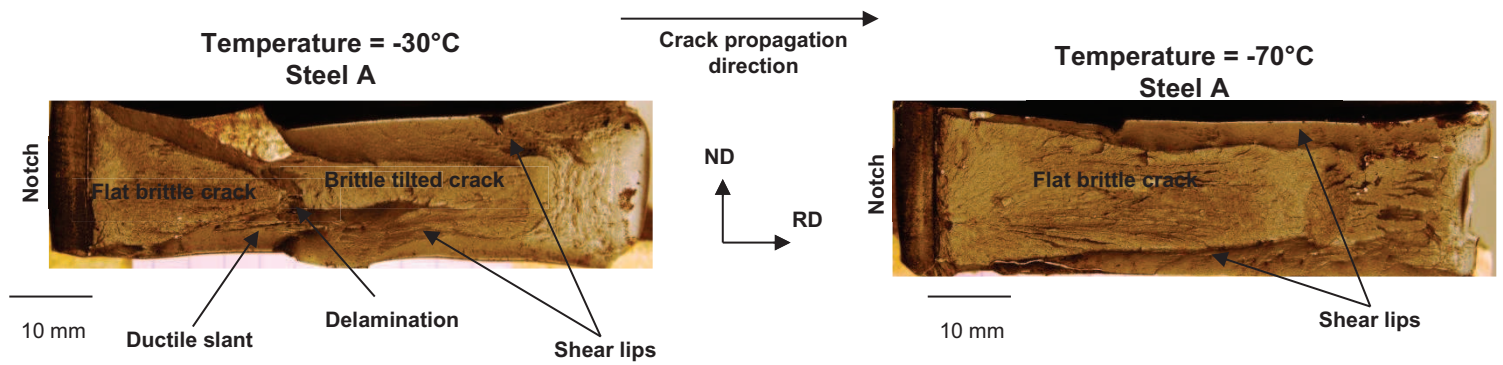


Figure II-17: Specimens with flat brittle crack initiated from the notch root

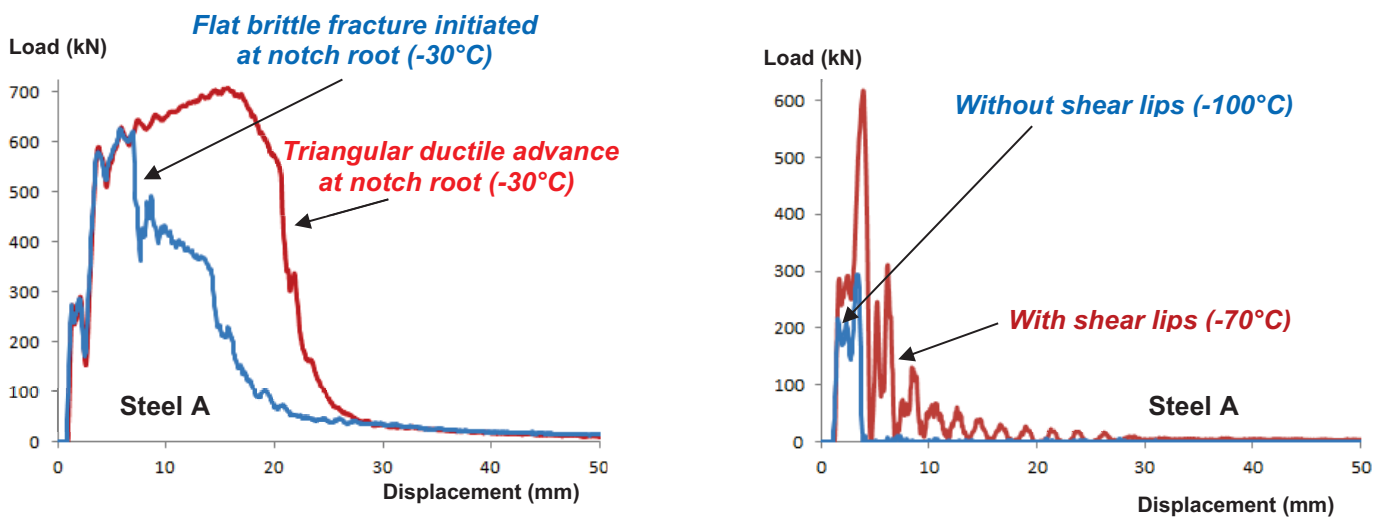


Figure II-18: Impact of flat brittle fracture from the notch root on load displacement curve

d) Delamination

For Steel A, delamination was observed for temperatures higher than -60°C . In fact, at -70°C and -100°C , the brittle crack initiated at the notch root propagated along the entire ligament and thus no delamination was observed. Steel B was more sensitive than Steel A to delamination. In fact, a delamination crack was still initiated from the triangular ductile crack at -80°C . Since the ductile triangular crack was initiated after prior plastic deformation, it is plausible to suspect that the plastic deformation facilitated the occurrence of delamination.

From interrupted tests reported in appendix A, delamination was generally initiated either from the ductile crack, or behind the ductile slant front. In some rare instances, it was initiated behind the flat brittle crack. Observation of the inside of delamination crack with SEM was difficult on DWTT specimens. Delamination does not seem to stop ductile slant fracture, which could propagate on both sides.

The occurrence of delamination was not associated to an abrupt drop of the load on the load vs displacement curves. Nevertheless, it might accelerate the decrease in load, since it introduces damage within the specimen. As a whole, the energy is less affected by delamination comparing to other brittle cracking modes.

e) Rotation of the delamination crack

The delamination crack was observed in some instances to rotate to join the plane perpendicular to the main loading direction. This fracture mode was sometimes observed close to the impact region of Steel A, but rarely in Steel B. The occurrence of this so-called delamination rotation was not obviously noticeable on the load vs displacement curves, perhaps because it happened rather close to the back

of the specimen. Delamination rotation brings additional brittle fracture area that is taken into account for shear area calculation.

f) Brittle tilted fracture (BTF)

Brittle tilted fracture macroscopically propagates along a plane tilted around RD by 40° with respect to the (RD, TD) plane. This plane is called “ θ -plane” thereafter. Brittle tilted fracture has been observed for temperatures lower than -30°C for Steel A and -20°C for Steel B.

Within the ductile to brittle transition temperature range, the BTF crack was commonly initiated either behind the delamination crack or close to the ductile slant front (Figure II-19). Within the propagation region of BTF, entities similar to macroscopic rivers were observed. These macroscopic rivers were more pronounced far from the initiation site (Figure II-19). SEM observations of the fracture surface were performed after tilting the specimen by 40° around RD, so that the BTF surface became perpendicular to the incident electron beam. A stair-shaped fracture mode has been observed around macroscopic rivers (Figure II-19 and Figure II-20). This suggests that BTF propagates along more than one θ -plane and that these parallel cracks along θ -planes are joined by ductile slant.

Brittle tilted fracture leads to an abrupt drop of the load on the load vs displacement curve. The larger the area of BTF, the higher the drop in load. Consequently, brittle tilted fracture reduces the impact energy.

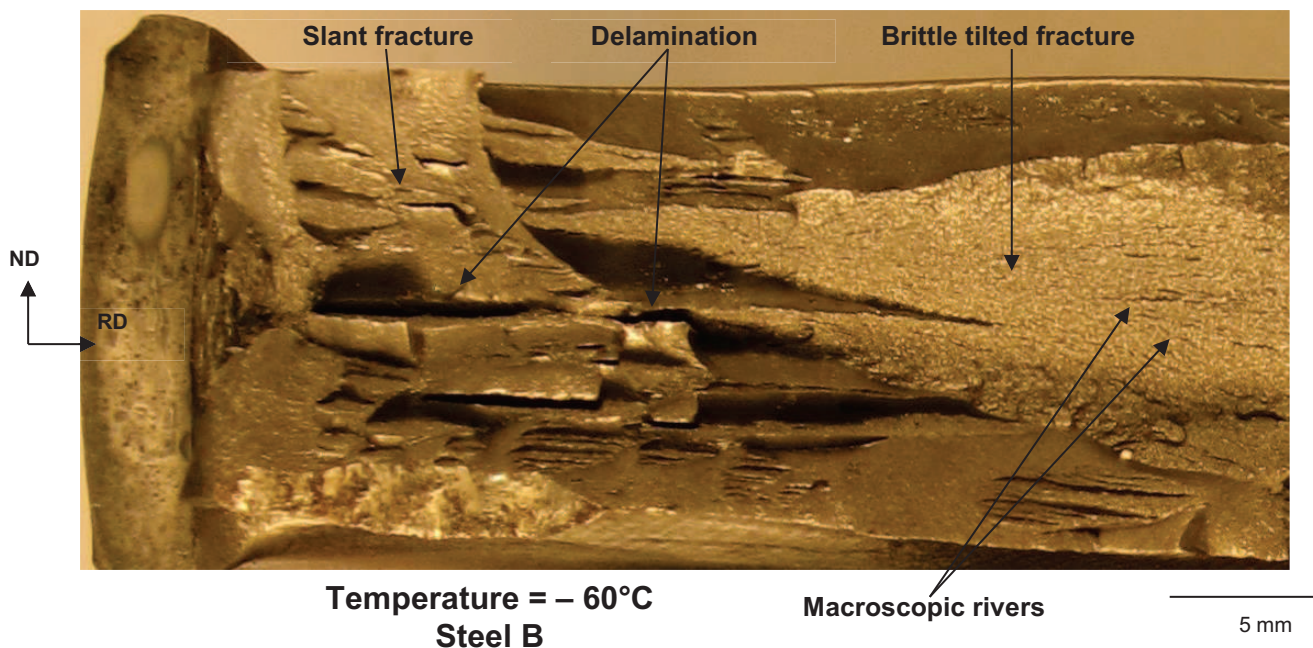


Figure II-19: Initiation of brittle tilted fracture from ductile slant and delamination

Summary of fracture modes observed in DWTT specimens and effect on load vs. displacement curves

Figure II-21 shows the seven typical load vs. displacement curve shapes observed after DWTT along TD. Brittle fracture leads to a drop in load which decreases the absorbed energy. By increasing the test temperature, the following fracture modes are observed:

- 1: Brittle fracture initiates at the notch root and propagates along the entire ligament. Full cleavage fracture without shear lips is observed.
- 2: Brittle fracture initiates at the notch root and propagates along the entire ligament, with shear lips.
- 3: Brittle fracture initiates at the notch root turns into ductile slant. BTF follows the ductile slant.
- 4: Brittle fracture initiates at the notch root turns into ductile slant (entire ligament).
- 5: Ductile slant initiates at the notch root after some triangular ductile crack advance. This ductile slant is followed by BTF which propagates along the entire ligament.

- 6: Ductile slant initiates at the notch root after a triangular ductile crack advance. This ductile slant is followed by BTF which turns into a final ductile slant.
- 7: Full ductile slant is observed.

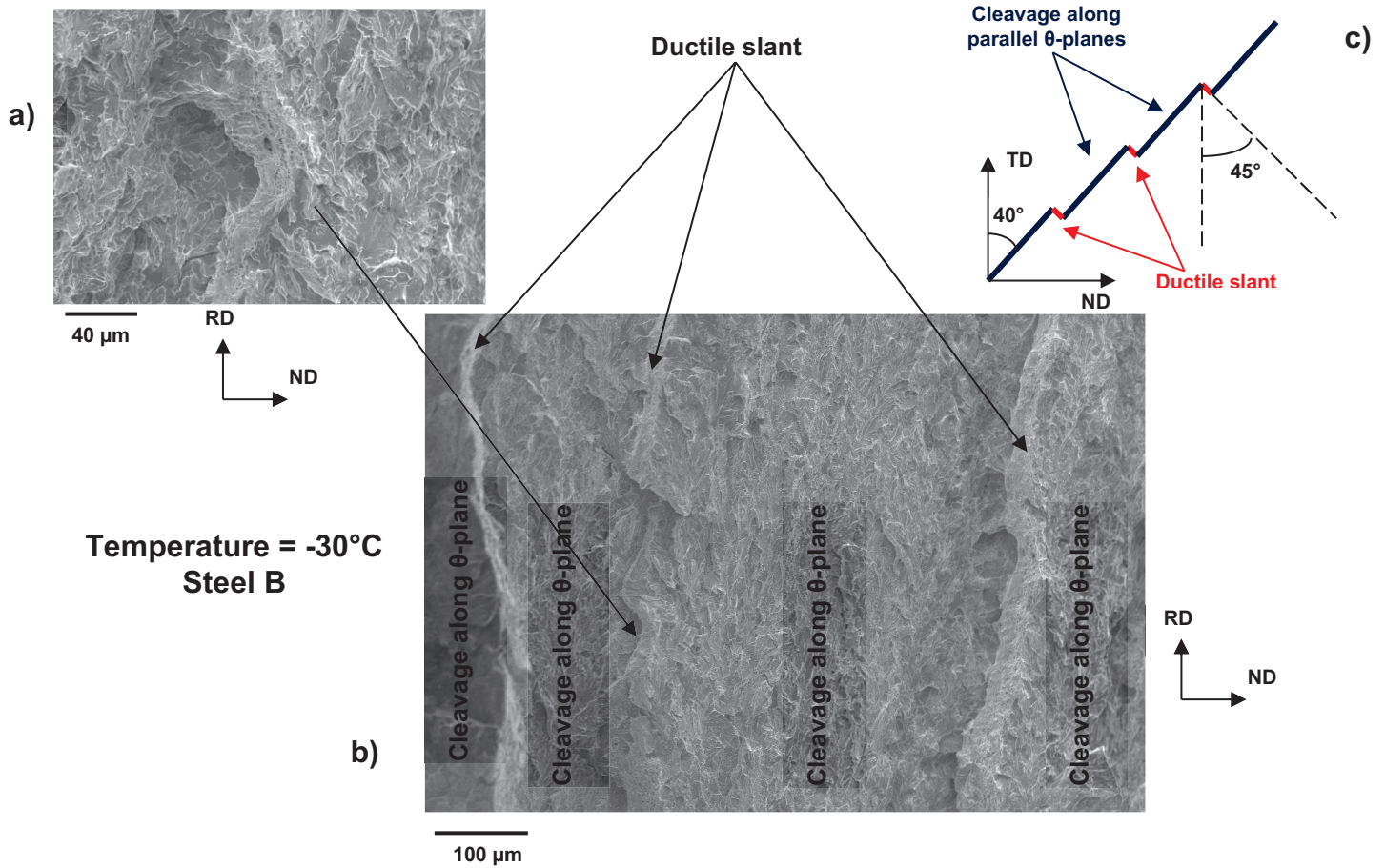


Figure II-20: BTF with a stair aspect: Parallel cleavage cracks which propagate along parallel θ -planes are joined together by ductile slant (a,b) SEM images; (c) schematic view of the macroscopic crack in the (TD, ND) plane.

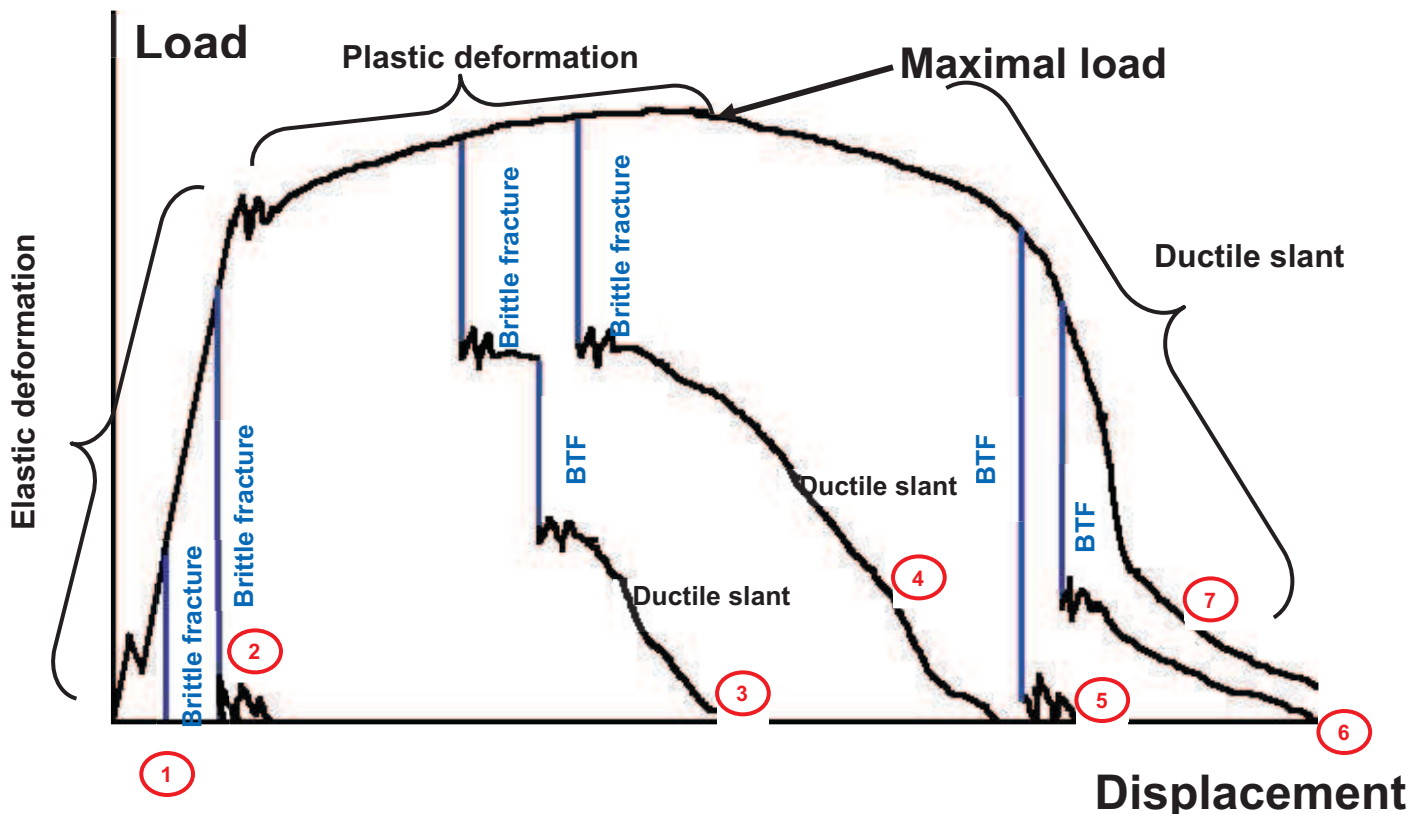


Figure II-21: Load vs displacement curves for the seven kinds of fracture surfaces observed after DWTT along TD. Labels also refer to the seven types listed in the text.

II.2.3. Effect of the loading direction

The main issue of this part is to determine whether the origin of BTF is mainly mechanical or mainly metallurgical (i.e. due to the microstructure and/or microtexture). To separate the mechanical contribution from the metallurgical one, complementary DWTTs have been performed along RD (with crack propagation along TD) on Steel B. It was assumed that the less pronounced average crystallographic texture within Steel B, might lead to a similar plastic behavior along RD and TD. The low plastic anisotropy within Steel B during tensile tests along RD and TD is confirmed in chapter III. Therefore, the stress state might not be considerably different between DWTT specimens of Steel B respectively tested along RD and along TD.

The transition curve obtained from the shear area percentage is presented in Figure II-22. A hyperbolic tangent function fitting data has been determined as proposed in [25], so that the ductile to brittle transition temperature (FATT) could be properly estimated. This transition temperature was respectively -70°C and -60°C for tests along RD and along TD. Moreover the transition domain started around -40°C for TD, compared to RD where the transition started around -60°C . Therefore, specimens loaded along RD have better toughness properties (as measured using DWTTs) than specimens loaded along TD.

To understand the difference in impact toughness resulting from the difference in loading direction, the fracture surface of specimens loaded along RD and along TD were analyzed. The main difference between both cases was the absence of BTF in specimens loaded along RD (Figure II-23). Within the ductile to brittle transition, brittle out-of-plane cracking observed on specimens taken along RD was identified as delamination, which rotated to join either the main loading plane, or a plane close to the θ -plane (which is now parallel to the loading direction). No brittle cracking was observed along a plane tilted by 40° around TD with respect to the (RD,TD) plane (referred to as an anti- θ -plane hereafter).

Assuming that the stress state in DWTT specimens respectively loaded along RD and TD was similar, the presence of BTF only for DWTT specimens loaded along TD might suggest that BTF could not be explained with a mechanical approach only. A metallurgical approach including the investigation of θ -planes, and possibly of anti- θ -planes, seems necessary.

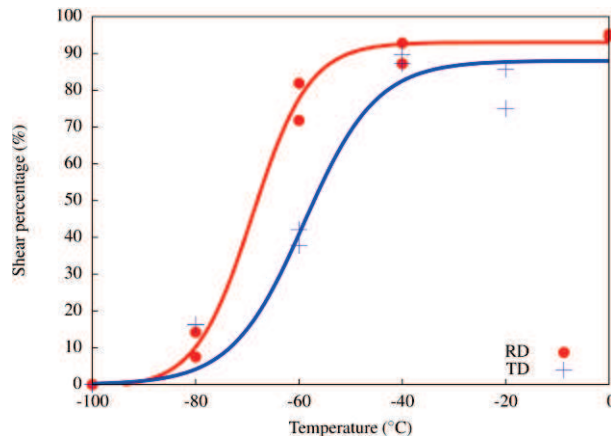


Figure II-22: Transition curves of drop weight tear tests along RD and TD (Steel B)

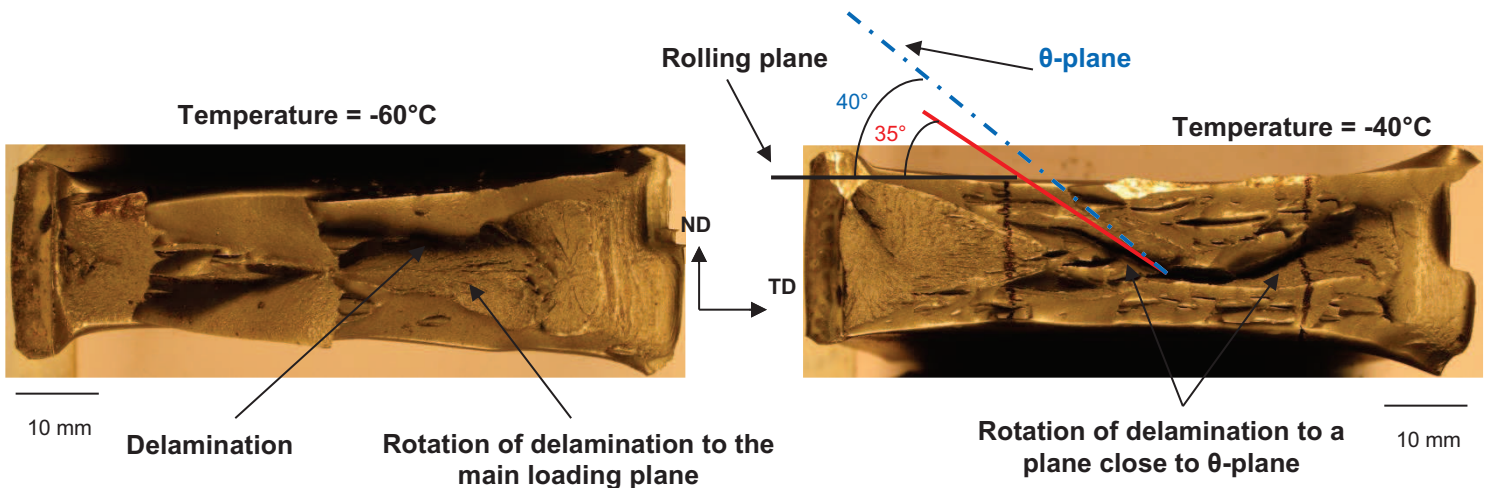


Figure II-23: Brittle out-of-plane fracture after DWTT on specimens loaded along RD

II.2.4. Summary

Drop weight tear tests have been performed on Steel A and B along TD. Appendix A gives detailed results of these tests.

Steels A and B have similar drop weight impact toughness with a ductile to brittle transition temperature around -60°C for tests along TD. This drop weight impact toughness was better for specimens of Steel B loaded along RD. Fracture surfaces of DWTT specimens have been analyzed to investigate how impact toughness could be affected by the occurrence of brittle out-of-plane cracking. These brittle out-of-plane cracks which were mainly delamination and brittle tilted fracture were more pronounced within the ductile to brittle transition temperature range.

Delamination cracks propagating within the rolling plane could sometimes rotate to join the plane perpendicular to the main loading direction. The effect of delamination on load vs. displacement curve was not obviously distinguishable and therefore it might not considerably affect the impact energy.

Brittle tilted fracture led to an abrupt load drop in the load vs. displacement curve and was consequently detrimental for impact toughness. Brittle tilted fracture was not observed for DWTT specimens loaded along RD, supporting in this way its metallurgical origin. Closer observations showed that BTF propagated within parallel θ -planes which were connected by ductile slant. These θ -planes correspond to planes tilted by around 40° with respect the rolling plane, with RD as the rotation axis. The anti- θ -planes (similar to θ -planes but with TD as the rotation axis) were never fractured by cleavage.

In the next section, the occurrence of brittle out-of-plane cracking is studied for Charpy tests with a similar approach for comparison purposes.

II.3. Results of Charpy tests

Charpy V-notch specimens have been taken from the mid-thickness of the plate (Figure II-24). Thereafter, Charpy specimen orientations will be denoted as X-Y, where X is the direction along which the specimen was taken and Y is the crack propagation direction. For both steels, RD-TD, TD-RD, RD-ND and TD-ND specimens were machined. The last two orientations, RD-ND and TD-ND, which are less conventional for an impact toughness study of linepipe steels, were only used to analyze the fracture mode anisotropy.

Tests on Steel A were performed at OCAS with an impact velocity of 5 m/s and a hammer of 60 kg. Cooling was achieved inside a climatic chamber. Tests on Steel B have been performed at RWTH Aachen with an impact velocity of 5.5 m/s and a hammer of 20 kg. In that case, cooling was achieved inside a climatic chamber for temperatures lower than -70°C and by immersion in a silicone bath solution for higher temperatures. The load was measured with a sensor fixed on the hammer, and the displacement was obtained using the Newton second law which gives a relationship between acceleration, mass and measured load. The load vs. displacement curves have been plotted for all specimens and for each specimen, impact energy has been calculated as the area under this curve.

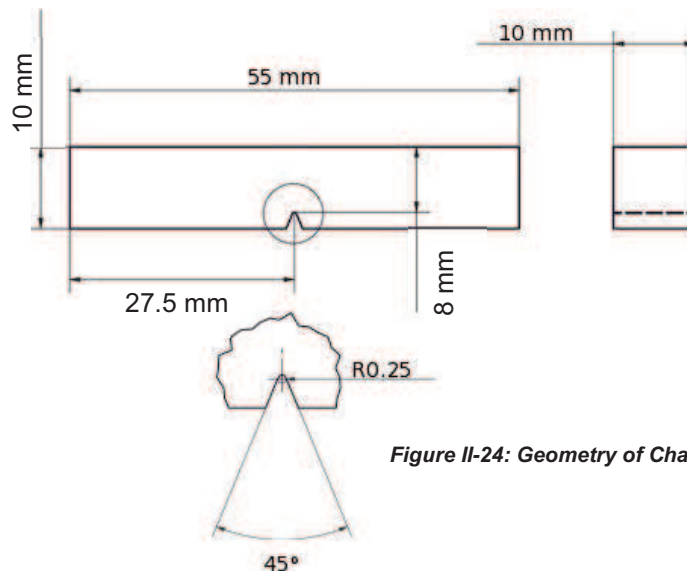


Figure II-24: Geometry of Charpy V-notch specimens

II.3.1. Charpy impact toughness of Steels A and B

The evolutions of impact energy with temperature of RD-TD and TD-RD specimens are presented in Figure II-25 and Figure II-26 respectively for Steels A and B. Results of unconventional direction RD-ND and TD-ND are available in appendix A. The ductile to brittle transition temperature of Steel A was found around -100°C for Charpy RD-TD and -90°C for Charpy TD-RD. This difference was slightly higher for Steel B, where the ductile to brittle transition temperature of Charpy RD-TD was around -120°C and the one for Charpy TD-RD around -100°C .

Therefore, for both steels, RD-TD specimens had higher Charpy impact toughness than TD-RD specimens. Moreover, Steel B has slightly higher Charpy impact toughness than Steel A. These results are in good agreement with DWTT results, where specimens loaded along RD had better impact toughness properties than those loaded along TD. Nevertheless, the ductile to brittle transition temperature (FATT) derived from DWTTs is around 40°C higher than the ductile to brittle transition temperature (on energy) predicted from Charpy tests. Therefore, for these data processing procedures, the Charpy test is less conservative than the DWTT. In order to understand this noticeable difference on impact toughness between DWTT and Charpy tests, fracture modes of Charpy specimens have been studied as reported in the following section.

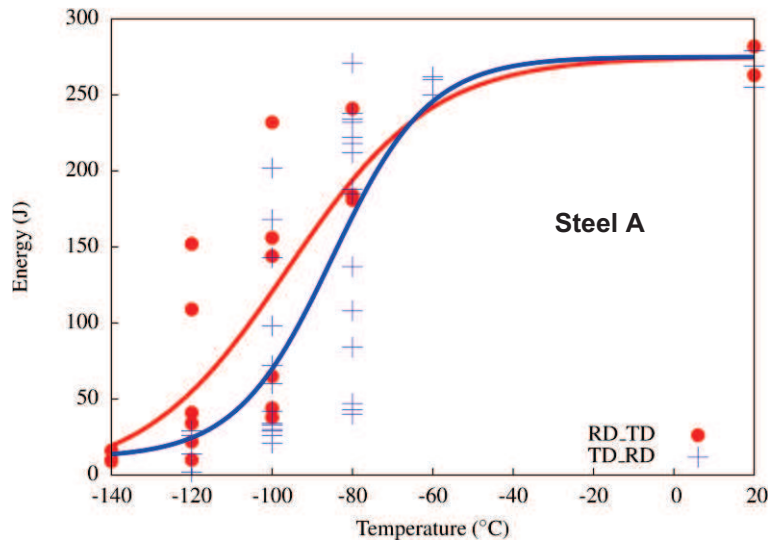


Figure II-25: Evolution of the Charpy impact energy with temperature for RD-TD and TD-RD specimens (Steel A)

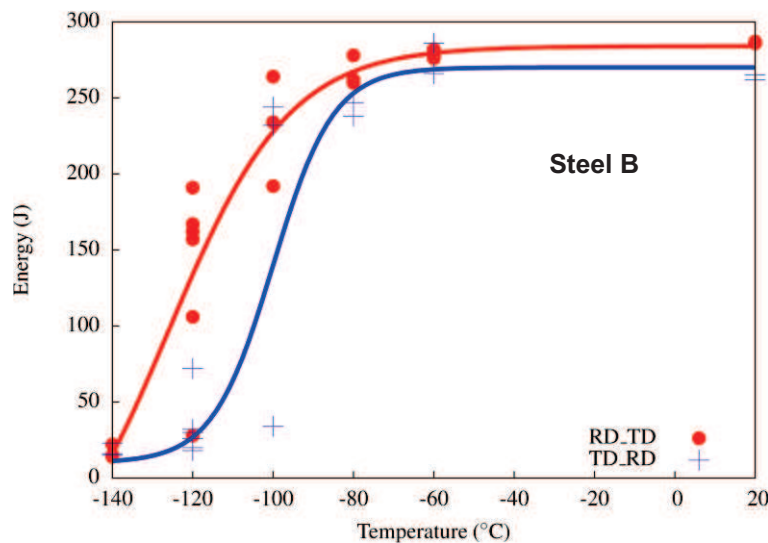


Figure II-26: Evolution of the Charpy impact energy with temperature for RD-TD and TD-RD specimens (Steel B)

II.3.2. Fracture mode and effect on impact toughness

As was done for drop weight tear tests, fracture modes occurring during Charpy tests were analyzed in order to investigate their effect on fracture toughness. This analysis has been performed for the four specimen orientations: RD-TD, TD-RD, RD-ND and TD-ND.

a) Ductile fracture

In contrast to the DWTT specimens, no ductile slant was observed on Charpy specimens. Flat ductile cracks with shear lips were observed (Figure II-27). Ductile crack propagation was associated to a gradual decrease in load in the load vs. displacement curves (Figure II-28).

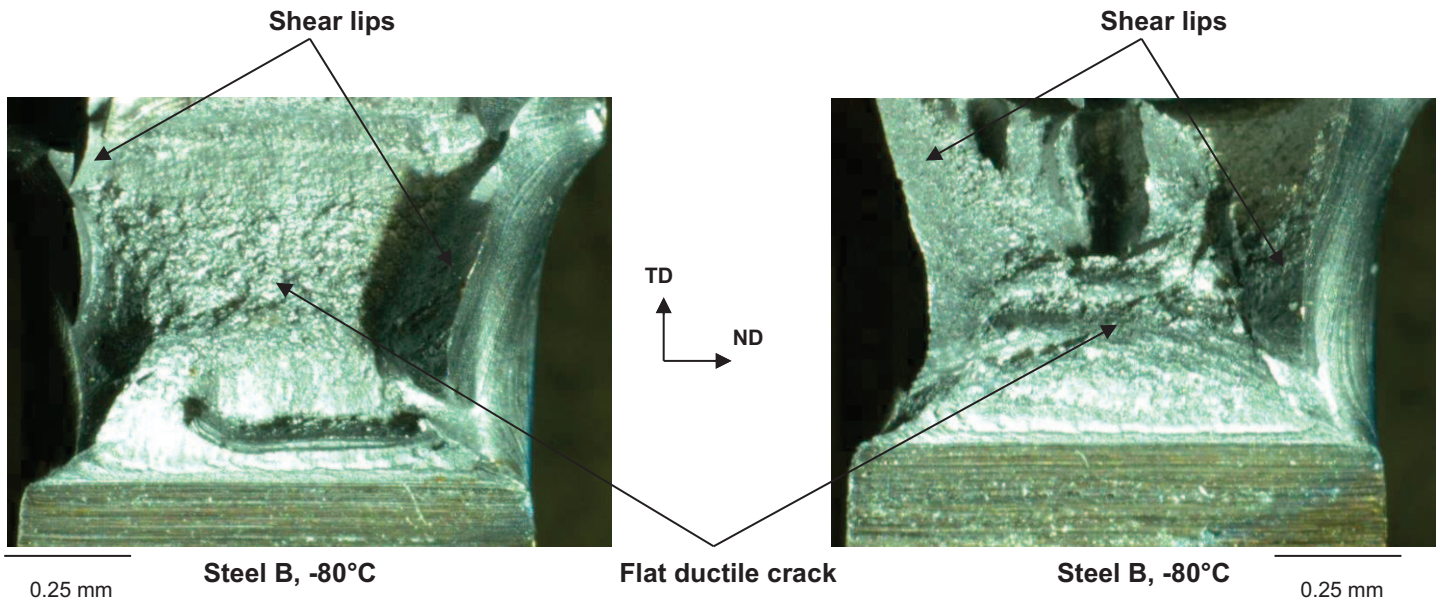


Figure II-27: Ductile fracture modes of Charpy specimens at -80°C (Steel B)

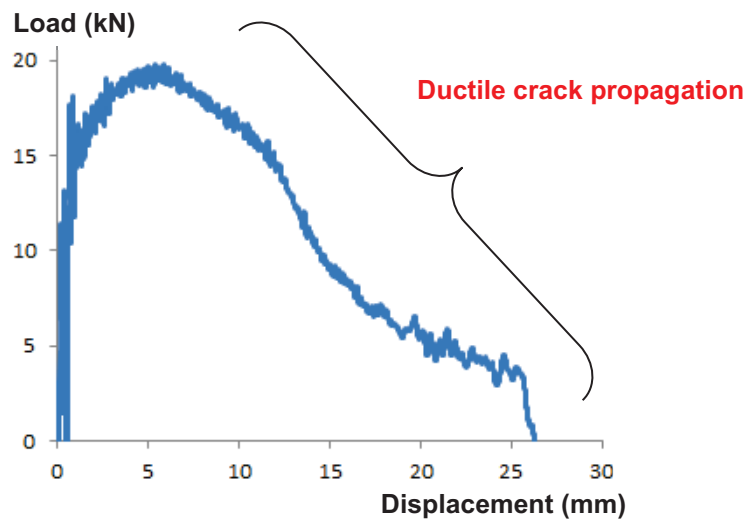


Figure II-28: Load vs. displacement curve at 20°C (Charpy RD-TD, Steel A)

b) Delamination

Two delamination configurations were observed depending on the specimen orientation. The first configuration is delamination which propagates along the same direction as the main crack propagation (Figure II-29). It was observed for RD-TD and TD-RD specimens. The second configuration is delamination which propagates perpendicularly to the main crack propagation (upper horizontal dark band in Figure II-30). This configuration was observed for Charpy RD-ND and TD-ND. It results from the orientation of the rolling plane with respect to that of Charpy specimens.

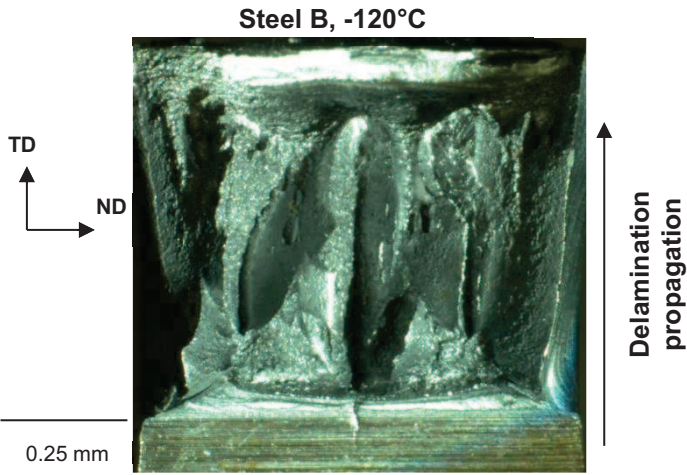


Figure II-29: Delamination configuration for RD-TD and TD-RD specimens

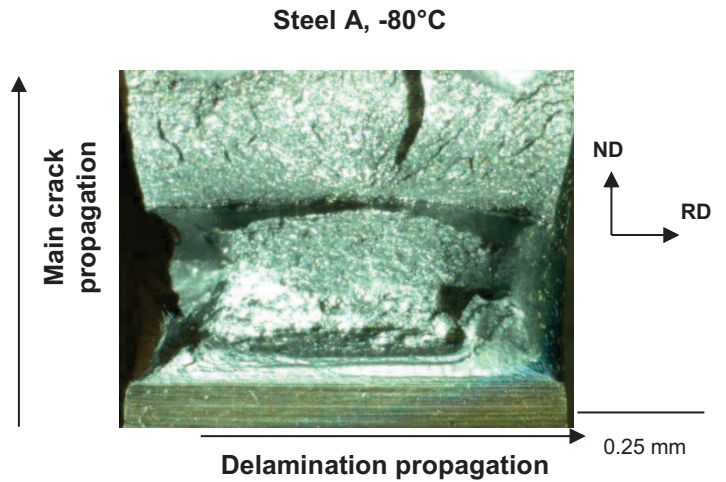


Figure II-30: Delamination configuration for RD-ND and TD-ND specimens

RD-TD and TD-RD specimens (configuration 1)

For both steels delamination occurred for temperatures lower than -80°C . Delamination could be classified into two types according to the initiation site. Type 1 delamination cracks were initiated just at the notch root, ductile crack advance was not necessary (Figure II-31). Type 2 delamination cracks were initiated after some ductile crack advance (Figure II-31). Typical load-displacement curves obtained from Charpy tests on specimens with type 1 and type 2 delamination cracks in configuration 1 are presented in Figure II-32. The delamination crack event is not easily noticeable on the Charpy curve; nevertheless this delamination seems to affect the slope of the load decreasing.

Type 1 delamination crack propagated even behind the notch and divided the specimen into two parts. The ductile crack advance occurred separately within the two parts and could lead to secondary delamination cracks. Type 1 delamination cracks occurred at lower temperatures, within the lower shelf domain and were commonly followed by other kinds of brittle out-of-plane cracks (Figure II-33). These brittle out-of-plane cracks propagated across almost the entire specimen, before occurrence of flat brittle cracking at the back of the specimen. That explained the abrupt drop in load observed on load vs. displacement curves and the low impact energy (Figure II-33).

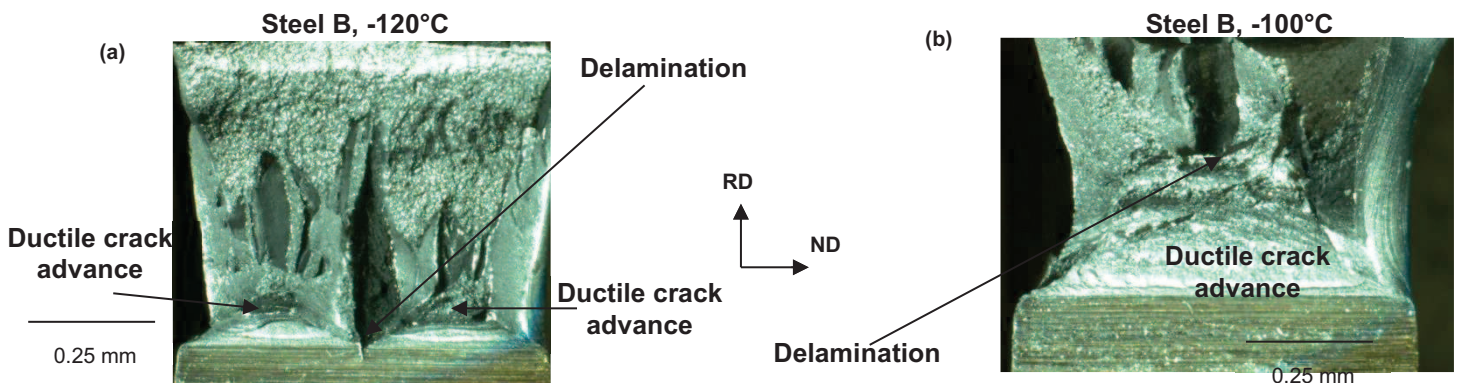


Figure II-31: Charpy specimens with configuration 1. (a) Delamination initiated at the notch root (type1). (b) Delamination initiated after ductile cracking (type2).

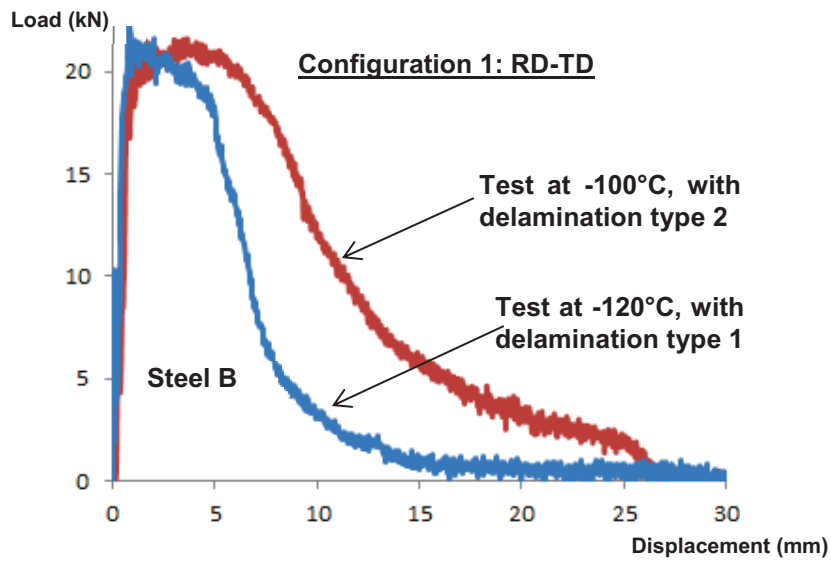


Figure II-32: Typical Charpy curves for specimens in configuration 1, with delamination type 1 and type 2

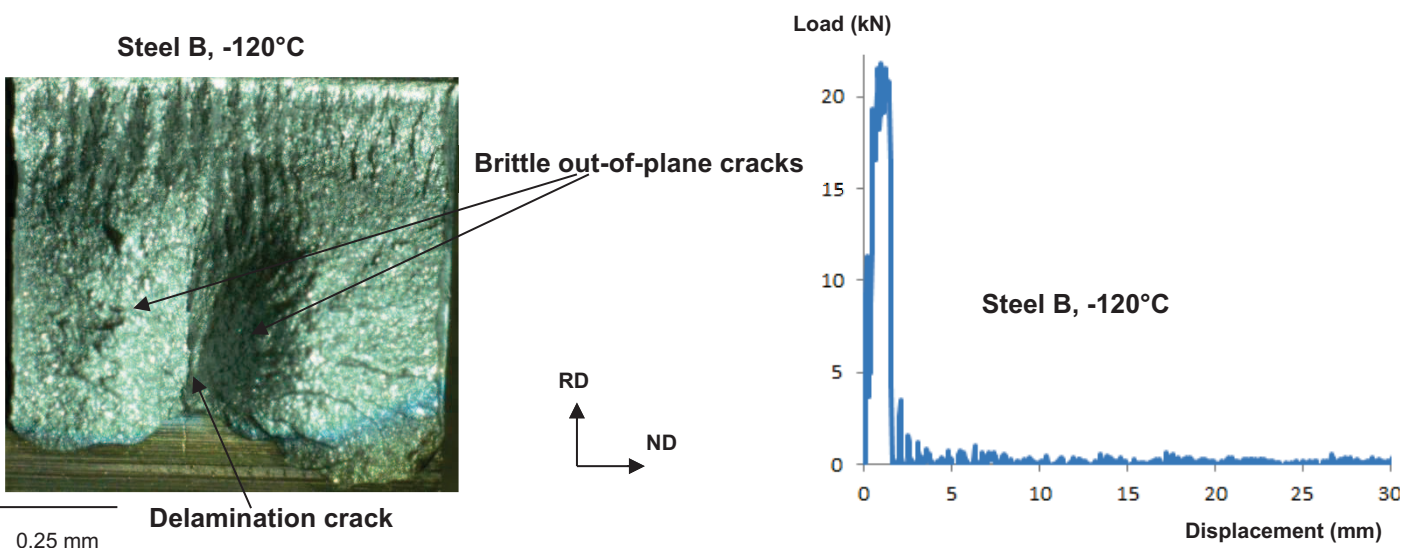


Figure II-33: Type 1 delamination followed by other brittle out-of-plane cracks

SEM observation was performed inside delamination cracks (Figure II-34). Cleavage fracture along the rolling plane first propagated within a region close to the notch, with elongated facets. The global cleavage fracture started from this region.

Type 1 delamination cracks start at -80°C for Steel A and -100°C for Steel B. Even if there is not enough data to draw a definitive conclusion, Steel A seems to be more sensitive to type 1 delamination than Steel B.

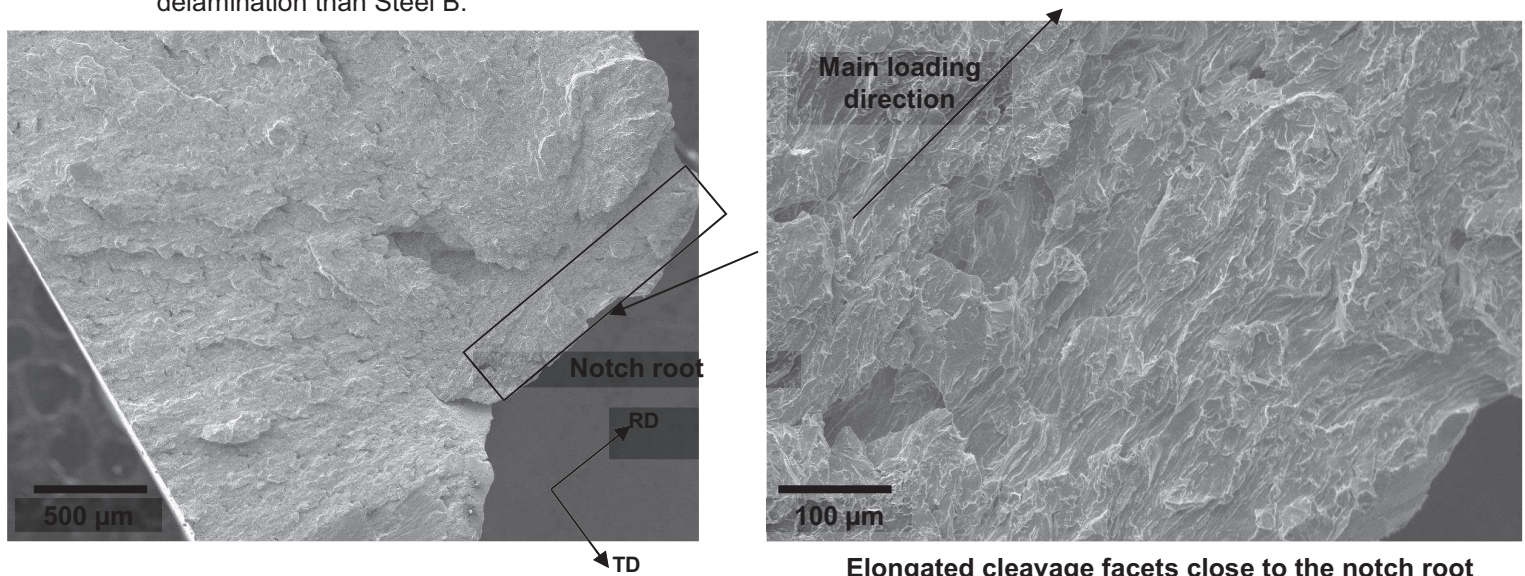


Figure II-34: SEM observation of the delamination fracture surface: Cleavage fracture started from a small region with elongated cleavage facets (RD-TD specimen Steel B)

Type 2 delamination cracks initiated after some ductile crack advance. The higher the extent of ductile crack advance, the higher the value of hammer displacement before rapid decrease in load associated to delamination propagation. Therefore, the absorbed energy calculated as the area under the load vs. displacement curve increased, when the extent of ductile crack advance increased. For temperatures close to the upper shelf domain, delamination occurred after a large ductile crack advance. In that case, the effect of delamination on the load vs displacement curve was not pronounced, and therefore the absorbed energy was not significantly affected. Type 2 delamination cracks were more representative to the ones observed for DWTT specimens, where a triangular ductile crack advance was observed behind delamination cracks.

RD-ND and TD-ND specimens (configuration 2)

Delamination occurred for temperatures lower than -60°C for Steel B. For Steel A, delamination started at least for temperature lower than -80°C , since no test was performed at -60°C . In all cases, delamination initiated after ductile crack advance. The size of the ductile crack advance is larger than for RD-TD and TD-RD Charpy specimens (could reach more than half of the total fracture area).

Typical load-displacement curves obtained from Charpy tests on specimens with delamination cracks in configuration 2 are presented in Figure II-35. For this configuration the delamination event is associated to an abrupt drop of the load. The earlier the drop of the load the smaller the ductile crack advance.

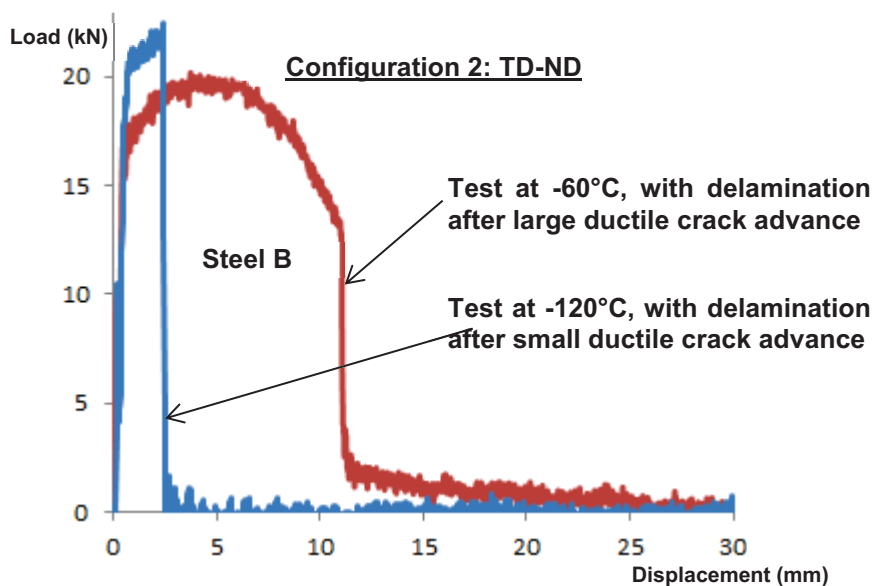


Figure II-35: Typical Charpy curves of specimens with delamination in configuration 2

c) Rotation of delamination

After propagation along the rolling plane, the delamination crack could apparently rotate to become more or less parallel to the main loading plane. For RD-TD and TD-RD Charpy specimens, this delamination rotation was observed after Type 1 delamination cracks (Figure II-36). For RD-ND and TD-ND Charpy specimens, this delamination rotation was observed after noticeable ductile crack advance (Figure II-36).

RD-TD and TD-RD specimens (configuration 1)

Type 1 delamination eventually responsible for delamination rotation on RD-TD and TD-RD Charpy specimens started around -100°C for Steel B and the first delamination rotations were observed at -120°C . Moreover, delamination rotation, less frequently observed on TD-RD specimens, was

replaced by brittle tilted fracture for Steel B. Not all broken specimens of Steel A were available, but from the available ones and from measured energies, Type 1 delamination cracking was expected to start around -80°C for Steel A. Delamination rotation which also started around -80°C in that steel was sometimes replaced by brittle tilted fracture for TD-RD Charpy specimens.

RD-ND and TD-ND specimens (configuration 2)

For RD-ND and TD-ND Charpy specimens, delamination rotation also occurred after ductile crack advance. This fracture mode occurred at least for temperature lower than -60°C for both steels. For some TD-ND specimens, delamination rotation was replaced by brittle tilted fracture and in that case only a small ductile crack, almost limited to the notch root, was observed.

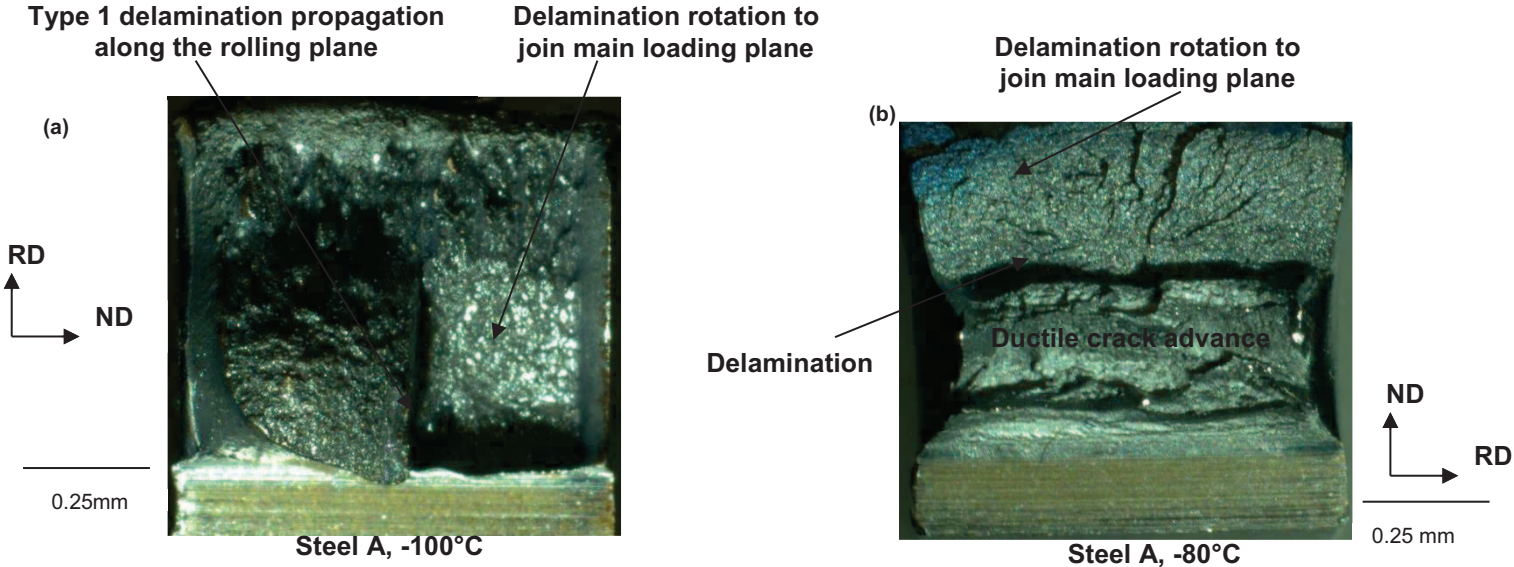


Figure II-36: Delamination rotation. (a) Configuration 1 TD-RD. (b) Configuration 2 TD-ND.

Delamination rotation was associated to an abrupt drop in load and consequently low absorbed energy was measured (Figure II-37). Since this fracture mode occurred more easily for Steel A, at least for Charpy RD-TD and TD-RD specimens, it could (at least partially) explain why the ductile to brittle transition temperature of Steel A was higher than for Steel B.

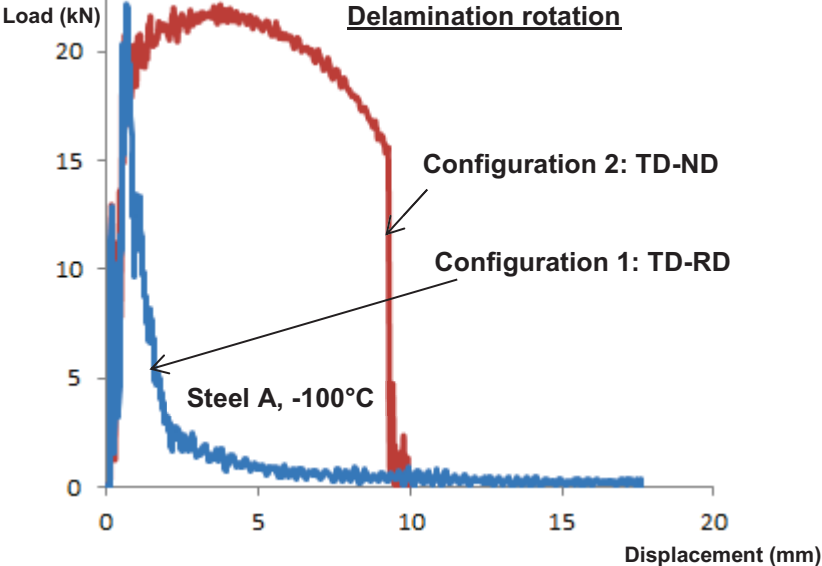


Figure II-37: Typical Charpy curves of specimens with delamination rotation. The delamination rotation leads to an abrupt drop of the load for configuration 1 (TD-RD) and configuration 2 (TD-ND).

d) Brittle tilted fracture (BTF)

This fracture mode was only observed for TD-RD and TD-ND (Figure II-38) Charpy specimens. The crack propagated within the θ -plane, which was already defined for drop weight tear tests. A small delamination crack was observed at the initiation site of brittle tilted fracture. This delamination was initiated at the notch root (Type 1) for TD-RD specimens and after a small ductile crack advance for TD-ND specimens. TD-RD Charpy specimens with brittle tilted fracture were slightly more frequently obtained on Steel B. As for DWTTs, no BTF along the anti- θ -plane was detected.

Brittle tilted fracture as delamination rotation was also associated to an abrupt drop of the load and considerable lower energies (Figure II-39). That may explain why TD-RD Charpy impact toughness was not as good as for RD-TD. In fact, delamination rotation was the only brittle out-of-plane fracture mode for RD-TD, in contrast to TD-RD, where BTF along the θ -plane was added to delamination rotation.

Charpy results are in good agreement with DWTT results concerning the occurrence of BTF: only specimen loaded along TD exhibited BTF.

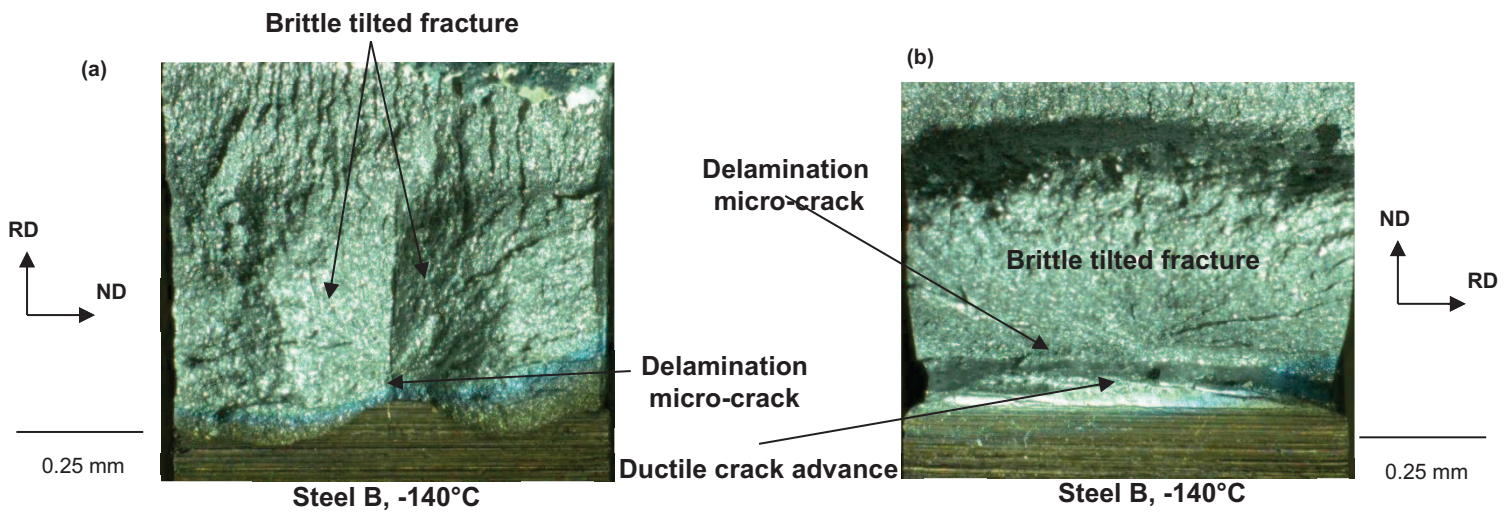


Figure II-38: Brittle tilted fracture. (a) Configuration 1 TD-RD. (b) Configuration 2 TD-ND.

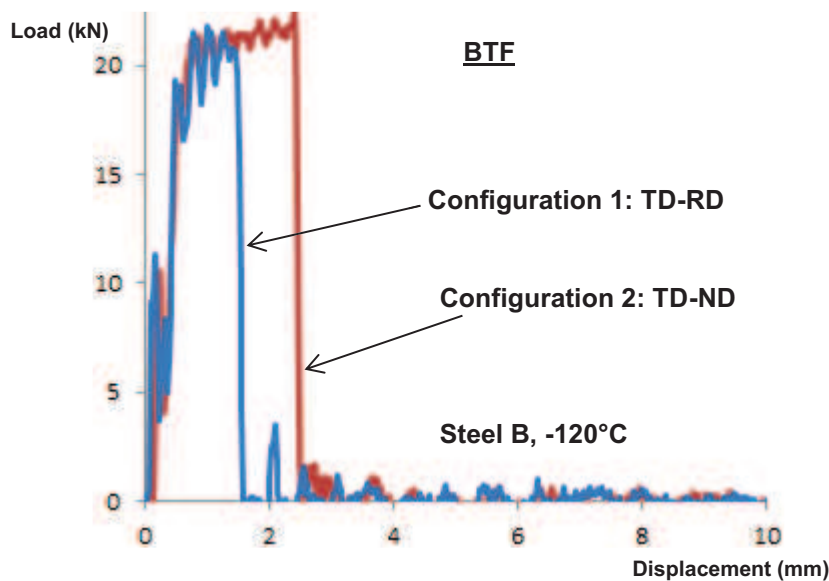


Figure II-39: Typical Charpy curves of specimens with BTF. The brittle tilted fracture leads to an abrupt drop of the load for configuration 1 (TD-RD) and configuration 2 (TD-ND).

e) Other brittle fracture modes

- Specimens entirely covered with flat brittle fracture were only scarcely found; only very few specimens exhibited full flat brittle fracture surface at -140°C (lowest temperature).
- In some (rare) instances, RD-TD Charpy specimens exhibited a brittle crack similar to delamination but which propagated along the θ -plane (Figure II-40). For this specimen configuration, the brittle crack propagating within the θ -plane is not called BTF, because BTF is associated to a brittle slant across the thickness as observed for TD-RD. Therefore, the Charpy impact toughness was less affected by such cracks. This fracture mode was similar to the one occurring during DWTTs for loading along RD.

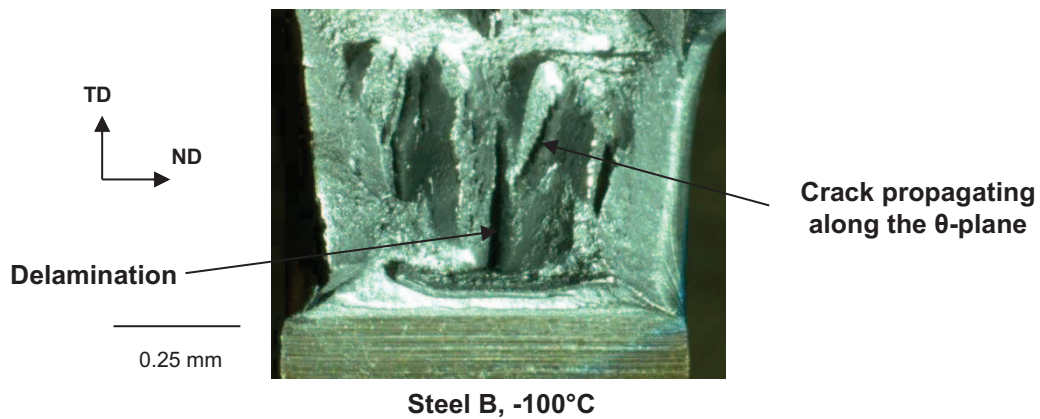


Figure II-40: Brittle crack propagating along the θ -plane

II.3.3. Summary of Charpy results and comparison to DWTT results

Charpy tests have been performed on steels A and B, using the four orientations: RD-TD, TD-RD, RD-ND and TD-ND. Detailed results are available in appendix A. Steel B has a higher Charpy impact toughness, with a ductile to brittle transition temperature shifted by $+20^{\circ}\text{C}$ for RD-TD and by $+10^{\circ}\text{C}$ for TD-RD specimens. Flat ductile crack propagation observed within the upper shelf domain was progressively replaced by brittle out-of-plane cracking for decreasing test temperatures. These brittle out-of-plane fracture modes were delamination, which could sometimes rotate to join the main loading plane, and BTF. Delamination started at around -60°C for both steels independently of the Charpy specimen orientation. For these relatively high temperatures, a noticeable ductile crack advance was observed before delamination occurrence. It corresponds to Type 2 delamination cracks. Type 1 delamination initiated at the notch root without noticeable ductile crack advance was only observed for RD-TD and TD-RD Charpy specimens. It started at -80°C for Steel A and -100°C for Steel B. SEM observation of the inside of type 1 delamination cracks showed elongated cleavage facets at the notch root from where delamination was initiated. Type 1 delamination cracks generally led to other kinds of brittle out-of-plane cracking. In fact, after propagating along the rolling plane, this delamination crack could rotate to join the main loading plane or could immediately tilt into the θ -plane and lead to BTF. Delamination rotation was more frequently observed for Steel A. Brittle tilted fracture, which was only observed for specimens loaded along TD, was more pronounced for Steel B.

Now, it seems interesting to compare DWTT and Charpy test results which are both impact tests on three-point-bending specimens. The fracture modes are similar for both tests, except that ductile slant observed for DWTT was replaced by flat ductile cracking for Charpy tests. This might result from geometry effects. Nevertheless, the ductile to brittle transition temperature obtained with DWTT was higher than for Charpy tests. In fact, the temperature below which brittle fracture appeared is higher for DWTT than for Charpy tests. Since this brittle fracture is due to brittle out-of-plane cracks

(delamination rotation and BTF) in most cases, this suggests that the higher ductile to brittle transition temperature of DWTT might result to the easier occurrence of brittle out-of-plane cracking for DWTT. This suggestion is plausible because, brittle out-of-plane cracking started around -20°C for DWTTs and -80°C for Charpy tests. The larger ligament of DWTT specimens might play a considerable role in this sensitivity to brittle out-of-plane cracking. For Charpy specimens, delamination rotation and BTF initiated at the notch root differently from the case of DWTT specimens, where delamination rotation and BTF could initiate after a noticeable ductile slant advance. In fact, because of the small size of Charpy specimen ligament, ductile crack could not propagate over a long distance without reaching the impact region (where brittle out-of-plane fracture was never observed). Therefore, the stress concentration generated by ductile slant for DWTT was not present for Charpy tests, and lower temperatures were needed to increase the stress state in Charpy specimens to trigger brittle out-of-plane fracture.

The summary of fracture modes observed after DWTT and Charpy tests along TD and RD are presented in Figure II-41 to Figure II-44.

The next step is to investigate brittle out-of-plane cracking during a quasi-static test, so that dynamic effects, which are more difficult to analyze from a mechanical point of view, could be avoided. These tests have been done on Compact Tensile (CT) specimens.

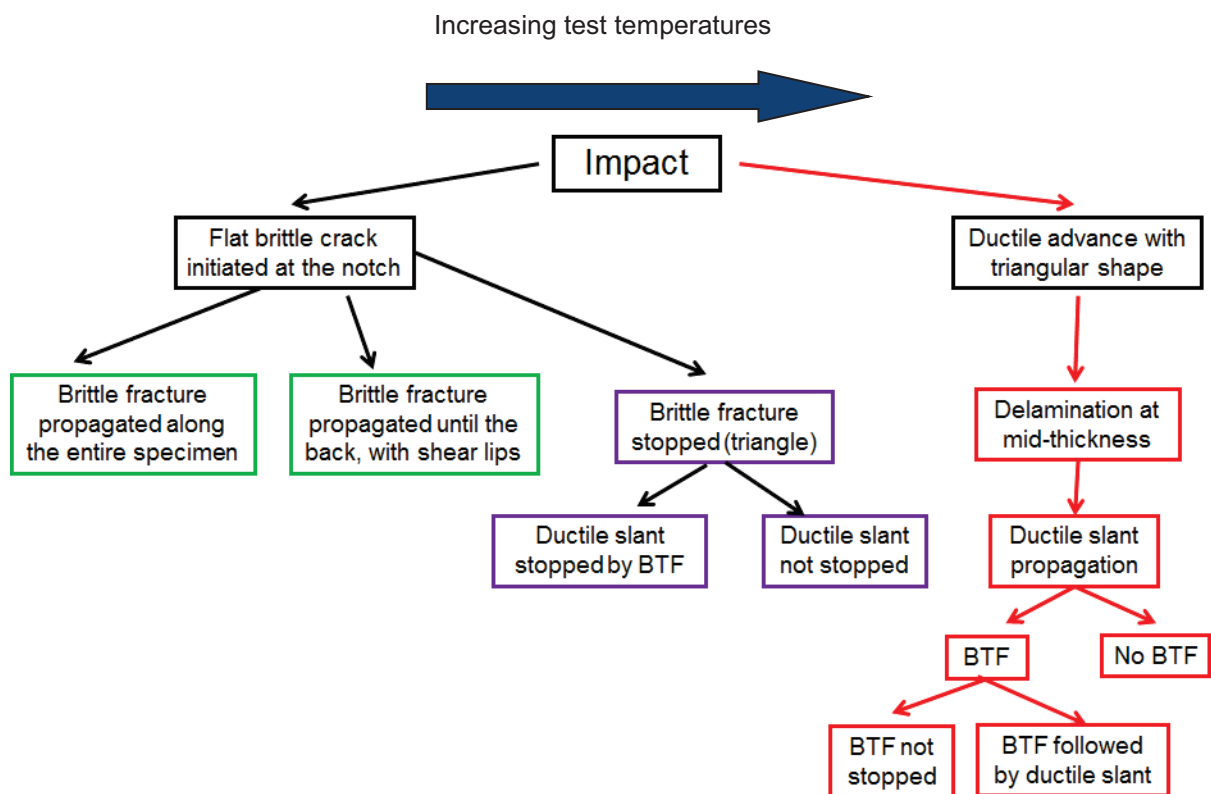


Figure II-41: Fracture modes observed after DWTT tests along TD

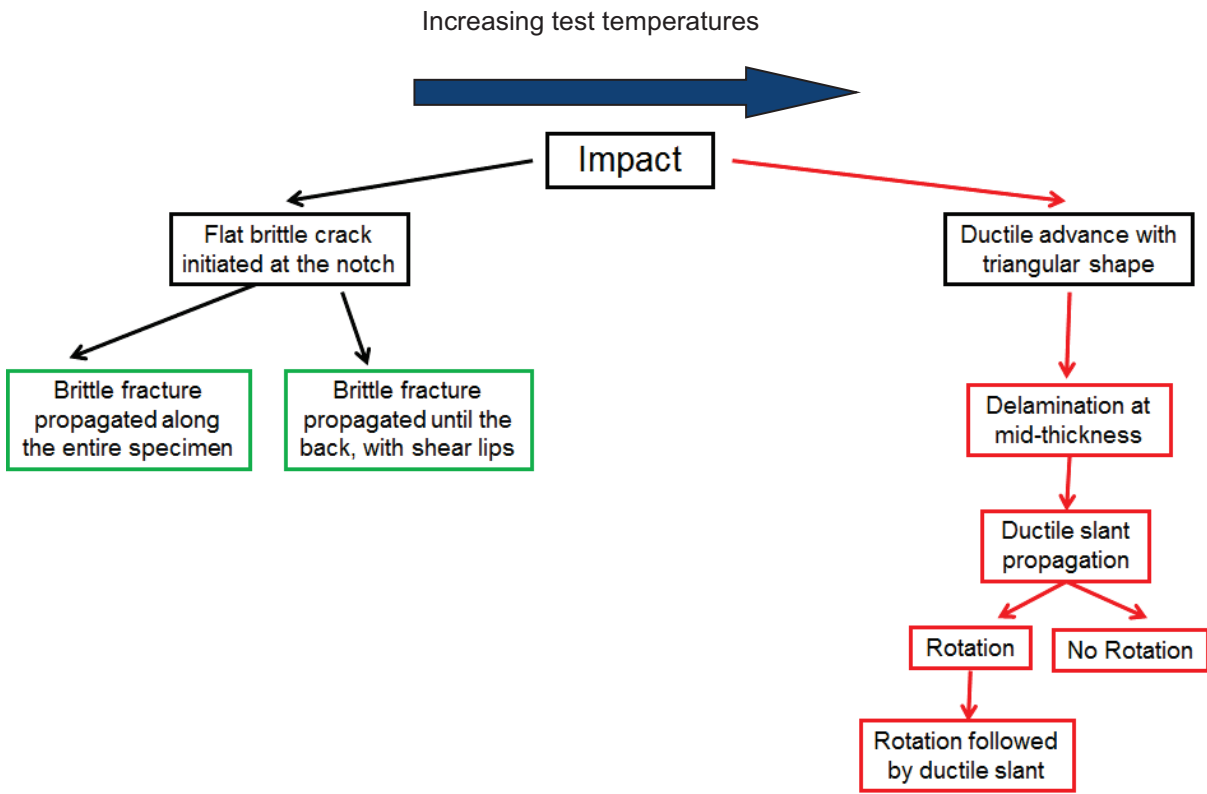


Figure II-42: Fracture modes observed after DWTT tests along RD

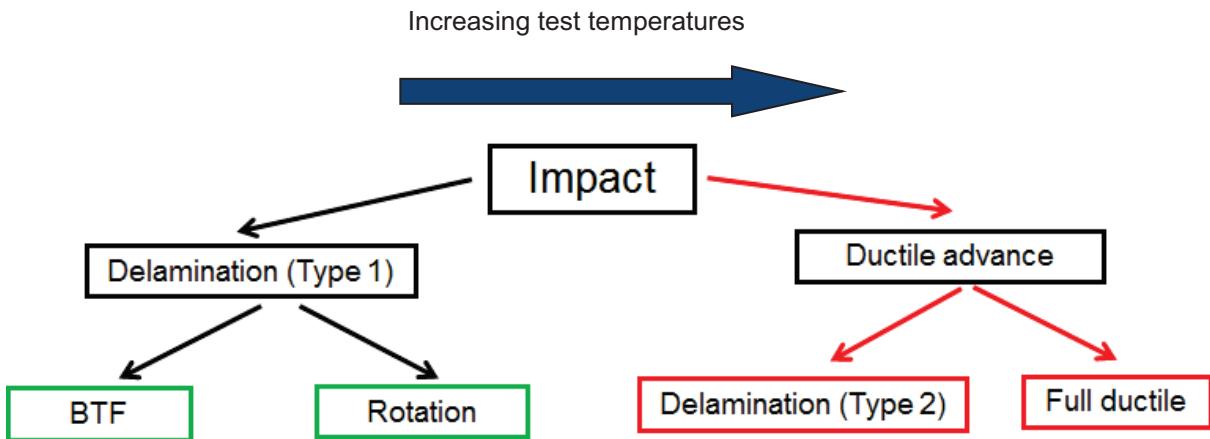


Figure II-43: Fracture modes observed after Charpy tests along TD

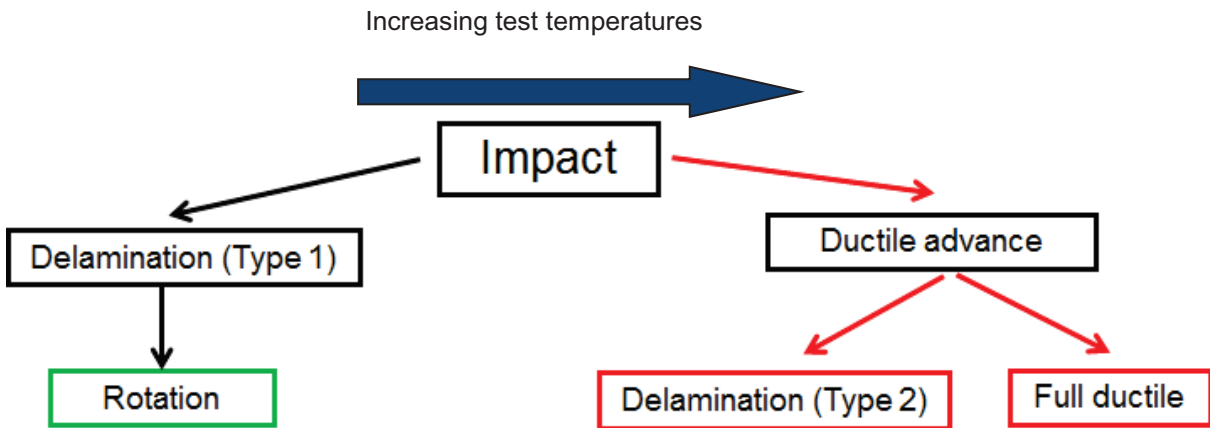


Figure II-44: Fracture modes observed after Charpy tests along RD

II.4. Brittle out-of-plane cracking during fracture toughness tests

Brittle out-of-plane crack propagation during quasi-static fracture toughness tests has been investigated with Compact Tensile (CT) specimens. CT specimens have been taken at mid-thickness along TD with the crack propagation direction along RD (Figure II-45). Specimens were fatigue pre-cracked at room temperature with an initial load of 3.2 kN and a final load of 2.7 kN for Steel A, and an initial load of 3.5 kN and final load of 1.8 kN for Steel B. A targeted fatigue pre-crack length of 1.5 ± 0.1 mm has been achieved for almost all specimens. After pre-cracking, side grooves have been machined as shown in (Figure II-46). Specimens were tested between -100°C and -140°C which correspond to a temperature range where cleavage fracture was expected to occur. One specimen taken from Steel B has been tested at -196°C in liquid nitrogen. All tests have been performed using a 250 kN servohydraulic Instron 8500 machine. The load line displacement rate of 3×10^{-3} mm/s used for Steel A has been increased to 2×10^{-2} mm/s for Steel B, in order to decrease the test duration. Because of the imperfect insulation of the climatic chamber, the temperature increased by 1°C per minute. Finally, the fracture surfaces of broken specimens were investigated with SEM.

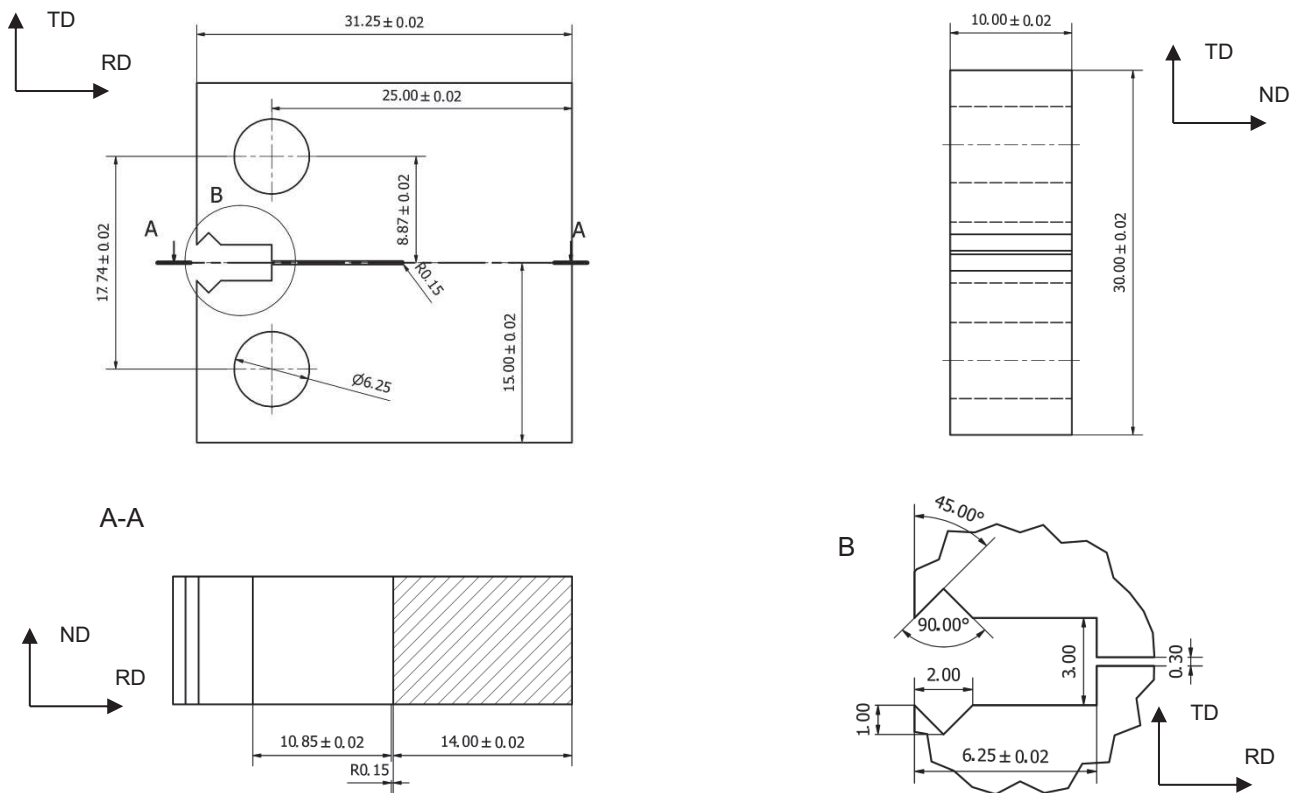


Figure II-45: Geometry of CT specimens (dimensions in mm)

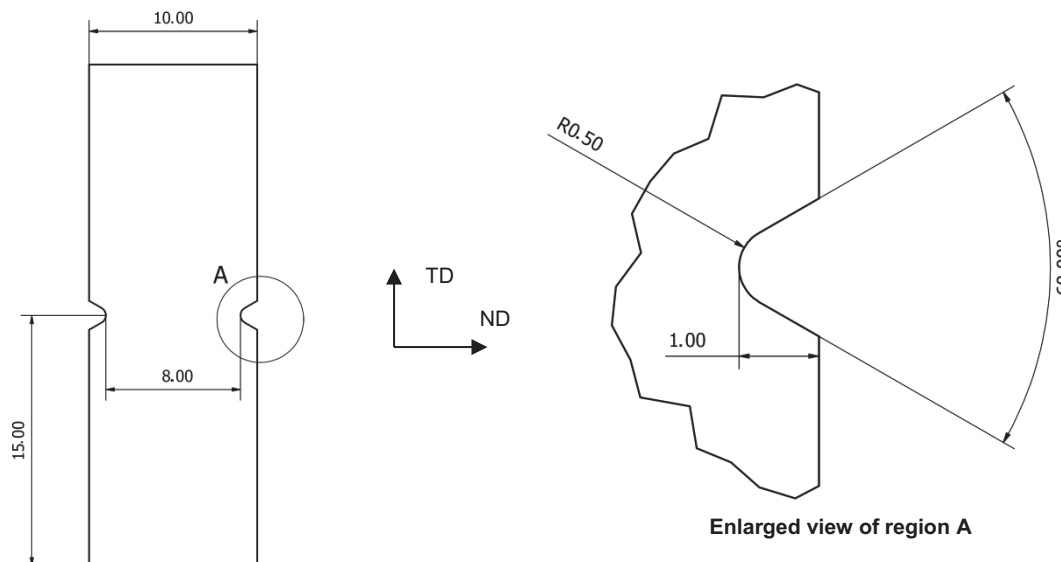


Figure II-46: Geometry of CT specimen after pre-cracking (side grooves), dimensions in mm

Load vs. displacement curves and fracture toughness values are not reported in this study for reasons explained thereafter. The only information needed was to know whether brittle out-of-plane cracking could occur during quasi-static tests, or if it was only associated to dynamic effects linked to impact loading.

II.4.1. Brittle out-of-plane cracking during tests on pre-cracked CT specimens

For the above considered temperatures, brittle out-of-plane cracking was observed. These brittle out-of-plane cracks are more detrimental for CT tests because a part of the fatigue pre-crack was hidden by these cracks which sometimes went backwards. Moreover, CT tests are used in standard mode I fracture toughness and other fracture modes are not allowed. For all these reasons, CT specimens with brittle out-of-plane cracking are not valid according to ASTM E1921-02 standard. It explains why fracture toughness values and the reference temperature (T_0) were not calculated in this study.

a) Delamination

Except at -196°C , for all specimens, short delamination cracks were observed in the front of the fatigue pre-crack. These delamination cracks were the initiation sites of brittle out-of-plane cracking.

b) Brittle tilted fracture

Brittle tilted fracture was the brittle out-of-plane cracking mode observed for CT specimens. For the temperature range considered, BTF was observed in front of the fatigue pre-crack except for -196°C , where BTF initiated around the middle of the ligament path. In most cases, this BTF crack also propagated backward and covered the fatigue pre-crack front (Figure II-47).

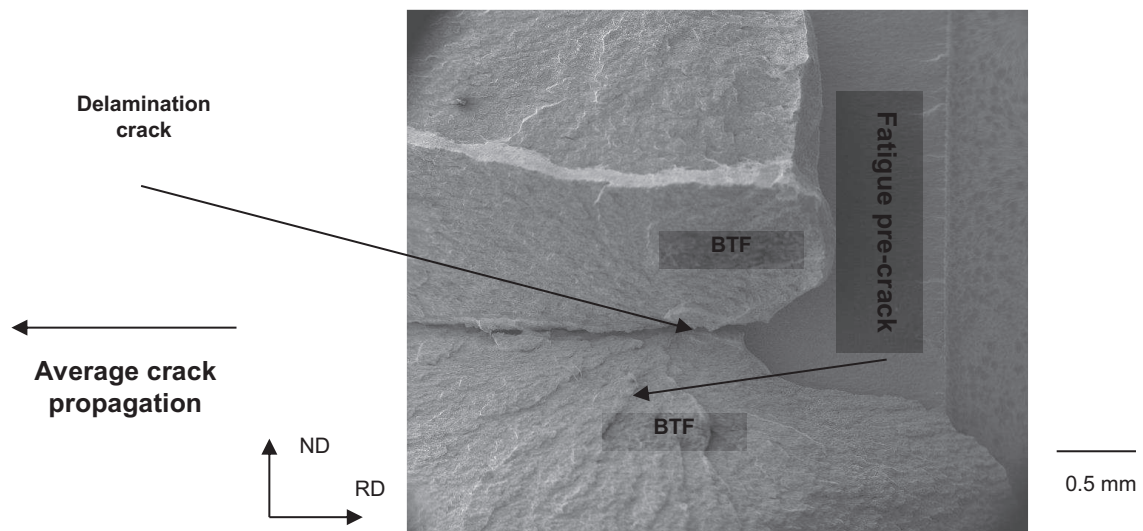


Figure II-47: Brittle tilted fracture going backward and partly covering the fatigue pre-crack front, Steel B

II.4.2. Comparison with impact tests

Brittle out-of-plane cracking was observed for both quasistatic fracture toughness tests on CT specimens and for both kinds of impact tests. For fracture toughness tests, delamination and BTF were the brittle out-of-plane fracture modes. Delamination rotation was not observed. These brittle out-of-plane cracks were detrimental for CT tests because the results could never be considered as valid according to ASTM E1921-02 standard on fracture toughness determination.

II.5. Discussion and conclusions

Investigations of impact and fracture toughness have been performed on Steels A and B. The observed fracture modes have been analyzed with special attention paid on brittle out-of-plane cracking.

Impact toughness was firstly investigated in DWTT. Steels A and B exhibited similar ductile to brittle transition temperatures (-60°C) even if Steel B had a slightly lower shear percentage because of more pronounced brittle tilted fracture (BTF). This BTF which propagated within parallel θ -planes (tilted around RD by 40° with respect to rolling plane) joined by ductile slant was only observed for specimen taken along TD. No similar fracture mode (along an anti- θ -plane, rotated around TD by 40° with respect to the rolling plane) was observed. Therefore, even if BTF is affected by the loading mode (i.e., by mechanical parameters), metallurgy (i.e., the steel microstructure) might play a considerable role in the origin of BTF. Delamination and ductile slant were the initiation sites of this BTF. Delamination cracks initiated from some ductile crack advance or from ductile slant could sometimes gradually rotate to become parallel to the loading plane.

Impact toughness was also evaluated using Charpy specimens, which have smaller dimensions than DWTT specimens. Brittle out-of plane cracking was also observed for Charpy specimens. Two delamination types were observed. Type 1 delamination cracks initiated from the notch root and Type 2 delamination cracks initiated after ductile crack advance. Type 1 delamination cracks were the ones generally leading to brittle out-of-plane cracking which covered the entire fracture surface. This type of delamination occurred at higher temperature for Steel A than for Steel B, and might explain the higher ductile to brittle transition temperature observed for Steel A. SEM investigations of delamination fracture surfaces exhibited elongated cleavage facets at the notch root where cleavage fracture started from. After a considerable propagation along the rolling plane, delamination cracks could gradually rotate to become parallel to the main loading plane. Another possibility is that, delamination micro-cracks could join the θ -plane without noticeable propagation along the rolling plane, leading to BTF for specimens loaded along TD. Steel A was more sensitive to delamination rotation and Steel B was more sensitive to BTF. By comparing results of DWTT and Charpy tests, it was found that fracture modes were similar for both tests. One noticeable difference between both tests was yet that brittle out-of-plane cracking occurred at higher temperatures for DWTT specimens than for Charpy specimen. This partially explains why the ductile to brittle transition temperature was higher for DWTT. The larger ligament size of DWTT specimens is suspected to play a role on this easier occurrence of brittle out-of-plane cracking.

Furthermore, quasi static-tests performed on CT specimens also led to delamination and BTF. This shows that these fracture modes are not linked to the dynamic nature of impact tests. These brittle out-of-plane cracks were more detrimental for CT tests, specimens showing these cracks could not be considered as valid according to ASTM E1921-02 standard.

From the results reported in this chapter, it is clear that brittle out-of-plane cracking affects the fracture and impact toughness of pipeline steels. The rolling plane and θ -plane, along which brittle out-of-plane crack propagated seemed to be more sensitive to cleavage than RD-ND and TD-ND planes that were loaded in mode I. This was not the case for the anti- θ -plane. This suggests an anisotropic cleavage resistance of these steels. Studying the origin of brittle out-of-plane cracking on Charpy and DWTT specimens in more detail was difficult because they are secondary cracks which makes them difficult to analyze with SEM. Consequently, it is necessary to use specimens where the main loading plane corresponds to the one expected for brittle out-of-plane cracking. Results of tests on specimens taken perpendicularly to the rolling plane (to study delamination), θ -plane (to study BTF) and along RD and TD directions which are more conventional, are presented in the following chapter.

Chapter III – *Plastic flow and fracture anisotropy*

Table of Contents

III.1.	Introduction and state-of-the-art	48
III.2.	Experimental approach.....	50
III.3.	Plastic anisotropy and elastic-plastic behavior	50
III.3.1.	Strain anisotropy	50
III.3.2.	Anisotropy in strength	51
III.3.3.	Evolution of the plastic flow behavior with temperature	52
III.3.4.	Summary on the plastic flow behavior.....	54
III.4.	Fracture resistance of the rolling plane (tensile tests along ND).....	54
III.4.1.	Fully ductile fracture mode	55
III.4.2.	Mixed ductile-cleavage fracture mode.....	57
III.4.3.	Full cleavage fracture mode	59
III.5.	Fracture resistance of the θ -plane (tensile tests along BTD)	60
III.5.1.	Fully ductile fracture mode	60
III.5.2.	Mixed ductile-delamination-cleavage fracture mode	61
III.5.3.	Full cleavage fracture mode	62
III.6.	Fracture resistance of the TD-ND plane (tensile tests along RD).....	63
III.6.1.	Fully ductile fracture mode	63
III.6.2.	Mixed ductile-delamination fracture mode.....	63
III.6.3.	Full cleavage fracture mode	65
III.7.	Fracture resistance of the RD-ND plane (tensile tests along TD)	66
III.7.1.	Fully ductile fracture mode	66
III.7.2.	Mixed ductile-delamination fracture mode.....	67
III.7.3.	Mixed delamination-brittle out-of-plane fracture mode	67
III.7.4.	Full cleavage fracture mode	68
III.8.	Discussion and conclusions	69

The previous chapter showed that, cleavage fracture preferentially propagates along two planes in Steel A and Steel B: The rolling plane (perpendicular to ND) which leads to delamination fracture and the θ -plane (perpendicular to BTD) which leads to so-called brittle tilted fracture. Analysis of delamination and BTF was difficult on impact specimens because of dynamic effects. But, because of the fatigue pre-crack, the modeling of CT specimens needs a significant mesh size refinement near the crack tip. Therefore, round bar notched specimens were preferred to study the plastic flow and fracture anisotropy.

The present chapter focuses on the cleavage fracture anisotropy. Fracture resistance of the rolling plane, the θ -plane, (TD-ND) plane and (RD-ND) plane were investigated with tensile tests on notched specimens. Tensile tests on smooth specimens were performed to study the plastic anisotropy. Fracture mode evolutions with temperature and cleavage fracture sensitivity were investigated for these four planes. This experimental database will be used in the next chapters to determine a quantitative cleavage fracture criterion

Résumé

L'étude de l'anisotropie de la résistance au clivage est le thème central de ce troisième chapitre. Des essais de traction sur éprouvettes lisses et entaillées sont réalisés dans les directions ND, BTD (perpendiculaire aux plans θ), RD et TD. L'étude du comportement plastique des deux aciers montre une anisotropie en déformation avec des coefficients de Lankford différents de 1, sans notable anisotropie en contrainte. L'effet de la température sur l'érouissage lors des essais de traction semble négligeable et l'évolution de la limite d'élasticité avec la température suit une courbe exponentielle.

La résistance à la rupture par clivage dans les quatre directions (ND, BTD, RD, TD) a été étudiée sur éprouvettes entaillées, pour des températures entre -196°C et 20°C afin de balayer la totalité de la transition ductile-fragile. Il en découle que les plans θ (perpendiculaires à BTD) et de laminage (perpendiculaire à ND) sont plus sensibles au clivage que les plans perpendiculaires à RD et TD.

Les éprouvettes sollicitées dans la direction ND présentent une rupture par clivage qui amorce sur une fissure ductile circulaire au centre. Cette fissure ductile diminue quand la température diminue et finit par disparaître aux très basses températures où la rupture se fait entièrement par clivage (-100°C pour acier A et -196°C pour acier B).

Les éprouvettes sollicitées dans la direction BTD sont moins sensibles au clivage que dans la direction ND pour l'acier A. Les essais entre -140°C et -110°C conduisent à une rupture par clivage amorcée sur des cupules et de microfissures de délaminage. La rupture entièrement par clivage a été observée à -196°C . L'acier B quant à lui semblerait être plus sensible au clivage pour les essais dans la direction BTD que pour ceux dans la direction ND au vu des déformations à rupture à -196°C . Des essais complémentaires à des températures intermédiaires sont nécessaires pour valider cette tendance.

Pour les directions RD et TD, le faciès de rupture présente un délaminage central entre -140°C et -40°C . Quelques microfissures de délaminage demeurent visibles pour certaines éprouvettes même à -196°C . L'analyse de la surface de délaminage souligne la présence de facettes de clivage allongées qui amorcent sur une fissure ductile au centre de l'éprouvette. Ce résultat est cohérent avec les observations faites sur éprouvettes prélevées

dans la direction ND, où le clivage amorce sur une fissure ductile au centre de l'éprouvette, à la seule différence de la forme allongée des facettes de clivage dans le cas du délaminage.

L'étude qualitative de l'anisotropie de la résistance au clivage a permis de montrer la sensibilité au clivage des plans θ et de laminage. Une étude quantitative sera menée pour consolider ce résultat.

III.1. Introduction and state-of-the-art

The occurrence of delamination and brittle tilted fracture suggests a higher sensitivity of rolling plane and θ -plane to cleavage fracture. Unfortunately, the fracture resistance of these planes under mode I loading have rarely been studied in literature. This is mainly because of the limited thickness of plates which does not allow machining of conventional specimens perpendicularly to these planes. To pass through this difficulty, two approaches could be used.

The first approach consists in increasing the steel thickness so that conventional specimen geometries could still be used along ND. This first approach was used in [26] and [16]. Authors in [26] produced plates of 25 mm thickness after hot rolling a 127 mm-thick slab, so that CT specimens could be taken along ND. Three plates were obtained by modifying the finish rolling temperature. The first steel plate with a finish rolling temperature (100°C) higher than the non-recrystallization temperature (950°C), did not exhibit anisotropy of critical cleavage stress. The other steel plates with finish rolling temperatures (750°C and 690°C) lower than the non-recrystallization temperature showed a critical cleavage stress along ND 15 % lower than other directions.

Author in [16], who only had a 12 mm-thick plate, welded additional materials on both sides of the plate, so that the plate thickness could be locally increased. Then, Charpy-like specimens were taken along ND. Seven steels were studied, having pronounced banding in the microstructure. Critical cleavage stress found along ND was 30% lower than for other directions.

In both studies, the rolling plane sensitivity was linked to the dimensional anisotropy of the ferrite grains or presence of heavy flat MnS particles. The effect of microtexture anisotropy was not investigated, only the average texture was determined.

The second approach is to design new specimen geometries, so that tests could be performed along ND. The advantage of this approach is that tests are performed on the as-received material. The microstructure is not modified even locally by welding. This approach was chosen for this study. For this purpose, notched round bar specimens were designed (Appendix B). The size of these specimens was fixed so that tensile tests could be performed perpendicularly to the rolling plane and the θ -plane. In order to study the cleavage anisotropy in a more competitive manner, complementary tests were done along RD and TD.

The direction perpendicular to θ -plane is called "BTD" thereafter. The four directions along which tensile tests were performed are presented in Figure III-1. All specimen geometries used on this study are presented in Figure III-2. Some tensile tests on Steel A along RD and TD were performed previously of the project, using NT1 and UT1 geometries. Therefore, NT1 and UT1 geometries were chosen to study directions RD and TD for both steels. Concerning, ND and BTD directions, NT2 and UT2 geometries were considered. At -196°C, RD and TD directions were investigated with NT2 geometry, so that high stress triaxiality could be reached and cleavage fracture could occur. Due to an error during the machining, a notch radius of 0.6 mm was used instead of 0.4 mm for NT2 specimens taken along RD and TD within Steel A. This new geometry was called NT2-modified.

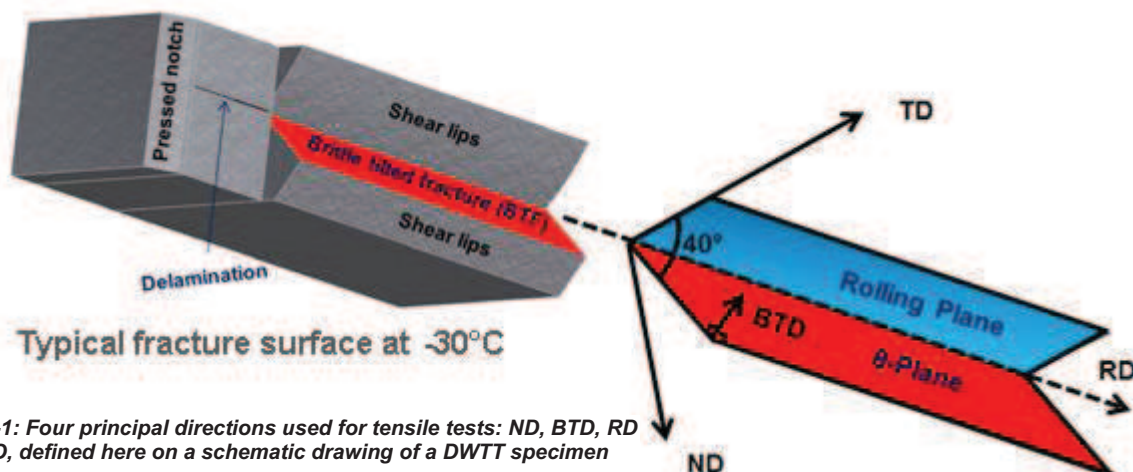


Figure III-1: Four principal directions used for tensile tests: ND, BTD, RD and TD, defined here on a schematic drawing of a DWTT specimen

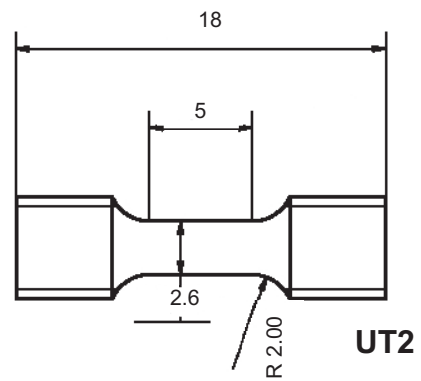
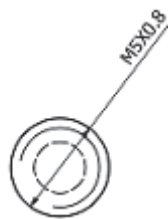
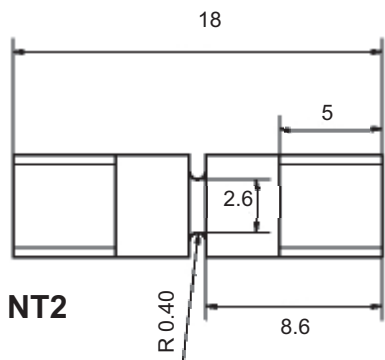
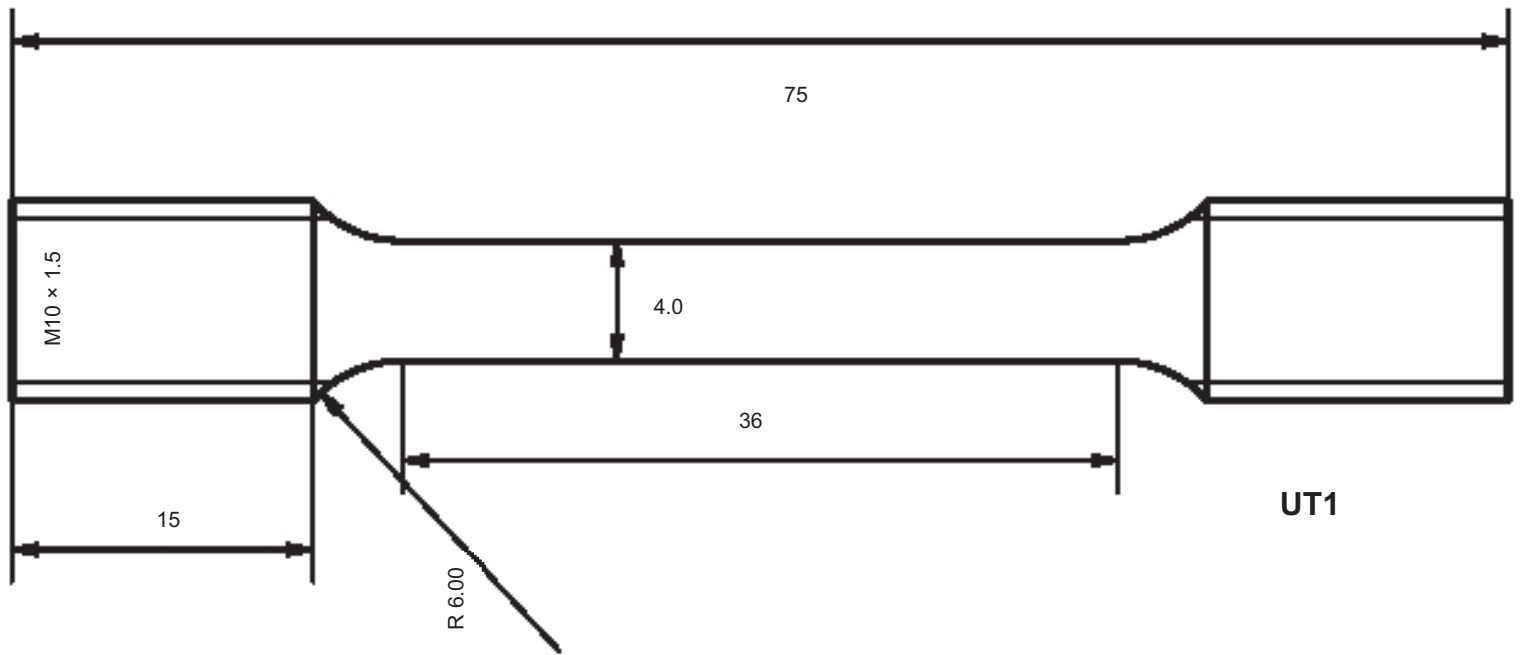
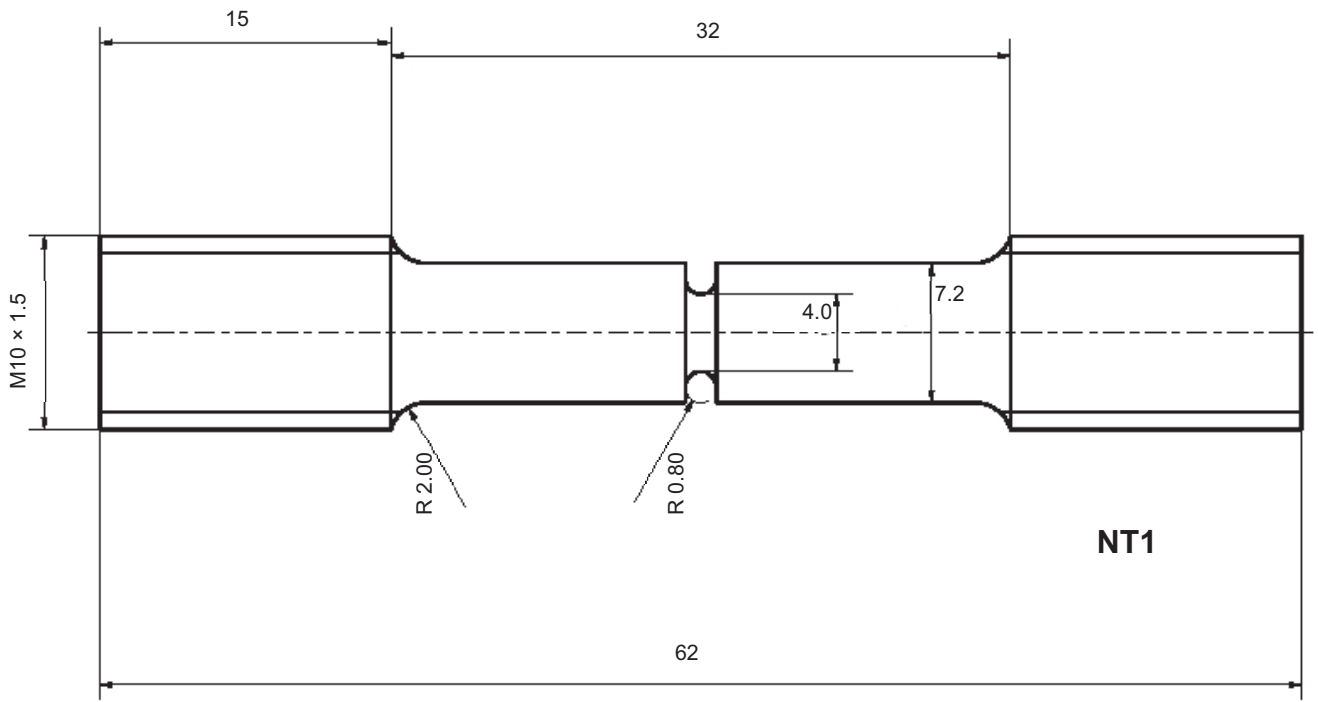


Figure III-2: Specimen geometries used for tensile tests (Same scale for all specimens).

III.2. Experimental approach

Cleavage was the fracture mode investigated in this study. The test temperatures were chosen so that specimens brake with full cleavage or mixed ductile+cleavage fracture modes. Additional tests were done at 20°C for both steels, independently of the specimen directions, to investigate the plastic behavior and the plastic anisotropy.

In practice, a first campaign of tensile tests along ND was done on NT2 geometry. The first test was performed at -100°C, because Charpy results showed that this temperature was in the ductile to brittle transition domain. On one side, the initial test temperature (-100°C) was increased 10°C by 10°C, until full ductile fracture was observed. On another side, the initial test temperature was decreased 10°C by 10°C, until -140°C, and the last tests were performed at -196°C. The fact that, load vs. displacement curves were ranked correctly even for close test temperature values, suggested a good reproducibility of results. The fracture surfaces of specimens were investigated to analyze fracture modes and determine the cleavage initiation sites. Steel A, showed atypical fracture surfaces for temperatures lower than -100°C. Therefore, only results of tensile tests for temperatures higher or equal to -100°C were presented in this study (For Steel A). Tensile tests on smooth specimens were only performed for temperatures where numerical calculations were expected to be done.

The second campaign concerned tests along TD. Tensile tests on Steel A for NT1 and UT1 geometries were performed previously to the project. For Steel B, which was tested in this project, the test temperatures were chosen so that the domain affected by delamination occurrence could be entirely determined. Complementary tests were performed at -196°C on NT2 geometry, so that full cleavage fracture could be expected. Tensile tests on smooth specimens were only performed for temperatures where numerical calculations were expected to be done.

The third campaign concerned tests along RD. Tensile tests on Steel A for NT1 and UT1 geometries were performed previously to the project. For Steel B, tests were only performed at 20°C, -100°C and -120°C for NT1, because of the lack of specimens. Complementary tests were also performed at -196°C on NT2 geometry, so that full cleavage fracture could be expected. Tensile tests on smooth specimens were only performed at 20°C and -196°C.

The fourth campaign concerned tests along BTd. For Steel A, NT2 specimens were tested at 20°C, at -196°C and for temperatures where local cleavage fracture was expected to occur. For Steel B, because of the lack of specimens, NT2 specimens were only tested at 20°C and -196°C.

III.3. Plastic anisotropy and elastic-plastic behavior

The plastic anisotropy and elastic-plastic behavior was investigated via tensile tests performed on a 250 kN servohydraulic Instron 8500 machine. Geometry UT1 was used for RD and TD directions and geometry UT2 was used for ND and BTd directions. A longitudinal extensometer was used to measure the specimen elongation, over a gauge length of 10 mm for UT1 and 5 mm for UT2. Tests were performed under load line displacement control, with a strain rate of 10^{-3} s^{-1} . The temperature was set to $\pm 3^\circ\text{C}$ using a climatic chamber for temperatures higher than -150°C and by immersion of the specimen in liquid nitrogen at -196°C.

III.3.1. Strain anisotropy

To assess the plastic strain anisotropy expected from the thermal mechanical processing condition, Lankford coefficients were calculated as the ratio between the minimal diameter reduction and the

maximal diameter reduction (Figure III-3). This definition of Lankford coefficient is the same that will be used in chapter IV for the identification of constitutive equations. The results of tensile tests performed prior to this project on Steel A, suggested that the ratio between the minimal diameter reduction and the maximal diameter reduction remained constant during the loading. Therefore, Lankford coefficients were post-mortem calculated on the broken surfaces of smooth specimens tested at -196°C (less pronounced necking). To avoid delamination observed after tests at -196°C along TD for Steel B, the Lankford coefficient was measured at -140°C . Moreover, broken specimens of Steel A taken along RD were not available and tests on Steel B along RD were only performed at 20°C . Consequently, there is no Lankford coefficient value along RD for Steel A and the Lankford coefficient value along RD of Steel B was determined at 20°C .

The Lankford coefficient values are presented in Table III-1. For both steels, Lankford coefficients are significantly different from 1, which suggests strain anisotropy. This strain anisotropy seems to be more pronounced for Steel A than for Steel B.

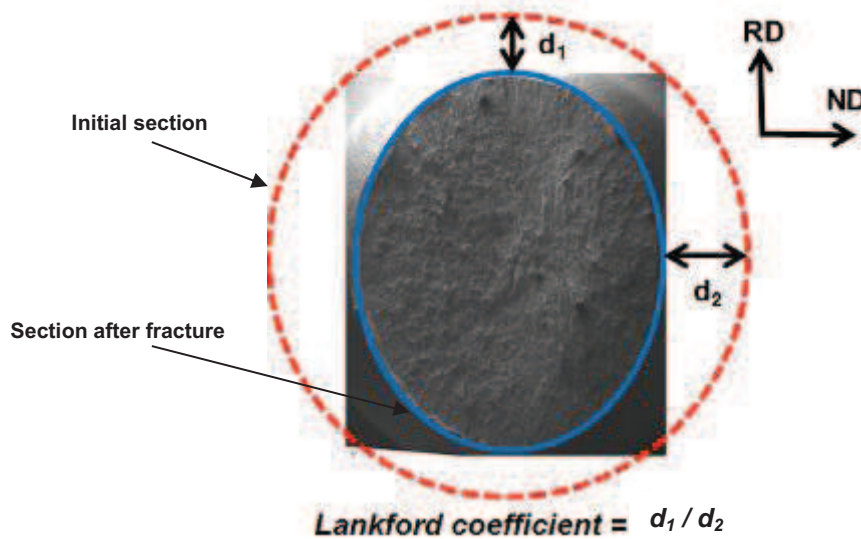


Figure III-3: Fracture surface after a tensile test on a smooth specimen taken along TD: Steel A, -196°C

	ND	BTD	RD	TD
Steel A	0.80 ± 0.05	0.77 ± 0.05	n.a	0.73 ± 0.05
Steel B	0.86 ± 0.05	0.80 ± 0.05	0.71 ± 0.05	0.83 ± 0.05

Table III-1: Lankford coefficients measured after smooth tensile tests along ND, BTD, RD and TD

III.3.2. Anisotropy in strength

The engineering stress-strain response along ND, BTD, RD and TD are compared at 20°C , because all the directions were tested at this temperature (Figure III-4). All the specimens showed a full ductile fracture surface. Since tensile test results after the decreasing of the load are affected by the necking, the tensile curves of smooth specimens were cut after the maximal stress.

The hardening is similar for all the directions. Existence of yield points, in particular for Steel B, makes difficult an estimate of the yield strength along the four directions. Nevertheless, except for TD direction which seems to be slightly stronger (less than 5%) on Steel A, the stress anisotropy was found to be negligible comparing to the strain anisotropy previously investigated with Lankford coefficients. This negligible plastic stress anisotropy was also observed for other temperatures (-100°C , -140°C).

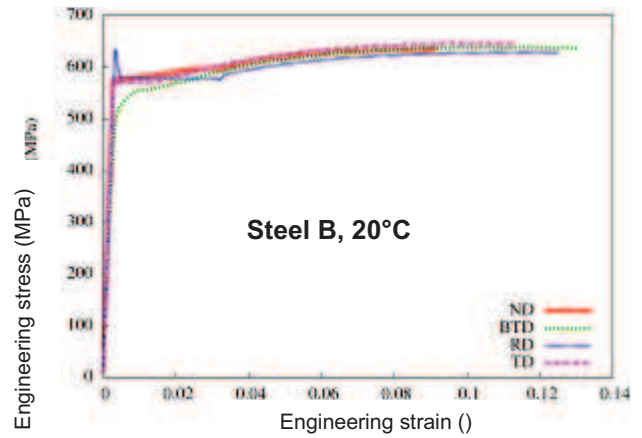
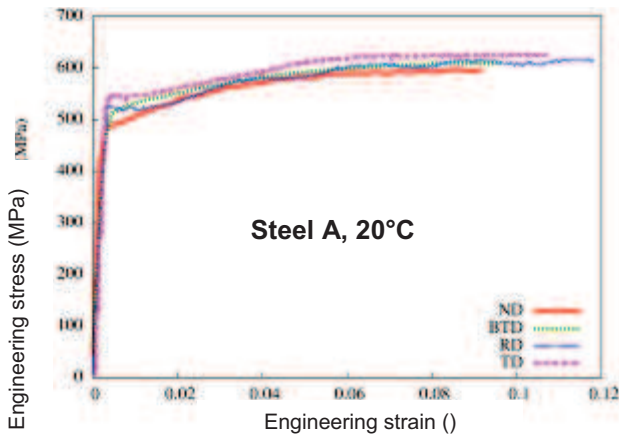


Figure III-4: Engineering stress-strain curves of tensile tests along ND, BTD, RD, TD: Steels A and B

III.3.3. Evolution of the plastic flow behavior with temperature

Tensile tests along ND, BTD and TD were performed between 20°C and -196°C to analyze the effect of temperature on plasticity regime. Because of the low plastic stress anisotropy observed at 20°C, tests were not performed along RD for other temperatures. For the same reason, tests on Steel B along BTD were only performed at 20°C and -196°C. The tensile curves are along ND, BTD and TD are presented in Figure III-5, Figure III-6 and Figure III-7 respectively.

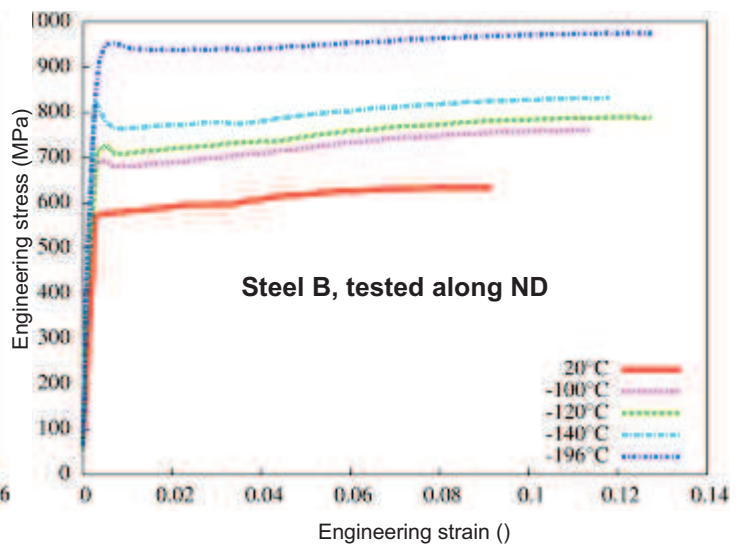
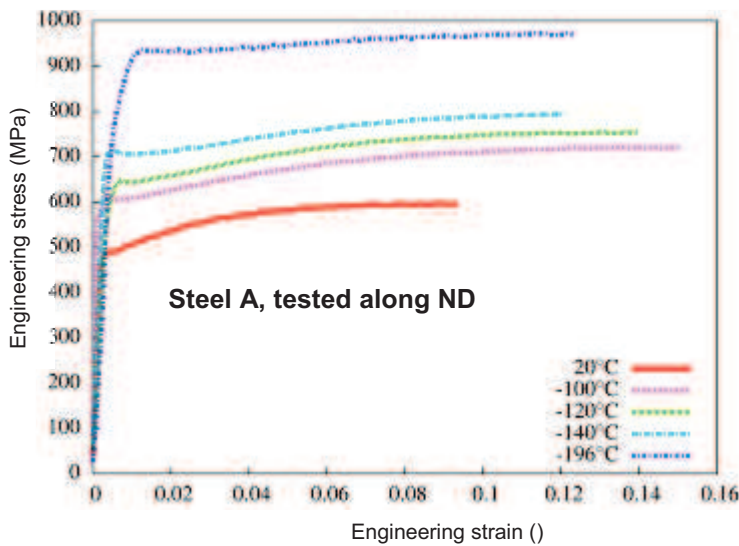


Figure III-5: Evolution of the plastic behavior with temperature: Tensile tests along ND

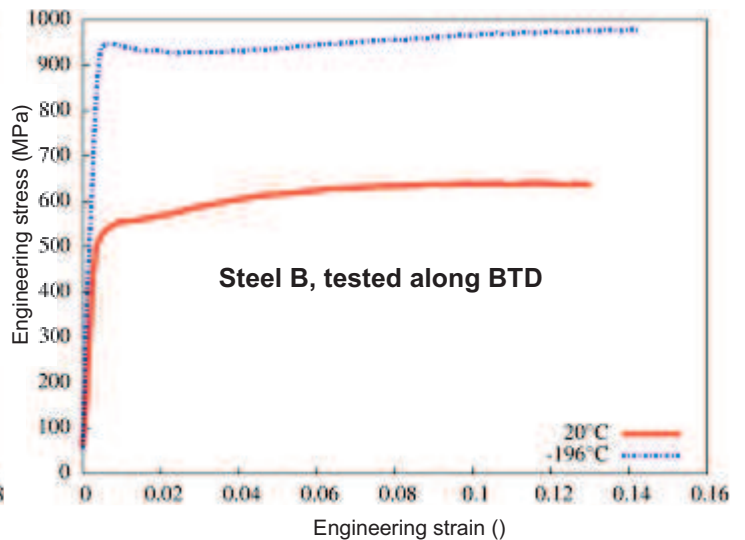
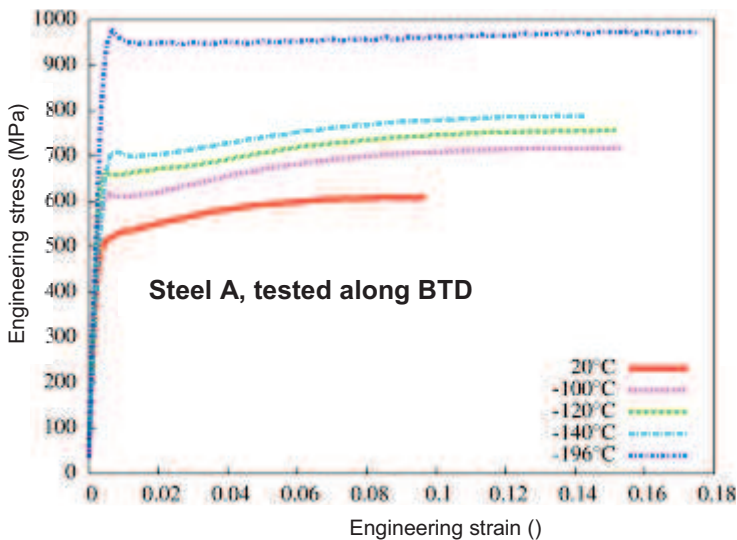


Figure III-6: Evolution of the plastic behavior with temperature: Tensile tests along BTD

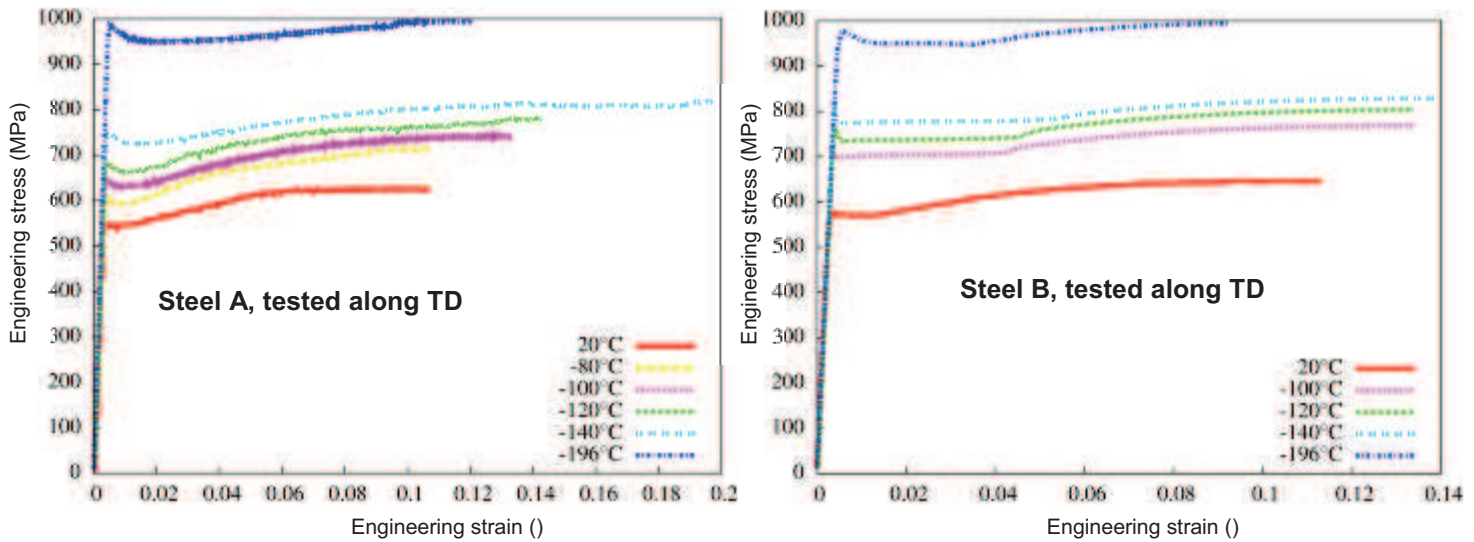


Figure III-7: Evolution of the plastic behavior with temperature: Tensile tests along TD

Whatever the steel and the loading direction, by decreasing temperature the steel strength increases. To study the dependence of the hardening to temperature, all the curves were shifted to remove the increasing of the yield strength produced by temperature decreasing. The curve at -196°C was chosen as the reference curve and the other curves were shifted so that they could have one point in common after the yield point. Figure III-8 gives a typical result obtained. The effect of temperature on work hardening was not pronounced between -100°C and -196°C . At 20°C , the hardening saturated earlier.

Therefore, temperature was assumed to mainly affect the yield strength. Because, of the presence of yield points, there is none unique way of estimation of this yield strength. For this study, the yield strength was estimated as the intersection of the linear part of the curve and the extrapolation hardening part. This is the same procedure used in [1]. The error on yield strength estimate was around 30 MPa.

An exponential law was used to fit the evolution of the yield strength with temperature (Equation III.1). Figure III-9 shows the evolution of the yield strength with temperature. The exponential fitting well represents the evolution of the yield strength with temperature.

$$\sigma_{y0}(T) = \sigma_a + b \times \exp(-c \times (T+273.15)) \quad (T \text{ en } ^{\circ}\text{C}) \text{ Equation III.1}$$

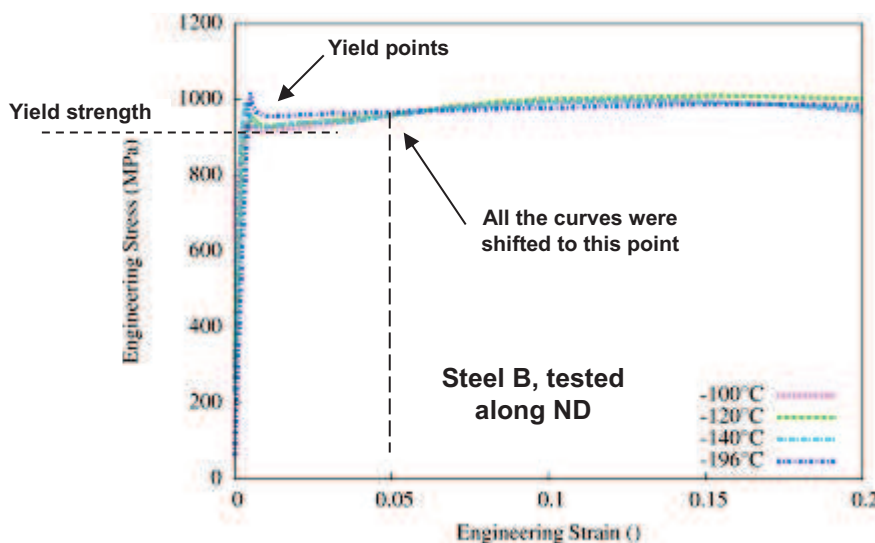


Figure III-8: The effect of temperature on work hardening was not pronounced between -100°C and -196°C .

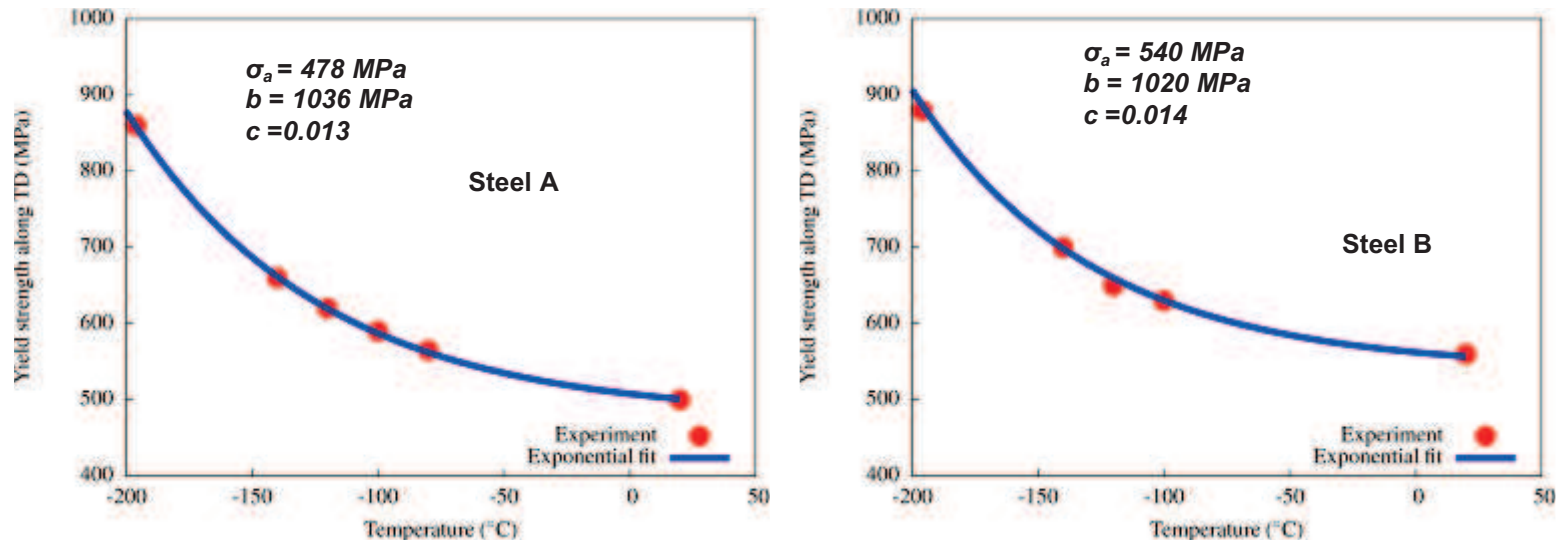


Figure III-9: Evolution of the yield strength with temperature along TD: Steels A and B

III.3.4. Summary on the plastic flow behavior

Tensile tests along the four directions at room temperature showed that the stress anisotropy was not pronounced within both steels. In fact, TD (strongest direction) was less than 5% stronger than other directions. This negligible stress anisotropy was also observed at other temperatures as -100°C and -140°C .

However, a strain anisotropy associated to Lankford coefficients different from 1 was observed. This strain anisotropy was more pronounced on Steel A.

No obvious evolution of the hardening with temperature was found between -100°C and -196°C . Temperature mainly affected the yield strength, which was higher for Steel B. An exponential function satisfactorily describes the evolution of the yield strength with temperature.

After the study of the plastic behavior, the fracture resistance of the rolling plane, the θ -plane, (TD-ND) and (RD-ND) planes are successively investigated. For each plane, the competition between fracture modes is analyzed, especially for temperatures within the ductile to brittle transition.

III.4. Fracture resistance of the rolling plane (tensile tests along ND)

Tensile tests on NT2 specimens were performed by using a 250 kN servohydraulic Instron 8500 machine. The notch geometry of specimens was measured by using a shape projector equipment (accuracy $10\mu\text{m}$). These measurements gave the actual geometry of the notch which was used for further numerical simulation of the tensile test. No remarkable variation in the notch radius was observed between the various specimens, but there was a little variation on the minimal diameter value between 2.55mm and 2.63mm depending on the specimen. Before starting every test, the minimal diameter of the specimen was measured and the knives of the radial extensometer were fixed to measure the diameter reduction along TD at the minimal section. The location of the knives was validated after comparing the diameter measured by the extensometer and the one obtained from the shape projector equipment. The effective stress was calculated as the load divided by the initial value of the minimal section and the diameter reduction was normalized by the initial diameter of the minimal section.

Tensile tests were performed with a prescribed load line displacement rate of $5 \times 10^{-3} \text{ mm/s}$ which corresponds to an initial strain rate of 10^{-3} s^{-1} for smooth specimens. The test temperature was set using a climate chamber or by immersion in liquid nitrogen, as it was done for smooth specimens. The

fracture surfaces were observed with SEM to investigate the fracture mode and to locate, if any, cleavage initiation sites.

After analysis of the evolution of diameter reductions at fracture (Figure III-10), three domains of temperature were determined. The first domain with highest diameter reductions at fracture was associated to specimens which showed full ductile fracture mode. The second domain with intermediate diameter reductions at fracture was associated to specimens which showed ductile + cleavage fracture modes. The dispersion on diameter reduction at fracture was more pronounced in that domain. The last domain associated to specimens with full cleavage fracture was difficult to investigate for Steel A, because specimens showed a fracture surface not representative of common fracture mode in such steels. For Steel B, this domain corresponded to temperatures around -196°C .

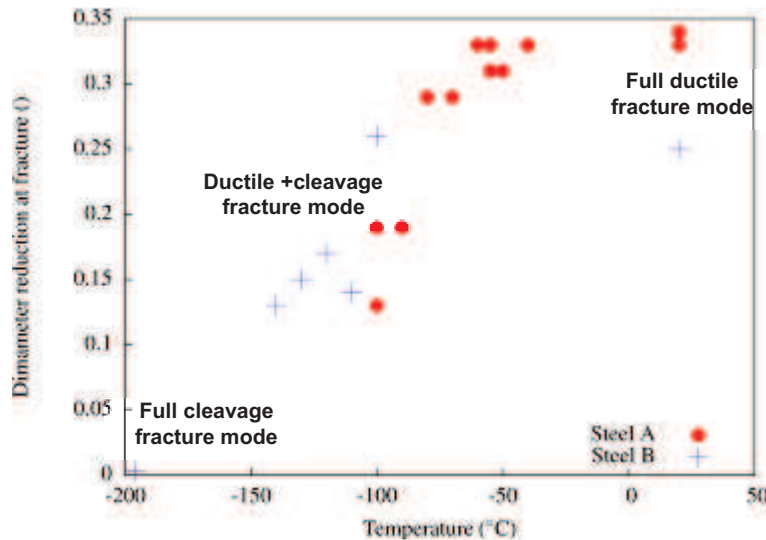


Figure III-10: Evolution of the diameter reduction at fracture with temperature for Steel A and Steel B. Three domains observed: Full cleavage, mixed ductile-cleavage, and full ductile modes

III.4.1. Fully ductile fracture mode

Full ductile fracture mode was observed for temperatures higher than -80°C for Steel A and -100°C for Steel B. Figure III-11 shows the results of tensile tests on notched specimens at 20°C . The effective stress increases up to a maximal value; then it slowly decreases until a critical diameter reduction is reached (see arrows in Figure III-11); after this critical diameter reduction, there is an acceleration of the decrease in effective stress leading to a change in the curve slope; right before the final failure of the specimen, there is further acceleration of the effective stress decrease. The first change of the slope is generally associated to the onset of stable ductile crack propagation. Steel B, which has the higher yield strength, exhibited a lower strain hardening ability and the first change of the curve slope occurred earlier for this steel (0.12). In fact, the diameter reduction observed at the first change of the slope for Steel B is 30% lower than the one for Steel A.

To understand the origin of this earlier stable ductile crack propagation within Steel B, the fracture surface of both steels after tensile test at 20°C was analyzed with SEM (Figure III-12 and Figure III-13). Steel A shows a noticeable scatter in the size of large dimples ($40 - 60 \mu\text{m}$ in size), which are separated by clusters of smaller dimples (around $3 \mu\text{m}$ in size). For Steel B, the size of large dimples is almost homogeneous (around $50 \mu\text{m}$) and smaller dimples are almost inexistent. Large dimples observed for both steels correspond to voids nucleated from inclusion interface at the beginning of the ductile damage. The nature of these inclusions is the same as those observed with inclusion analysis in chapter I (Rich in Al, Ca, Mg, O, Mn, S). This first population of dimples is larger because they could considerably grow before the onset of coalescence. For Steel B, the first population of dimples covers

the almost entire fracture surface; the second population of dimples (cluster of fine dimples) was rarely observed. This second population of dimples was more observed for Steel A. Therefore, the number density of the first population of dimples is larger for Steel B. It is in good agreement with the results of inclusion analysis presented in chapter I, where a smaller average inter-inclusion distance was found for Steel B and consequently a greater amount of ductile nucleation sites. The fracture surface of Steel B also exhibits finely dispersed inclusions with almost homogenous sizes (around 3 μm). Coalescence was therefore more pronounced for Steel B which had a higher density in number of first population dimples, because the interaction between primary voids is higher in that case. Steel A which has a similar inclusion volume fraction but higher inter-inclusion distance, exhibited a lower density in number of these first population dimples. Consequently, the interaction between primary voids was lower and the coalescence by internal necking was less pronounced within Steel A.

After comparing the ductile fracture resistance of both steels at room temperature, the evolution of ductility with temperature was investigated (Figure III-14). The steel strength gradually increased when temperature decreased. Globally, the first change of the slope on tensile curve was delayed by decreasing temperature. In fact, void nucleation was more difficult when temperature decreased. Consequently, all the ductile damage process was delayed.

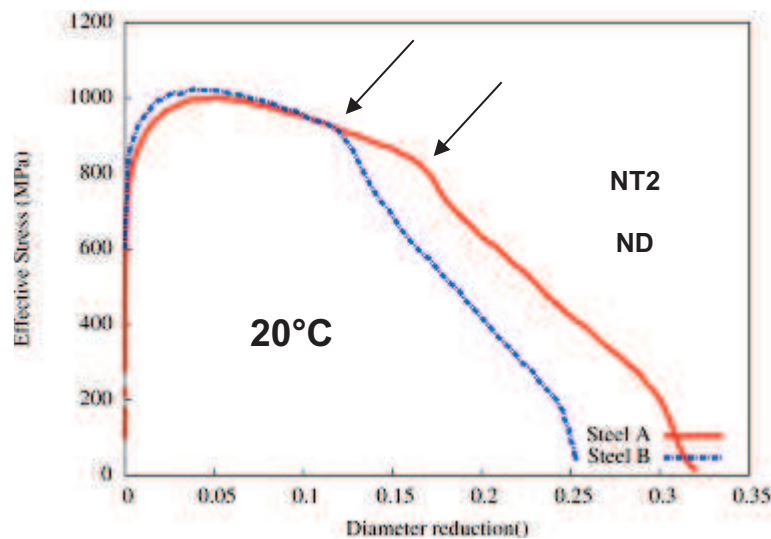


Figure III-11: Tensile curves of steels A and B at 20°C (NT2 geometry). The load drop associated to stable ductile crack propagation started earlier for Steel B.

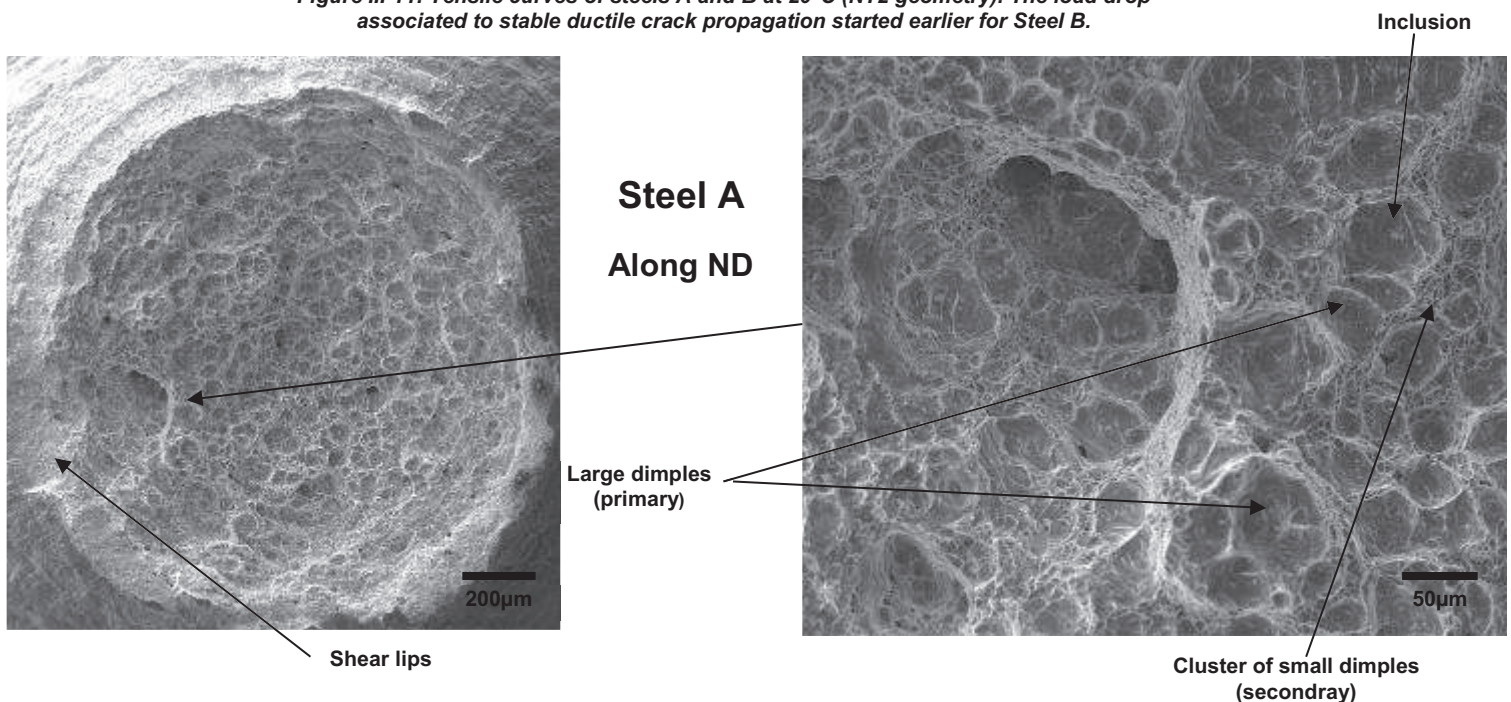


Figure III-12: Fracture surface of Steel A at 20°C (NT2 geometry). There is noticeable scatter in dimple size distribution.

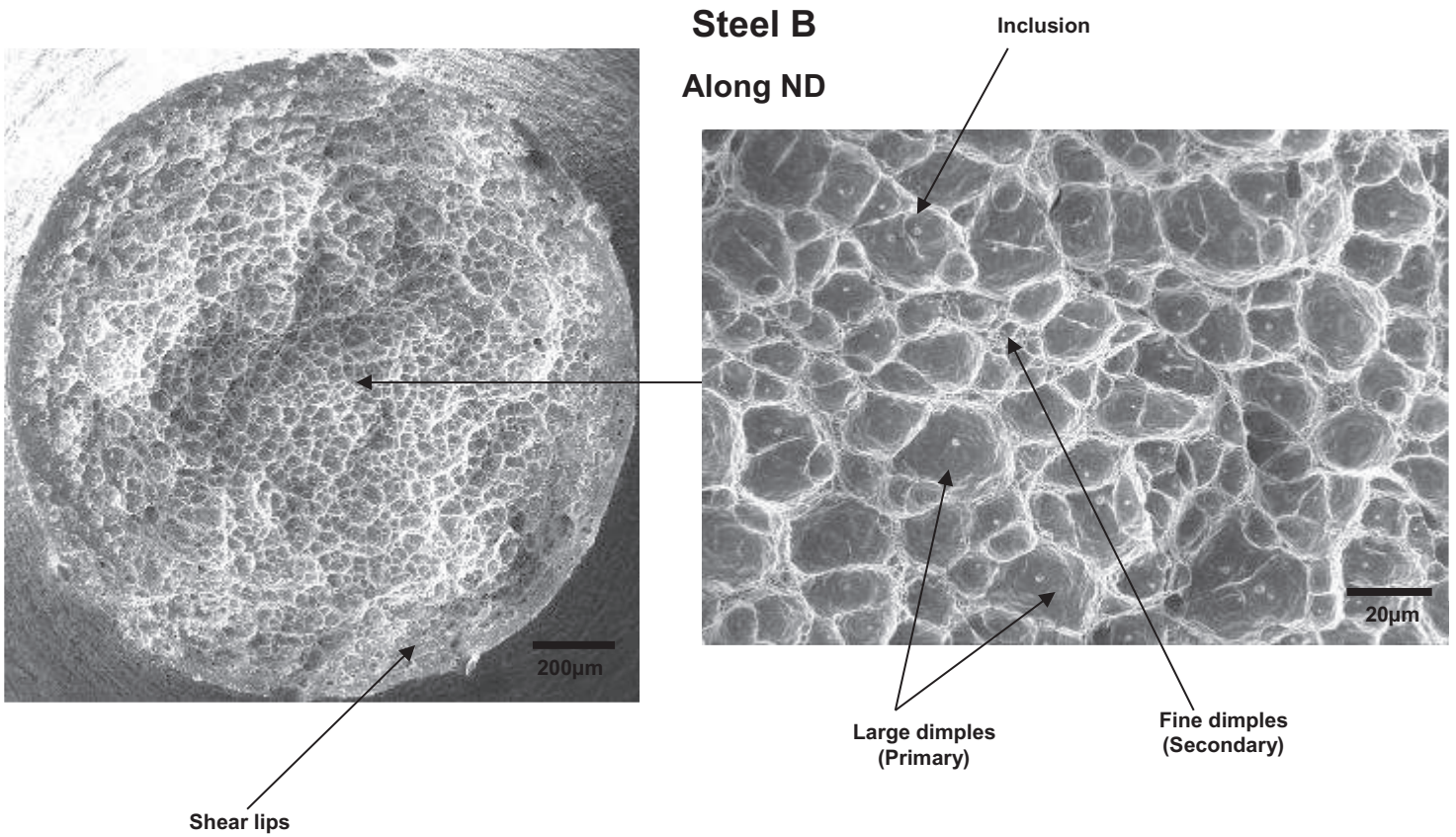


Figure III-13: Fracture surface of Steel B at 20°C (NT2 geometry). The dimple size is almost homogenous.

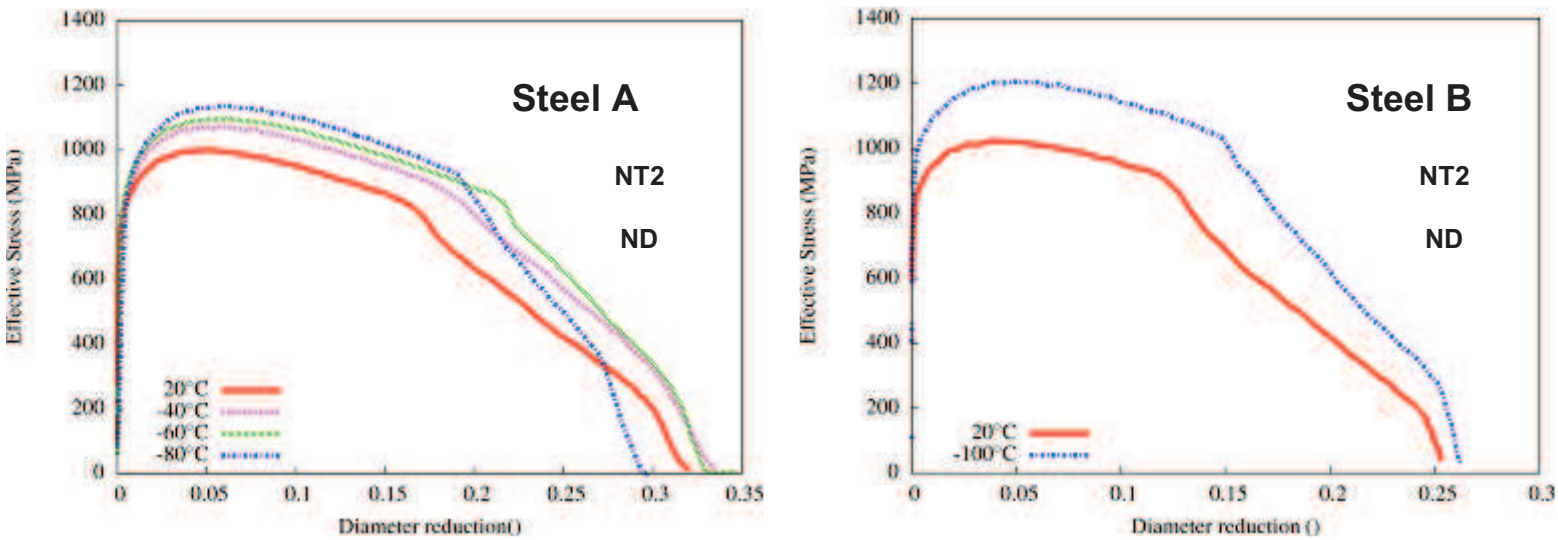


Figure III-14: Tensile curve of steels A and B. Full ductile fracture mode.

III.4.2. Mixed ductile-cleavage fracture mode

At some temperatures, ductile cracks initiated at the center of specimens could lead to cleavage fracture (Figure III-15). This fracture mode was more frequently observed in Steel B which exhibited the earlier propagation of stable ductile crack. For steel A, only two specimens exhibited this fracture mode: One at -90°C and the other one at -100°C.

Tensile tests on Steel B between -110°C and -140°C were performed to investigate this fracture mode (Figure III-16). Except at -110°C where cleavage fracture initiated early from many separated clusters of dimples, the diameter reduction at brittle fracture decreased with temperature. At -120°C and -130°C, the specimen was broken right after the first change in slope. In that case, cleavage was initiated from an almost circular ductile crack at the center of the specimen. The diameter of this

ductile crack decreased with decreasing temperature (Table III-2). At -140°C , the fracture surface revealed two separated ductile micro-cracks of $100\ \mu\text{m}$.

By decreasing the test temperature, steels become stronger. Therefore, the stress state within specimens becomes higher for a given value diameter reduction. Consequently, a critical cleavage stress could be reached for a smaller amount of ductile crack propagation (stress concentrator) when temperature is decreased. It explains why the ductile crack size decreased with temperature (Table III-2).

This mixed ductile-cleavage fracture mode, might be responsible for the type 2 delamination observed within Charpy specimens, where delamination occurred after ductile crack advance.

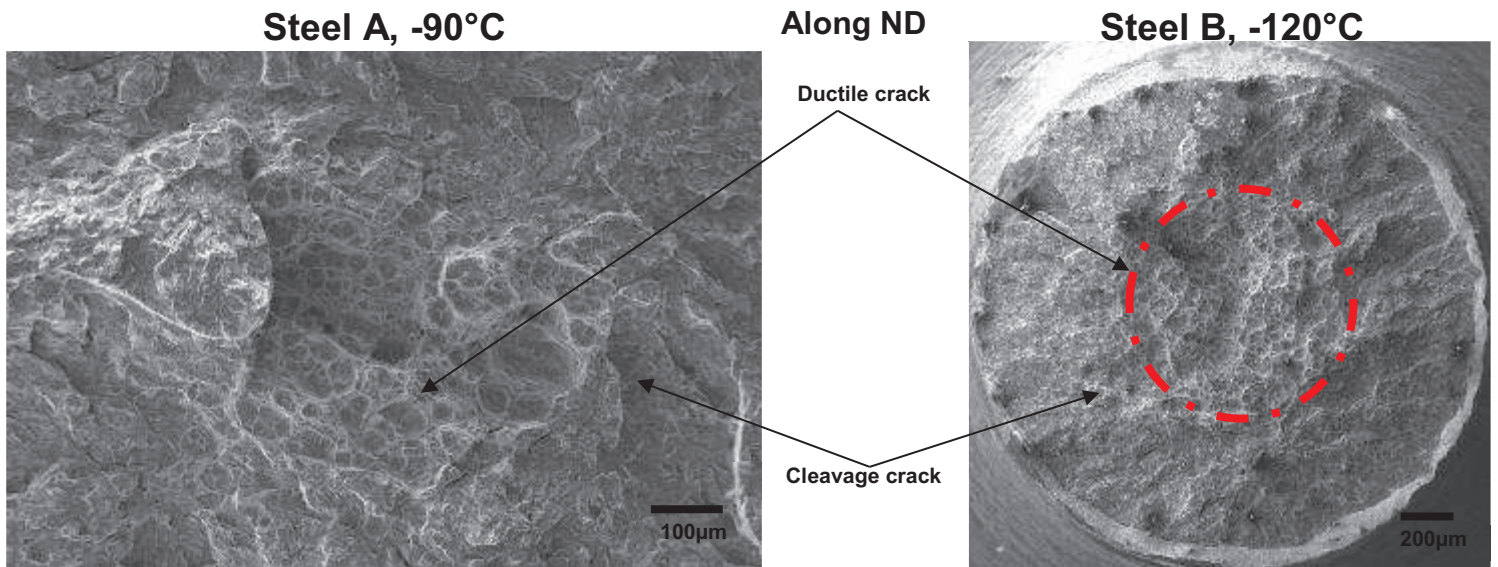


Figure III-15: Mixed ductile-cleavage fracture surface observed within steels A and B

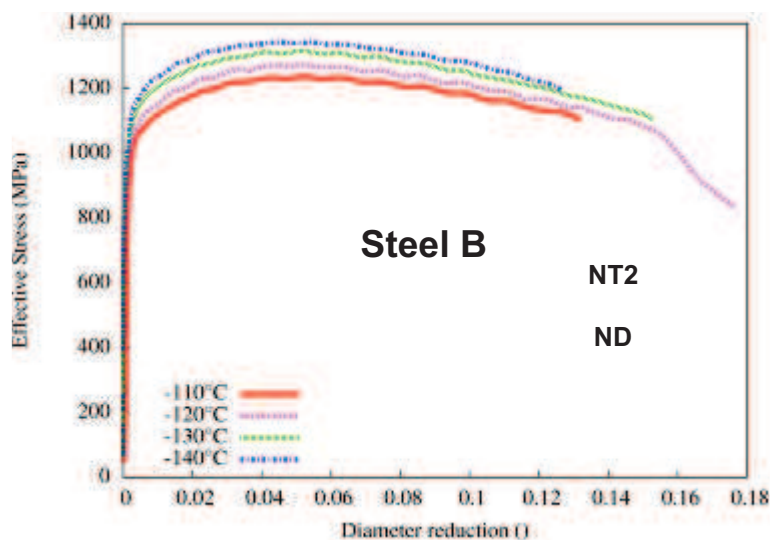


Figure III-16: Tensile curve of Steel B. Mixed ductile-cleavage fracture surface observed.

	-90°C	-100°C	-110°C	-120°C	-130°C	-140°C
Steel A	550 μm	330 μm	n.a.	n.a.	n.a.	n.a.
Steel B	Fully ductile	Fully ductile	Many clusters of dimples	920 μm	550 μm	Two micro-cracks of 100μm in length

Table III-2: Evolution of the ductile crack size with temperature (Steels A and B).

III.4.3. Full cleavage fracture mode

Full cleavage fracture mode was observed at -100°C for Steel A and -196°C for Steel B (Figure III-17). No particle could be found at the fracture initiation site. The average cleavage facet size around the initiation site was 60 μm for Steel A and 25 μm for Steel B. Thus, cleavage crack in Steel A was able to propagate along a greater distance without be arrested. The large size of cleavage facets within Steel A well correlates with its higher cleavage sensitivity. In fact, Steel A exhibits full cleavage fracture at considerably higher temperature than Steel B (fully ductile at -100°C and covered with dimples down to at least -140°C).

The tensile curves of steels A and B respectively at -100°C and -196°C are presented in Figure III-18. The diameter reduction at fracture is considerably higher for Steel A tested at -100°C. This suggests that a large plastic deformation occurred before initiation of cleavage fracture. At this step, we did not know the effect of such large plastic deformation on cleavage occurrence.

The easier occurrence of full cleavage fracture in Steel A might explain why this steel was more sensitive to the type 1 delamination, observed in Charpy specimens without ductile crack advance (Chapter II).

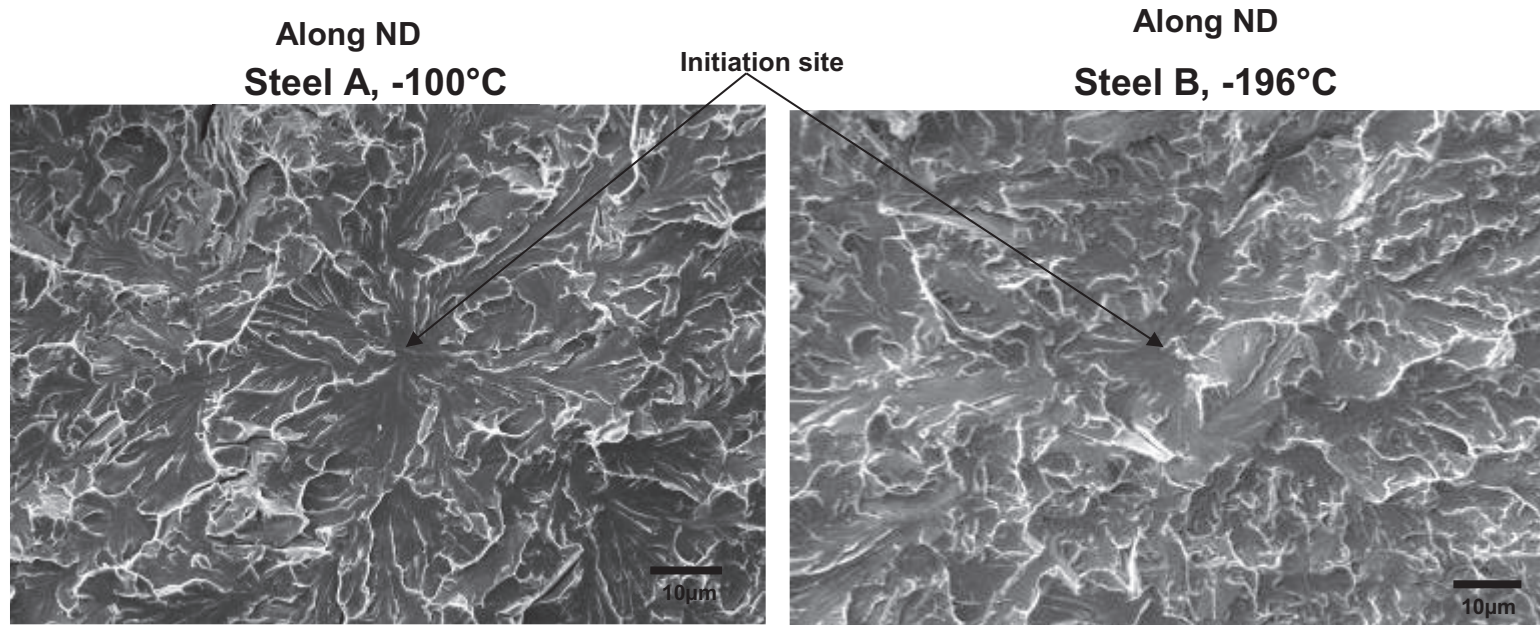


Figure III-17: Full cleavage fracture surface of steels A and B

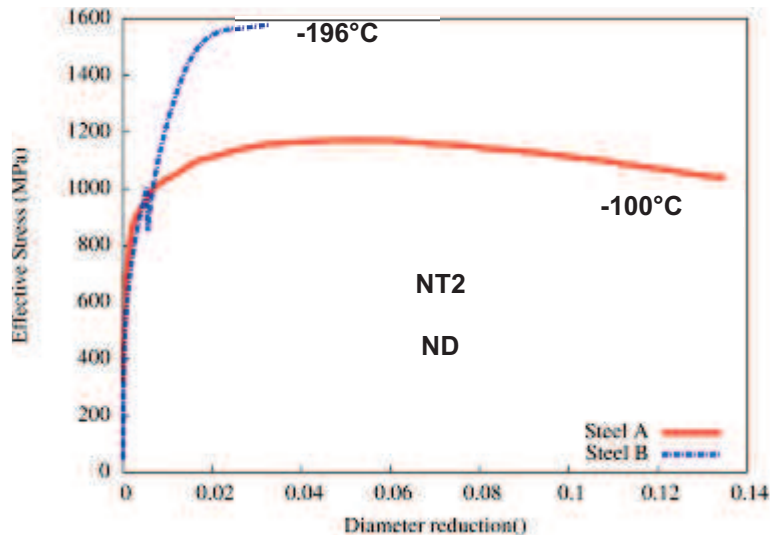


Figure III-18: Tensile curve of steels A and B in the full brittle (cleavage) temperature range

III.5. Fracture resistance of the θ -plane (tensile tests along BTD)

Tensile tests were performed on both steels at 20°C and -196°C; so that full ductile and full cleavage fracture could be observed. Complementary tests were carried out at intermediate temperatures -90°C and -140°C to study the fracture mode evolution with temperature. These complementary tests were performed on Steel A only. From tests on Steel A, three types of fracture modes could be observed depending on temperature: fully ductile, mixed ductile-delamination-cleavage and fully cleavage by cleavage. The knives of the radial extensometer were fixed to measure the diameter reduction along the direction perpendicular to RD.

III.5.1. Fully ductile fracture mode

Full ductile fracture modes occurred for both steels at 20°C. From tests performed on Steel A, full ductile fracture surface might be observed for temperatures higher than -90°C. The tensile curves obtained at 20°C are presented in Figure III-19. As it was for along ND, the diameter reduction at the first change of the curve slope (arrows in Figure III-19) is lower for Steel B than for Steel A. It suggests that stable ductile crack propagation starts earlier for Steel B. However, the diameter reduction at the first change of the slope initially found as 0.12 and 0.17 respectively for Steel A and Steel B along ND was now 0.15 and 0.20 along BTD. Therefore, the coalescence might be delayed for specimens along BTD comparing to specimens along ND. The delay of the onset of coalescence is in good agreement with the fact the area covered by secondary dimples on the fracture surface of specimens tested along BTD was larger than for specimens tested along ND.

The difference between Steel A and Steel B in term of strength along BTD is greater than the one observed along ND. In fact, the strength obtained along BTD for Steel A is lower than expected, by assuming the negligible stress anisotropy determined on smooth specimens.

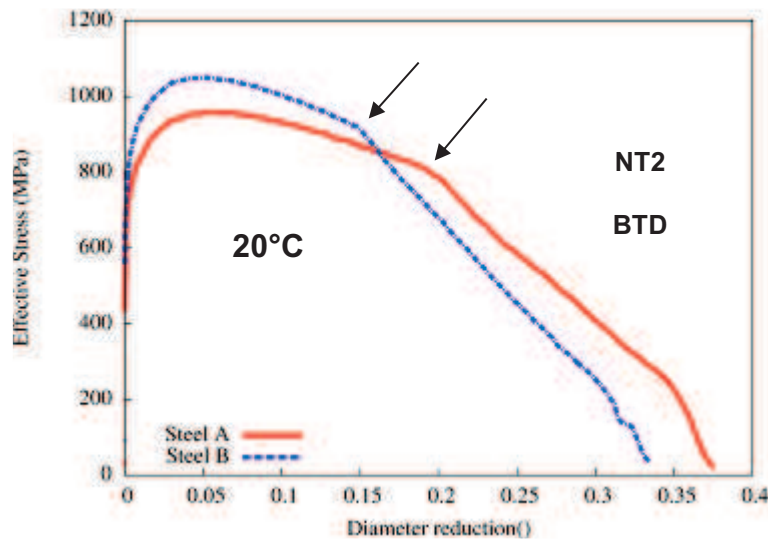


Figure III-19: Tensile curve of steels A and B in the full ductile temperature range

III.5.2. Mixed ductile-delamination-cleavage fracture mode

This type of fracture surface was observed at -90°C and -140°C on Steel A (Figure III-20). At -90°C , ductile fracture was the predominant fracture mode with many dimples. Cleavage cracks within the θ -plane were locally observed at this temperature. These cleavage cracks were initiated from delamination micro-cracks. At -140°C , cleavage fracture within the θ -plane was the predominant fracture mode. Small delamination cracks and very few dimples were also observed.

Tensile curves at -90°C and -140°C are presented in Figure III-21. Since ductile cracking was predominant at -90°C , the tensile curve is similar in shape to the one obtained for a full ductile fracture surface. Nevertheless, the load drop was sharper compared to the one at 20°C , probably because of local cleavage micro-cracks. The tensile curve at -140°C shows an abrupt load drop associated to brittle fracture.

Along BTD
Steel A, -90°C

Along BTD
Steel A, -140°C

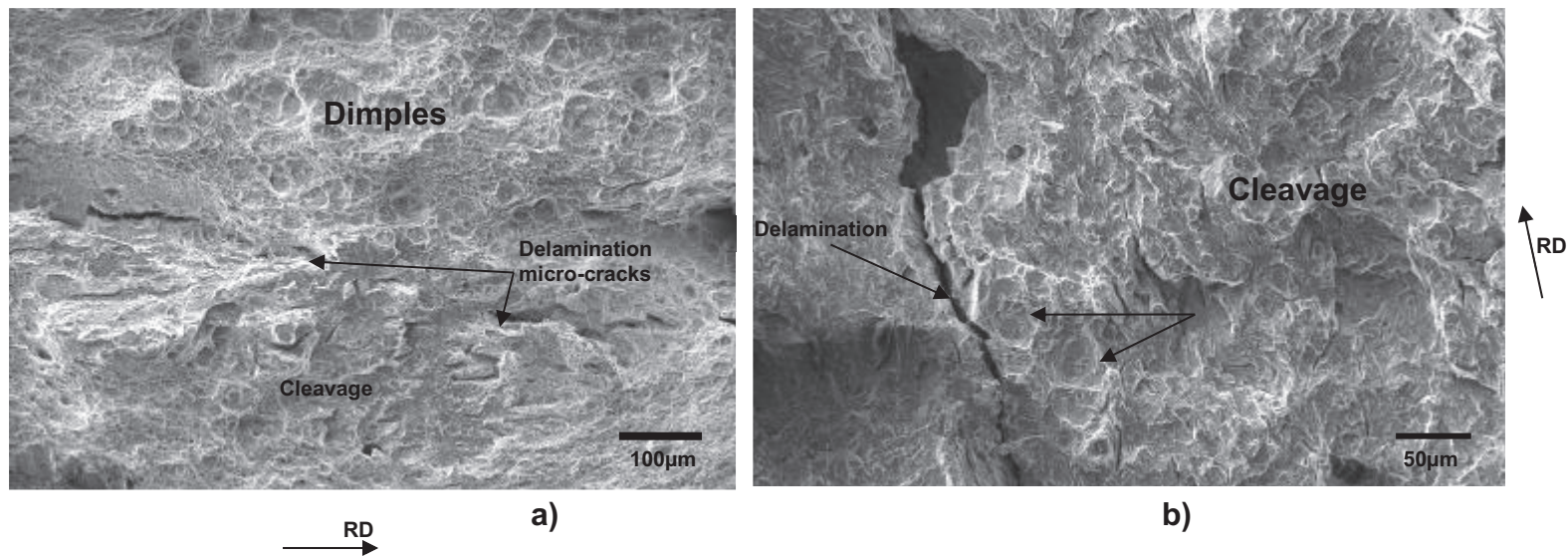


Figure III-20: Mixed ductile-delamination-cleavage fracture surfaces, (a) at -90°C and (b) -140°C , Steel A

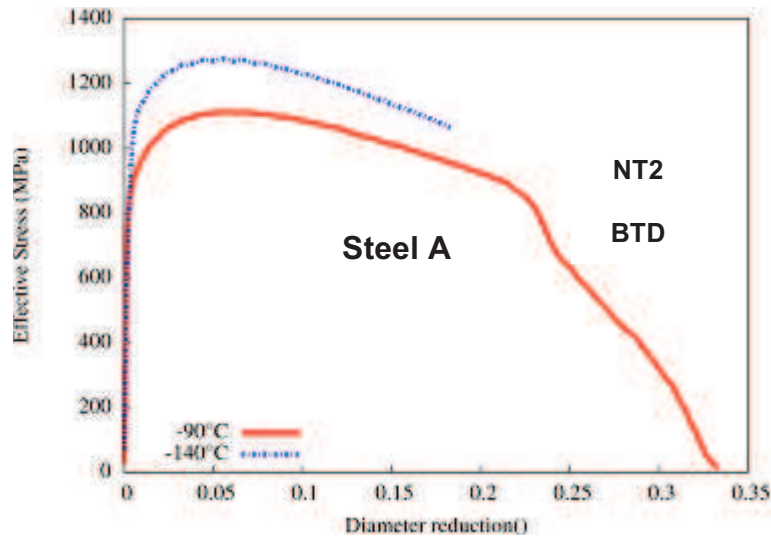


Figure III-21: Tensile curves of Steel A. Mixed ductile-delamination-cleavage fracture surface observed.

III.5.3. Full cleavage fracture mode

Investigation of full cleavage fracture mode was done at -196°C for both steels (Figure III-22). The initiation particle could not be found at the fracture surface. Tensile curves of steels A and B are presented in Figure III-23. These tensile curves are almost similar, except that Steel B was broken at lower diameter reduction compared to Steel A. Consequently, the critical cleavage stress of the θ -plane for Steel B might be lower than that for Steel A. This result is in good agreement with impact tests, where brittle tilted fracture (along the θ -plane) was more pronounced for Steel B.

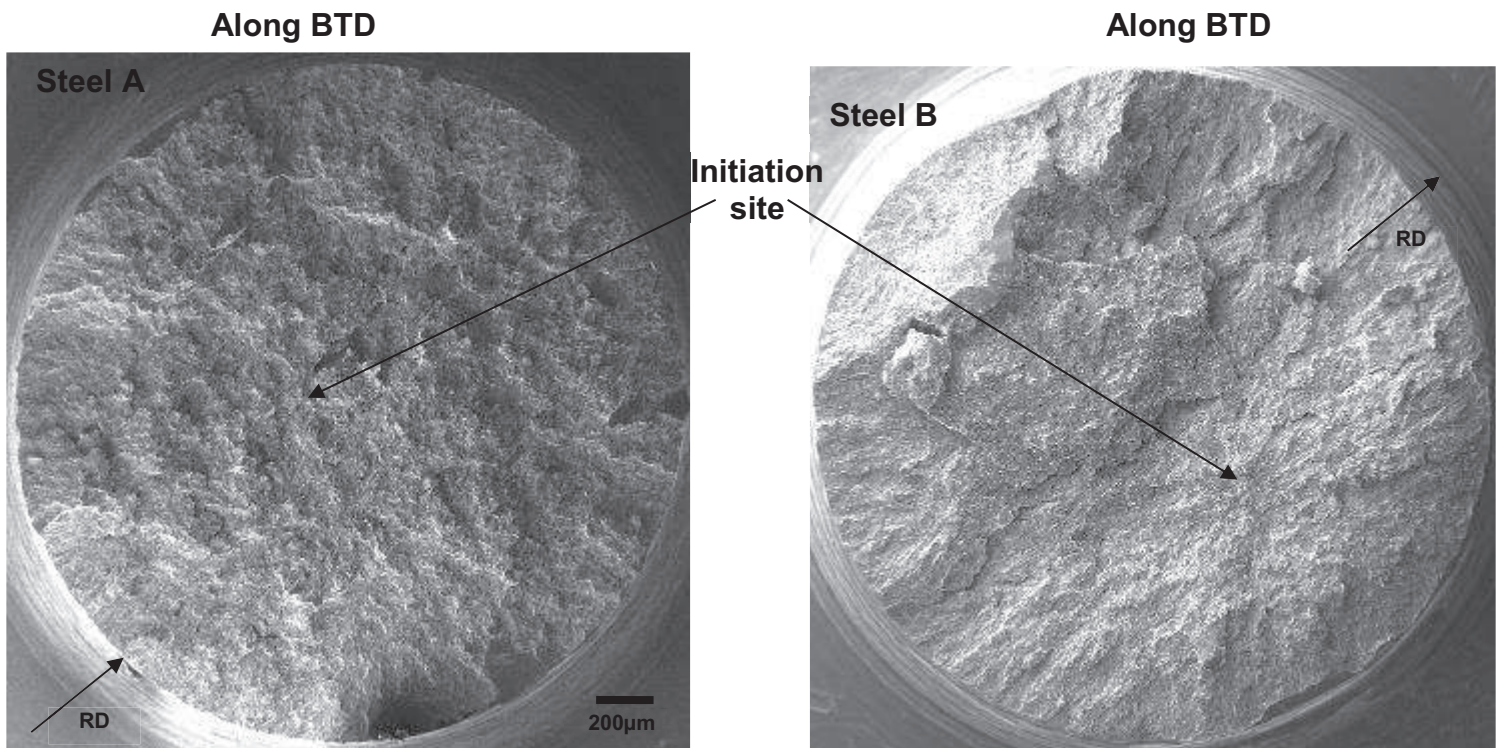


Figure III-22: Full cleavage fracture surface of steels A and B at -196°C

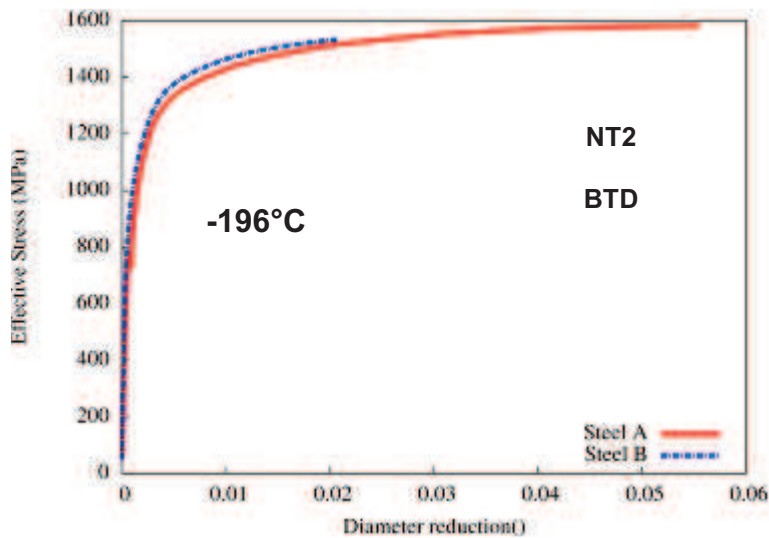


Figure III-23: Tensile curve of steels A and B in the full brittle (cleavage) temperature range.

III.6. Fracture resistance of the TD-ND plane (tensile tests along RD)

As presented in the experimental approach, tensile tests along RD were performed on NT1 specimens, except at -196°C where NT2 specimens were used. A longitudinal extensometer with a 10 mm gauge length was used for NT1 specimens and a radial extensometer which measured the diameter reduction along ND was used for NT2 specimens at -196°C . Three types of fracture modes could occur depending on temperature: Fully ductile, mixed ductile-delamination and full cleavage.

III.6.1. Fully ductile fracture mode

Full ductile fracture was observed for both steels at 20°C . The tensile curves obtained at 20°C are presented in Figure III-24. As it was observed during tests along ND and BTD, the change in the curve slope occurs after lower displacement for Steel B than for Steel A. This suggests that the stable ductile crack propagation starts earlier in Steel B.

III.6.2. Mixed ductile-delamination fracture mode

At lower temperatures, a fracture surface with central delamination crack surrounded by ductile slant on both sides was observed (Figure III-25). Dimples were still observed at the center of the specimen. The inside of the delamination crack was investigated with SEM in order to analyze its fracture mechanism and its initiation site (Figure III-26). Cleavage facets elongated along the loading direction (RD) were observed on the delamination fracture surface. The aspect ratio of cleavage facets could have been modified by the large plastic strain reached before delamination occurrence. Moreover, as presented in chapter VI, the microtexture could be modified by plastic strain. The fracture surface of the delamination crack also shows that cleavage fracture initiated from a ductile crack, as it was the case for tensile tests along ND with mixed ductile-cleavage fracture surface.

Because of the limited number of tested specimens, the critical temperature below which full ductile fracture surface is replaced by mixed ductile-delamination fracture could not be accurately determined. Nevertheless, this mixed ductile-delamination fracture mode was observed at -80°C , -100°C and -140°C for Steel A; and at -100°C and -120°C for Steel B. Tensile curves of steels A and B are presented in Figure III-27. These curves exhibit abrupt load drops before final failure. Interrupted

tests just after this abrupt load drop, which was associated to a loud noise, showed the presence of one delamination crack at the middle of the specimen. This delamination crack had already propagated all over the notched region.

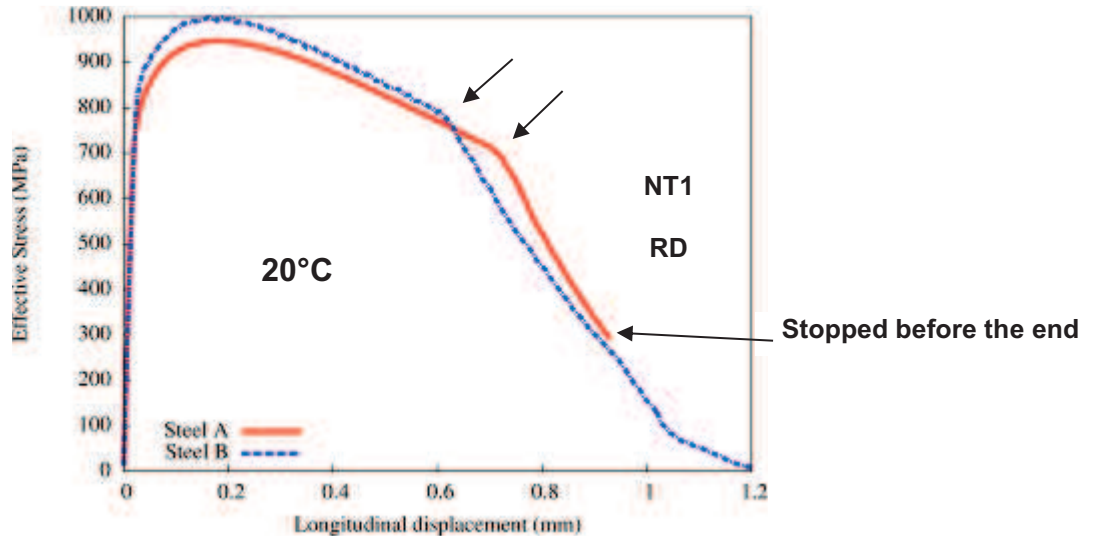


Figure III-24: Tensile curve of steels A and B. Full ductile fracture mode.

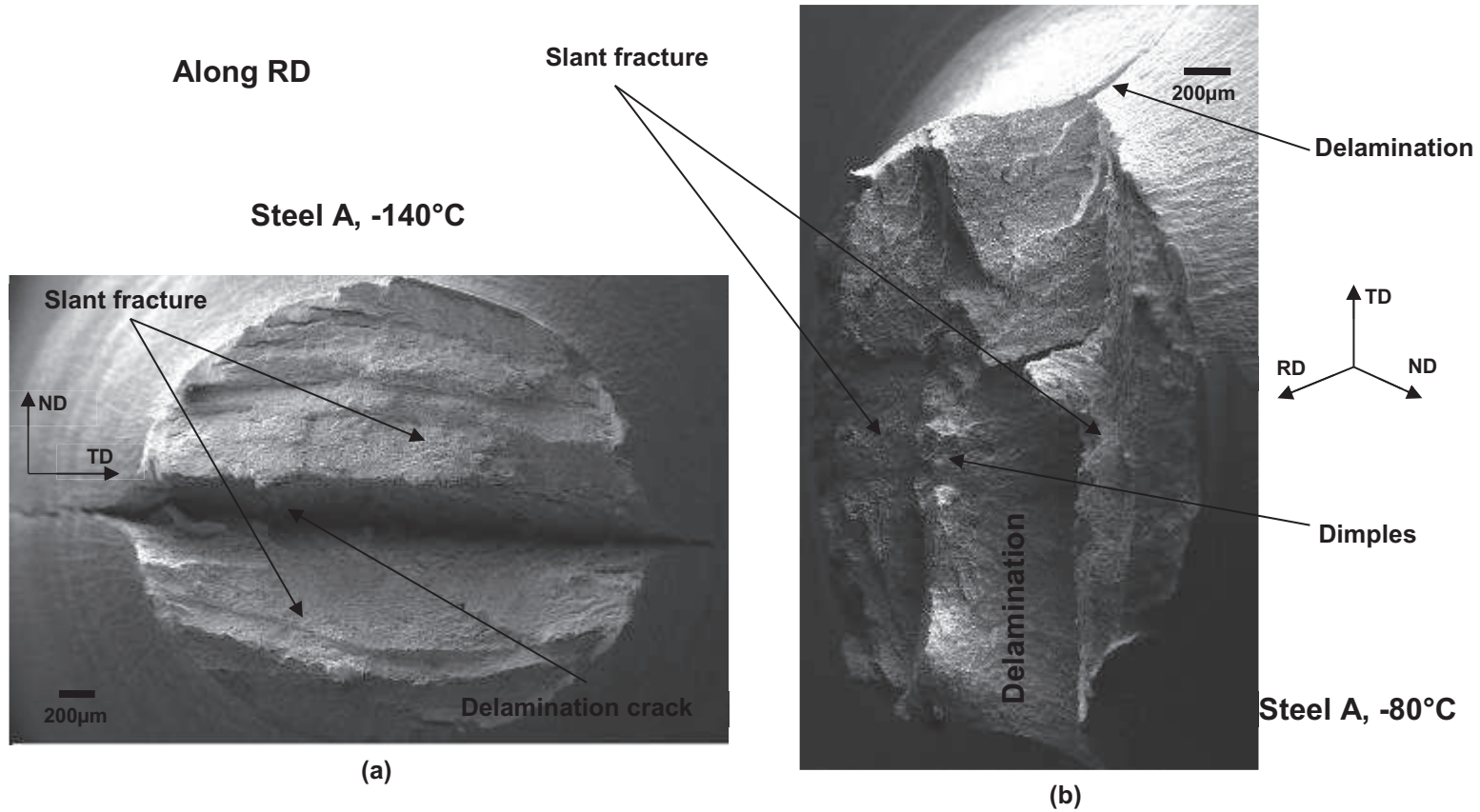


Figure III-25: One central delamination crack with ductile slants on both sides. Presence of dimples at the center of the specimen
 (a) Top view, Steel A, -140°C; (b) Slide view, Steel A, -80°C

Along RD

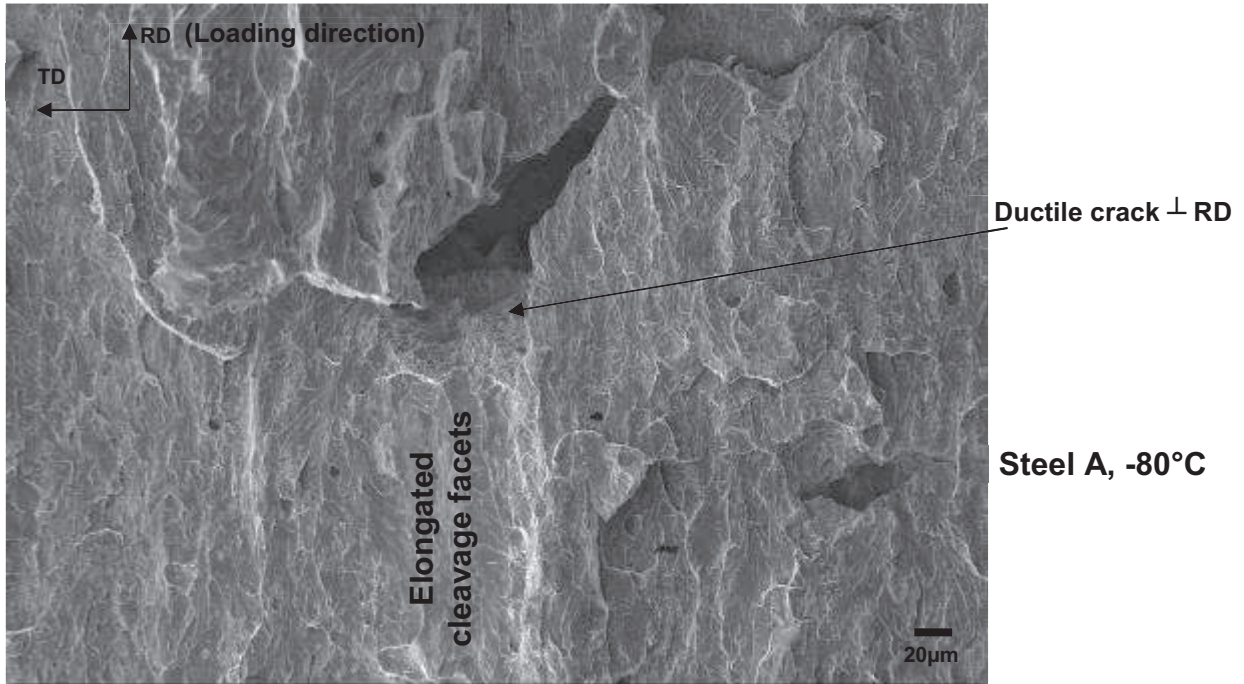


Figure III-26: Fracture surface of the delamination crack at the initiation site

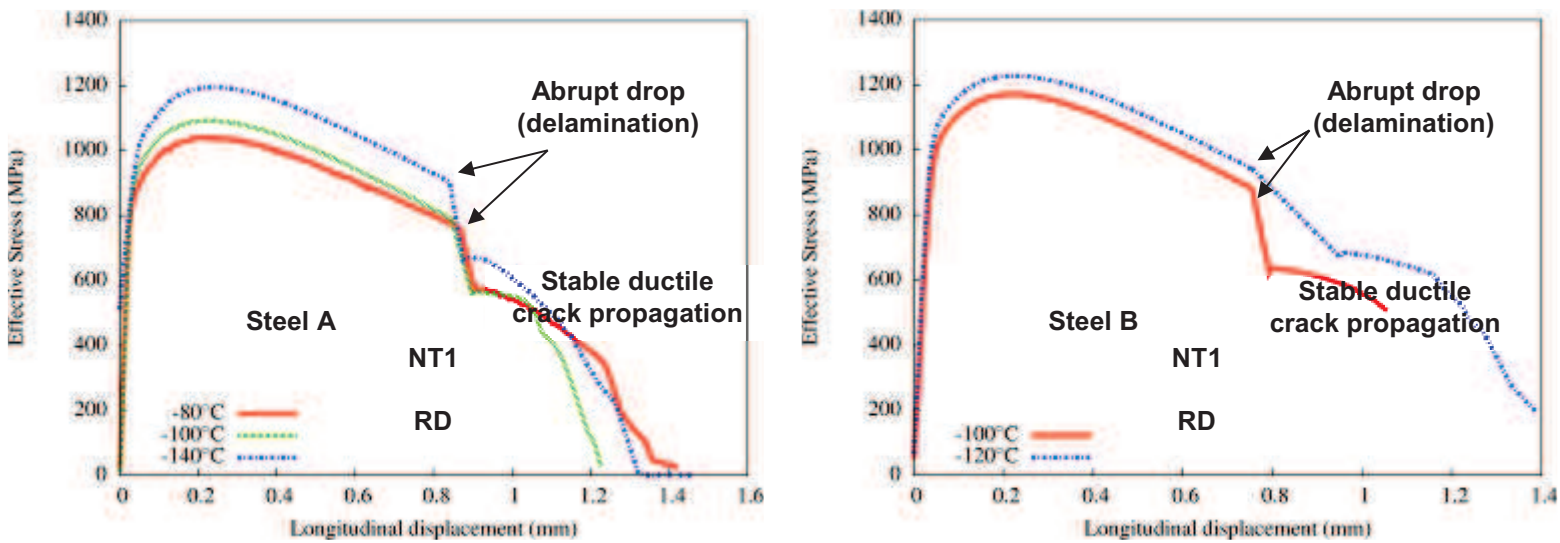


Figure III-27: Tensile curves along RD (NT1 specimens) of steels A and B in the mixed ductile-delamination domain.

III.6.3. Full cleavage fracture mode

Investigation of full cleavage fracture was done at -196°C for both steels (Figure III-28). No particle could be found at the fracture initiation site. Even if micro-delamination cracks were observed at the fracture surface of Steel A, cleavage fracture did not initiate from delamination crack as observed in Figure III-28.

Tensile curve of steels A and B are presented in Figure III-29. Steel B was broken for lower diameter reduction than Steel A, but since the tested specimens did not have exactly the same geometry, we could not conclude at this step about the cleavage sensitivity of both steels along RD.

Along RD

Along RD

Steel A, -196°C

Initiation site

Steel B, -196°C

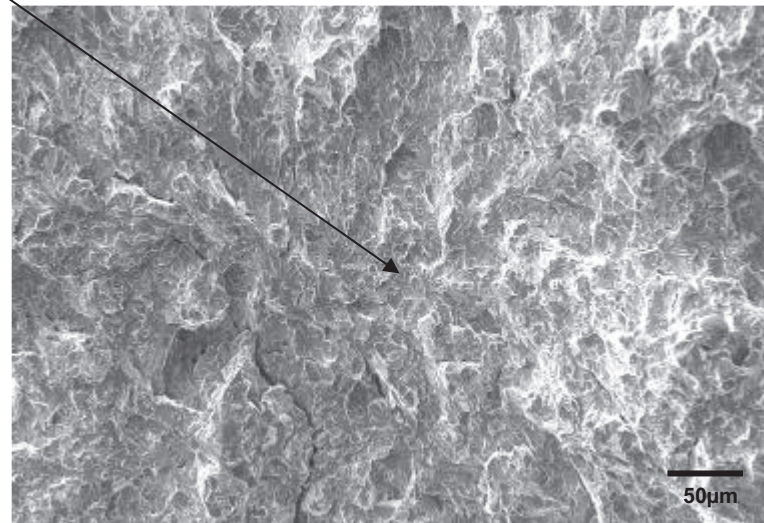
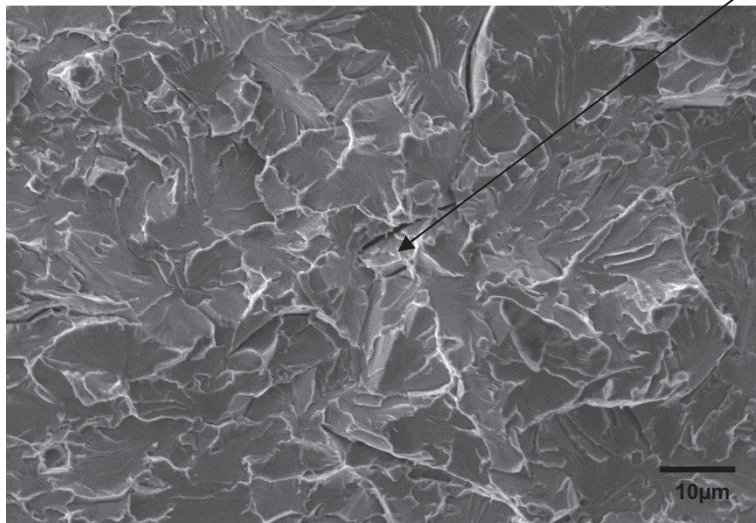


Figure III-28: Full cleavage fracture surface of steels A and B

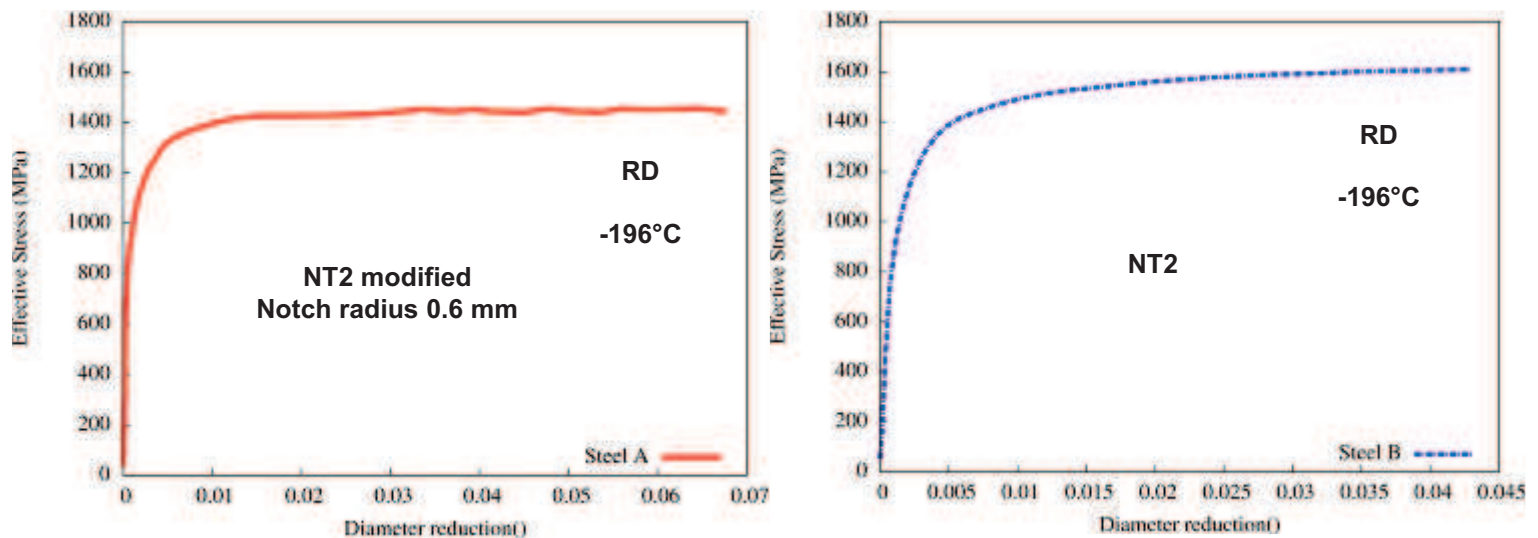


Figure III-29: Tensile curves along RD (NT2 specimens) of steels A and B. Full cleavage fracture.

III.7. Fracture resistance of the RD-ND plane (tensile tests along TD)

Four types of fracture modes occurred depending on temperature: Full ductile, mixed ductile-delamination, mixed delamination-brittle out-of-plane and full cleavage fractures.

III.7.1. Fully ductile fracture mode

Full ductile fracture surface on Steel A was observed for temperature down to -60°C. Steel B was more sensitive to delamination and full ductile fracture surface was observed for temperatures down to -40°C. Tensile curves are presented in Figure III-30. The tensile data of Steel B at 20°C have not been recorded, that explains why only the tensile curve at -40°C was plotted for Steel B. Moreover, the presence of one delamination micro-crack at -40°C did not lead to a noticeable abrupt drop of the load. Only a sharp decreasing of the load was observed.

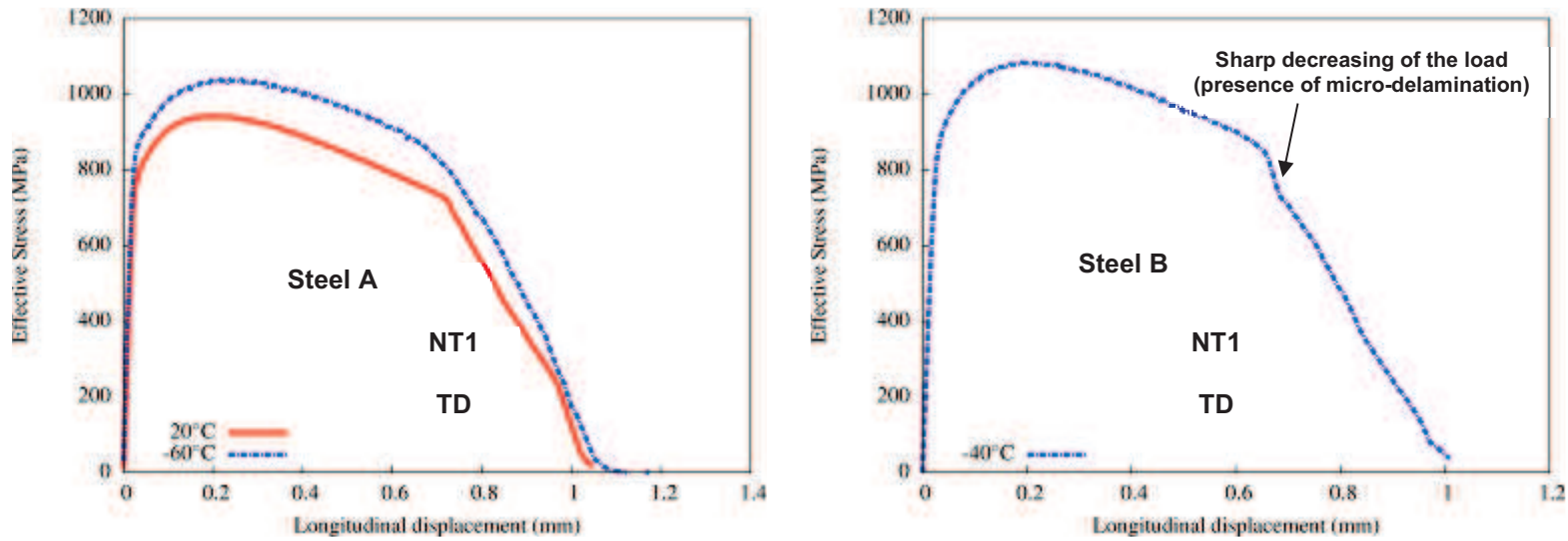


Figure III-30: Tensile curves along TD (NT1 specimens) of steels A and B. Full ductile fracture surface observed.

III.7.2. Mixed ductile-delamination fracture mode

As observed for tests along RD, at lower temperatures a central delamination crack appears and leads to ductile slant fracture. According to Figure III-31, the longitudinal displacement at the delamination occurrence in Steel B decreases when temperature increases. It was found earlier that the ductile crack nucleation was more difficult at lower temperature. Therefore the ductile crack might play an important role on delamination occurrence.

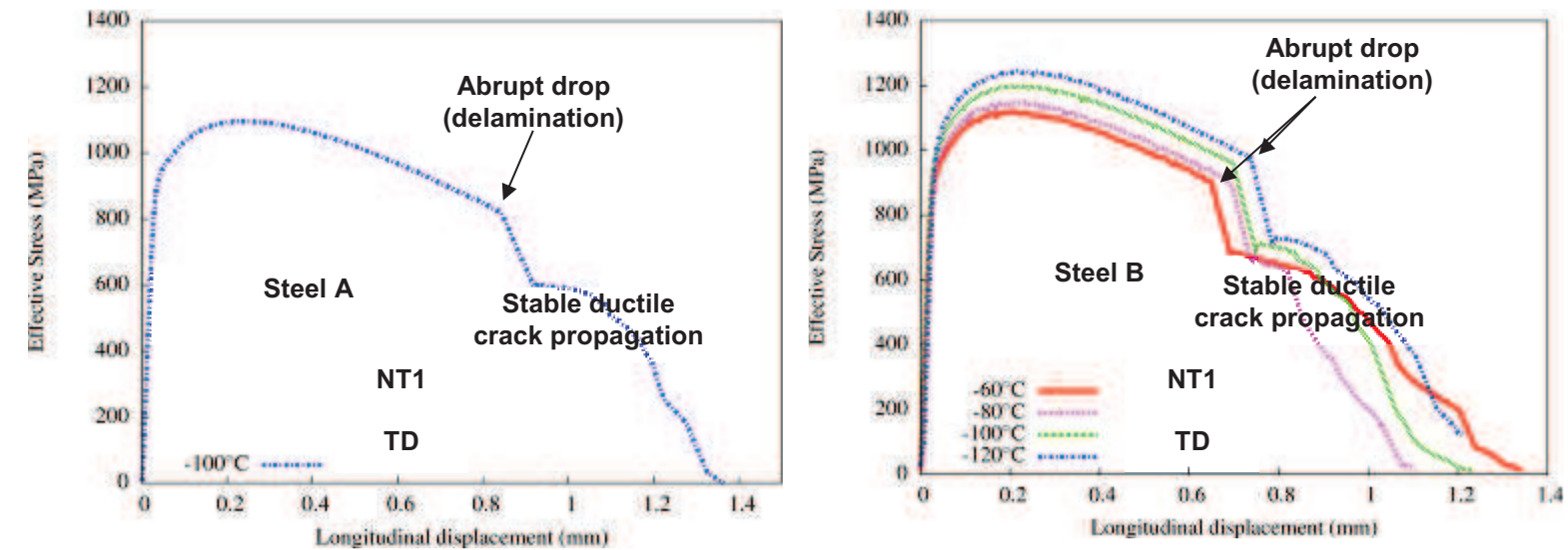


Figure III-31: Tensile curves along TD (NT1 specimens) of steels A and B. Mixed ductile-delamination fracture surface observed.

III.7.3. Mixed delamination-brittle out-of-plane fracture mode

For three specimens pulled along TD, the delamination was not followed by ductile slant, but by brittle out-of-plane cracking. These brittle out-of-plane cracks could be the brittle tilted fracture or delamination rotation (Figure III-32). For Steel A, brittle tilted fracture was observed at -100°C and -140°C. Steel B did not exhibit brittle tilted fracture, but only a rotation of the delamination crack which finally joined the (RD-ND) plane at -140°C.

Tensile curves are presented in Figure III-33. The more pronounced load drop is associated to delamination followed by BTF for Steel A, or delamination followed by rotation for Steel B. The fact that Steel A is more sensitive to BTF during that tensile test was not expected. Therefore, tensile tests do not be directly compare with impact toughness tests where Steel B was more sensitive to BTF.

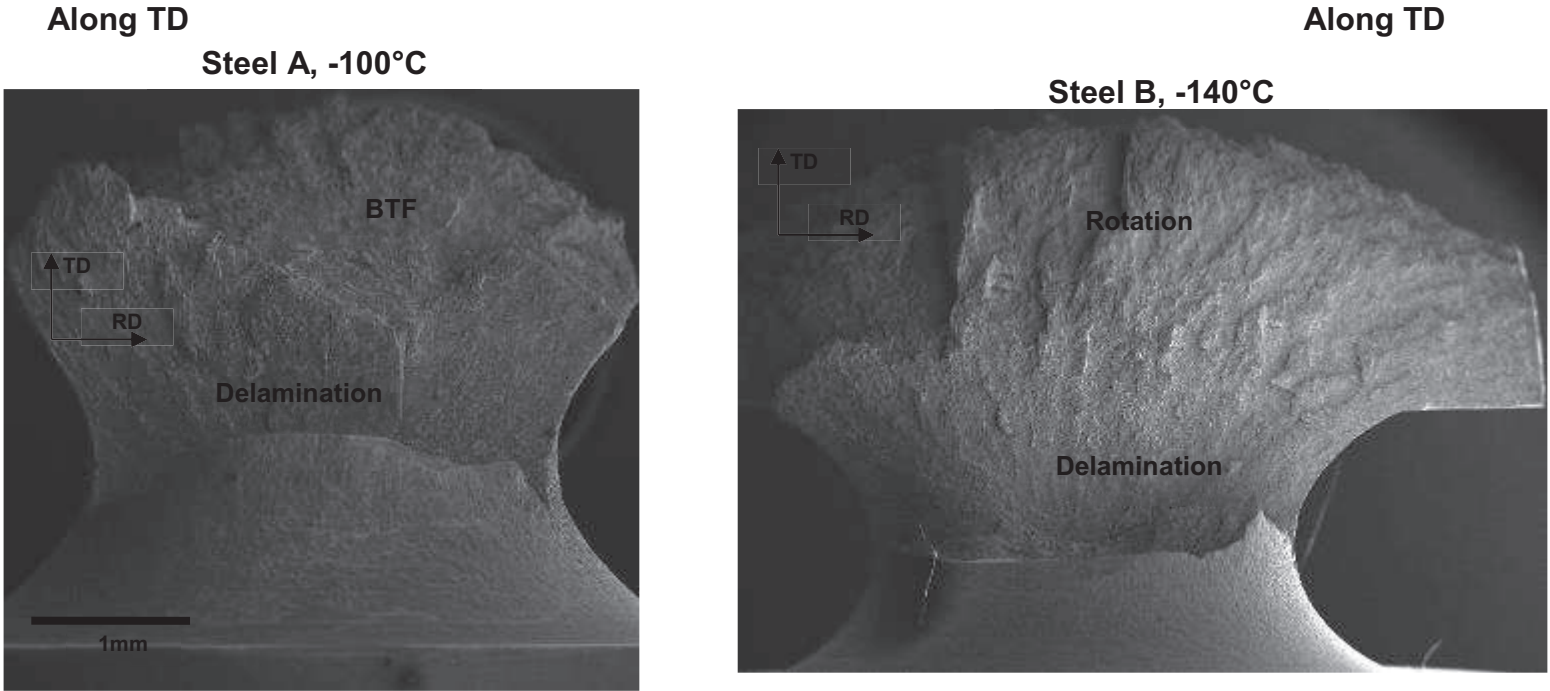


Figure III-32: One central delamination followed by brittle tilted fracture or rotation

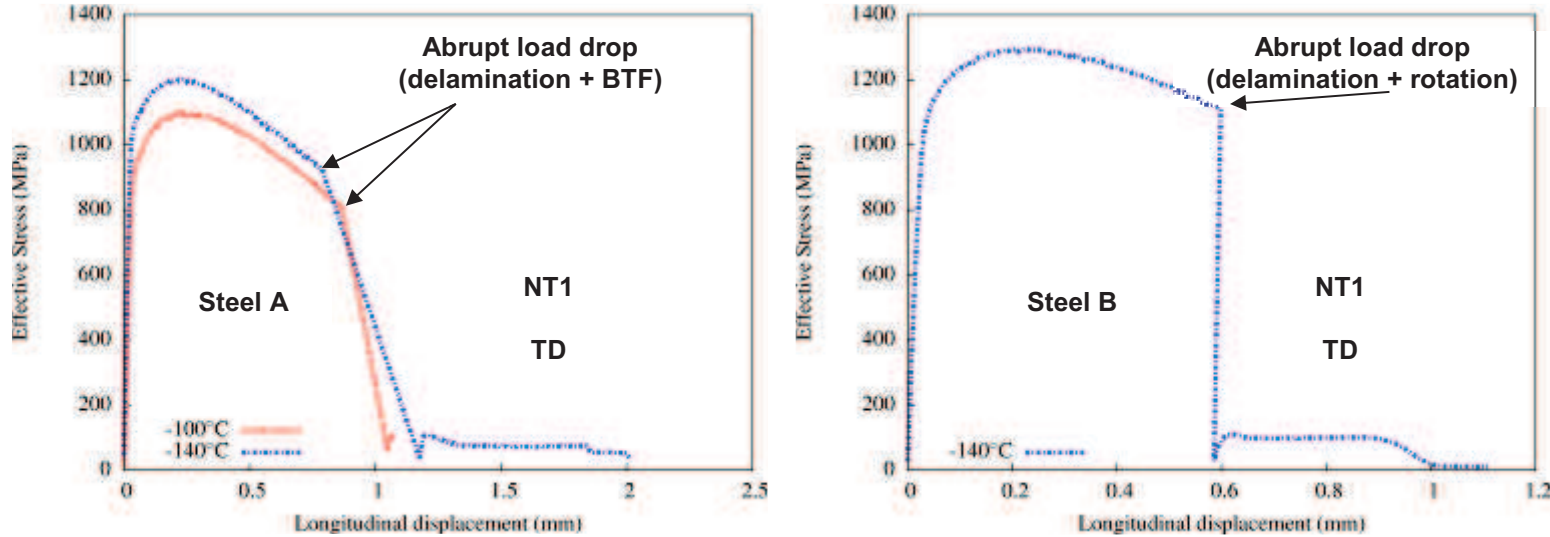


Figure III-33: Tensile curves along TD (NT1 specimens) of steels A and B. Mixed delamination-brittle out-of-plane cracking.

III.7.4. Full cleavage fracture mode

Investigation of full cleavage fracture was done at -196°C for both steels (Figure III-34). Cleavage fracture initiated from small delamination cracks for both steels. Tensile curves of steels A and B are presented in Figure III-35.

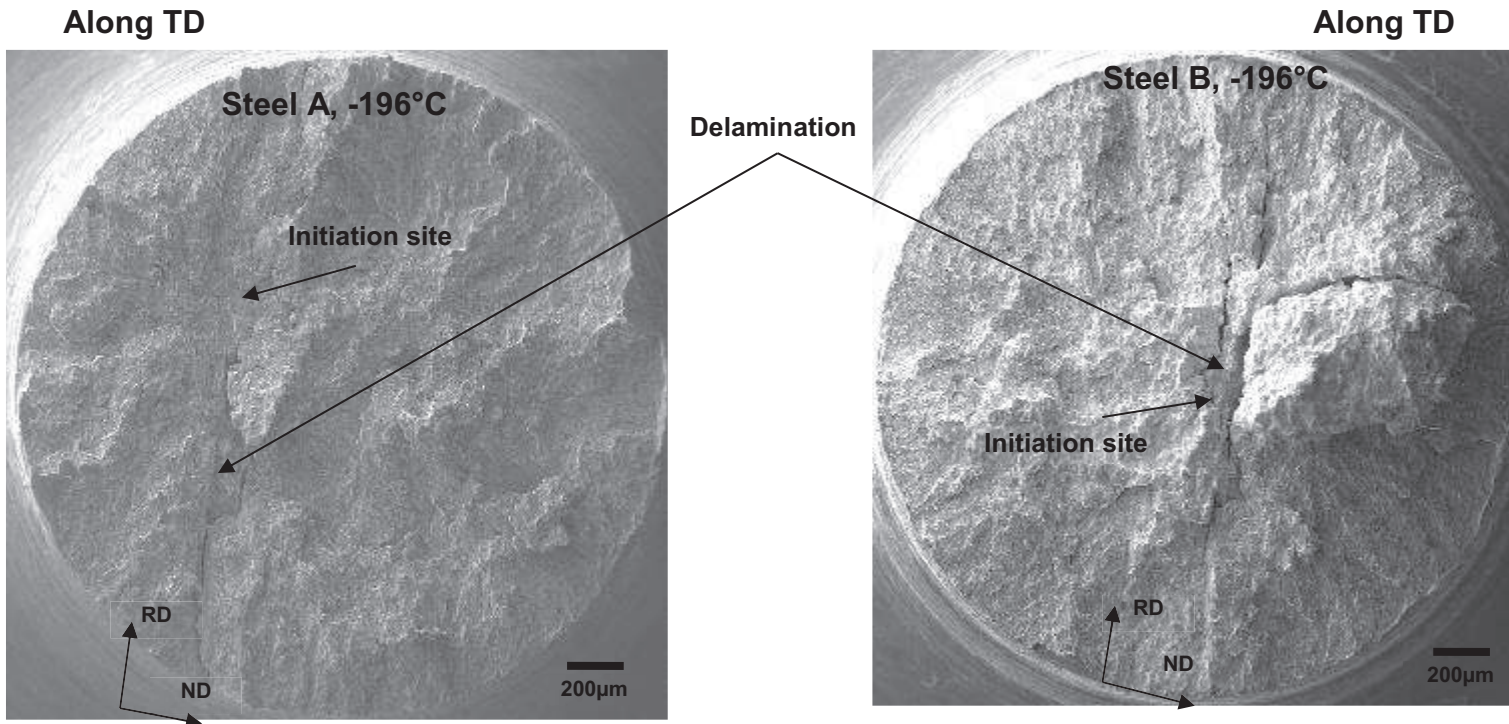


Figure III-34: Full cleavage fracture surface of steels A and B

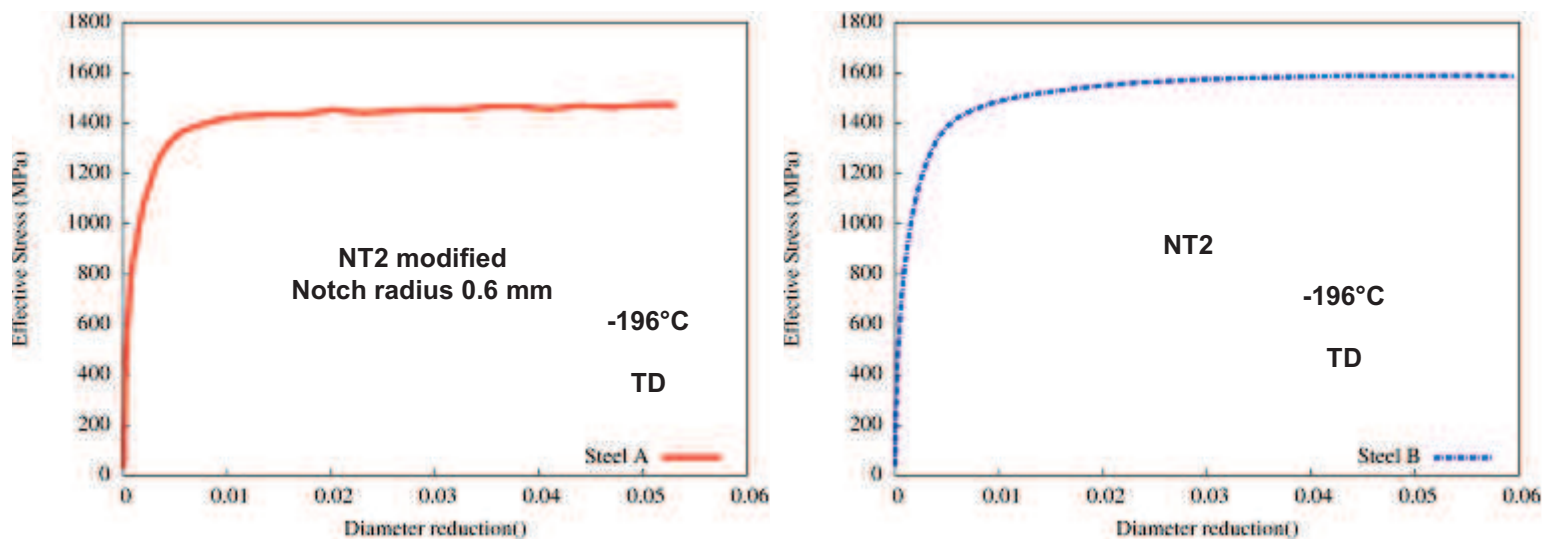


Figure III-35: Tensile curves along TD (NT2 specimens) of steels A and B. Full cleavage fracture.

III.8. Discussion and conclusions

The four directions **ND**, **BTD**, **RD** and **TD** were investigated in term of **plastic behavior** and **fracture resistance**, via tensile tests on smooth and notched specimens.

Concerning the **plastic behavior**, tensile tests were performed on smooth specimens taken along ND, BTD, RD and TD. Even if the **stress anisotropy** was not pronounced, noticeable **strain anisotropy** was observed with Lankford coefficients different from one. **Temperature** mainly affected the **yield strength** with negligible effect on plastic hardening. The yield strength evolution with temperature can be accurately represented with an exponential equation.

Concerning the **fracture resistance** of the four studied directions, tensile tests on notched specimens were carried out between +20°C and -196°C, so that the entire ductile to brittle transition domain could be investigated. It is clear that both steels tested along ND and BTd are more sensitive to **cleavage fracture** than along conventional RD and TD directions. The higher sensitivity to cleavage fracture of the steel when tested along ND compared to other directions was already observed on high strength low allowed steels studied in [26].

Tensile tests **along ND** showed that cleavage was initiated from **ductile crack** within the center of specimens. The size of this ductile crack decreased with temperature, and ductile cracking totally disappeared at very low temperatures, leading to **full cleavage fracture** observed at -100°C and -196°C for steels A and B respectively.

Tests **along BTd** were less sensitive to cleavage than **along ND** for **Steel A**. The fracture surface of specimens tested at -110°C and -140°C showed cleavage fracture initiated from **dimples** and **delamination micro-cracks**. Full cleavage fracture was only observed at -196°C. Concerning Steel B, tests **along BTd** seemed to be more sensitive to cleavage than **along ND**. The only tensile tests performed at -196°C showed full cleavage fracture. Even if tests were not performed at as many temperatures as for Steel A, delamination micro-cracks are not expected within Steel B for specimens pulled along BTd. In fact as presented in [26], a condition for delamination occurrence is that ND direction should be more sensitive to cleavage than the loading direction which for this case is BTd. This condition was not fulfilled for Steel B.

A pronounced central **delamination crack** was observed on specimens tested **along RD and TD** for temperatures between -40°C and -140°C. Directions RD and TD were so sensitive to delamination that delamination micro-cracks were still observed even for tests at -196°C. Delamination fracture surfaces showed elongated cleavage facets, which initiated from a ductile crack within the center of the specimen. The cleavage fracture initiated from ductile crack is in good agreement with the fracture surface of specimens taken along ND within the ductile to brittle transition. Nevertheless, cleavage facets observed on delamination fracture surfaces are much more elongated than the one observed after tensile test along ND.

The delamination crack was followed by ductile slant, except for tensile tests along TD for Steel A at -100°C and -140°C, where BTF was observed. Since Steel B was more sensitive to BTF than Steel A according to impact tests, the fact that BTF easily occurred within Steel A during tensile tests shows that tensile tests may not be representative to impact tests in term of brittle out-of-plane cracking occurrence. A summary of temperatures where delamination cracking was observed is presented in Figure III-36

From this chapter, it is clear that both steels tested along ND and BTd are more sensitive to cleavage fracture than along conventional RD and TD directions. An experimental database was built so that the difference in cleavage sensitivity could be quantitatively investigated after detailed mechanical analysis of the tests. This might partially explain the occurrence of brittle out-of-plane cracking during DWTT and Charpy tests. The cleavage fracture sensitivity needs to be further studied by associating a value on this sensitivity, so that the cleavage fracture anisotropy could be properly investigated.

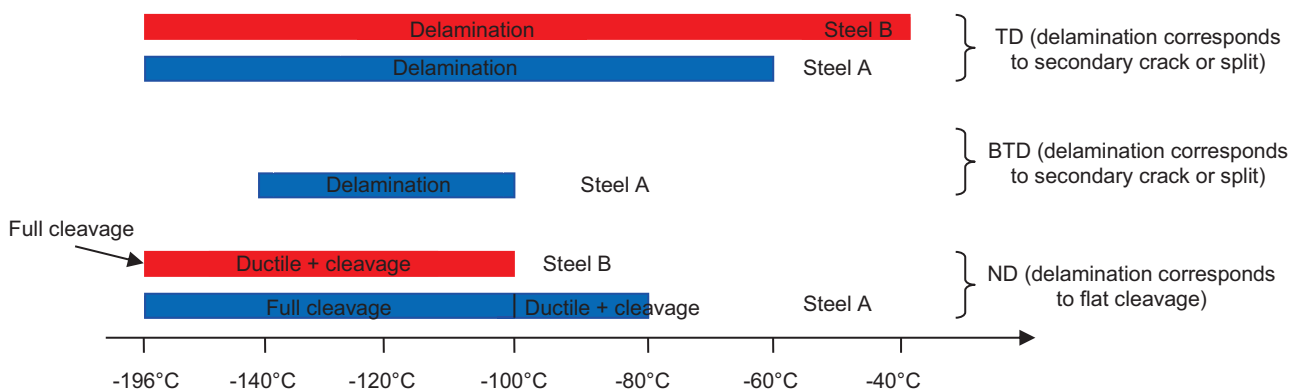


Figure III-36: Summary of temperatures where delamination was observed for ND, BTd and TD directions. For ND delamination is a fat cleavage crack which propagates along the main loading plane.

Chapter IV – *Quantitative study of cleavage stress anisotropy*

Table of Contents

IV.1.	Literature survey	73
IV.1.1.	Microstructural parameters controlling cleavage fracture in bcc steels	74
IV.1.2.	Local approach to fracture	76
IV.1.3.	Literature survey of physically-based cleavage fracture models.....	77
IV.2.	Anisotropy in potential cleavage facet distribution	83
IV.2.1.	The concept of potential cleavage facets	83
IV.2.2.	Analysis of potential cleavage facets for different planes of the plate.....	87
IV.3.	Anisotropy in critical cleavage stress, correlation with PCFs	91
IV.3.1.	Procedure	91
IV.3.2.	Critical cleavage stress along ND, BT, RD and TD	92
IV.3.3.	Correlation between PCF size and critical cleavage stress	93
IV.4.	Conclusions	94

Tensile tests performed along ND, BT, RD and TD showed anisotropy in fracture mode. The sensitivity of both steels to cleavage fracture was found to depend on the tested direction. The rolling plane and the θ -plane were more sensitive to cleavage fracture than the (TD-ND) and (RD-TD) planes. The present chapter aims at quantifying this anisotropy and at understanding its origin via a microstructure analysis and a mechanical investigation of critical cleavage stresses along the planes of interest.

The first part focuses on a literature survey on cleavage fracture, where the microstructural parameters controlling cleavage fracture are investigated. The local approach to cleavage fracture and the associated models is also presented.

In the second part, the microstructures along the planes of interest are analyzed and compared. EBSD analyses were performed in order to obtain quantitative parameters of the microtexture which controls cleavage fracture. So-called “potential cleavage facets”, which were assumed to act as barriers for cleavage fracture, have been defined and determined for all planes of interest. The size distribution of these potential cleavage facets has been analyzed for correlation with cleavage sensitivity.

In the third part, critical cleavage stresses of the two steels along ND, BT, RD and TD were determined from tensile tests at -196°C. To this aim, an elastoplastic constitutive model was used to estimate the local stress states at fracture in the specimens. The values of critical cleavage stresses well correlate to potential cleavage facet sizes.

Résumé

Ce chapitre vise à quantifier l'anisotropie de la résistance au clivage et à en comprendre l'origine. Une approche microstructurale reposant sur une analyse des microtextures et une approche mécanique avec une analyse des contraintes critiques de clivage pour les quatre directions (ND, BTD, RD et TD) ont été utilisées.

Dans une première partie, une étude bibliographique sur la rupture par clivage et les paramètres microstructuraux qui la contrôlent a été menée. L'approche locale de la rupture a notamment été présentée dans cette partie.

Dans l'approche microstructurale, la microtexture des plans θ , de laminage, (TD-ND) et (RD-ND) des deux aciers ont été analysées par EBSD. On définit des « facettes de clivage potentielles » (PCF) qui corrélient bien avec les larges entités allongées observées au microscope optique. Elles se trouvent être des barrières microstructurales pour la propagation du clivage. Une anisotropie sur la distribution des PCF a été observée et les plans perpendiculaires à ND et BTD qui sont les plus sensibles au clivage, contiennent les plus grandes PCF. Ainsi, l'anisotropie initiale de la microtexture est corrélée avec l'anisotropie de la résistance au clivage.

Dans l'approche mécanique, les essais de traction suivant les directions ND, BTD, RD et TD ont été simulés numériquement par la méthode des éléments finis. Une loi de comportement élastoplastique avec une surface de charge de type Barlat a été utilisée pour déterminer les contraintes critiques de clivage à basse température. Les plus basses contraintes critiques de clivage correspondent aux éprouvettes prélevées suivant les directions ND et BTD.

Une approche du type Griffith a été utilisée pour coupler les résultats de l'analyse microstructurale et ceux de l'analyse mécanique. Une corrélation entre l'inverse de la racine carrée de la taille des PCF et les contraintes critiques de clivage a été établie. Néanmoins une dispersion qui serait liée à la méthode de calcul de la taille moyenne de PCF et aux incertitudes sur les contraintes critiques de clivage demeure.

Les contraintes critiques de clivage déterminées pour un chargement en mode I des plans θ et de laminage seront utilisées pour étudier l'apparition des modes de rupture fragiles hors-plan.

IV.1. Literature survey

Analysis of the fracture modes observed during impact and quasi-static tests showed brittle out-of-plane cracking which propagated by cleavage. Analyses of tensile tests along ND, BTD suggested a higher sensitivity to cleavage of the rolling plane and of the θ -plane, compared to those of (TD-ND) and (RD-ND) planes. To understand this anisotropy in sensitivity, the cleavage fracture mechanisms have to be properly studied.

As shown in Table IV-1, cleavage fracture occurs along some privileged lattice planes ($\{100\}$ families for ferritic steels). Thus, only $\{100\}$ planes will be considered as potential cleavage fracture planes in the following of this chapter.

Structure	Cleavage plane	Some materials
BCC	$\{100\}$	Ferritic steels, Mo; Nb, W
FCC	$\{111\}$	Very rarely observed
HCP	$\{0002\}$	Be, Mg, Zn
Diamond	$\{111\}$	Diamond, Si, Ge
NaCl	$\{100\}$	NaCl, LiF, MgO, AgCl
ZnS	$\{110\}$	ZnS, BeO
CaF ₂	$\{111\}$	CaF ₂ , UO ₂ , ThO ₂

Table IV-1: Cleavage planes in some materials [27]

Theoretically, in a perfect crystal, cleavage fracture results in the separation of crystallographic planes, after fracture of interatomic bonds. The normal stress needed to initiate cleavage could therefore be obtained using the following relationship:

$$\sigma_c^{th} = \sqrt{\frac{E\gamma}{b}} \quad \left\{ \begin{array}{l} E \text{ Young's modulus (Pa)} \\ \gamma \text{ Energy for the formation of two new free surfaces (J/m}^2\text{)} \\ b \text{ Interatomic equilibrium distance (m)} \end{array} \right. \quad (\text{Equation IV-1})$$

In practice, this theoretical value is much higher (typically, by a factor of 50) than the experimental values found for classical materials. Two explanations introducing stress concentrators (defects and dislocations) are proposed by Pineau [27] to interpret this discrepancy:

- Cleavage fracture is related to the existence of defects acting as stress concentrators and which are not taken into account in the equation above.
- Plastic deformation is a prerequisite to initiate cleavage fracture. But the effect of dislocations was not taken into account in the equation above.

Consequently, to perform a realistic cleavage fracture stress analysis, it seems necessary to investigate both the defects susceptible to initiate cleavage and the effect of local plastic deformation. The dependence of a so-called *critical cleavage (fracture) stress* on temperature is not clear in literature. Even if many authors such as Bowen [28] considered critical cleavage stress to be independent of temperature, a tendency on decreasing critical cleavage stress when the temperature decreases has been reported for some manganese steels.

This literature survey on cleavage fracture of bcc steels is organized in three parts: In the first part, microstructural parameters controlling cleavage fracture are detailed. In the second part, the so-called *local approach to fracture* (focused on the cleavage cracking mechanisms) is presented. The last part is dedicated to the description of some cleavage fracture models using the framework of the local approach.

IV.1.1. Microstructural parameters controlling cleavage fracture in bcc steels

Cleavage fracture, like other fracture modes, could be decomposed into an initiation stage and a propagation stage. The cleavage fracture surface generally exhibits rivers, and analysis of these rivers supplies information about the crack propagation path and about crack initiation sites. Depending on the material and experimental conditions, the initiation stage or the propagation stage could be the critical one. When the initiation stage is critical, cleavage cracking could be considered as nucleation controlled; when the propagation stage is critical, cleavage cracking could be considered as growth controlled.

At lower temperatures, i.e., within the lower shelf domain, the yield strength is highest and cleavage fracture is limited by the onset of plasticity and the fracture of at least one particle. As soon as a micro-crack is initiated, the critical stress for unstable cleavage propagation is reached and the specimen is broken. Chen et al. [30] reported this nucleation-controlled cleavage mechanism for a carbon-manganese steel tested between -150 and -130°C.

For higher temperatures, i.e., within the ductile-to-brittle transition, the onset of plasticity is readily reached and fracture or decohesion of particles is easier. In that case, micro-cracks are early initiated and because the critical stress for unstable cleavage propagation is not yet reached, they will not lead to fracture. Cleavage fracture of ferritic steels tested within the ductile to brittle transition is assumed to be growth controlled (Pineau, [29]).

Therefore, cleavage fracture could be modeled in two ways, depending on whether focus is on nucleation-controlled or on growth-controlled cleavage fracture. For nucleation-controlled cleavage, the critical stress for cleavage is linked to the probability to encounter an initiation site (distribution of defects) within the plastic zone of the tested specimen. For growth-controlled cleavage, the micro-crack should pass the first high-angle grain boundary; therefore, the critical stress should cover a characteristic distance chosen as two grain sizes in the above mentioned RKR model.

Microstructural parameters controlling cleavage fracture are thus sorted in two categories: Those which control initiation and those which control propagation of a cleavage crack.

a) Parameters controlling cleavage crack initiation

Ductile micro-crack:

Tanguy [1] who worked on a 16MND5 reactor pressure vessel steel (0.16C-1.25Mn-0.76Ni-0.51Mo), with a tempered bainite microstructure, observed that cleavage fracture in Charpy specimens initiated from near ductile micro-cracks within the ductile-to brittle-transition (-60°C and -80°C).

Non-metallic inclusions:

The work of McRobie et al. [31] revealed the presence of cracked non-metallic inclusions near the cleavage initiation site in a C-Mn weld metal. Qualitative analysis of these inclusions revealed the presence of elements such as: Mn, Ti, Si, S. MnS inclusions were also considered to be the microstructural parameter responsible for cleavage initiation in precracked compact tension (CT) specimens taken from a pressure vessel steel (Rosenfield, [32]). Tests were made at 22 and 82°C, and CT specimens were loaded at a high rate (760 or 550 mm/s).

Carbide particles:

The work of Bowen [28], performed on a pressure vessel steel, showed that carbides may be preferential sites for the nucleation of cleavage cracks and also that the effects of carbides depend on their size and shape. In fact, the authors considered two martensitic steel microstructures with similar prior austenite grain size and different sizes of coarser carbides. They compared their evolutions in terms of fracture toughness with temperatures between -180°C and +20°C. They concluded that microstructures with coarser carbide sizes were more sensitive to cleavage fracture. In the same manner, the authors tested the effect of carbide shape by considering steels with plate carbides and spheroidal carbides respectively. They showed that for a given carbide thickness, plate carbides are more detrimental to cleavage fracture than spheroidal carbides.

To summarize, coarse plate carbides are the most dangerous ones for cleavage resistance and improvement of steel toughness could be obtained by refining carbide size. But, they might be some saturation on the beneficial effect of carbide refinement, because when the carbides become very fine, cleavage fracture will initiate from another defects.

M-A constituents:

M-A (Martensite Austenite) constituents result from an incomplete transformation of the austenite into bainite during cooling. Lambert-Perlade et al. [33] investigated initiation sites of cleavage fracture in a ferrite-pearlite steel and simulated weld heat-affected zones with upper bainite microstructures. They found that cleavage fracture initiated near M-A constituents. These M-A constituents were broken in a brittle manner for higher values of stress triaxiality, while only interfacial decohesion of the M-A constituent was observed for lower values of stress triaxiality.

Sun et al. [26] studied the microstructure of a Nb-Ti micro-alloyed pipeline steel, finished rolling at 1000°C, 750°C and 690°C. They concluded that the M-A density increases when the finish rolling temperature decreases. Therefore the process ended with lower finish rolling temperatures could generate higher density of M-A particles where cleavage fracture could initiate from.

Concerning the steels under study, as observed in the previous chapter, cleavage fracture was mainly initiated from ductile cracks or from brittle out-of-plane cracks. Only tensile tests on notched specimens at -196°C showed, at least for the ND direction, full cleavage fracture surfaces without ductile cracking or brittle out-of-plane cracking. In that case, river patterns converged to a unique site, which might be associated to one particle. This particle was always missing, leaving just a hole on both halves of the fracture surface. Therefore, the nature of particle responsible for cleavage fracture at -196°C was unknown. Nevertheless, as will be shown in this chapter, cleavage fracture well correlates to parameters controlling cleavage crack propagation. Ductile cracks, brittle out-of-plane cracks or particles play the role of stress concentrators.

b) Microstructural parameters controlling cleavage crack propagation

Average crystallographic texture:

Crystallographic texture could control the propagation of cleavage cracks, since a high density of {100} planes perpendicularly oriented to the maximal principal stress could facilitate cleavage fracture. Kotrechko et al. [34] which performed polycrystalline calculations showed that texture smearing decreases the cleavage stress anisotropy. The so-called cleavage-stress anisotropy coefficient was defined as the ratio between cleavage stresses calculated along two perpendicular directions. The cleavage-stress anisotropy coefficient calculated on polycrystals with initial smearing texture was lower than for polycrystals with very sharp texture and pronounced fibers.

Bainite packet size:

In bainitic steels, bainite packets define a crystallographic unit cell delimited by high-angle boundaries. There is a size relationship between the prior austenite grain and the bainite packet that grows within that parent austenite grain. Brozzo et al. [35] who worked in a 2Mn-3Cr bainitic steel found that the average size, d_B , of bainitic packets was linked to the average size, d_A , of the parent austenite grain via the relation:

$$d_B = 1.4d_A^{0.55} \quad (\text{Equation IV-2})$$

(Brozzo, [35]) and (Di Shino, [36]), considered that the size of the bainite packet is an important parameter controlling the cleavage stress in bainitic steels. According to these authors, critical cleavage fracture stress could be estimated, by applying a Griffith criterion to a microcrack with the size of a bainite packet. The following relationship is obtained:

$$\sigma_{cf} = \sqrt{\frac{4E\gamma_p}{(1-\nu^2)}} \cdot d_B^{-1/2}$$

E Young's modulus

γ_p Energy for the formation of two fresh free surfaces

ν Poisson's ratio

(Equation IV-3)

In bainitic steels, the sensitivity of cleavage resistance to bainite packet size could perhaps be explained by the fact that high-angle boundaries between bainite packets are microstructural barriers for cleavage crack propagation (Pineau, [29]). The unit crack path (UCP) is the size of a region within which the crack propagates in a nearly straightforward manner. If we assume that within a bainite packet, the crystallographic misorientation between laths is low, then there may exist a relationship between the UCP and the bainite packet size. (Brozzo, [35]), after plotting the average UCP values versus the bainitic packet sizes, obtained the following linear relationship:

$$UCP = 1.3d_B \quad (\text{Equation IV-4})$$

The double barrier model proposed in [44] was originally applied to ferritic steels. The first barrier is the carbide-matrix interface and the second barrier is the ferrite grain boundary. This second barrier was adapted for bainitic steels in [33], using data from EBSD analyses. For the steels in the present study which are mainly ferritic, a new microstructural barrier should be defined, so that it could be set as the second barrier. Microtexture analyses have been used to define these microstructural barriers, namely, so-called "potential cleavage facets" (PCFs). PCF definition is based on two requirements that stem from the observation of fracture surfaces: a PCF must contain {100} planes well oriented with respect to the maximal principal stress, so that cleavage could easily propagate inside; a PCF must contain only low angle boundaries that do not hinder cleavage crack propagation. The two threshold angles used for definition of these PCFs are presented later on in this chapter.

IV.1.2. Local approach to fracture

Two types of approaches have been developed for the study of fracture mechanisms. The first one, the so-called "global approach to fracture" was most popular during the past decades. In this approach, it is assumed that the fracture resistance can be measured in terms of a single mechanical parameter, such as K_{IC} , J_{IC} , or a critical value of the crack-tip opening displacement (CTOD). Even if this approach is useful and largely used for mechanical applications and standards, there are some limitations. One of those limits can be observed for steels tested in the brittle or the ductile-to-brittle transition domains. In that case, global approaches are specimen-dependent and it becomes difficult to evaluate the effect of microstructure on the fracture resistance, for further improvement of the steel. Thus, another approach, the so-called "local approach to fracture" taking physical fracture mechanisms into account, has been developed. This local approach is based on local fracture criteria and needs to get good knowledge of the material microstructure (defect size and spatial distribution for instance) and good knowledge of the stress-strain field at the location of the fracture initiation site. A sketch showing a simplified methodology of the local approach is presented in Figure IV-1.

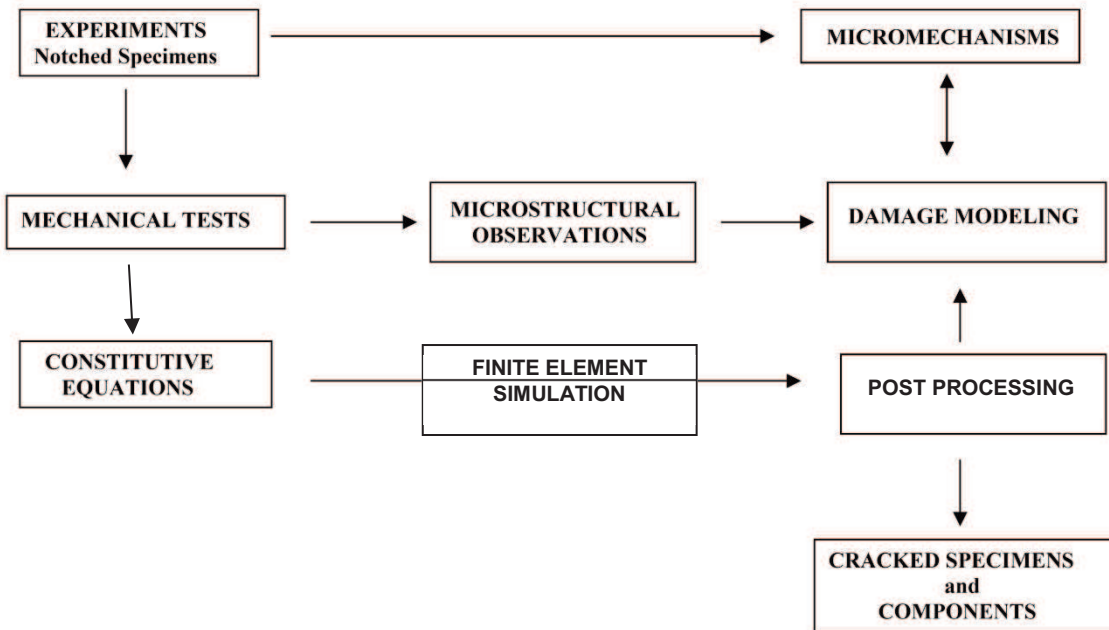


Figure IV-1: Sketch showing a simplified methodology of local approach for cleavage fracture, from [29]

It can be observed from Figure IV-1 that performing mechanical tests on notched specimens is the first step for the local approach study. In fact, information about fracture micromechanisms can be extracted from these experimental tests via microstructural observations, and then a cleavage fracture criterion could be established thanks to analysis of the experiments with finite element simulations. This cleavage fracture criterion which is linked to the microstructure becomes an intrinsic characteristic of the material. Thus, the crack event in cracked specimens or more complex components could be predicted using the stress-strain field obtained with finite element simulations and the cleavage fracture criterion.

Since the fracture criterion plays a central role in the local approach to fracture, it is necessary to choose among models that are available from literature, the most appropriate one to the studied problem. Some of these existing models will be discussed in the following sections.

IV.1.3. Literature survey of physically-based cleavage fracture models

For a detailed review of cleavage fracture models, the reader could refer to (Pineau, [29], Pineau, [27]). A complete cleavage fracture model must describe the following two stages: Nucleation of the crack and propagation of the crack across microstructural barriers. Some models only consider one of these stages since they suppose that it corresponds to the critical one. In the ductile-to-brittle transition domain, arrested cleavage micro-cracks are generally observed in the fracture surface of broken specimens (Chen, [43]). This supports the fact that crack nucleation is not the critical event and hence, models that are only based on the nucleation stage will not be presented in that part. Readers interested in such models can refer to (Zener, [37]), (Stroh, [38]), (Cottrell, [39]), (Smith, [40]) and (Curry, [41]).

Cleavage fracture models can be deterministic or probabilistic. Both of them are reported below.

a) Deterministic RKR (Ritchie-Knott-Rice) model

The RKR model was the first to be developed in the spirit of the local approach. In the RKR model, unstable cleavage fracture is assumed to occur as soon as the maximum principal stress, σ_{yy} , exceeds a critical value, σ_f , over a characteristic distance larger than one grain diameter (Ritchie, [42]). In a high nitrogen mild steel containing uniform equiaxed ferrite grains and carbide particles, the authors

found that a typical value of the characteristic distance was twice the ferrite grain size. Figure IV-2 shows a schematic representation of the critical fracture event. According to that figure cleavage fracture occurred when σ_{yy} is higher than σ_f over the two grains ahead of the crack tip (in a two-dimensional analysis).

Despite the simplicity of RKR model that is necessary for the assessment of structures in practical applications, this model has some drawbacks: The plasticity effect is not explicitly taken into account by the RKR model (nucleation stage). Another difficulty in the use of this model is the choice concerning the characteristic distance which depends on the microstructure of the steel and of cleavage crack propagation mechanisms.

The RKR model is used in this chapter to determine critical cleavage stresses in the studied steels, since focus was only made on the cleavage propagation stage. In fact, the nucleation stage was in some cases affected by ductile crack initiation and brittle out-of-plane cracking, which make it difficult to model the nucleation stage. Moreover, this study focuses on the ductile-to-brittle transition, where cleavage cracking is growth-controlled. Tests performed at -196°C only aims at avoiding micro-delamination. The characteristic distance is fixed to twice the average ferrite grain size ($10\ \mu\text{m}$) and critical cleavage stress is to be correlated to microstructural parameters (here, the size of potential cleavage facets).

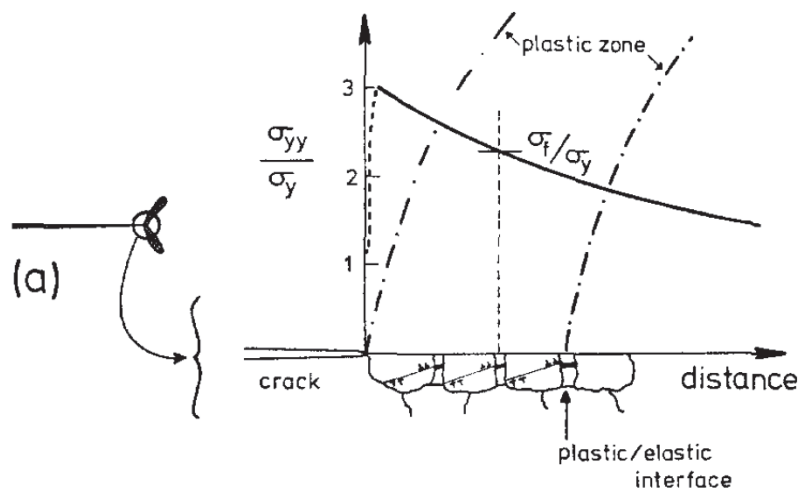


Figure IV-2: Application of the RKR model at a crack tip, the critical stress σ_f is to be exceeded over twice the grain size. The value of σ_{yy} is derived from slip-line field theory [42]

b) Probabilistic Beremin Model

The Beremin model is one of the most famous probabilistic models that take microstructure into account to determine a cleavage fracture criterion. This model lays on a mathematical statistics for the defect distribution and the weakest link assumption. It is assumed that some plastic strain is necessary for the cleavage occurrence and the process zone (PZ) is taken to be the plastic zone (a threshold of 10^{-6} was taken by Lambert-Perlade et al. [33]; the exact value does not affect the results as long as it remains very small). Then, the process zone of volume V is divided into q independent units having the same volume (V_0). As presented in (Lambert-Perlade, [33]), “the value of V_0 must be high enough to contain a cleavage crack initiator with a reasonable probability and low enough to allow one to neglect the stress gradients within V_0 ”. The authors took $V_0 = (100\mu\text{m})^3$, which corresponds to the volume of eight prior austenite grains. This value was also been chosen by Tanguy [1]. But it seems to be larger for the NT2 geometry used in this study.

- ❖ The probability for a given elementary unit volume V_0 to fracture under given maximum principal stress (σ_1) is given by

$$P_0(\sigma_1) = \int_{a_c(\sigma_1)}^{+\infty} p(a).da \quad (\text{Equation IV-5})$$

Where $p(a)$ is the size distribution density of defects in every unit of volume V_0 . It is assumed to obey the following equation

$$p(a) = \alpha.a^{-\beta} \quad \left\{ \begin{array}{l} a \text{ is the defect size} \\ \alpha \text{ and } \beta > 1 \text{ are } V_0\text{-dependent material constants.} \end{array} \right. \quad (\text{Equation IV-6})$$

$a_c(\sigma_1)$ is the critical size of defect for the initiation of cleavage yields stress σ_1 with a Griffith criterion. Inverting equation IV-3 and replace d_B by $a_c(\sigma_1)$

$$a_c(\sigma_1) = \frac{2.E.\gamma_p}{\pi.(1-\nu^2).\sigma_1^2} \quad \left\{ \begin{array}{l} E \text{ Young's modulus} \\ \gamma_p \text{ Energy for the formation of two fresh free surfaces} \\ \nu \text{ Poisson's ratio} \end{array} \right. \quad (\text{Equation IV-7})$$

By introducing Equation IV-6 and Equation IV-7 into Equation IV-5, the probability for a given elementary unit V_0 to fracture under the maximum principal stress (σ_1) is given by:

$$P_0(\sigma_1) = \left(\frac{\sigma_1}{\sigma_u} \right)^m \quad (\text{Equation IV-8})$$

$$\text{With } m = 2\beta - 2 \quad \text{and} \quad \sigma_u = \left(\frac{m}{2\alpha} \right)^{\frac{1}{m}} \sqrt{\frac{2.E.\gamma_p}{\pi(1-\nu^2)}} \quad (\text{Equation IV-9})$$

Parameter m is the so-called ‘‘Weibull modulus’’. It is linked to the size distribution of defects in the unit element V_0 .

Parameter σ_u is associated to the cleavage resistance of the material. This parameter σ_u is thought to be independent of temperature.

- ❖ Having determined the fracture probability P_0 of an elementary unit V_0 under σ_1 , we are interested in determining the failure probability all over the process zone (PZ). According to the weakest link theory, failure occurs if at least one of the q elementary volumes V_0 within the PZ fails. Thus, the specimen survives if all q elementary volumes V_0 located inside the PZ survive. This can be mathematically translated in the following equation:

$$1 - P_f = \prod_{i=1}^q (1 - P_i) \quad (\text{Equation IV-10})$$

By introducing a logarithm function on both sides of equation IV-10, one obtained:

$$\ln(1 - P_f) = \sum_{i=1}^q \ln(1 - P_i) \quad (\text{Equation IV-11})$$

Since the right term in Equation IV-11 looks like an average, a continuous expression of this average with $V_0 \ll V$ is

$$\frac{1}{q} \sum_{i=1}^q \ln(1 - P_i) \approx \frac{1}{V} \int_{PZ} \ln(1 - P_0) dV \quad \text{where } V \text{ is the volume of the PZ} \quad (\text{Equation IV-12})$$

Combining Equation IV-11 and Equation IV-12, yields:

$$\ln(1 - P_f) = \frac{q}{V} \int_{PZ} \ln(1 - P_0) dV \quad (\text{Equation IV-13})$$

If we consider that the probability P_0 remains small, we can assume that $\ln(1 - P_0) \approx -P_0$ so that:

$$\ln(1 - P_f) \approx -\frac{q}{V} \int_{PZ} P_0 dV \quad (\text{Equation IV-14})$$

Since:

$$V_0 = \frac{V}{q} \quad (\text{Equation IV-15})$$

Combination of Equation IV-9 and Equation IV-15 with Equation IV-14 gives:

$$\ln(1 - P_f(\sigma_I)) = -\frac{1}{V_0} \int_{PZ} \frac{\sigma_I^m}{\sigma_u^m} dV \quad (\text{Equation IV-16})$$

So, we define the Weibull stress as the m^{th} -order momentum of σ_I i.e :

$$\sigma_W = \left(\int_{PZ} \sigma_I^m \frac{dV}{V_0} \right)^{1/m} \quad (\text{Equation IV-17})$$

The introduction of this Weibull stress in Equation IV-16 gives:

$$\ln(1 - P_f(\sigma_W)) = -\left(\frac{\sigma_W}{\sigma_u} \right)^m \quad (\text{Equation IV-18})$$

Finally, by introducing an exponential function on both sides of Equation IV-18, the expression below is obtained at any time during the fracture test:

$$P_f(\sigma_W) = 1 - \exp \left[-\left(\frac{\sigma_W}{\sigma_u} \right)^m \right] \quad (\text{Equation IV-19})$$

Taking plastic strain into account in the Beremin model

The Beremin model has been modified when cleavage fracture occurs after a large plastic yield. In that case, the Weibull stress calculation was modified by introducing an exponential function of plastic strain. Therefore, the plastic strain could affect the mechanical fields, but not the intrinsic critical stress σ_u for the cleavage fracture of the steel, which is kept constant. In chapter VI, it will be shown that this way of introducing plastic strain effect is disputable, since critical cleavage stress was found to vary with plastic strain. Consequently, it might be more appropriate to set a dependence of σ_u on plastic strain.

$$\sigma_W = \left(\int_{PZ} \sigma_I^m \frac{dV}{V_0} \exp \left(-\frac{m\varepsilon_I}{k} \right) \right)^{1/m} \begin{cases} \varepsilon_I & \text{Local plastic strain in the direction of the maximum principal stress } \sigma_I \\ k & \text{Parameter generally taken as 2 or 4 in literature [1]} \end{cases} \quad (\text{Equation IV-20})$$

Application of the Beremin model

The most important step during application of the Beremin model is the identification of parameters σ_u and m . For an accurate estimate of these parameters, an experimental database with different temperature conditions should be used to obtain statistically relevant results. A good estimate of the stress-strain distribution in the specimen is also needed. The identification procedure described below was proposed by Tanguy [1]:

Step 0: Identification of the constitutive equations of the material at the temperatures of the study. These constitutive equations are generally extracted from smooth tensile tests.

Step 1: Experimental tests are performed on chosen geometries: Round notched tensile bars, precracked specimens or Charpy specimens... These tests may be performed on only one of those geometries. Generally, the round notched tensile bars are chosen for the simplicity of numerical simulation of the test. Test temperatures are chosen so that full cleavage fracture could occur. With the hypothesis that σ_u and m are independent of temperature, strain rate and specimen geometry, these tests could be carried out at various temperatures as soon as full cleavage fracture appearance is observed in each specimen.

Step 2: Numerical simulations are performed for the mechanical analysis of the experimental test to extract the local stress-strain distribution. It is important to check that there is good agreement between simulations and experimental (remote) measurements, so that local stresses could be estimated with a good accuracy. For example, with a round notched tensile bar, it is important to check that the load vs. average diameter reduction or notch displacement curves are accurately reproduced by the model.

Step 3: An initial value of Weibull parameter, m , is arbitrarily chosen. A value of m equal to 20 is reasonable for bainitic and ferritic steels (Tanguy, [1]).

Step 4: The Weibull stress is calculated for every test, using the preliminary value of m and the value of elementary volume V_0 already defined, at the stage of experimental fracture occurrence.

Step 5: The tests are ranked in the order of increasing Weibull stress and the fracture probability associated to each test is estimated. An example of mathematical expression for the probability fracture is: $P_f = (i-0.5)/N$, where i is the number of specimens broken for the value of Weibull stress considered, and N is the total number of tested specimens.

Step 6: New values of σ_u and m are calculated using the linear regression below:

$$\ln \left[\ln \left(\frac{1}{1 - P_f} \right) \right] = m \ln \sigma_w - m \ln \sigma_u \quad (\text{Equation IV-21})$$

Step 7: An iterative procedure is used (steps 3 to 6) until the value of m converges, and then the final values of m and σ_u are deduced.

After identification of Weibull parameters, the model could predict the fracture probability for any given value of Weibull stress or load. Tanguy [1] found that the second formulation of the Beremin Model with the effect of large plastic strain taken into account (*Equation IV-20*) leads to better agreement between model predictions and experiments. In fact, this formulation was used to represent the increase in fracture stress experimentally observed on NT specimens prestrained by tensile strain. The evolution of critical cleavage stress after prestraining has been found chapter VI.

The main drawback of the Beremin model is its complexity and its time consuming character with a high number of experimental tests required for the identification of Weibull parameters, although this is only a post-processing procedure in the numerical simulation.

c) Probabilistic with two successive microstructural barriers model

The double barrier model was originally proposed for ferritic steels with fracture initiated from carbides. This model has been used by Martin-Meizoso et al. [44], as a probabilistic model based on the weakest link model for cleavage cracking of carbide-containing bainitic steels. Lambert-Perlade et al. [33] adapted this model for bainitic steels containing M-A constituents. This modified version of the double barrier model is presented in this section.

As in the Beremin model, the process zone is the plastic zone (PZ) and for the sake of simplicity, the crack was assumed to nucleate from an intragranular M-A constituent. According to this model, cleavage fracture occurs, as soon as a microcrack, initiated from a M-A constituent, passes both the first barrier (particle-matrix interface) and the second barrier (matrix-matrix interface).

The authors considered that cleavage fracture occurs by following these steps (Figure IV-3):

Step 0: A crack initiates from brittle fracture of a M-A constituent under critical stress σ_{M-A}^c

Step 1: The microcrack instantaneously reaches the particle/matrix interface. For crossing of the first microstructural barrier, local yield is required ($\sigma_I > \sigma_y$) and the maximal principal stress must exceed a critical value, σ_{pm} . If these two conditions are fulfilled, the microcrack can propagate into the matrix.

Step 2: The first barrier is crossed and the microcrack propagates into the matrix until encountering the first matrix-matrix interface. For crossing this microstructural barrier, the maximal principal stress must exceed a critical value σ_{mm} .

Step3: The microcrack propagates across the matrix/matrix interface, leading to final failure.

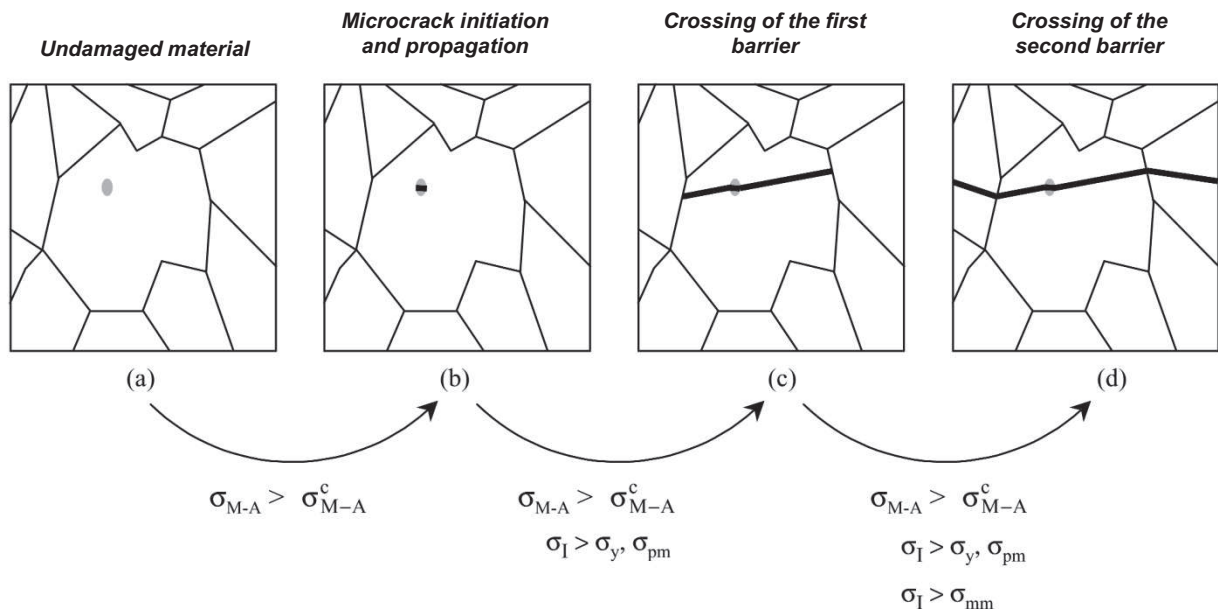


Figure IV-3: Schematic representation of the role of microstructural barriers on failure micromechanisms (from [33])

Using the weakest-link assumption, the fracture probability of the specimen is given by the combined conditional probabilities of these three events to successively occur at the same location on the specimen (steps 1, 2 and 3). A detailed application of this model is presented by Lambert-Perlade et al. [33].

This model has not been used in this study, because a considerable number of tests is needed per condition (15 in paper [33]), and its isotropic formulation is not appropriate for the study of anisotropy of cleavage fracture. Moreover, the initiation step of cleavage for the studied steels is not simple and the nature of the particle at the initiation site is unknown.

d) Micromechanical models involving crystal plasticity

For detailed review, the reader is referred to [45]. Polycrystal plasticity frameworks were used to describe cleavage fracture by considering individual grains in full-field models. The statistical origin of cleavage was described quantitatively from both microstructural defects and stress-strain heterogeneities due to crystalline plasticity at the grain scale.

Models based on crystal plasticity were not considered for our study.

IV.2. Anisotropy in potential cleavage facet distribution

IV.2.1. The concept of potential cleavage facets

As presented in the last section, the study of cleavage crack propagation requires a definition of microstructural barriers, wherein cleavage cracks could freely extend. The investigation of these microstructural barriers has been carried out via microtexture analyses, since cleavage fracture was assumed to preferentially propagate along $\{100\}$ crystallographic planes. A typical inverse pole figure of Steel A along (RD-TD) plane is presented in Figure IV-4. In this figure, regions containing $\{100\}$ crystallographic planes, which are represented in red color, correspond to regions where cleavage could easily propagate under a stress applied along the normal to that plane.

If we assume that any cleavage crack propagating within a red region, will not be stopped by encountering crystallographic planes only slightly misoriented with respect to $\{100\}$ planes, the previous domain wherein cleavage might freely propagate could be significantly increased. Figure IV-5 shows the same inverse pole figure, where only regions within cleavage crack might freely propagate (under stress applied along ND) are highlighted. These regions have been called **potential cleavage facets** (PCFs) in this study.

Therefore, to delimit these PCFs regions, a first criterion has to be set for the maximal value of the misorientation angles ω_i between the normal $\langle 001 \rangle_i$ and ND (direction of opening stress) in any grain "i" considered in this region; and a second criterion for the maximal value of the misorientation angles ω_{ij} between the normal $\langle 001 \rangle_i$ and the normal $\langle 001 \rangle_j$ that are closest so the loading directions (Figure IV-6).

Regions containing $\{100\}$ planes "well oriented" for cleavage cracking under tensile stress applied along ND

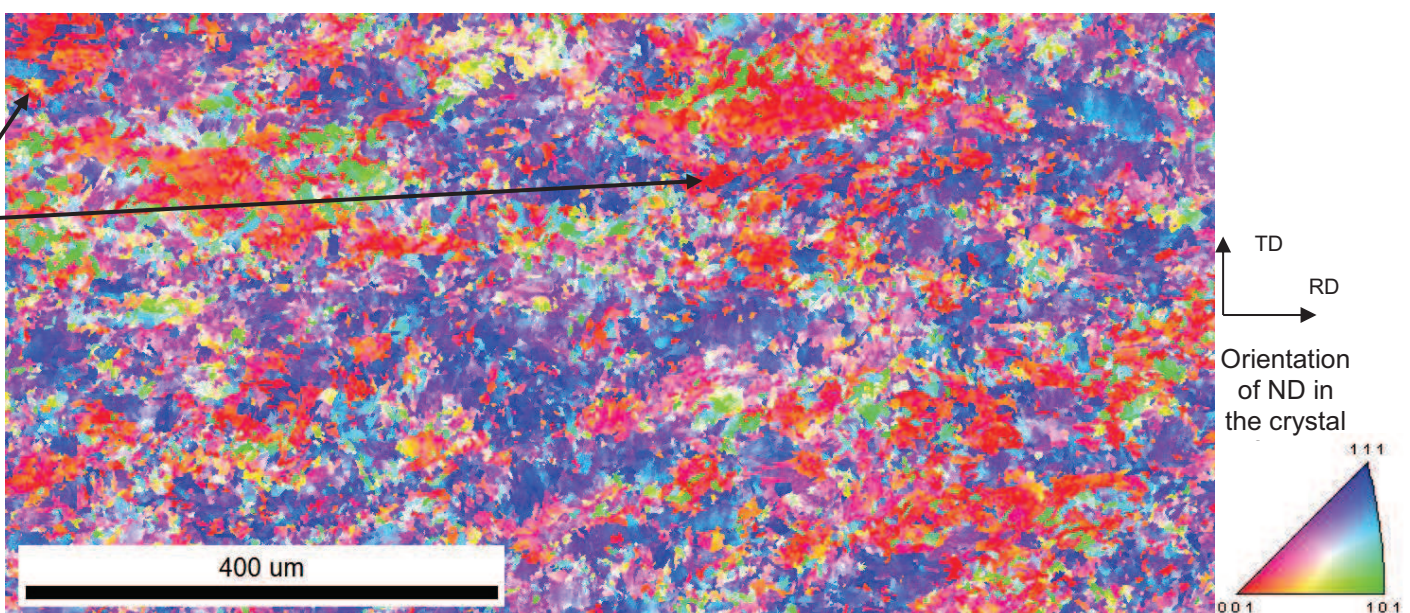


Figure IV-4: Inverse pole figure of Steel A within (RD-TD) plane. Red regions contain $\{100\}$ planes plane "almost" perpendicular to sample normal

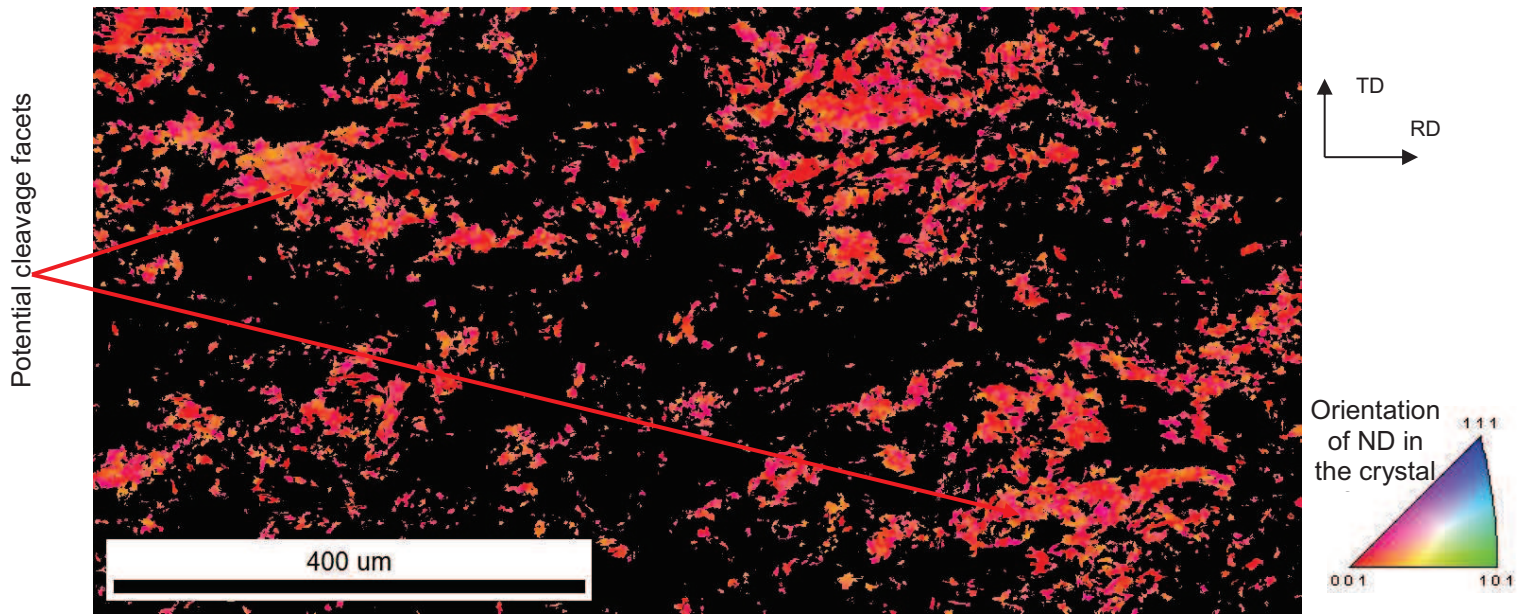


Figure IV-5: Potential cleavage facets extracted from inverse pole figure analysis. Steel A within (RD-TD) plane “almost” perpendicular to sample normal

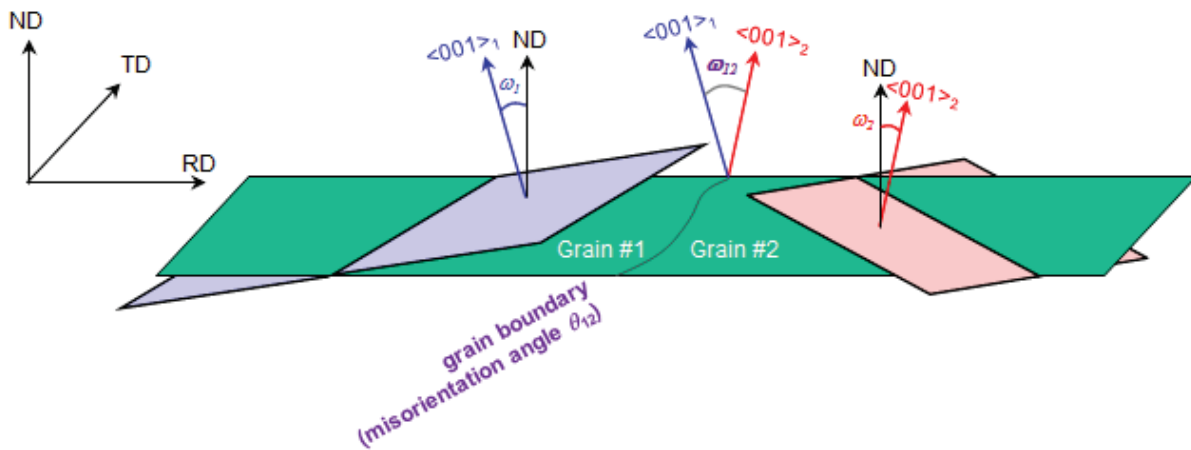


Figure IV-6: Analysis of misorientation angles for PCF identification: w_i and w_{ij} . The example of loading along ND is taken here. The green plane is the (RD,TD) plane.

PCF sizes are more than 10 times larger than the average ferrite grain size. Thus, the cleavage resistance is associated to a microstructural distance that is larger than the average ferrite grain size. The influence of microtexture, and not only of either individual grain size or average texture, is thus significant. In fact, as will be shown below, PCFs are representative of coarse elongated entities observed with optical light microscopy in chapter I, and which were chosen as defects for notched specimen design.

The procedure for quantitative investigation of PCFs is as follows:

- Choice of threshold values for misorientation angles ω_i and ω_{ij} , which are noted ω_{ic} and ω_{ijc} . Quantitative fractography and microstructure results were used to calibrate ω_{ic} and ω_{ijc} .
- The identified ω_{ic} and ω_{ijc} were used to analyze PCF distribution along the rolling, the θ -plane and other plane of interest of both steels. Thus the initial anisotropy was evaluated.
- Finally, the anisotropy obtained with PCF analysis was compared to the anisotropy in critical cleavage stress.

a) Sensitivity of the total area of potential cleavage facets to ω_{fc}

The domain covered by potential cleavage facets has been analyzed for the following critical deviation angles: 5°, 10°, 15°, 20°, and 25°. For each value, the area ratio occupied by potential cleavage facets has been measured. These values are presented in Table IV-2. This table shows that the area fraction of the domain covered by PCFs becomes higher when ω_{fc} increases. This tendency is confirmed with Figure IV-7, where the area of each PCF seems to have increased with ω_{fc} . Nevertheless, for ω_{fc} higher than 15°, the difference in area of larger PCFs is less affected by a further increase in ω_{fc} .

Deviation angle	5°	10°	15°	20°	25°
Area ratio (%)	3.5	12.0	22.0	30.0	37.0

Table IV-2: Evolution of the area ratio occupied by potential cleavage facets with critical deviation angle ω_{fc}

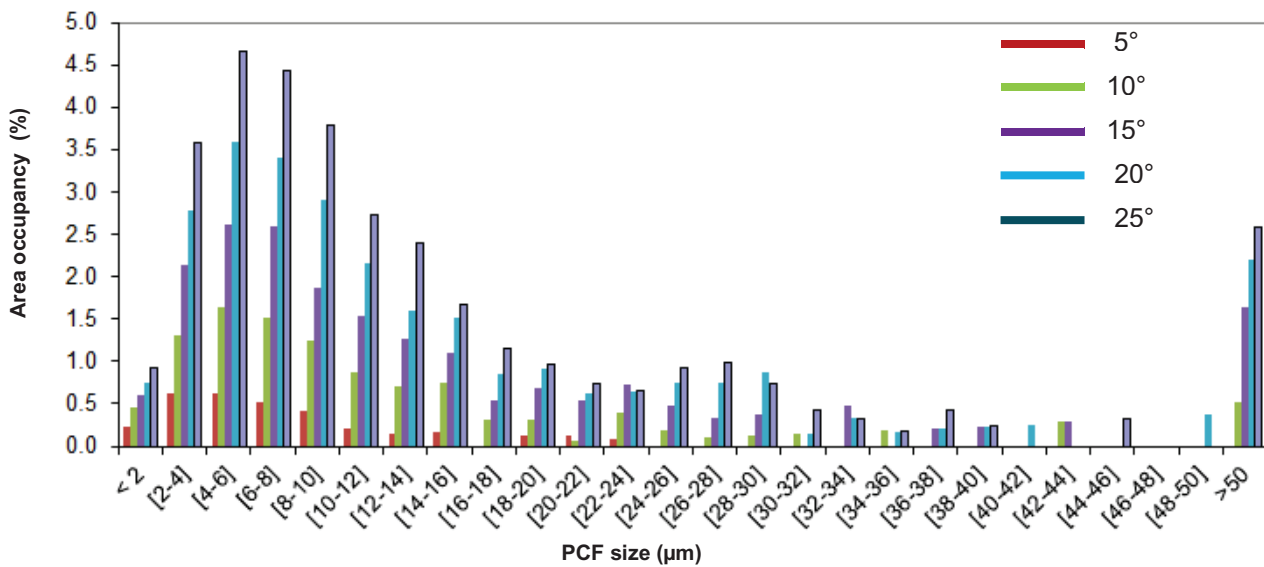


Figure IV-7: PCF size distributions for various values of ω_{fc} : 5°, 10°, 15°, 20°, 25°

b) Critical deviation angles obtained from quantitative fractography analyses

Deviation angles between cleavage facets were analyzed by quantitative fractography. First, an image of the zone of interest was taken with SEM at high magnification. Then, the specimen was tilted by -6° and by +6°, and images within the same zone of interest were taken. With these three images, a 3D reconstruction of the zone of interest was obtained (by the so-called “stereological pairs” method) using the MeX software. The local normal direction to cleavage fracture was determined in a number of points. The tilt and twist components of deviation angles between neighboring facets were finally calculated with an in-house software.

This analysis was carried on the fracture surface of a notched specimen where full cleavage was observed. A specimen of Steel A tested at -100°C along ND has been considered, so that the section of minimal area perpendicular to the applied load corresponds to (RD-TD) plane. In fact, it was one of the few specimens which did not exhibit delamination micro-cracks, and has large facet sizes making the analysis easier. The result of this analysis was expected to be useable for Steel B and for other loading directions, since the cleavage propagation physics might be the same due to similar microstructures.

The tilt and twist components of deviation within the initiation cleavage facet and also on each side of the facet boundary were determined (Figure IV-8). The measurements within this facet give an indication of deviation angles which could not stop cleavage crack propagation. The angle between each side of the cleavage facet boundary indicates which deviation angles could stop cleavage crack propagation. The results of these measurements are plotted in Figure IV-9. Open symbols correspond

to measurements within the facet and full symbols to measurements from each side of the boundary facet.

From this analysis, a critical deviation angle between 15° and 20° seems to be a suitable criterion for the definition of potential cleavage facets, since cleavage propagation might not be stopped for deviation angle lower than that value.

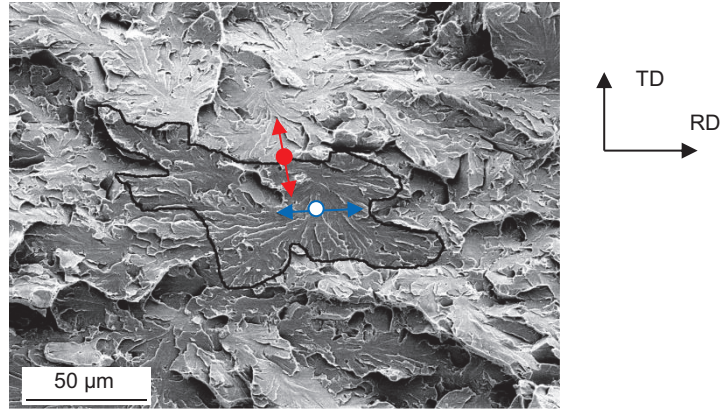


Figure IV-8: Fracture surface of Steel A tested at -100°C along ND. Focusing on the initiation cleavage facet (boundaries delineated in black)

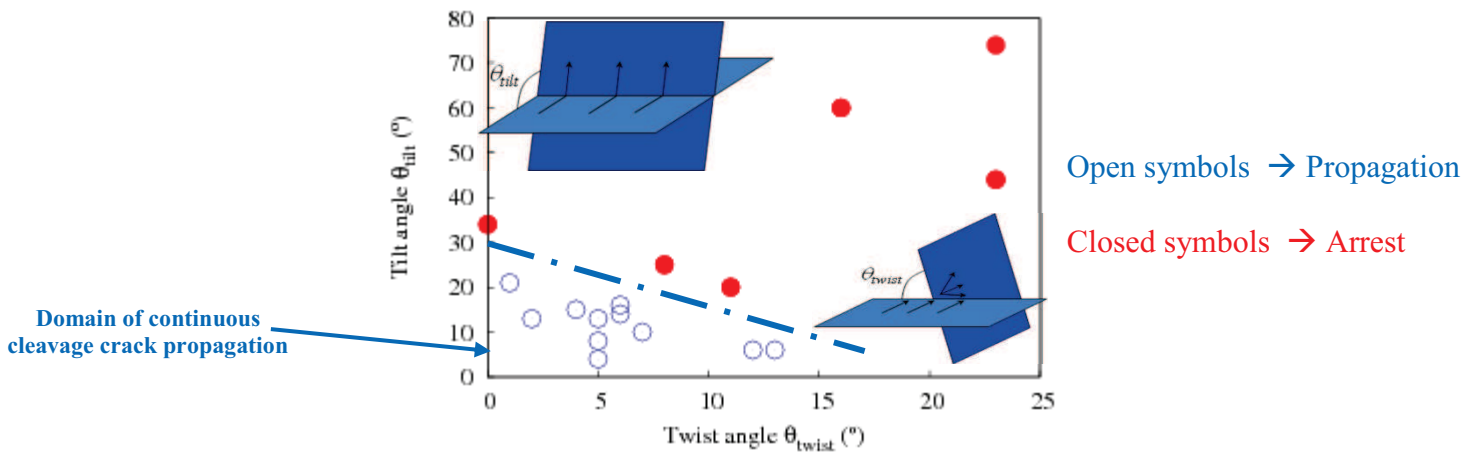


Figure IV-9: Tilt and twist components of the deviation angles for the propagation or arrest of cleavage crack initiated on the specimen of figure IV-8

c) Final choice of ω_{ic} and ω_{jc}

The area scanned during EBSD analyses on Steel A along (RD-TD) plane has been observed on light optical microscope, with the purpose to link the microtexture to microstructural observations. A parametric study on ω_{ic} , performed between 15° and 25°, showed that for $\omega_{ic} = 20^\circ$, the area covered with PCFs well correlated to the one occupied by coarse elongated entities observed with light optical microscopy. Moreover, for $\omega_{jc} = 10^\circ$, PCF boundaries are the same as for these coarse elongated entities (Figure IV-10). Thereafter, ω_{ic} and ω_{jc} have been set to 20° and 10° respectively.

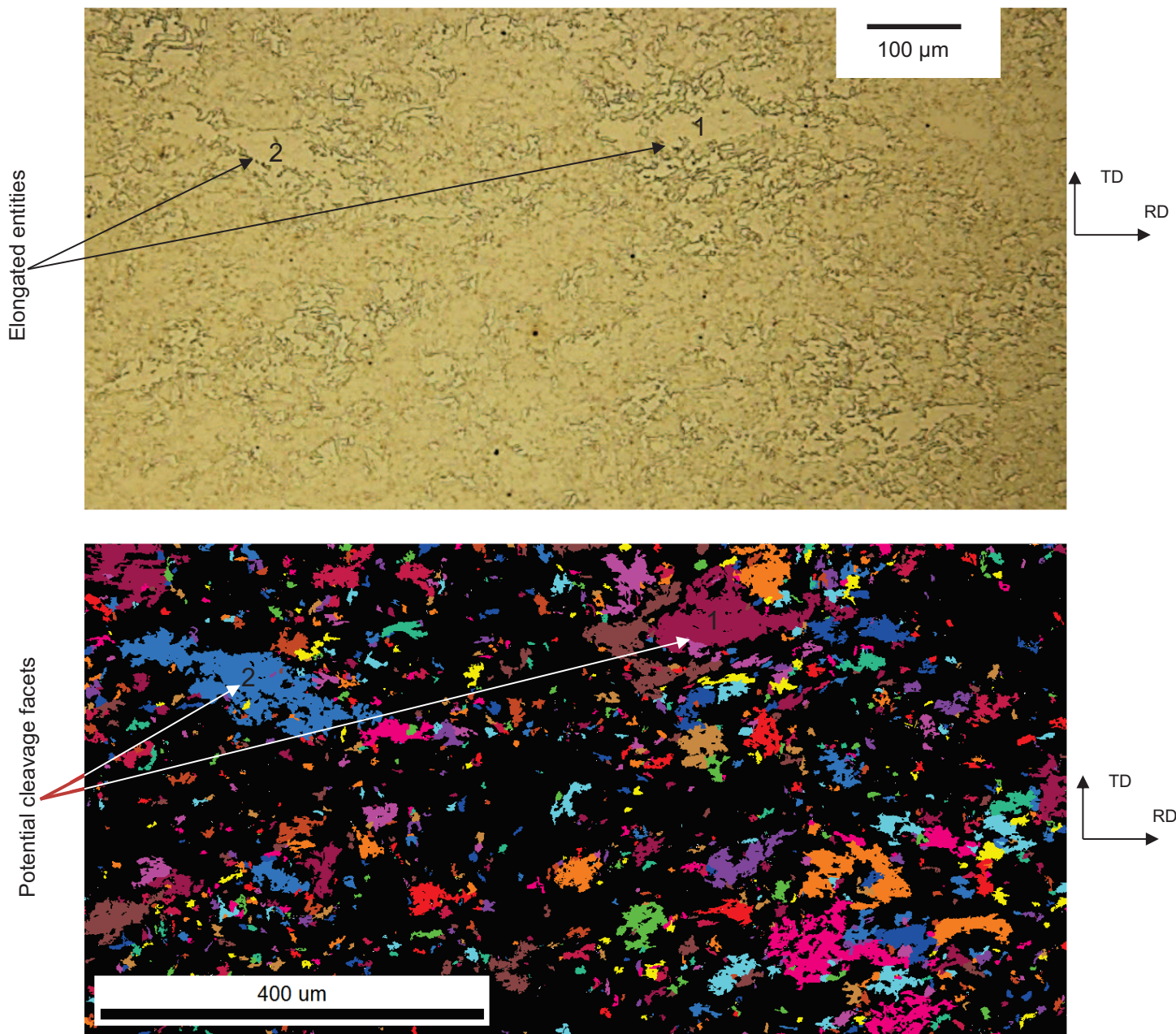


Figure IV-10: Light optical micrograph and EBSD map (one arbitrary color per PCF) of the same region of Steel A within (RD-TD) plane: Correlation between potential cleavage facets and elongated entities. Some of them are indicated with arrows

IV.2.2. Analysis of potential cleavage facets for different planes of the plate

To understand the higher sensitivity to cleavage perpendicular to ND and BTD directions compared to other directions of the two investigated steels, the size and distribution of potential cleavage facets were investigated along the four planes tested via tensile tests in the previous chapter: (RD-TD) perpendicular to ND, θ -plane perpendicular to BTD, (TD-ND) perpendicular to RD and (RD-ND) perpendicular to TD. A complementary plane, the above mentioned anti- θ -plane, was studied. This plane tilted by 40° around TD with respect to rolling plane, is one where BTF might have propagated during drop weight tear tests along RD, but did not (see chapter II)

a) Experimental procedure

For each investigated plane, EBSD analysis was carried out over a large map (1mm×0.5mm) resulting from the merging of eight neighboring maps (250µm×250µm), to obtain statistically relevant results. A fine step size (0.5µm, i.e. 10 times lower than the average grain size) was used to catch every detail of the matrix microstructure. This EBSD analysis was done in a field emission gun (FEG) scanning electron microscope (under magnification ×350) using the following EBSD setup parameters: high voltage 30 kV, tilt angle 70°, working distance 17 mm. More than 99.8% of points were reliably indexed. A grain dilation cleanup procedure was applied with a grain tolerance angle of 5° and a minimum grain size of 5 pixels. Criteria on the misorientation angles $\omega_{ic}=20^\circ$ and $\omega_{jc}=10^\circ$ were used to determine PCFs. The total area ratio of PCF was obtained by dividing the cumulated area of PCFs by the total scanned area.

b) Size distribution of potential cleavage facets

Figure IV-11 and Figure IV-12 give the distribution of potential cleavage facets along the five planes of interest for both steels. For each plane of interest, the EBSD map and the size distribution of PCFs are reported. Large PCFs elongated along RD were observed in the (RD-TD) plane and in the θ -plane, with higher surface covered with PCFs and larger distribution tail. That might qualitatively explain why planes perpendicular to ND and BTD directions have a higher sensitivity to cleavage fracture.

As a result, the anisotropy in PCF size distribution is well correlated to the observed anisotropy of cleavage fracture. This tends to show that microtexture plays an important role in the resistance of these steels to cleavage fracture, at least at -196°C.

The next step is to correlate the PCF size distribution to a critical cleavage stress of the plane of interest. Two approaches could be used to investigate this correlation. The first one is a statistical approach as e.g. in the Beremin model, where the defect size distribution could be set as the PCF size distribution. The other one is a determinist approach where an “effective” PCF size calculated for each distribution could be correlated to critical cleavage stress of the selected plane. The first approach was not chosen for this study, due to the lack of a unique adequate mathematical function which could describe the PCF size distributions along the five planes of interest. The second approach was therefore chosen. Since cleavage is controlled by larger defects, the calculation of effective PCF size was performed by averaging the size of larger PCFs, i.e., of the distribution tail. Hence, it was necessary to define a threshold size to define the distribution tail. The fact that the distributions were not bimodal made the choice of the threshold PCF size (arbitrarily set to 8 µm) difficult. The value of 8 µm corresponds to the PCF size at the distribution peak.

This so-called *effective PCF size* (PCF_{eff}) was defined as the fictive diameter that all PCFs of the distribution tail would have, if they all had the same area.

$$Cumulated_PCF_area = number_PCF \times \pi \times (PCF_eff/2)^2 \quad (Equation\ IV-22)$$

$$\text{Thus, } PCF_eff = 2 \times (Cumulated_PCF_area / (number_PCF \times \pi))^{0.5} \quad (Equation\ IV-23)$$

A study on the sensitivity of PCF_{eff} to the threshold PCF size was done for values of 8 µm, 10 µm, and 12 µm. The PCF_{eff} square roots (Griffith's like approach) were evaluated for each threshold value. The maximum difference observed was around 5%. Therefore, a threshold PCF size of 8 µm was adopted in the remaining of the study for the calculation of PCF_{eff} .

Steel A

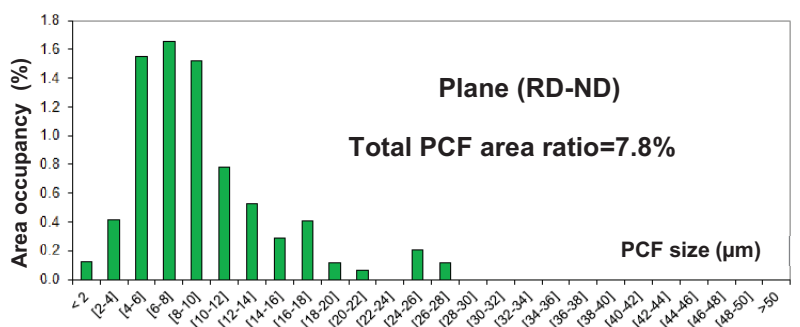
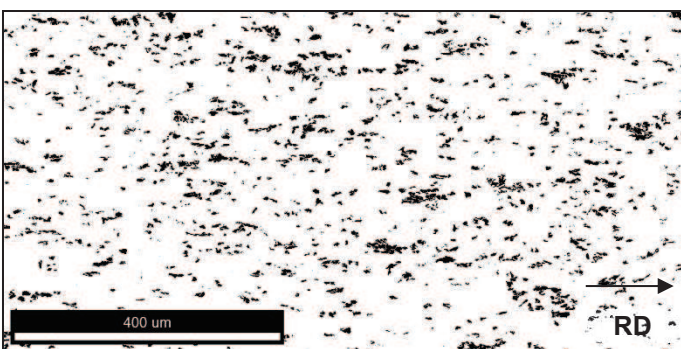
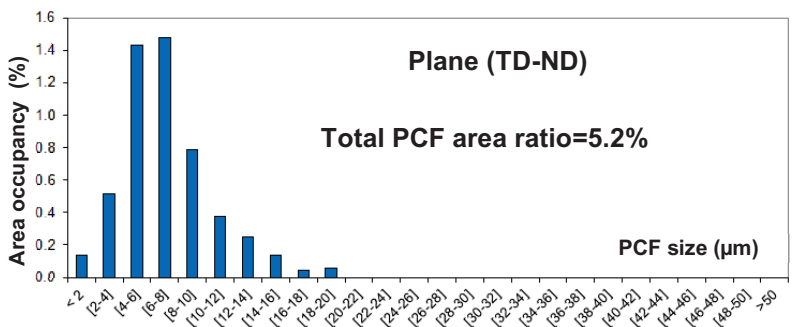
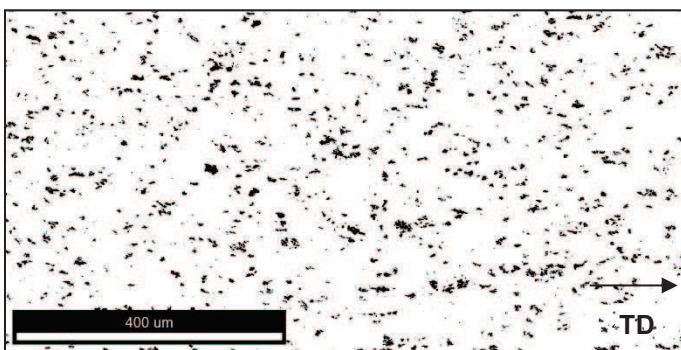
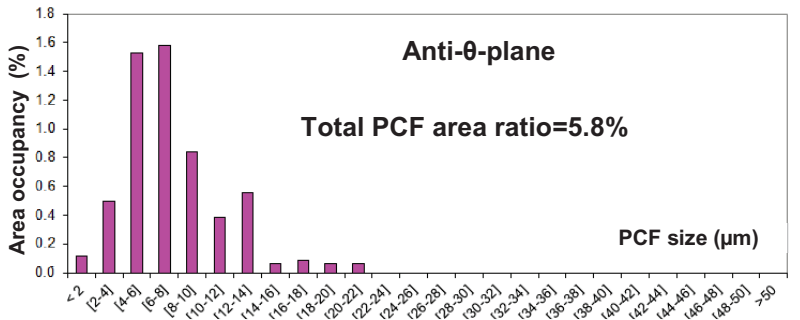
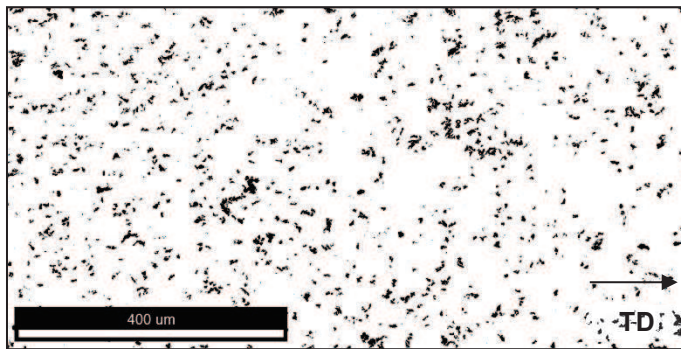
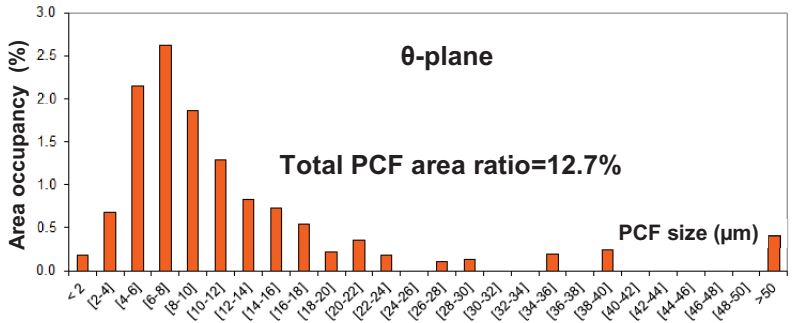
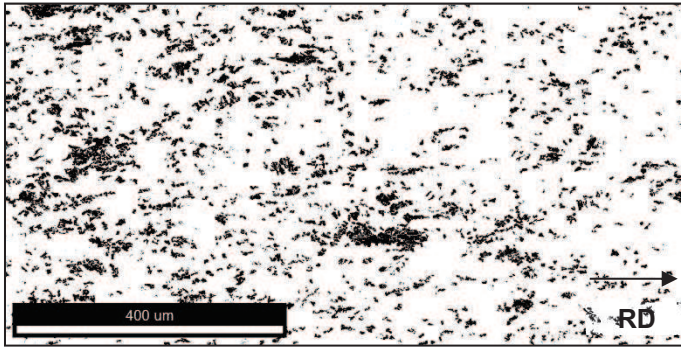
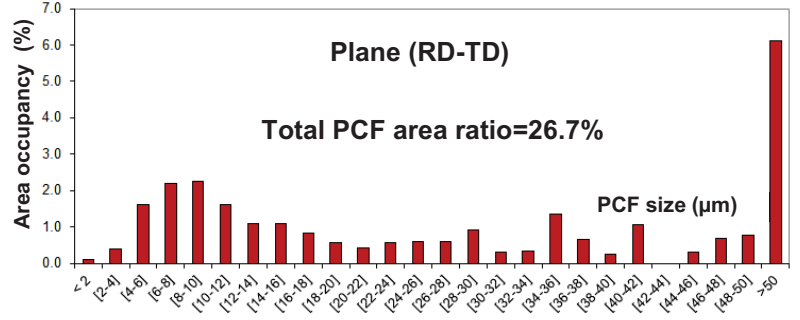
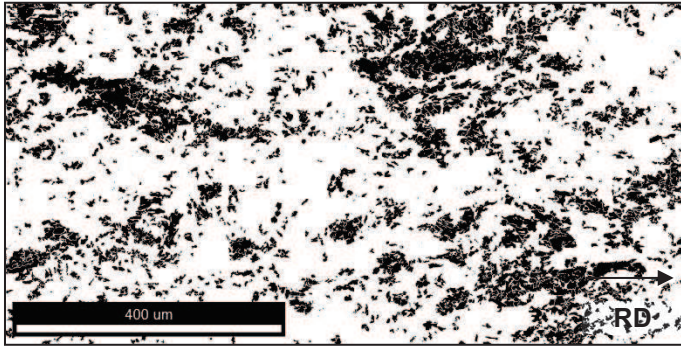


Figure IV-11: Anisotropy in the distribution of potential cleavage facets within the 5 planes of interest for Steel A

Steel B

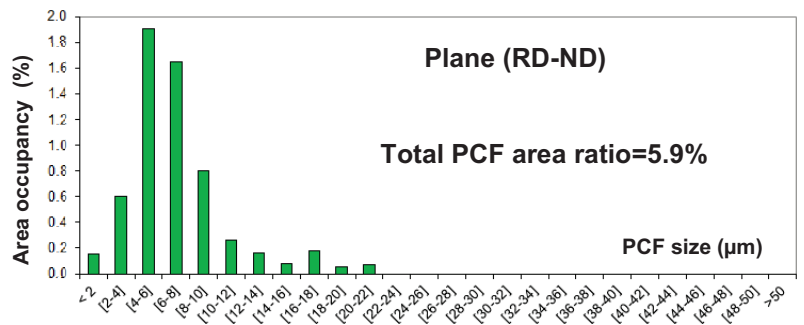
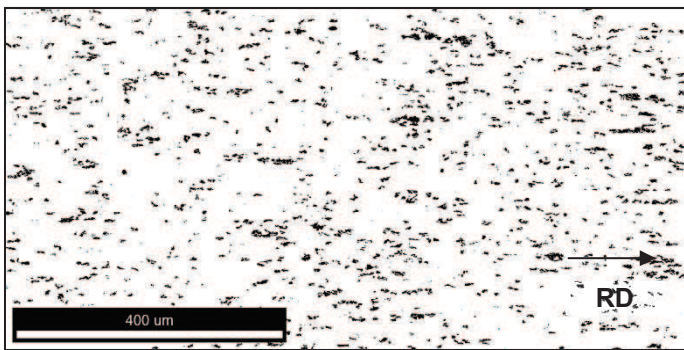
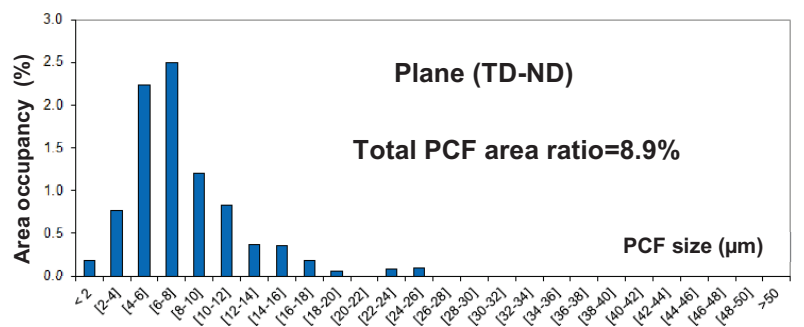
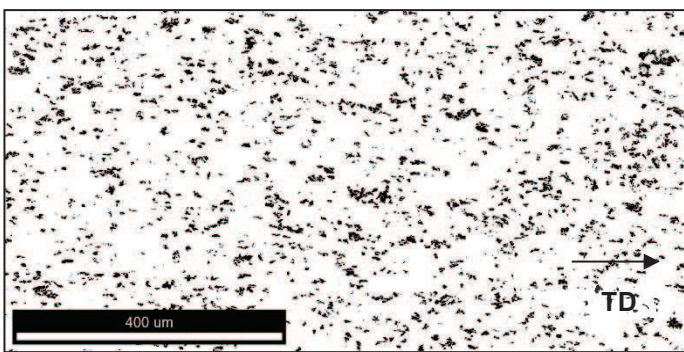
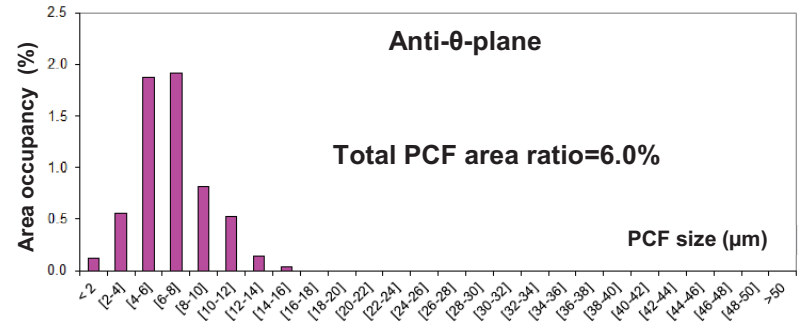
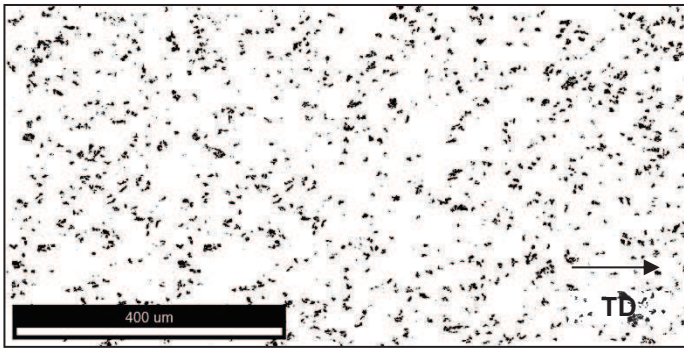
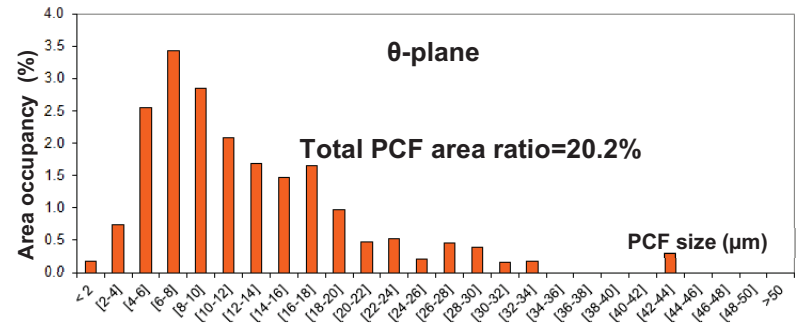
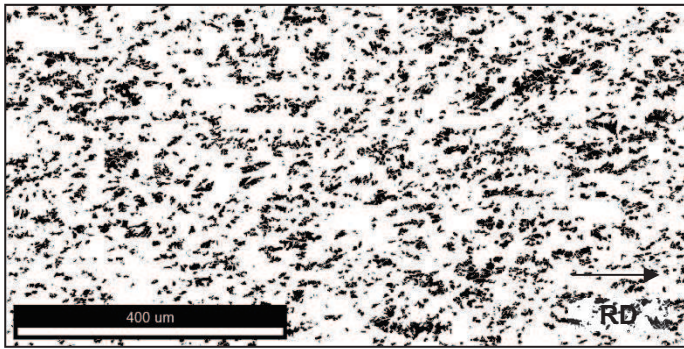
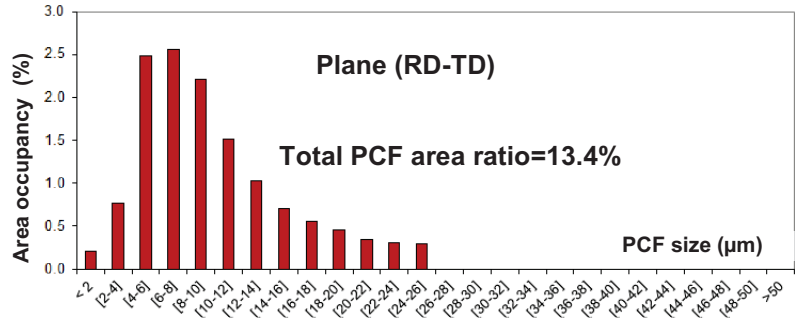
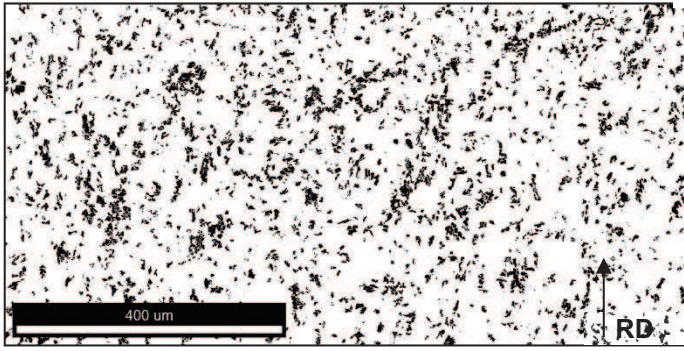


Figure IV-12: Anisotropy in the distribution of potential cleavage facets within the 5 planes of interest for Steel B

IV.3. Anisotropy in critical cleavage stress, correlation with PCFs

IV.3.1. Procedure

Critical cleavage stresses were determined by extracting the critical axial stress at the onset and at the location of in-plane cleavage fracture during tensile tests on notched specimens. Except for the ND direction of Steel A, where the analysis was done at -100°C , critical cleavage stresses were determined at -196°C for all the cases. A fracture surface which exhibited full cleavage fracture was targeted, so that critical cleavage stress value could not be underestimated because of presence of secondary cracks. Nevertheless, for RD and TD directions of Steel A, and for TD direction of Steel B, delamination microcracks could not be avoided even at -196°C . Therefore, a critical cleavage stress determined for these directions might be underestimated.

A proper analysis of the stress distribution at the cleavage initiation site was necessary to extract relevant values of a critical cleavage stress. Finite element calculations were performed using quadratic bricks, finite strain formalism, a Newton-Raphson iterative scheme for global convergence and an implicit integration scheme for constitutive equations. After a study of the mesh size effect and the element type effect (reported in detail in appendix C), quadratic elements with $15\ \mu\text{m}$ in length were used at the center of the specimen. One-eighth of the specimen was modeled and uniform displacement was prescribed at the bottom edge together with usual symmetry conditions (Figure IV-13).

The identification and choice of the constitutive model is presented in appendix C. Three models using different plastic yield criteria were analyzed: a model with a von Mises yield criterion, a Hill yield criterion and a Barlat yield criterion. For each of these models, a linear-exponential Voce-like isotropic strain hardening (model parameters: (H, b, Q)), independently of temperature below -100°C was chosen (see chapter III). Only the initial yield strength evolved with temperature in an exponential manner, as also reported in chapter III. The tensile curves (smooth and notched specimens), the Lankford coefficients (with memory of corresponding directions) and strain anisotropy ratios predicted by each model were compared to experimental results. The model with Barlat criterion with the set of parameters presented in (Table IV-3 and Table IV-4) exhibits best agreement with experiment. This model was therefore chosen to describe the stress state inside the specimen, which is necessary for the estimation of critical cleavage stress.

Numerical calculations were stopped at the diameter reduction measured at the onset of brittle fracture. Critical cleavage stress was determined as the axial stress at the cleavage initiation site. An uncertainty of $50\ \text{MPa}$ has been assumed for this determination, because this value corresponded to the maximal variation in axial stress over $100\ \mu\text{m}$ of the initiation site. Since the value $100\ \mu\text{m}$ was larger than the average size of two ferrite grains and also of PCFs, the characteristic distance of at least two times the grain size, requested by the RKR model was fulfilled. For specimens which exhibited delamination cracks, only a lower bound of critical cleavage stress could be determined, by considering the higher axial stress within the specimen (at the center), i.e. by not considering mechanical influence of the (already present) delamination crack.

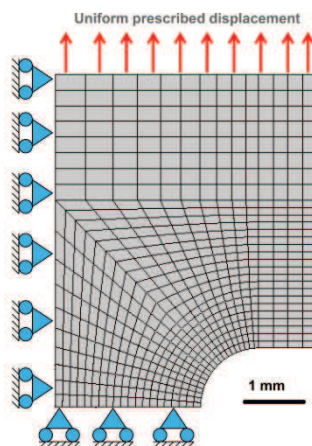


Figure IV-13: Boundary conditions applied on the NT1 specimen geometry

Steel A				Steel B			
	H (MPa)	b	Q (MPa)		H (MPa)	b	Q (MPa)
T=20°C	435	28	165	T=20°C	340	16	160
T≤-100°C	430	17	220	T≤-100°C	682	26	180

Table IV-3: Strain hardening parameters of Steel A and Steel B

Steel A						
a	c ₁	c ₂	c ₃	c ₄	c ₅	c ₆
12	1.038	1.057	0.952	1.041	1.034	1.032

Steel B						
a	c ₁	c ₂	c ₃	c ₄	c ₅	c ₆
12	1.028	1.034	0.982	0.999	1.032	1.062

Table IV-4: Parameters of Barlat yield criterion for Steel A and Steel B, considered as independent of temperature

IV.3.2. Critical cleavage stress along ND, BTD, RD and TD

The values of critical cleavage stresses, as determined using the above mentioned model, are reported in Table IV-5. In addition to the 50 MPa associated to uncertainty induced by numerical simulation, there is another uncertainty linked to experiment conditions and sampling effect. A considerable number of specimens should be tested per condition to assess this experimental error, and it was not the case for our study where a maximum of two specimens was considered per condition. This uncertainty cannot therefore be quantified.

All results were obtained by analysis of the tests performed at -196°C, except for Steel A along ND for which the values was obtained at -100°C, because specimens of Steel A tested at -196°C along ND showed atypical fracture surfaces, as already mentioned. At this stage, possible effects of large plastic deformation before cleavage fracture (occurring for a diameter reduction of 0.15) on the value of critical cleavage stress were not analyzed. They will be discussed later on in chapter VI, based on complementary experimental results.

	ND	BTD	RD	TD
Steel A	1800 ± 50 MPa*	2200 ± 50 MPa	≥ 2200 ± 50 MPa	≥ 2200 ± 50 MPa
Steel B	2200 ± 50 MPa	2000 ± 50 MPa	2400 ± 50 MPa	≥ 2500 ± 50 MPa

Table IV-5: Critical cleavage stress along ND, BTD, RD and TD for both steels. (*) direction ND of Steel A tested at -100°C, showed large deformation before cleavage fracture (15% in diameter reduction). Lower bounds are for tests where some delamination microcracks were observed prior to flat cleavage fracture.

As already observed from PCF distribution analysis for these four directions, there is a significant anisotropy in cleavage sensitivity of both steels. ND and BTD are more sensitive to cleavage fracture with lower critical cleavage stress. This anisotropy is now quantified, to be at least 20% from the obtained values.

The higher the total PCF area fraction, the lower critical cleavage stress. Therefore, the PCF size might affect critical cleavage stress value. It was thus attempted to link the PCF size obtained from microstructural analyses to critical cleavage stress obtained from mechanical analyses.

IV.3.3. Correlation between PCF size and critical cleavage stress

PCF_eff was defined in (IV.2.2) using a threshold PCF size of 8 μm . Table IV-6 shows the values obtained for the five analyzed planes.

	(RD-TD)	θ -plane	anti- θ -plane	(TD-ND)	(RD-ND)
Steel A	18.1 μm	12.3 μm	10.6 μm	10.2 μm	11.1 μm
Steel B	11.6 μm	12.7 μm	9.7 μm	10.7 μm	10.3 μm

Table IV-6: Effective PCF sizes for the five planes analysed with EBSD

The literature survey showed that in classical models using the local approach to cleavage fracture, critical cleavage stress was inversely proportional to the square root of the size of the microstructural barrier, i.e. of the size of the first microcrack (Griffith-like criterion). In our case, this microstructural barrier size was tentatively chosen as PCF_eff. Critical cleavage stress vs. inverse of effective PCF size square root curve is presented in Figure IV-14. Only data points associated to reliable critical cleavage stress values have been taken into account. Therefore, data points associated to directions ND, RD and TD for Steel A and TD for Steel B were not used.

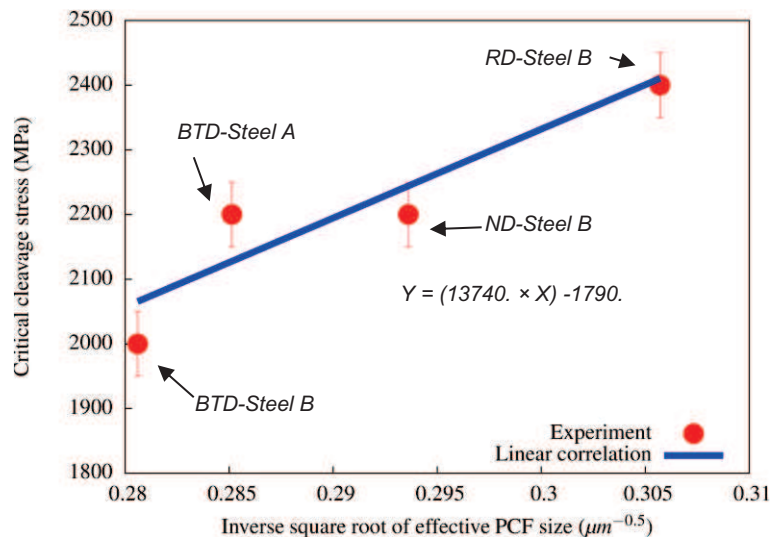


Figure IV-14: Tentative linear correlation between critical cleavage stress and the inverse of the square root of effective PCF size

There is a fairly good correlation between the inverse square root of effective PCF size and critical cleavage stress, via a linear equation. This supports the fact that a Griffith-like approach might be relevant to describe the anisotropy in sensitivity to cleavage fracture. Using this equation, critical cleavage stress may be estimated from effective PCF sizes and compared to the one actually measured. These results are summarized in Table IV-7. Critical cleavage stress estimated along ND for Steel A is considerably lower compared to the measured value. The fact that the cleavage stress was obtained after large strains at -100°C (0.2 compared to 0.003 – 0.02 at -196°C), might play a role.

Moreover the uncertainty related to the evaluation of PCF_eff and to the statistical effects resulting from sampling of PCFs might also affect this correlation.

	ND	BTD	RD	TD
Steel A (measured)	1800 ± 50 MPa*	2200 ± 50 MPa	≥ 2200 ± 50 MPa	≥ 2200 ± 50 MPa
Steel A (predicted)	1440	2130	2510	2330
Steel B (measured)	2200 ± 50 MPa	2000 ± 50 MPa	2400 ± 50 MPa	≥ 2500 ± 50 MPa
Steel B (predicted)	2240	2060	2410	2500

Table IV-7: Comparison between determined values of critical cleavage stress and those based on the PCF size distribution and a Griffith-like criterion

IV.4. Conclusions

The quantitative study of cleavage fracture anisotropy was performed via two approaches:

- The first approach is a microstructural one. The microtextures along the rolling plane, the θ -plane, and the (TD-ND) and (RD-ND) planes were investigated via EBSD measurements for the two steels. PCFs, which well correlate with coarse elongated entities observed with light optical microscopy were found as microstructural barriers for cleavage crack propagations. The analysis of the four planes of interest showed anisotropy in PCF size distributions. The larger the PCFs, the more sensitive (to cleavage) the studied plane. By considering PCF size distributions, specimens tested along ND and BTD were expected to be more sensitive to cleavage, in agreement with experimental tensile tests. The initial anisotropy of the microtexture well correlated with the cleavage fracture anisotropy.
- The second approach is a mechanical approach. Tensile tests along ND, BTD, RD and TD were numerically simulated via finite element calculations. An elastoplastic model with a Barlat plastic yield criterion was used to estimate the local stresses inside the specimens at the onset of cleavage fracture. The axial stress extracted at the fracture initiation site was considered as critical cleavage stress. This critical cleavage stress was not the same for ND, BTD, RD and TD, with the lower values obtained for ND and BTD directions. Therefore, anisotropy of critical cleavage stress was observed.

The two approaches were successfully linked using a Griffith-like approach, where the inverse square root of the average PCF size was tentatively correlated to critical cleavage stress. Some uncertainty related to the calculation of the average PCF size and to statistical effects resulting from sampling of PCFs might also affect the correlation.

The results of the present chapter will be used in the following chapters to quantitatively study brittle out-of-plane cracking. First, the anisotropy in critical cleavage stress has been used to predict brittle out-of-plane fracture (chapter V). Secondly, the microstructure of Steel B was modified via heat treatment or prestraining to change the initial PCF area and size distribution (chapter VI).

Chapter V – *Prediction of brittle out-of-plane cracking with a deterministic approach*

Table of Contents

- V.1. Introduction and state-of-the-art 97
- V.2. Prediction of the onset of brittle out-of-plane cracking during quasi-static tensile tests on notched specimens 98
 - V.2.1. Application of the macroscopic critical stress criterion to the prediction of delamination.. 99
 - V.2.2. Effect of stress triaxiality 100
 - V.2.3. Effect of the ductile crack on the stress state at the onset of delamination 101
 - V.2.4. Effect of prior plastic deformation on critical cleavage stress..... 105
 - V.2.5. Discussion of the criterion for numerical prediction of brittle out-of-plane cracking 106
- V.3. Prediction of brittle out-of-plane cracking occurrence during impact tests on Charpy specimens 107
- V.4. Conclusions 109

The anisotropy of critical cleavage stress was found from tensile tests performed along ND, BTD, RD and TD. Critical cleavage stresses of directions ND and BTD were around 20% lower than for RD and TD. The occurrence of brittle out-of-plane cracking was consequently expected to result from lower critical cleavage stresses observed along ND and BTD for a given specimen tested along TD or RD.

The present chapter proposes a criterion based on the anisotropy in critical cleavage stress to predict the occurrence of delamination. A first analysis was done on NT specimens where the numerical modeling is straightforward and the delamination event was detected by an abrupt drop of the load. Then, a second analysis was done on Charpy tests which are more complex to model numerically.

Résumé

Un critère s'appuyant sur l'anisotropie des contraintes critiques de clivage a été utilisé pour prédire l'apparition du délaminage dans les éprouvettes tractions entaillées et Charpy. Le délaminage est supposé être déclenché quand la contrainte dans la direction ND atteint une contrainte critique de clivage.

La première analyse faite sur les éprouvettes de traction entaillées montre que la contrainte dans la direction ND au déclenchement du délaminage est deux fois plus petite que la contrainte critique de clivage déterminée à partir d'essais de traction à -196°C en mode I dans la direction ND. Pour expliquer cette différence, l'effet de la fissure ductile d'où s'amorce le délaminage a été pris en compte, en introduisant une entaille elliptique de dimensions similaires à la fissure ductile observée au centre de l'éprouvette. La présence de cette entaille elliptique augmente localement d'environ 60% la contrainte dans la direction ND. Cette nouvelle valeur de contrainte reste néanmoins inférieure à la contrainte critique attendue. Par conséquent, un effet de la déformation plastique sur la contrainte critique de clivage est suspecté. Cette hypothèse s'appuie sur la forme allongée des facettes de clivage observée sur le faciès de délaminage.

Une analyse similaire a été effectuée sur des éprouvettes Charpy. Dans ce cas un effet de la déformation plastique sur la contrainte critique de clivage semble aussi probable. En d'autres termes, la contrainte critique de clivage et son anisotropie ne seraient pas un paramètre intrinsèque au matériau. Les résultats du chapitre VI valideront cette affirmation.

V.1. Introduction and state-of-the-art

The rolling plane and θ -plane have been found to be more sensitive to cleavage fracture because of lower critical cleavage stresses along ND and BTD respectively. A plausible cause of the occurrence of these brittle out-of-plane cracks was found to be that anisotropy in critical cleavage stresses which was correlated to the microtexture in Chapter IV. Predicting the occurrence of delamination and BTF is the next target of this study.

From open literature there is no criterion for BTF occurrence and very few authors proposed a criterion for delamination occurrence by cleavage fracture. Baldi [16] is one of these rare authors who presented a criterion for delamination occurrence. This criterion is based on a macroscopic critical stress. According to the author, delamination fracture happens when the stress along the short transverse direction ND, here denoted as σ_{zz} becomes higher than the critical fracture stress of the plate along that direction, denoted σ_{zz}^{cf} . This criterion was validated on four-point slow-bending specimens taken from HSLA steels (yield strength between 500-800 MPa). The value of σ_{zz}^{cf} was extracted from tests performed along ND at the nil-ductility temperature, so that cleavage fracture could initiate at the onset of general yielding. Then, tests along RD and TD were performed between -140°C and -180°C , so that the first delamination crack also formed at the onset of general yielding. Elastic-plastic mechanical analysis was carried out on these tests using a Hill criterion, to determine the through-thickness stress at delamination, which was associated to a load drop visible on the load vs. deflection curve. This value of σ_{zz} was found close to the critical cleavage fracture stress, σ_{zz}^{cf} , and consequently validated the delamination criterion in that particular case.

The critical stress criterion proposed in [16] has some drawbacks which make their direct application to the present study difficult. The delamination occurrence was studied at very low temperatures, i.e., without ductile crack advance. In the present study, delamination occurs within the ductile-to-brittle transition regime, so that large plastic strain occurred in NT specimens before delamination occurrence. This cannot be directly taken into account in such an approach. Moreover, Type 2 delamination after preliminary ductile advance, commonly observed in DWTT specimens and also in NT specimens, could hardly be predicted with this criterion. In fact, Carassou [46] who worked on in-plane cleavage cracking showed that cleavage occurrence could be affected by the presence of ductile cracks. In his study [46], cleavage fracture was initiated from dimples nucleated from MnS particles. The ductile crack, i.e., the region covered with these MnS-induced dimples was modeled as an oblate elliptical notch with a ratio between major and minor axes of 20. Unit cell calculations with prescribed remote axial stress Σ_1 and prescribed remote stress triaxiality set to 1.2 were used to investigate the effect of this ductile crack on the local stress distribution (Figure V-1).

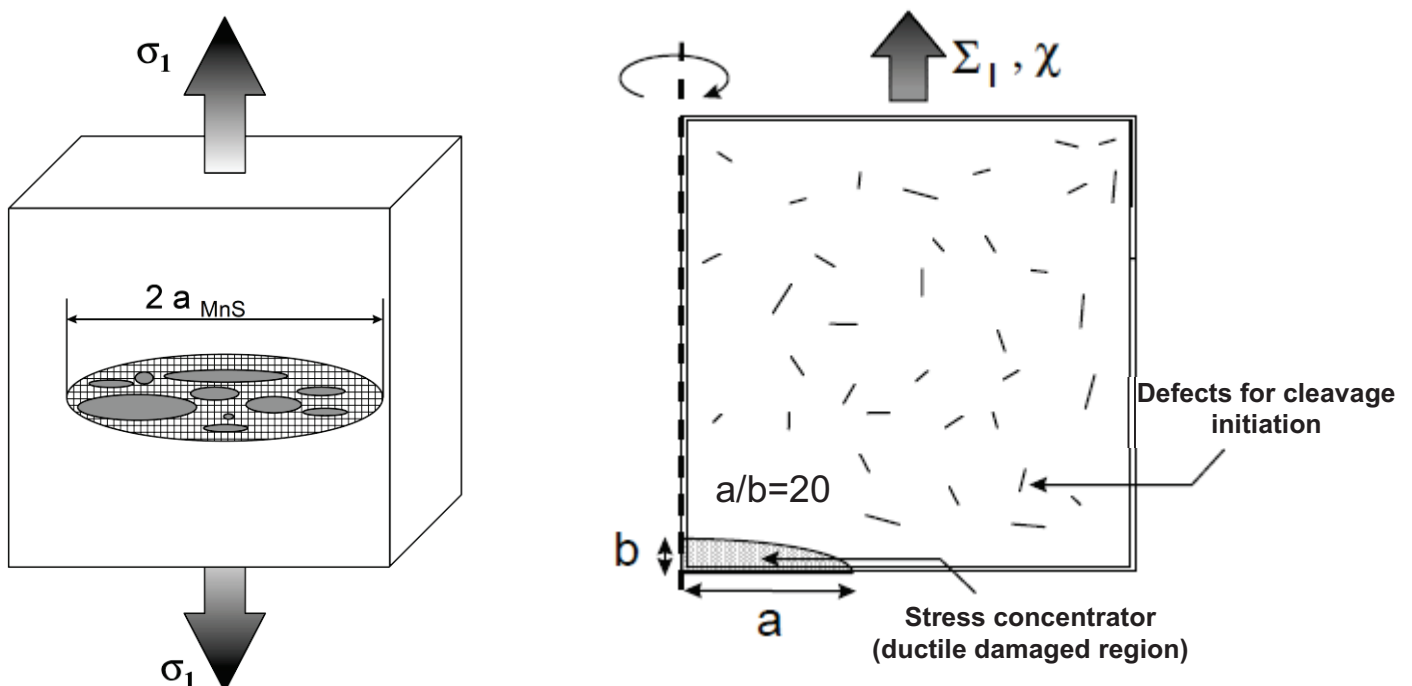


Figure V-1: Effect of MnS particles on the local stress. The area covered by MnS particles was modelled as a ductile crack of radius a . [46]

The axial stress profiles ahead of the ductile crack were plotted for three considered values of crack length, a : 30 μm , 65 μm and 125 μm (Figure V-2). Two values of Σ_1 were chosen: 1500 MPa and 1700 MPa. The value of 1500 MPa corresponded to the onset of yielding at the notch root, and the stress concentration was more pronounced for larger ductile cracks. On the contrary, for $\Sigma_1 = 1700$ MPa the ductile notch tip readily blunted, and the stress concentration, which covered a larger region, was less affected by the ductile crack size, a . In that case the local axial stress was increased by up to around 30% with respect to its macroscopic value because of the presence of the ductile crack.

Unfortunately, the stress concentration induced by the presence of the ductile crack was not reported concerning the radial stress with is responsible (in our case) for delamination occurrence.

To predict the occurrence of brittle out-of-plane cracking for the investigated steels, a first analysis was done on quasi-static loading with tensile tests on notched specimens. The macroscopic critical stress criterion, chosen as a first approach was thus improved. A final analysis was then carried out on Charpy specimens under impact loading.

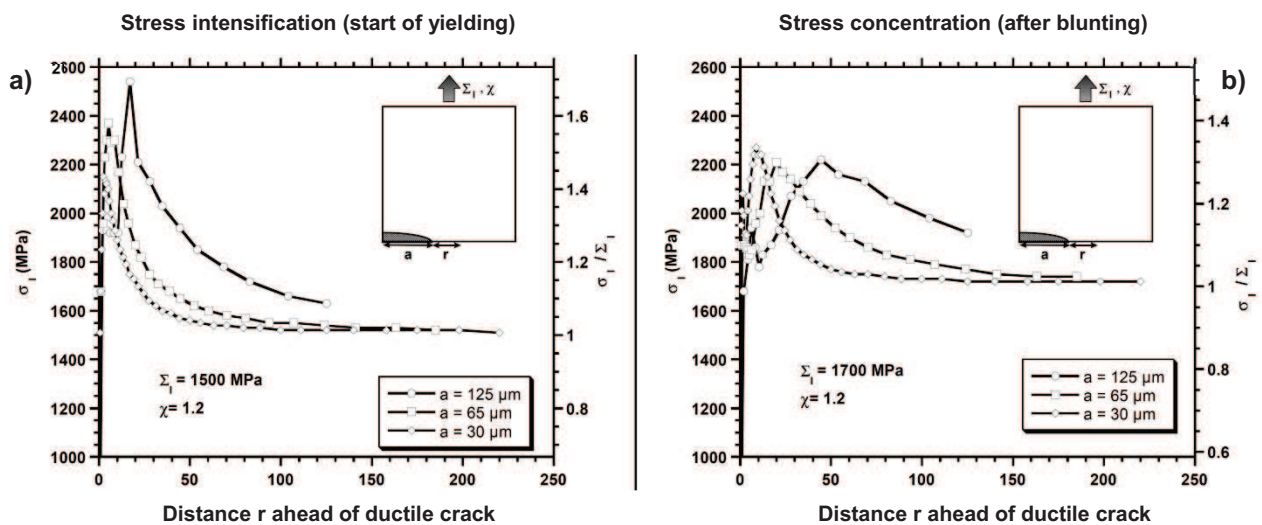


Figure V-2: Evolution of the axial stress generated by the presence of a ductile crack. For the lower remote axial stress (1500 MPa), the stress concentration increases with the crack size. For the higher remote axial stress (1700 MPa), stress concentration is less affected by the crack size. [46]

V.2. Prediction of the onset of brittle out-of-plane cracking during quasi-static tensile tests on notched specimens

The study of criteria for the prediction of brittle out-of-plane cracking was firstly done on notched specimens tensile loaded under quasi-static regime. Numerical analysis of this loading mode was easier compared to that of impact tests. Another advantage of analyzing tensile specimens was the fact that the longitudinal displacement at delamination event could easily be determined, since a sharp drop in load was noticed on the macroscopic curves (see chapter III). Since delamination occurred prior to BTF and since BTF was less pronounced on tensile specimens than on Charpy specimens, the methodology of determination of a criterion for brittle out-plane-cracking was set on the case of delamination. This approach was expected to be also usable for BTF, after taking into account the local stress concentration induced by delamination cracks on the opening stress to fracture along the θ -plane. As a consequence, the stress state along the θ -plane just before delamination occurrence was only tentatively evaluated at the end of this section.

As a first approach, a delamination criterion based on a macroscopic critical stress along ND similar to the one used in [16] was considered. This criterion was then improved so that it could well predict the occurrence of delamination in tensile specimens. This improvement was achieved after

analyzing the role of phenomena such as the presence of a ductile microcrack or texture modification during the test.

V.2.1. Application of the macroscopic critical stress criterion to the prediction of delamination

One specimen (NT1 geometry) of Steel B, taken along TD and which showed a central delamination at -100°C was used for this analysis. Numerical calculations were performed to determine stress states within the specimen. The constitutive equations involving a Barlat yield criterion, identified in chapter IV and appendix C were used to model the tensile test up to the load drop associated to delamination. First, agreement between the global tensile curve experimentally obtained and its prediction by the model was checked (Figure V-3). Then, the local stress inside the specimen was further analyzed. Figure V-4 shows the distribution of the stress along ND at the onset of delamination. The maximal value was found at the center of the specimen.

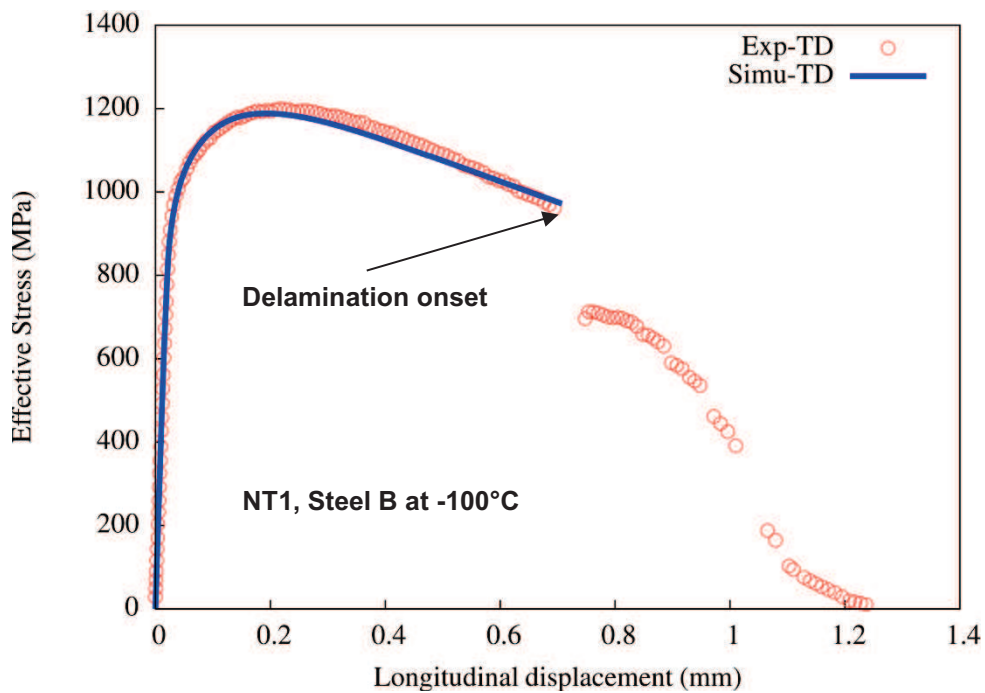


Figure V-3: Experimental and predicted tensile curves on NT1 specimen of Steel B taken along TD at -100°C . Numerical simulation was performed up to the delamination onset with Barlat yield criterion in constitutive equations.

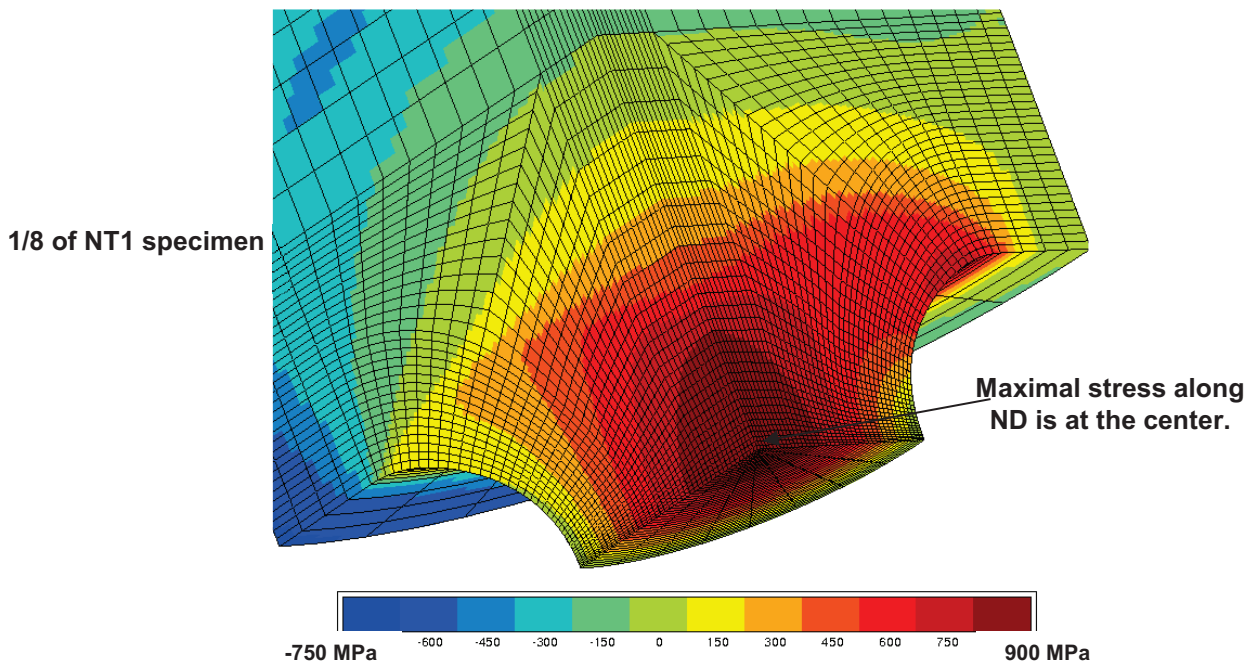


Figure V-4: Distribution of the stress along ND at the onset of delamination. Maximal stress was found at the center of the specimen.

Since the maximal stress along ND at the onset of delamination was found at the center of the specimen, the evolutions of the axial stress (along TD) and of the radial stress (along ND) were then analyzed at the center of the specimen. Figure V-5 shows how the axial and the radial stresses at the center of the specimen evolved up to delamination. In contradiction to the axial stress at the center which gradually increases during the test, the radial stress saturates after 0.35 mm of longitudinal displacement. The axial stress along TD at the onset of delamination was found around 2200 MPa and the radial stress along ND around 1050 MPa.

According to tensile tests performed along ND on NT2 specimen geometry at -196°C , where full cleavage fracture was observed, a critical cleavage stress along ND of 2200 MPa was expected. Therefore, by applying a macroscopic critical stress criterion as suggested in [16] for delamination onset, the specimen of this analysis should not have exhibited any central delamination crack at that stage of the test. Actually, the radial stress calculated at the onset of delamination is less than one half of the expected critical stress. Moreover, saturation of the macroscopic stress along ND after 0.35 mm of longitudinal displacement suggests that other phenomena, which should play an important role in the onset of delamination, might be involved even after saturation of the stress along ND.

Identification of these complementary phenomena and determination of their impact on the occurrence of delamination are the aims of the next sections.

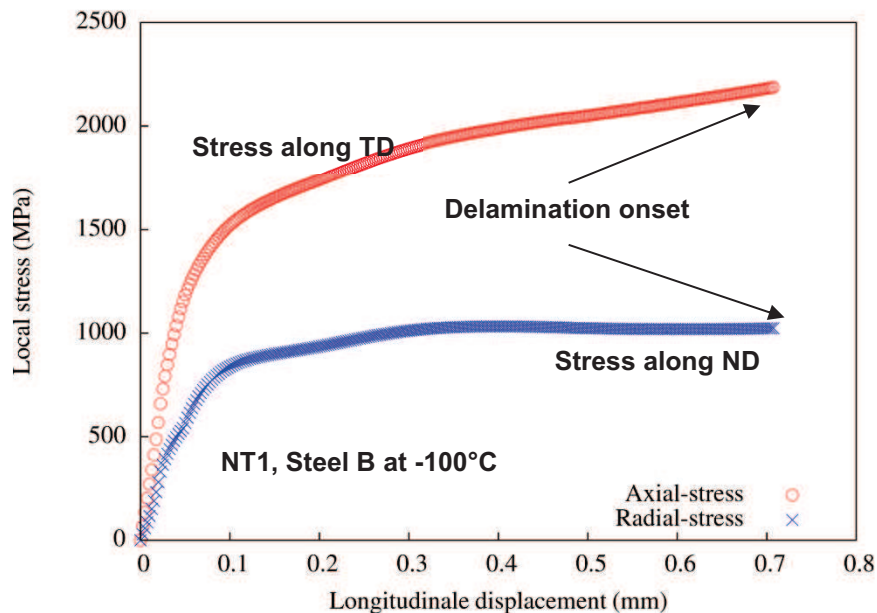


Figure V-5: Evolution of the axial stress (along TD) and of the radial stress (along ND) at specimen center during loading of NT1 specimen at -100°C (Steel B).

V.2.2. Effect of stress triaxiality

The stress triaxiality levels at the center of NT2 and NT1 specimens calculated with Barlat yield criterion were 1.6 and 1.4 respectively at the onset of fracture. On the one hand, critical cleavage stress along ND was determined for a stress triaxiality of 1.6 (NT2 specimens) and on the other hand the delamination was investigated on NT1 specimens, i.e., for a stress triaxiality around 1.4. Therefore an effect of stress triaxiality (in addition to that of a stress normal to ND) could be imagined.

To determine whether, or not, stress triaxiality has a significant (first-order) effect on the occurrence of delamination, experimental results of tensile tests along TD on NT1 specimens and NT2 specimens at -100°C were analyzed. This analysis was carried out for Steel A, where some tensile tests along TD were also performed on NT2 specimens. As a consequence, direct comparison between the two specimen geometries could be made. The macroscopic stresses along ND determined at the onset of delamination for NT1 and NT2 geometries were respectively 1050 MPa and 1000 MPa.

Therefore, stress triaxiality does not seem to significantly affect the delamination occurrence at least at first sight. Nevertheless, higher stress triaxiality is generally associated to easier propagation of ductile cracks and ductile cracking was actually observed close to the initiation point of delamination cracks. As such, the next step was to analyze the effect of that ductile crack on the local stress state at the onset of delamination.

V.2.3. Effect of the ductile crack on the stress state at the onset of delamination

A critical stress criterion for cleavage crack initiation, as determined in the previous section, does not consider the increase in local stress caused by the presence of a ductile crack at the center of the specimen. Yet delamination was found to initiate from a ductile crack as presented in chapter III. Concerning the NT1 specimen of Steel B tested along TD at -100°C , where the delamination criterion was applied in previous sections, a ductile crack of around $120\ \mu\text{m}$ in size was observed at the delamination crack initiation site (Figure V-6). Analysis of the local stress state near that ductile crack is necessary to investigate whether or not prior ductile cracking has a first-order effect on delamination conditions.

A first approach might consist in coupling the previous elastic-plastic constitutive model with a ductile damage model (such as that of Gurson-Tvergaard-Needleman, GTN), so that the evolution of the ductile crack could be intrinsically taken into account and therefore the local stress state could be accurately determined. The second possible approach is similar to the one used in [46], where an oblate elliptical notch representative of the ductile crack was inserted at the center of the NT specimen. The advantage of the first approach is its robustness, since the development of ductile cracking all along the test may be described. However, because of the small size of the ductile crack in investigated NT specimens, a very fine mesh size should be used, and an analysis with a ductile damage model such as GTN, which is element size dependent, would have been very time consuming for parameter identification and final calculations. This first approach should be more appropriate for DWTT or Charpy tests where ductile crack advance is more significant. It is thus reported at the end of this chapter. The most significant drawback of the second approach is the fact that the elliptical notch is inserted from the beginning of the test, even if the ductile crack is not expected to initiate from the very beginning of the test. Moreover, there are some issues to set the initial dimension of the elliptic notch. Nevertheless, the second approach was tentatively used in the present study because it is less time consuming compared to the first approach and because only first-order effects were searched for.

To investigate the effect of the ductile crack, a first (reference) calculation was done on a specimen without any internal elliptical notch. As will be explained below, only axisymmetric calculations were conducted for the internal notch-bearing specimens. Consequently, constitutive equations involving a von Mises yield criterion, determined in chapter IV were used in this part to preserve symmetry of the problem. This calculation was done on Zset software, with a 3D mesh already available for internal notch-free specimens.

The second calculation was done on a specimen where an oblate elliptical notch was inserted at the center. The initial ratio between the major and minor axes, respectively denoted “a” and “b”, was set to 20 as in [46]. The value of “a” was taken as $120\ \mu\text{m}$ to be representative of the ductile crack length measured using SEM in the considered specimen after fracture. Calculations were performed on Abaqus software because of its available tools for mesh design. Quadratic elements of $1\ \mu\text{m}$ in size were used near the elliptic notch so that the stress state could be finely described. Axisymmetric calculations were performed to keep the processing time to reasonable values (30 min). The same constitutive model as for the internal notch-free specimen was used for Abaqus calculations.

The global tensile curves obtained for both specimens are presented in Figure V-7. The presence of a notch at the center does not significantly affect the load vs. displacement curve. Since delamination was observed at 0.7 mm of longitudinal displacement, the stress analysis was first carried out at this value. However, these preliminary analyses showed that the notch shape after such high displacement was no more representative of the ductile crack because deformation occurred at that notch tip from

the beginning of the test, whereas this internal crack only appears after significant longitudinal displacement in the experiment. Moreover, elements were very heavily deformed. Consequently, the stress analysis was performed for a longitudinal displacement of 0.15 mm, corresponding to the maximal load in the experiment. The stress concentration factor obtained at 0.15 mm could be used at first sight to assess the one expected at the onset of delamination onset. In fact, parametric analyses performed at other values of longitudinal displacement (0.1 mm, 0.2mm, 0.25 mm) led to a difference in the stress concentration factor lower than 10%. Moreover, according to results reported in [46], the stress concentrator factor (at least perpendicularly to the notch plane) was found not to significantly change after blunting.

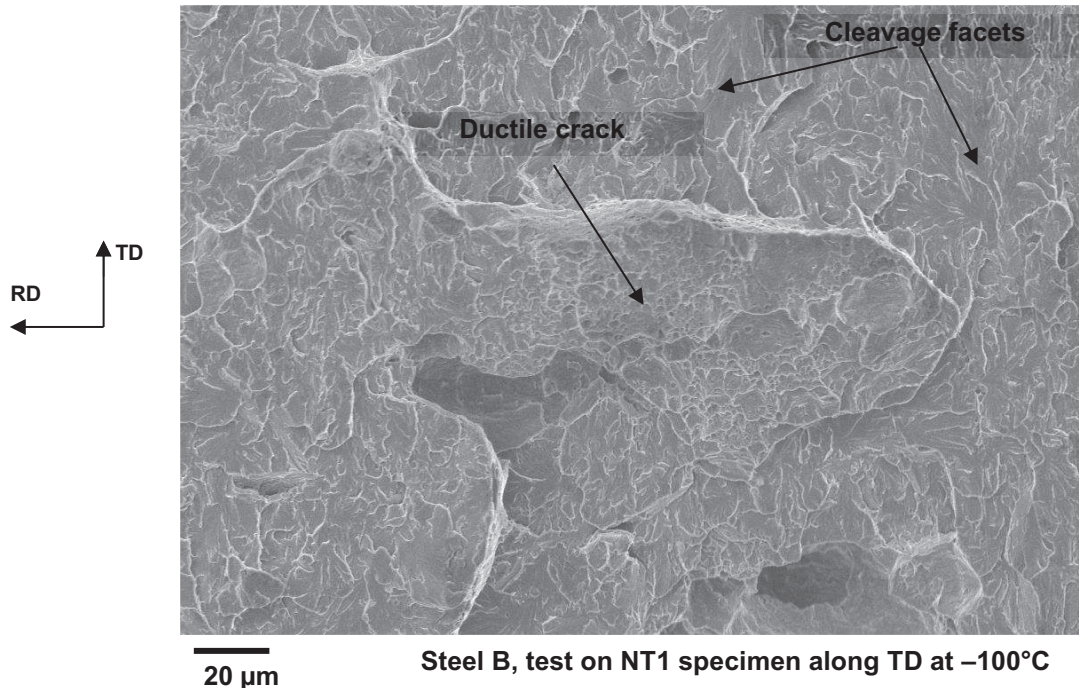


Figure V-6: Fracture surface at the initiation site of a delamination crack. Cleavage initiated from that ductile crack.

The distributions of axial stress (along TD) and of radial stress (along ND) at a displacement of 0.15 mm for the internal notch-free specimen are presented in Figure V-8. The maximal axial and radial stresses, which are found at the center of the specimen, are respectively 1650 and 900 MPa.

The axial and radial stress distributions at macroscopic displacement of 0.15 mm for the specimen with an internal elliptical notch are presented in Figure V-9 and Figure V-10 respectively. The presence of the elliptical notch strongly modifies the stress state near the center, compared to the reference specimen. There is an increase in the local axial and radial stresses over a distance of around 70 μm with a maximum at around 20 μm from the notch tip. The maximal axial stress in that case was 2100 MPa and the maximal radial stress was 1450 MPa. Therefore the presence of the elliptical notch increased the maximal axial stress by around 30%. This result is in good agreement with [46]. Concerning the radial stress, the presence of the elliptical notch increased the maximal value by around 60%. By assuming the fact that the ductile crack acts in the same manner as the modelled elliptical notch, it is obvious that this ductile crack plays a significant role on the onset of delamination, since the local stress along ND could be increased by around 60%.

This significant effect of ductile cracking could also be supported by the fact that the value of the longitudinal displacement at the onset of delamination increased when the test temperature decreased, despite the fact that the macroscopic stress along ND is higher at lower temperatures due to the increase in yield strength (Figure V-11). Even if not apparent on macroscopic curves, the ductile crack probably appears at larger longitudinal displacement when the temperature decreases. The

correlation between ductile cracking retardation and delamination retardation (with decreasing temperature) suggests a strong effect of the ductile crack on the onset of delamination.

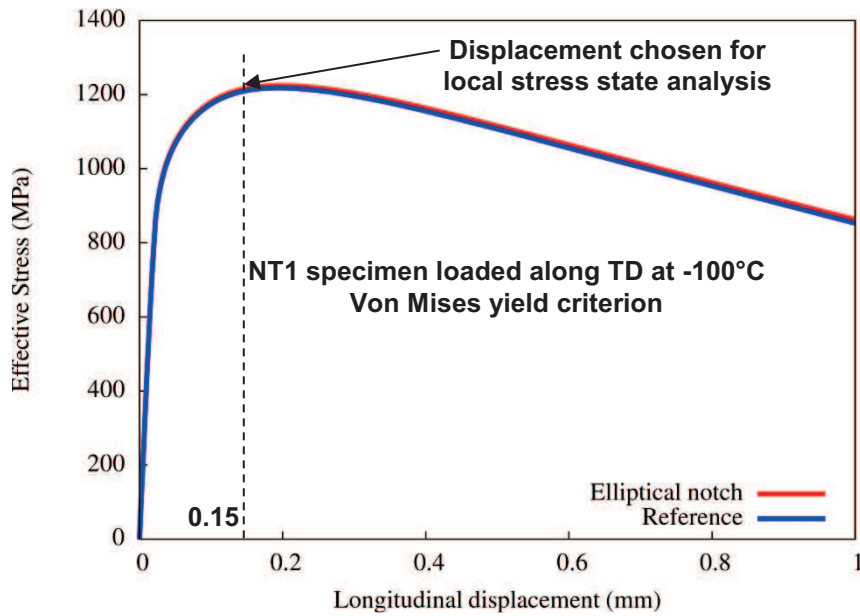


Figure V-7: Effective stress vs. longitudinal displacement curves obtained after numerical calculations on specimens without (Reference) and with an internal elliptical notch.

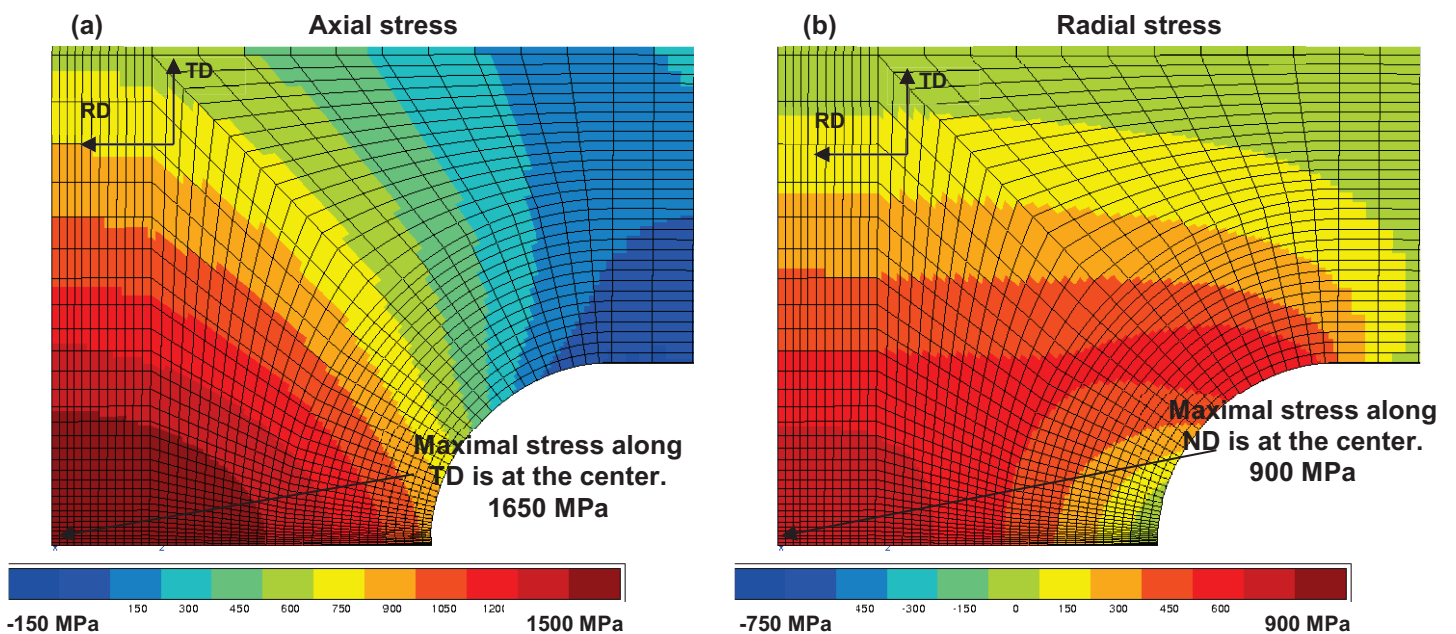


Figure V-8: Distribution of the axial (a) and radial (b) stress in the internal notch-free (i.e., reference) specimen

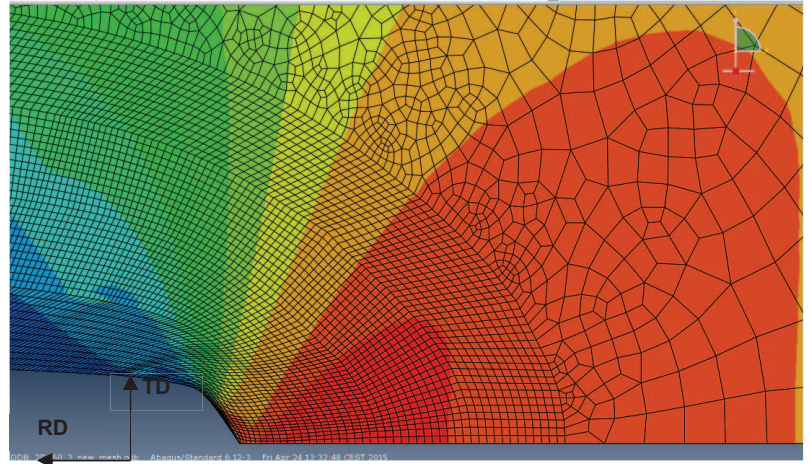
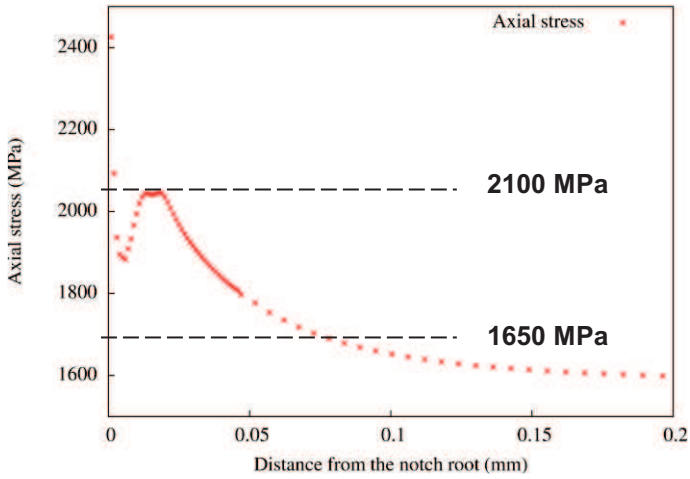
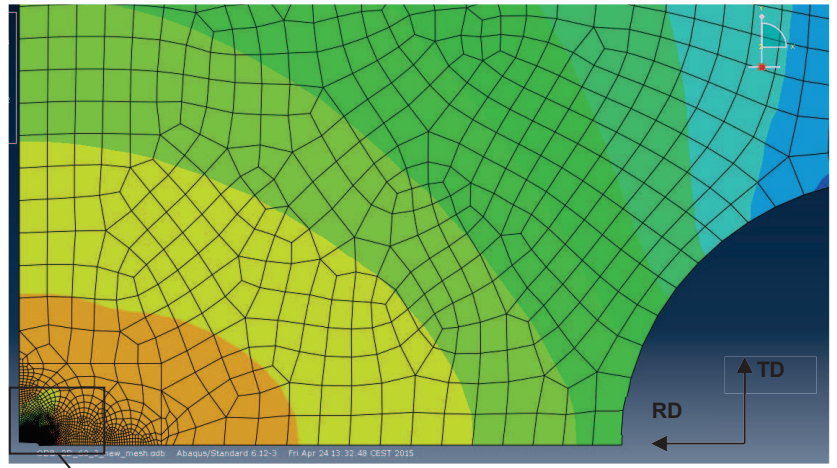
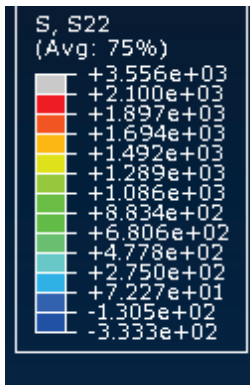


Figure V-9: Distribution of the axial stress in the specimen with an elliptical notch at its center. Evolution of the axial stress along the ligament.

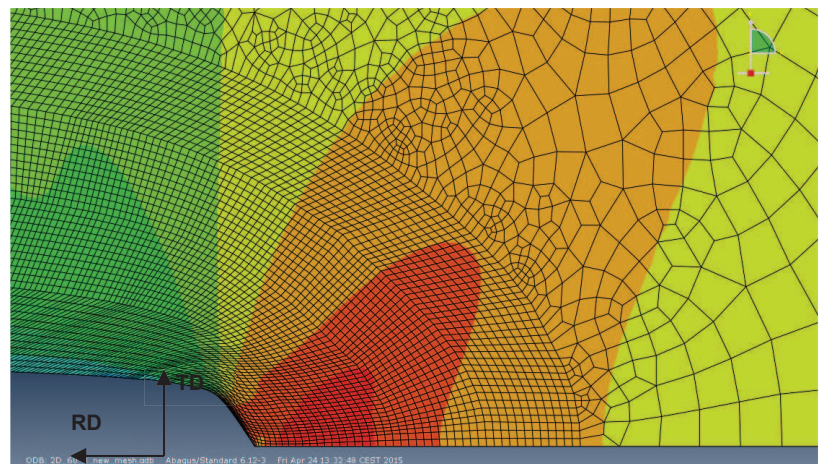
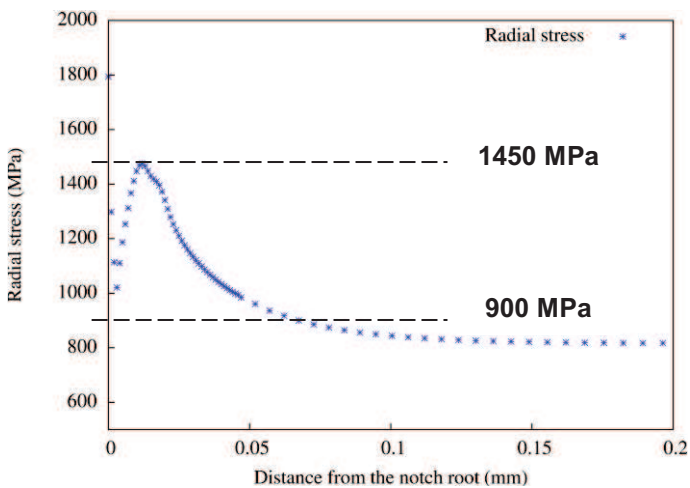
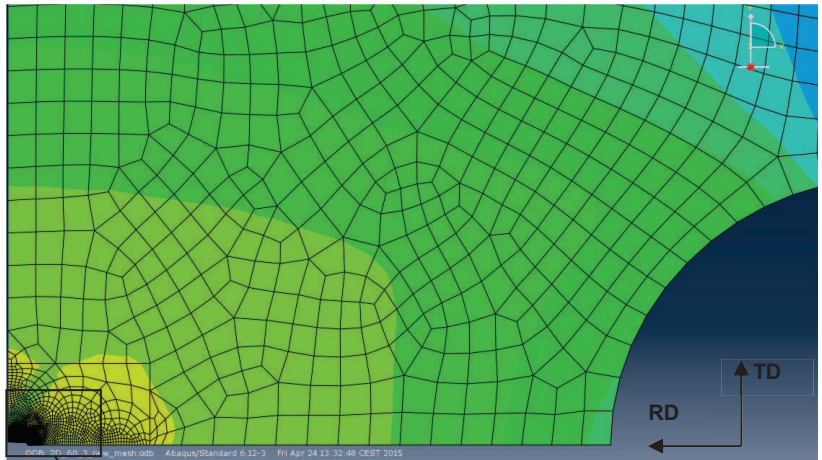
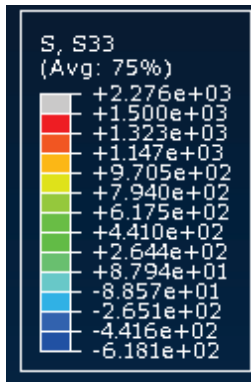


Figure V-10: Distribution of the radial stress in the specimen with an elliptical notch at the center. Evolution of the radial stress along the ligament.

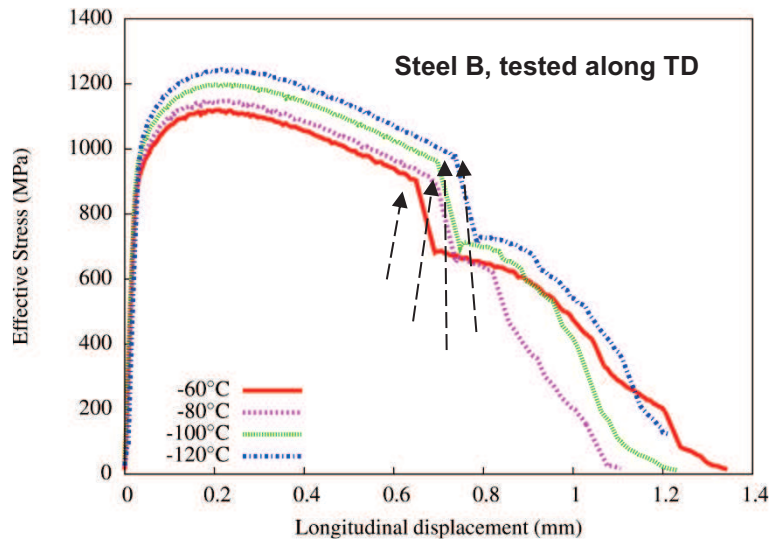


Figure V-11: Global tensile curve on specimens of Steel B taken along TD. The longitudinal displacement value at delamination onset increases when temperature decreases.

Even if it is now obvious that the ductile crack plays a significant role for the initiation of delamination in NT specimens, taking into account the effect of this ductile crack in our previous macroscopic criterion is not enough for accurate numerical prediction of delamination onset. In fact, after increasing by 60 % the macroscopic stress along ND at the center of the specimen, the new estimate of maximal stress along ND at the onset of delamination is 1700 MPa. This value is by 30% lower than expected critical cleavage stress along ND (2200 MPa); therefore, according to that criterion, delamination should still not have happened. Moreover, the ductile crack might also have increased the axial stress by 30%, which corresponds to a new maximal axial stress of 2700 MPa. For such high values of maximal axial stress, flat cleavage fracture could more likely occur from that ductile crack than delamination. Experimentally, it was not the case even at -140°C .

Consequently, another phenomenon should play a significant role on the onset of delamination. This phenomenon might facilitate the delamination criterion to be fulfilled and at the same time prevent flat cleavage occurrence.

V.2.4. Effect of prior plastic deformation on critical cleavage stress

Up to this section, the criterion proposed for delamination onset assumed that critical cleavage stress in a material parameter varying with the loading direction, but not with plastic strain. As a consequence, the anisotropy in critical cleavage stress was not considered to depend on the amount of plastic strain. This explains why critical cleavage stresses determined along the four directions at -196°C (low plastic strain before cleavage fracture) were used for other temperatures to predict delamination occurrence.

In the present study, observations of delamination fracture surfaces showed cleavage facets elongated along the loading direction (Figure V-6), compared to cleavage facets observed after tensile tests along ND at low temperature, which were more equiaxed (chapter III). The cumulative plastic strain estimated by finite element calculations at the center of the NT1 specimen of Steel B tested along TD at -100°C , was 0.5. The principal strains at the center of the specimen were also approximately estimated as 0.5 in axial elongation and 0.25 in radial reduction. It is plausible that the high amount of plastic strain at the center of the specimen could have modified the microtexture and the shape of PCFs. Since the PCF size appears to be correlated with critical cleavage stress (chapter IV), plastic deformation may have modified critical cleavage stresses along each of the four directions of interest. **We can assume the anisotropy in critical cleavage stress to be modified by plastic strain.**

In order to evidence the effect of prior plastic strain on the PCF size distribution, EBSD analyses have been carried out after a slight polish of the delamination fracture surface, after the above

mentioned tensile test on Steel B along TD at -100°C . Because of work-hardening induced by plastic deformation, the quality of diffraction patterns was less good than in the undeformed case. For this reason, only a qualitative investigation of PCFs is presented in Figure V-12. PCFs under the delamination crack seem to be elongated along the loading direction. Moreover, the area occupied by the PCFs seems higher than in the undeformed state. Critical cleavage stress along ND might thus be lower in the deformed state.

To summarize, during the tensile test along TD, plastic strain is expected to decrease critical cleavage stress along ND and to increase critical cleavage stress along TD. This could explain why delamination cracking competes with flat cleavage fracture in the ductile-to-brittle transition in this steel. As such, this could partially explain the predominance of delamination over flat cleavage in the presence of a ductile crack as underlined in the previous section.

The next step is to check whether this decrease in critical cleavage stress in the rolling plane might reach 30%, so that the numerical prediction of delamination could be validated. To this aim, the effect of plastic strain on the critical cleavage fracture stress must be more quantitatively studied, if possible on more homogeneously deformed material. This point is addressed in the first section of chapter VI.

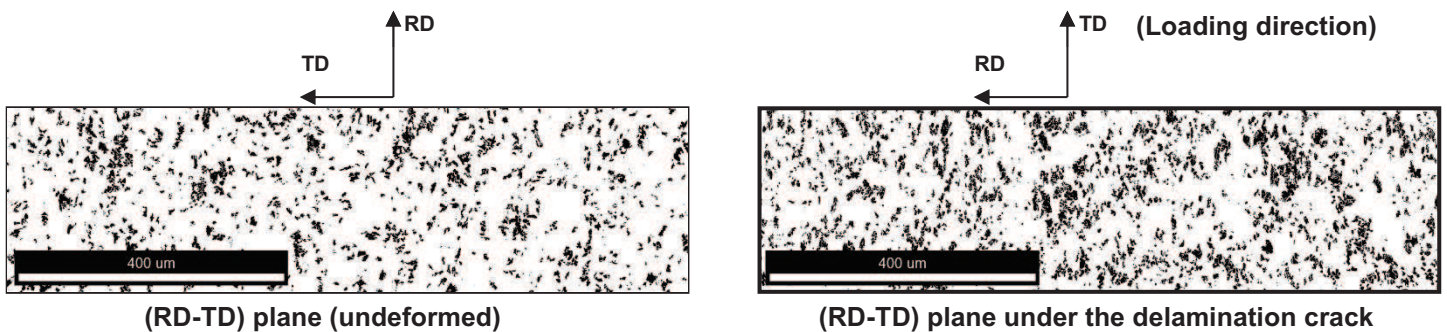


Figure V-12: PCF distribution along the rolling plane in the undeformed state (left) and under the delamination fracture surface after a tensile test along TD. NT1 specimen of Steel B, tested at -100°C .

V.2.5. Discussion of the criterion for numerical prediction of brittle out-of-plane cracking

A macroscopic critical fracture stress criterion was not found to satisfactorily predict the onset of delamination on notched tensile specimens that occurs in the ductile-to-brittle transition domain. In fact, the stress along ND calculated at the onset of delamination was more than 50 % lower than critical cleavage stress determined from brittle cleavage fracture tests perpendicular to ND. In order to improve this criterion, the effect of the ductile crack from which delamination initiates and the effect of large plastic strain at the center of the specimen were investigated.

In numerical simulations, an elliptic notch has been inserted at the center of the notched tensile specimen to be representative of observed ductile cracks. The presence of this elliptical notch increased the local stress along ND by 60%. Despite this increase in the local stress along ND, critical cleavage stress (determined at lower temperatures) was still not reached.

Investigation of the microtexture of the rolling plane at the onset of delamination showed PCFs elongated along the rolling direction and a larger occupied area, compared to the undeformed material. Since critical cleavage stress could be correlated to the area fraction of PCFs, critical cleavage stress along ND is expected to decrease with increasing plastic strain, during tensile tests along TD. Therefore, the evolution of critical cleavage stress with plastic strain has to be included in the delamination criterion.

Even if BTF was not observed on notched specimens of Steel B, we decided to investigate the distribution of stresses perpendicular to BTd at the onset of delamination. This analysis was done on the same NT1 specimen tested at -100°C . A post-processing was performed to obtain the value of the opening stress along BTd. The maximal value was found at the center as was the case for stresses

along ND. The macroscopic stress along BTd at delamination was 1500 MPa without the internal elliptical notch, which is higher than the value of 1050 MPa determined along ND. The presence of an internal elliptical notch was found to increase the maximal stress along BTd by 40%. Therefore the local stress along BTd at the onset of delamination could be around 2200 MPa after taking the internal elliptic notch into account. This value is higher than critical cleavage stress determined along BTd at low temperature (2000 MPa) but BTF was not observed experimentally in that specimen. We can imagine that plastic strain might also affect critical cleavage stress along BTd. In that case, critical cleavage stress might increase when the plastic strain increases, as also expected for TD. As for delamination, a more systematic study on homogeneously deformed material is required to validate this hypothesis.

V.3. Prediction of brittle out-of-plane cracking occurrence during impact tests on Charpy specimens

The aim of this part is to check whether the approach proposed for the prediction of brittle out-of-plane cracking in tensile tests could be applied in the case of Charpy tests. By contrast to tensile tests where the displacement at the onset of delamination could be readily determined experimentally, the hammer displacement at the onset of delamination was more difficult to obtain in Charpy tests. Only delamination observed on Charpy TD-ND or RD-ND specimens could be easily correlated to an abrupt load drop. Therefore, Charpy TD-ND specimens were used to numerically investigate the conditions for the onset of delamination.

This analysis was carried out at -100°C , where significant ductile crack advance was observed before the onset of delamination. Consequently, accurate modeling of the ductile crack advance was of prime importance. As significant ductile cracking occurred prior to delamination, and as the propagation of the ductile crack had to be taken into account, the first approach described in Section V.2.3. was adopted, i.e., continuum damage mechanics was used to predict the ductile crack development during the test. To this aim, a Gurson-Tvergaard-Needleman ductile damage model (referred to as "GTN" hereafter) was coupled to elastic-plastic constitutive equations determined in chapter IV and Appendix C. Among the various criteria tested in this study, the von Mises yield criterion was used after careful selection (see Appendix D). The strain rate dependence was modeled using a power-law (stress exponent 5, reference stress 55 MPa). The complete numerical model selected to analyze Charpy tests is presented in appendix D together with underlying hypotheses and expected limitations.

For Steel A, GTN model parameters were identified on NT2 specimens taken along ND and BTd, and tested at 20°C . For Steel B, a first set of GTN model parameters was identified on NT2 specimens tested at 20°C but did not correctly predict the decrease in load due to ductile cracking in Charpy curves. In fact, further analysis of the ductile fracture surface of notched tensile specimens pulled along ND, BTd and TD and also of Charpy specimens showed pronounced anisotropy of ductile damage and significant differences in dimple populations between tensile and Charpy specimens. More details are reported in Appendix D. Finally, GTN model parameters identified on Steel A were also used for the simulation of ductile crack advance in Charpy specimens of Steel B tested at -100°C .

The GTN model parameters identified on Steel A are presented in Table V-1. Predicted load vs. displacement curves of TD-ND Charpy specimens tested at -100°C are compared with experimental curves in Figure V-13 and Figure V-14 for Steel A and Steel B, respectively. The difference between model predictions and experimental results was expected to be caused by (i) the use of isothermal conditions instead of adiabatic conditions and (ii) the use of a von Mises yield criterion for the elastic-plastic constitutive modeling. The pronounced difference observed for Steel B might also be caused by artifacts on experimental curves as discussed in appendix D. The ductile crack advance was numerically determined for the hammer displacement corresponding to the load drop in the experimental curve. Agreement with experimental observation of the fractured specimen is very satisfactory (see appendix D for more details).

q_1	q_2	f_c	f_F	f_n	ϵ_n	s_n
1.5	1	0.025	0.19	0.005	0.45	0.2

Table V-1: GTN model parameters identified at 20°C on Steel A

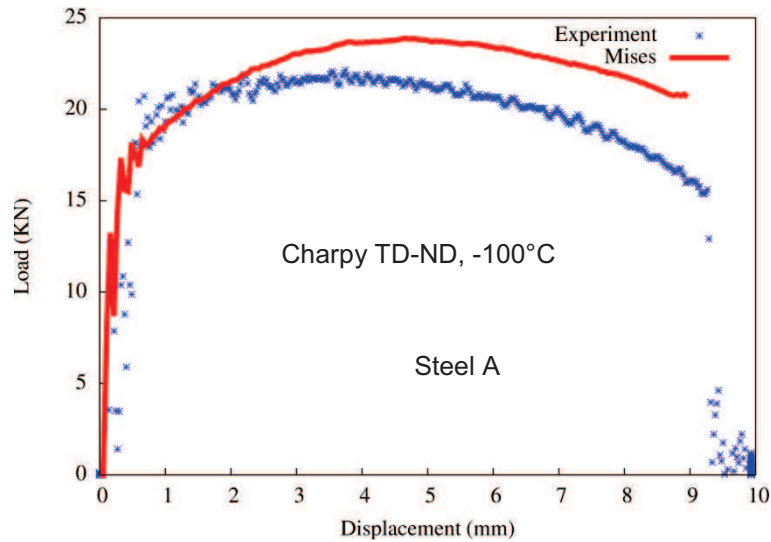


Figure V-13: Charpy TD-ND test on Steel A at -100°C. The numerical simulation overestimates the load

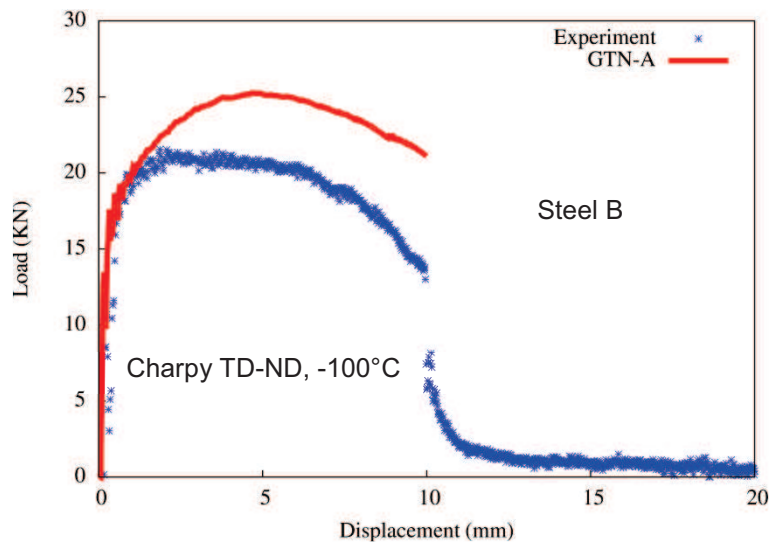


Figure V-14: Charpy TD-ND test on Steel B at -100°C. The numerical simulation overestimates the load

The stresses along ND at the load drop i.e. at the onset of delamination are presented in Figure V-15 and Figure V-16 for Steel A and Steel B respectively. Maximal values of respectively 1620 MPa and 1860 MPa were estimated along ND at that point. Despite the expected overestimation of the stress along ND (by around 20%, see Appendix D) resulting from the choice of a von Mises yield criterion and numerical simulation with isothermal conditions, the stress along ND at the onset of delamination was lower than critical cleavage stress along ND for undeformed materials (respectively, 1800 MPa for Steel A and 2200 for Steel B). Therefore, plastic strain might also affect critical cleavage stress as it was suspected to be the case for notched specimens, since a cumulative plastic strain of around 0.6 was observed in front of the ductile crack. This point is further clarified in the next chapter.

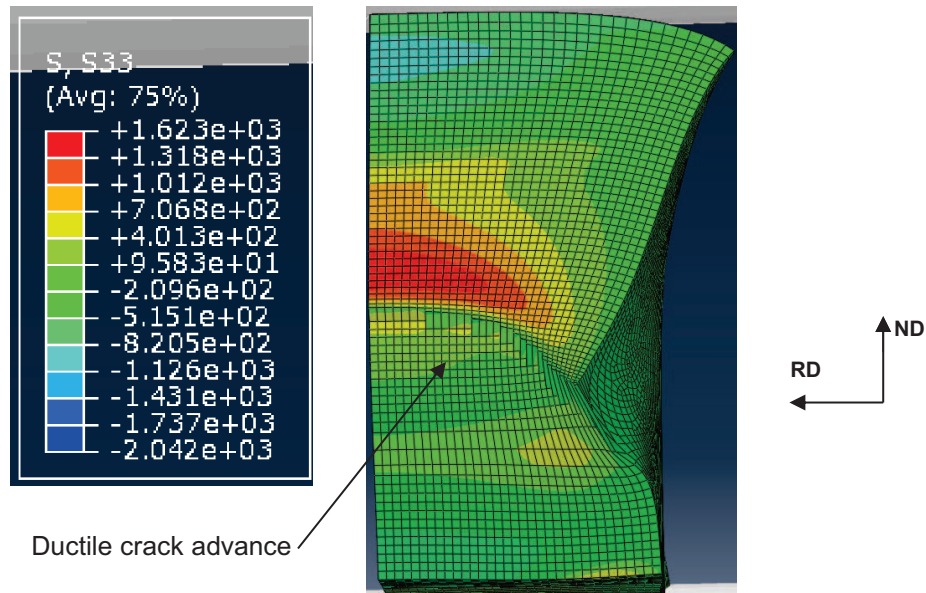


Figure V-15: Stress along ND at the onset of delamination. TD-ND Charpy specimen tested at -100°C. Steel A

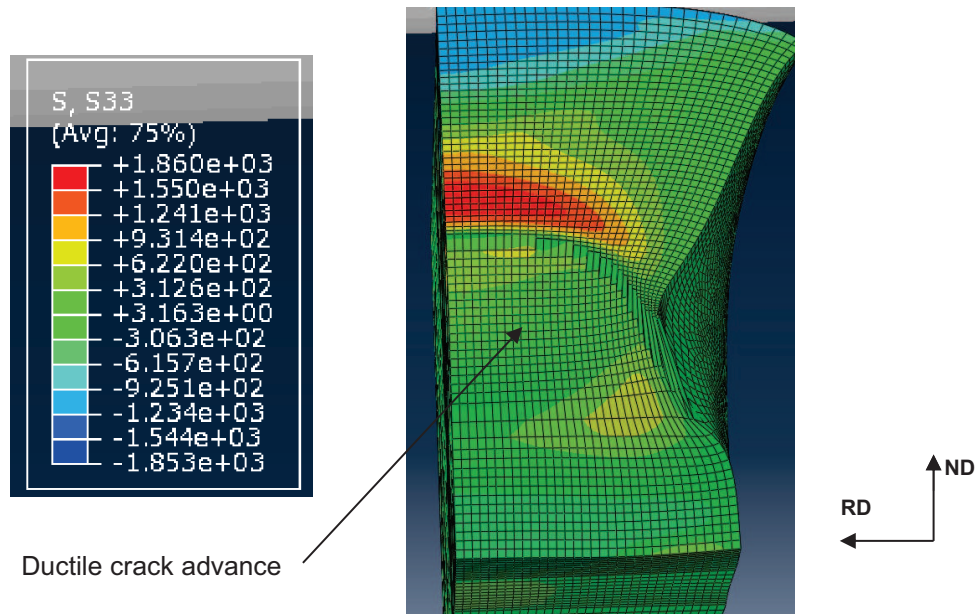


Figure V-16: Stress along ND at the onset of delamination. TD-ND Charpy specimen tested at -100°C. Steel B.

V.4. Conclusions

A critical cleavage stress criterion has been chosen to predict the onset of delamination cracking on NT and Charpy specimens, by assuming that delamination fracture starts as soon as the stress along ND reaches a critical value.

The first analyses performed on NT specimens showed that the stress along ND at the onset of delamination was two times lower than a critical cleavage stress determined from tensile tests along ND at -196°C. To explain the difference between critical cleavage stress and the estimated stress, the effect of the central ductile micro-crack from which delamination initiates was considered. The introduction of a notch at the center of the specimen, which might play the role of the ductile crack, led to an increase of the local stress along ND by around 60%. Therefore the difference between the measured stress along ND and critical cleavage stress along ND was reduced. Nevertheless, this reduction was not enough to validate the criterion. An effect of the plastic strain on critical cleavage stress value was suspected. This hypothesis was supported by the elongated shape of cleavage facets observed on the delamination fracture surface.

A similar approach was used for Charpy specimens. In that case, the local stresses inside the specimens were overestimated because of the numerical model used (von Mises criterion and

isothermal conditions). Nevertheless, the stress along ND at the onset of delamination remained lower than critical cleavage stress estimated from tensile tests at -196°C . Therefore, as for NT specimens critical cleavage stress was also assumed to be affected by plastic deformation. As such, **the critical cleavage stress, and even its anisotropy, might not be an intrinsic material parameter**. This assumption is validated in chapter VI.

Chapter VI – *Application: Study of delamination on pre-strained and on heat treated Steel B*

Table of Contents

VI.1.	Study of delamination on prestrained Steel B (20pct-steel)	113
VI.1.1.	Metallurgical characterization of the 20pct-steel	113
VI.1.2.	Results of Charpy tests on 20pct-steel.....	115
VI.1.3.	Quantitative study of the cleavage sensitivity along (RD-TD) plane of the 20pct-steel ..	116
VI.2.	Sensitivity of Steel B to delamination after a heat-treatment	120
VI.2.1.	Metallurgical characterization of the heat-treated steel.....	120
VI.2.2.	Charpy impact behavior of the heat-treated steel	122
VI.2.3.	Tensile behavior in the ductile to brittle transition domain.....	122
VI.2.4.	Cleavage fracture behavior of the heat-treated steel	124
VI.3.	Conclusions	127

Brittle out-of-plane cracking seems to be related to the initial microtexture anisotropy and to the evolution of the microtexture with plastic deformation, and consequently also critical cleavage stress. To better understand this dependence, heat treatment and pre-straining were separately applied to the as-received steel, so that the modified microstructures could be investigated in terms of critical cleavage stresses.

These exploratory modifications were applied to Steel B, which was properly characterized in previous chapters. The pre-straining step was done by multiple passes cold rolling up to 20% and the heat treatment was done by an austenitization + tempering process.

For both modified steels, the microstructure was first characterized; then, Charpy tests were performed to analyze the new sensitivity to delamination. Tensile tests on smooth and notched specimens were then performed to determine values of critical cleavage stresses. A discussion section is eventually included for each case.

This chapter might be considered as preliminary testing of some ideas in order to open perspectives. Due to time and material restrictions, the number of tests and all the procedure were optimized to perform a limited number of experiments. Therefore, experimental and numerical results were mainly used to interpret phenomena in a qualitative manner.

Résumé

Au vu des chapitres précédents, la rupture fragile hors-plan semble être reliée à l'anisotropie initiale de la microtexture, mais aussi à l'évolution de cette anisotropie microtexturale avec la déformation plastique. Ce dernier chapitre un peu exploratoire, vise à comprendre cette dépendance. Deux pistes de modifications de la microtexture de l'acier B ont été analysées : Une pré-déformation par laminage à froid, afin d'étudier la dépendance de la contrainte critique de clivage envers la déformation plastique. Un traitement thermique avec ré-austenisation, trempe et revenu, afin de supprimer l'anisotropie initiale de la microtexture.

Après pré-déformation de l'acier B par laminage à froid dans la direction TD, l'analyse EBSD du plan de laminage présente des PCF plus larges que dans l'état initial. La rupture par délaminage est plus marquée lors des essais Charpy. La contrainte critique de clivage identifiée à l'aide d'essais de traction sur éprouvettes entaillées est 30% plus faible dans l'acier pré-déformé par rapport à l'acier dans l'état initial. La corrélation entre la taille de PCF et la contrainte critique de clivage établie pour l'acier à l'état initial permet de prédire une grande partie de la diminution de la contrainte critique de clivage après pré-déformation.

Le traitement thermique de trempe et revenu appliqué sur l'acier B a permis de le rendre plus isotrope en microtexture et aussi en contrainte critique de clivage initiale. Aucun délaminage n'a été observé sur les éprouvettes Charpy. Par contre, des fissures secondaires radiales ont été observées sur les éprouvettes de traction entaillées, ce qui suggère l'absence de direction principale pour la propagation du clivage, contrairement à l'acier non traité où le délaminage semble être un mode de fissuration secondaire privilégié.

VI.1. Study of delamination on prestrained Steel B (20pct-steel)

Cleavage facets observed on delamination fracture surfaces of as-received Steel B were elongated along the loading direction. For Charpy specimens, cleavage facets were also elongated at the notch root from where delamination was initiated. This elongated shape of cleavage facets which was assumed to result from the high plastic strain level locally experienced before fracture, was expected to affect the cleavage sensitivity of the rolling plane. The simulation of tensile tests performed on notched specimens pulled along TD revealed a plastic strain level along ND of around 0.2 at the center, from where delamination occurred.

This part aims at investigating the sensitivity to delamination of Steel B modified by prestraining with an amount of strain close to 0.2. Focus was made on the evolution of critical cleavage stress and of the microtexture in the rolling plane after prestraining. One half of a flat API tensile specimen of Steel B was modified by multipass cold rolling. Since the initial tensile specimen was machined along TD, cold rolling could only be performed along TD to pass through geometry limitations. The thickness was reduced from 23 mm to 18 mm, so that a plastic strain around 0.2 could be reached along ND. Only the head of the flat specimen was considered, to avoid heterogeneous plastic strain induced by prior tensile test performed on the gage region. Therefore, the amount of material available for experimental characterization was limited.

This prestrained material, thereafter called “20pct-steel” was metallurgically characterized via light optical observations, hardness measurements and global texture analyses. Then, Charpy tests were performed to investigate its sensitivity to delamination. Finally, the rolling plane was quantitatively investigated in terms of PCFs and critical cleavage stresses.

VI.1.1. Metallurgical characterization of the 20pct-steel

a) Microstructure

The microstructure of the 20pct-steel along the (RD-TD) plane was observed using light optical microscopy after Nital etching (Figure VI-1). Some coarse entities (around 20-30 μm), slightly elongated along TD were observed. These entities look like the elongated entities observed for the as-received material, except that they were elongated along RD in the as-received microstructure.

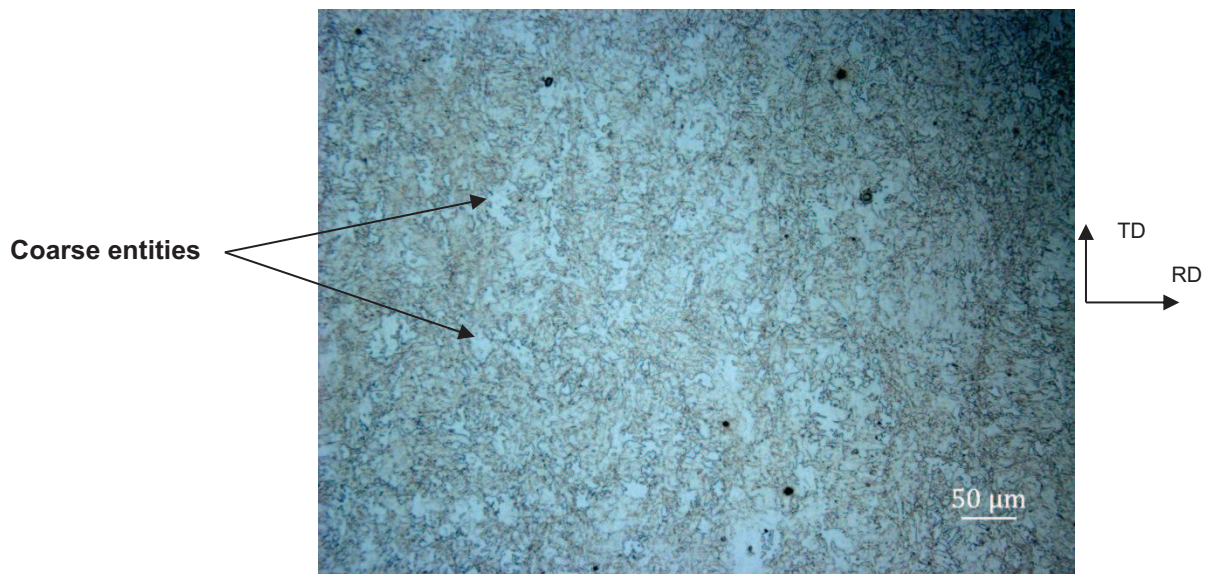


Figure VI-1: Optical observation of 20pct-steel. Some entities slightly elongated along TD are observed as it was the case for the as-received material with elongated entities along RD.

b) Average texture

The orientation distribution function (ODF) sections at $\phi_2 = 45^\circ$ were determined by X-ray diffraction for the 20pct-steel in the same conditions as for the as-received steel (chapter I). The result is presented in Figure VI-2. The 20pct-steel has a relatively stronger average texture than the as-received steel, with a more pronounced γ fiber. The rotated cube component, which is known to be stable during cold rolling, is still present in the 20pct-steel as expected and represents the maximum value of the ODF section. Note that this orientation is favourable to cleavage fracture along the rolling plane.

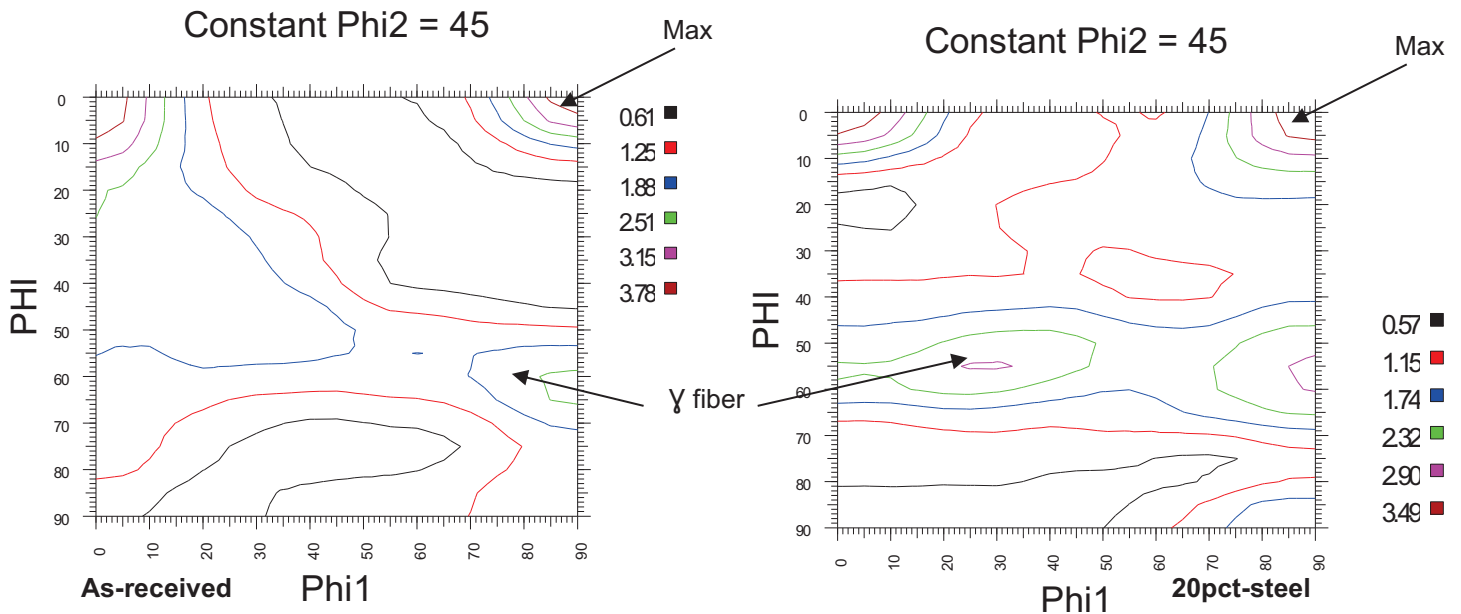


Figure VI-2: ODF section ($\phi_2 = 45^\circ$) of as-received steel (left) and 20pct-steel (right)

c) Hardness

The hardness evolution across the thickness of the steel plates has been measured within the (TD-ND) plane, using the same procedure as for the as-received steel (Figure VI-3). The hardness was initially homogenous across the thickness for the as-received material but became more heterogeneous after cold rolling. The average values of hardness are respectively $HV_{0.3} = 220 \pm 10$ and $HV_{0.3} = 260 \pm 20$ for the as-received steel and 20pct-steel. Therefore, the strength was expected to increase after cold rolling.

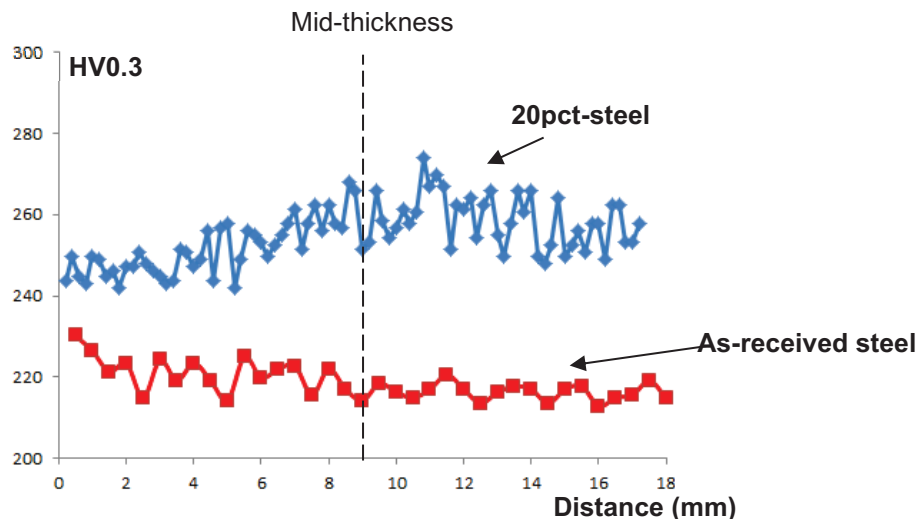


Figure VI-3: Hardness evolution across the thickness of 20pct-steel and as-received steel

VI.1.2. Results of Charpy tests on 20pct-steel

Only three (TD-RD) Charpy specimens could be machined from available 20pct-steel. Therefore, tests had to be done at one temperature only. In order to analyze how the pre-straining stage affected the sensitivity to delamination, it was necessary to choose a temperature where no delamination was observed in the as-received steel. The value of -60°C was selected, because except for room temperature, it was the highest temperature investigated on the as-received steel in the upper shelf domain without delamination cracking observed.

The data points extracted from these Charpy tests are compared to the energy transition curve obtained for the as-received steel (Figure VI-4). The energy absorbed by specimens taken from the 20pct-steel is considerably lower (by more than 50%) compared to the one absorbed by the as-received steel. First observations of the fracture surface of 20pct-steel revealed pronounced delamination cracks, separated from both sides by ductile cracks. (Figure VI-5).

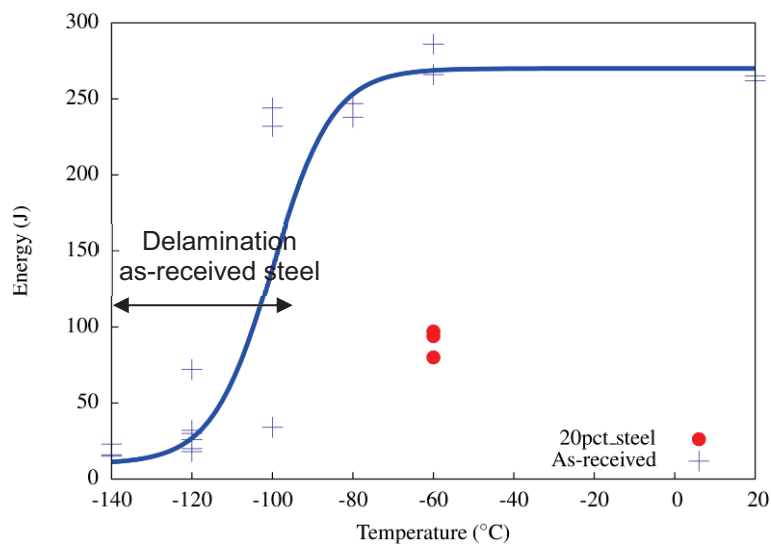


Figure VI-4: Results of Charpy tests on 20pct-steel together with the transition curve of the as-received material

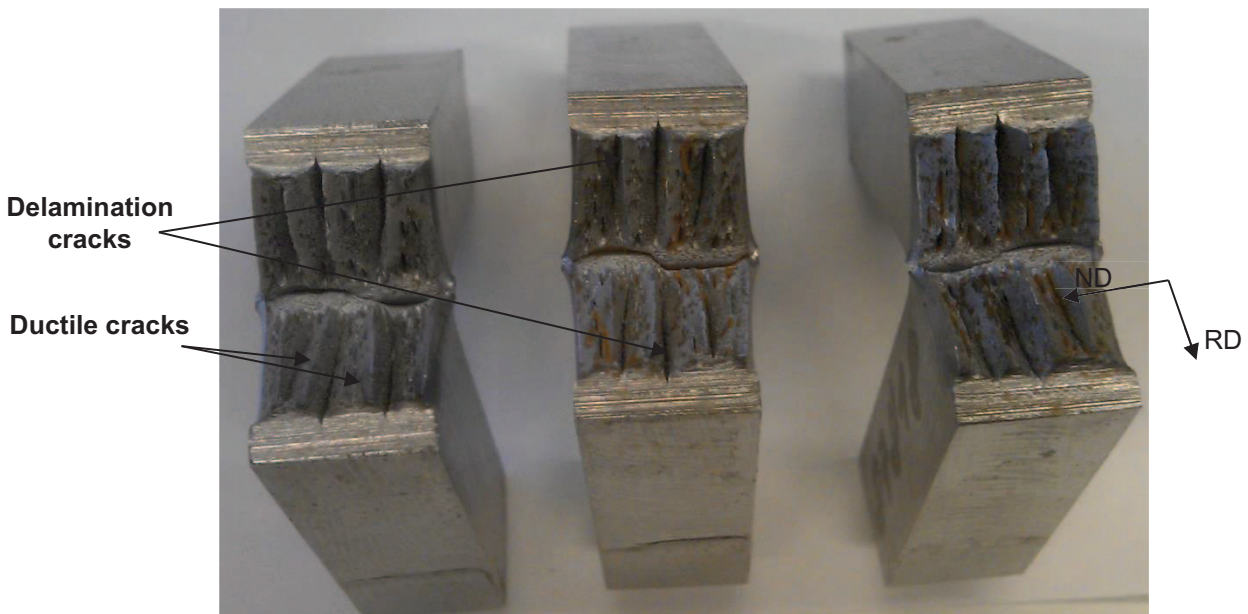


Figure VI-5: Fracture surface of Charpy specimens taken from 20pct-steel at -60°C . Pronounced delamination cracks were observed

Therefore, the prestraining step made 20pct-steel more sensitive to delamination cracking even for temperatures within the upper shelf domain of the as-received material. These delamination cracks, initiated at the notch root, deteriorate the impact toughness by strongly decreasing the absorbed energy. One part of the pronounced delamination sensitivity could be explained by the higher stress state within 20pct-steel for a given temperature, compared to the as-received steel. Nevertheless, the increase in yield strength by cold rolling does not account for the observed difference, since the yield strength measured along ND at -60°C on 20pct-steel is close to the one at -80°C for the as-received steel. However, no delamination crack was detected at -80°C in the as-received steel. Therefore, this increase in sensitivity to delamination might be an evolution of the intrinsic sensitivity of the (RD-TD) plane to cleavage fracture due to the pre-straining step. This assumption was thus considered in the analysis of the cleavage cracking behavior.

VI.1.3. Quantitative study of the cleavage sensitivity along (RD-TD) plane of the 20pct-steel

a) Identification of a critical cleavage stress

As was done in chapter IV, a critical cleavage stress was estimated by analyzing the axial stress around the initiation site of notched specimens taken along ND with full cleavage fracture surface. Only three smooth specimens (UT1) along RD, TD and ND and one NT2 notched specimen along ND were available to model the constitutive behavior. The first test was performed on the NT2 specimen at -60°C , leading to full cleavage fracture. Then, tests on UT specimens were performed at the same temperature to complete the experimental database. Because of the low amount of experimental data, a Barlat yield criterion could not be properly identified as it was the case for the as-received steel. Therefore, a Hill yield criterion was chosen to describe the plastic strength anisotropy. A Voce equation was chosen to describe the evolution of the plastic strain hardening. Studies on the as-received material showed that the axial stress estimated at the center of the specimen was underestimated by around 8% compared to that estimated using a Barlat yield criterion. Although cold rolling has modified the texture and consequently the plastic anisotropy of the material, the same error (underestimate by 8%) will also be assumed in the case of the 20pct-steel.

The engineering tensile stress-strain curves of smooth specimens taken along RD, TD and ND are presented in Figure VI-6. Cold rolling drastically decreased the uniform elongation of the steel. For the three directions, as soon as macroscopic plastic yielding starts, the maximal stress is reached and strain localization takes place. The yield strength is the lowest for the tensile test along ND. The identified parameters of the constitutive equations are presented in Table VI-1.

After simulation of the tensile test on the notched specimen with the identified model, a critical cleavage stress of 1600 ± 50 MPa was estimated. The plastic strain at cleavage onset was similar to the one estimated from as-received steel at -196°C (0.01). If we consider the fact that using a Hill yield criterion underestimates the axial stress at the center by around 8% compared to the usage of a Barlat criterion, critical cleavage stress along ND of 20pct-steel could range between 1550 and 1750 MPa. This value is around 30% lower than the value estimated for the as-received steel along the same direction (2200 MPa).

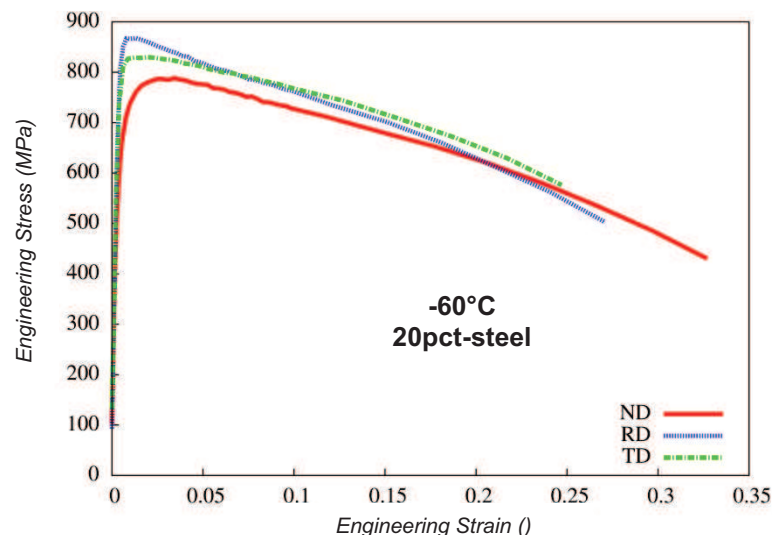


Figure VI-6: Tensile curves at -60°C along ND, RD, TD of the 20pct-steel

	σ_0 (MPa)	H (MPa)	b	Q (MPa)	h_1	h_2	h_3	h_4	h_5	h_6
20pct-steel (-60°C)	730	400	500	120	0.82	0.974	1.282	0.878	1.037	1.577
As-received steel (-80°C)	608	682	26	180	1.022	0.986	1.033	0.878	1.037	1.577

Table VI-1: Parameters of the model identified on 20pct-steel at -60°C with a Hill yield criterion

b) Analysis of the fracture surface of NT2 specimens pulled along ND

Analysis of cleavage fracture surfaces could give an idea of how easy was cleavage crack propagation. First, a macroscopic analysis was done with 3D roughness measurements on fracture surfaces of 20pct-steel and as-received steel which exhibited full cleavage fracture. Finer scale analysis was then carried out with SEM, where cleavage facets were observed (Figure VI-7). The as-received steel has a pronounced fracture surface relief with terraces of hundred micrometers in height, compared to the 20pct-steel which has a macroscopically flatter fracture surface. Moreover, the size of cleavage facets seems to be larger for the 20pct-steel compared to the as-received steel. Analyses of potential cleavage facets were performed to complete the investigation of cleavage sensitivity for the 20pct-steel compared to the as-received steel.

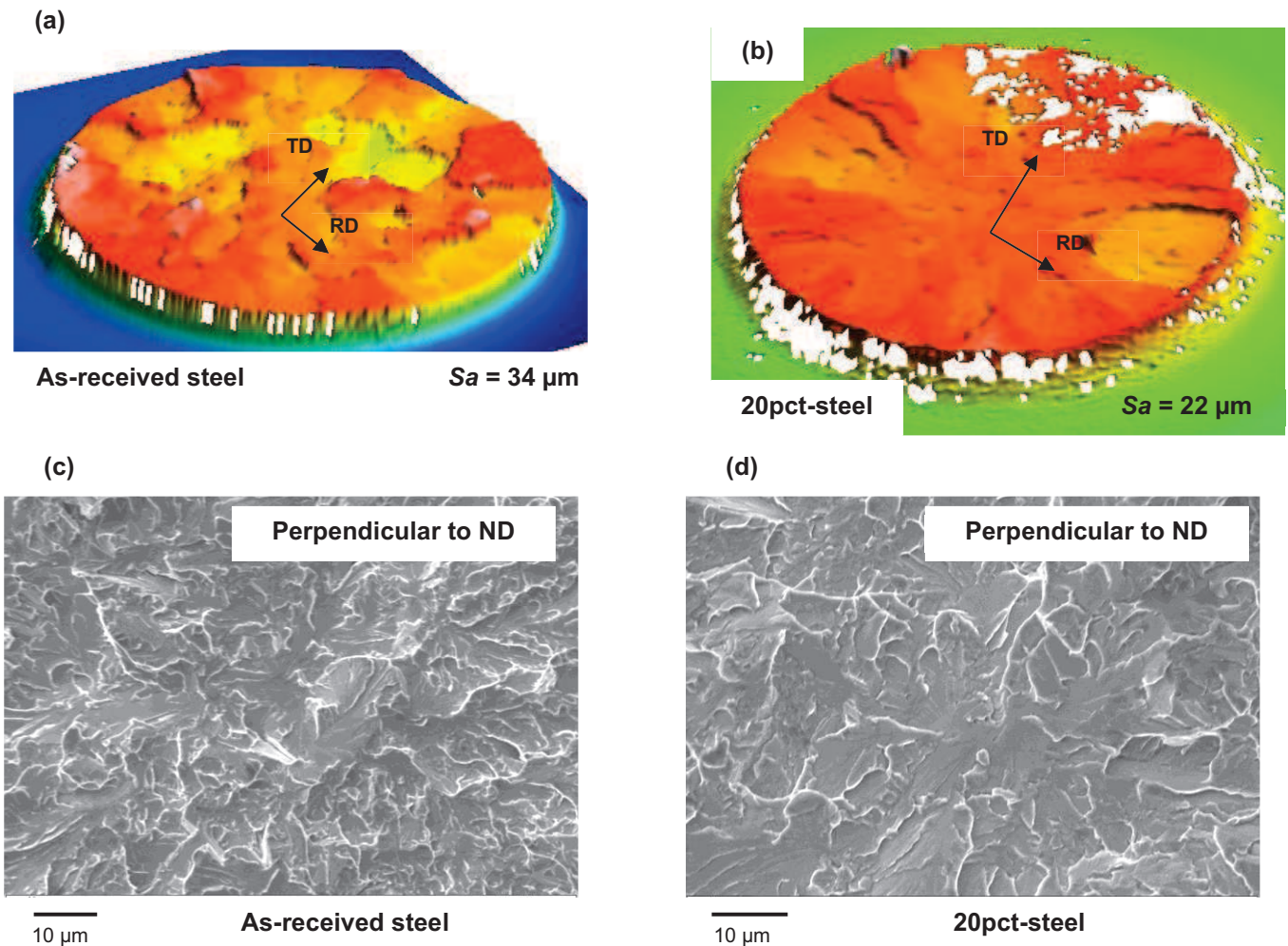


Figure VI-7: 3D roughness analysis on the fracture surfaces of as-received steel (a) and 20pct-steel (b). S_a is the arithmetic roughness parameter. Light colors correspond to higher altitude and dark colors to lower altitude. White color is associated to regions where the measurements are not reliable. SEM observations of the fracture surfaces of as-received steel (c) and of 20pct-steel (d)

c) Effect of prestrain on potential cleavage facets

The size and spatial distribution of PCFs in the as-received steel and 20pct-steel were investigated along the (RD-TD) plane. The procedure presented in chapter IV was applied for this analysis. The spatial and size distributions of potential cleavage facets are presented in Figure VI-8 and Figure VI-9 for the as-received steel and 20pct-steel, respectively. Potential cleavage facets are larger in the 20pct-steel. This could result from the rotation of crystal orientation during cold rolling and/or from the change in morphology of ferrite grains.

Even if the as-received steel and 20pct-steel were intrinsically different, the correlation between PCF size and critical cleavage stress proposed in chapter IV was tentatively applied to the 20pct-steel (Figure VI-10). According to the effective PCF size observed in the 20pct-steel, critical cleavage stress is expected between 1850 and 1900 MPa. This value is larger by around 200 MPa (i.e., by around 10%) than the one determined from tensile tests. Nevertheless, the contribution from the PCF size explains a considerable part of the decrease in critical cleavage stress generated by the pre-straining treatment. To further interpret the discrepancy between predicted and experimental values, complementary effects still have to be investigated. Supplementary tests should be carried out to ensure better statistical significance of the value of cleavage fracture stresses. The application of a probabilistic approach could be a good alternative to really take the entire PCF size distribution into account.

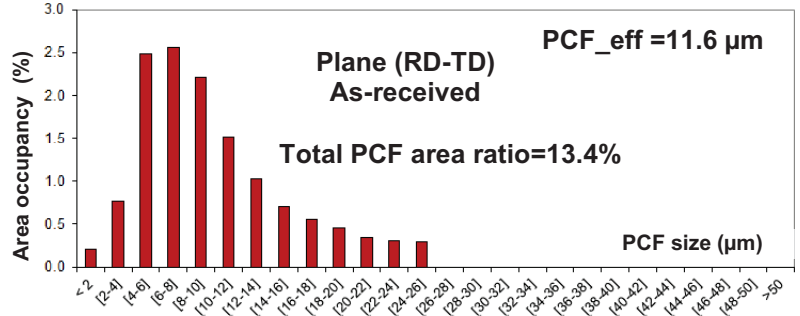
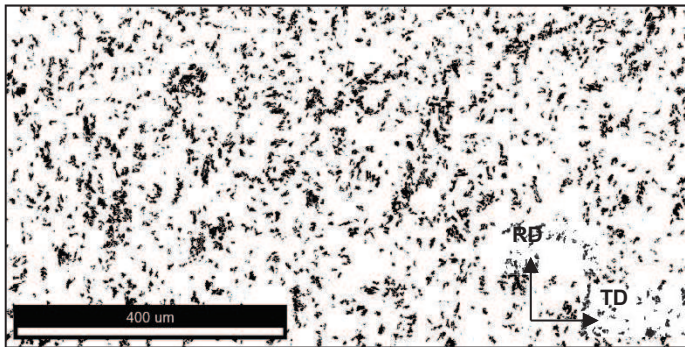


Figure VI-8: Distribution of potential cleavage facets in the (RD-TD) plane for the as-received steel. PCFs are in black.

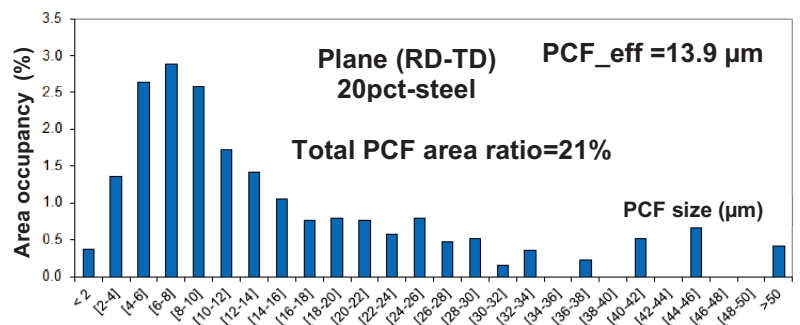
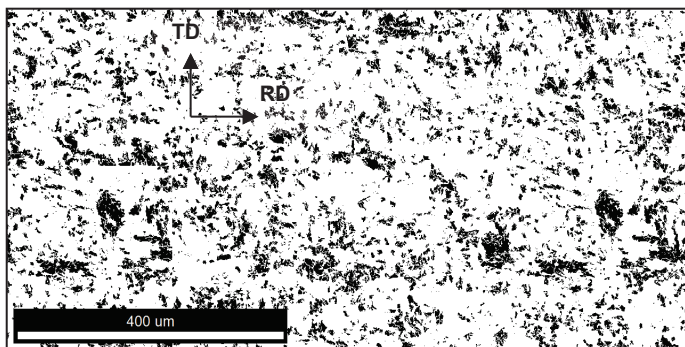


Figure VI-9: Distribution of potential cleavage facets in the (RD-TD) plane for the 20pct-steel. PCFs are in black.

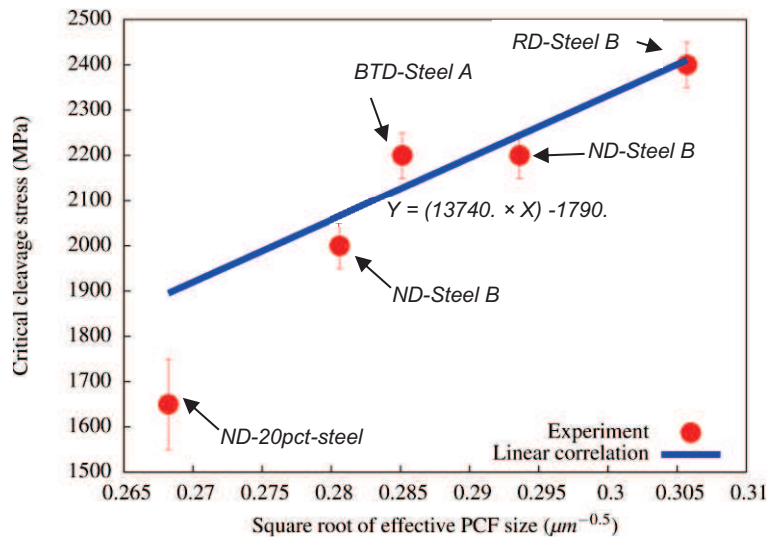


Figure VI-10: Correlation between the critical cleavage stress and the inverse square root of effective PCF size. Predicted critical cleavage stress of 20pct-steel is overestimated by the correlation model.

d) Discussion

By prestraining the as-received steel by 20% cold rolling along TD, the microtexture of the rolling plane was modified and in particular PCFs became larger. This increase in PCF size was correlated to a decrease in critical cleavage fracture stress along ND. The role of work hardening generated during cold rolling on cleavage fracture was not studied. The effect of these dislocations on the decrease in critical cleavage stress should be investigated. Tensile tests along ND after tempering of 20pct-steel could be done, i.e., on a material with the same microtexture as the 20pct-steel but with a dislocation density comparable to that of the as-received steel. By doing so, the effect of strain hardening could be separately studied from that of the change in microtexture.

Pre-straining along TD might also affect the microtexture in the (RD-ND) plane. In that plane, PCF sizes are expected to decrease and if the geometry effect is actually dominant, therefore critical cleavage stress along TD is expected to increase. In other words, prestraining along TD might increase critical cleavage stress along TD. Therefore, it is plausible to assume that when the plastic strain increases, critical cleavage stress along the main loading plane could increase and flat cleavage fracture might be delayed. This result is in agreement with the decrease in critical cleavage stress when temperature decreases. In fact, for a given material, a critical cleavage stress determined at lower temperatures might be lower than another critical cleavage stress determined at higher temperature, probably because at higher temperatures, local plastic strain experienced before cleavage fracture is higher. This explains why critical cleavage stress determined along ND at -100°C for Steel A was assumed to only give an upper limit of the actual value.

Finally, it might be useful to investigate the PCF distribution of 20pct-steel within the θ -plane, so that the evolution of critical cleavage stress along BTB after prestraining could be investigated. From the size of PCFs in the θ -plane after prestraining, a tendency of critical cleavage stress along BTB after prestraining could be estimated.

After modification of the initial microtexture by prestraining which induced dislocations, it was decided to modify the initial microtexture by heat treatment in order to study the occurrence of delamination with minimum difference in dislocation structure with respect to the as-received steel.

VI.2. Sensitivity of Steel B to delamination after a heat-treatment

This part of the study aims at understanding the role of initial critical cleavage stress anisotropy on the occurrence of delamination. To this aim, a heat treatment process was applied on Steel B, so that the initial microtexture anisotropy could be reduced, and consequently, critical cleavage stress could be more isotropic than in the as-received state.

The considered approach was to re-austenitize the steel, so that anisotropy induced by the TMCP process could be (at least partially) removed. After that, the coupon was water quenched to get an isotropic microstructure and finally tempered so that the final hardness could remain similar to that of the as-received steel. A targeted average grain size of around 5 μm was expected to be representative of the initial microstructure of as-received Steel B.

After testing different conditions, the heat treatment eventually used for Steel B is the following: re-heating and austenitizing at 925°C for 30 min, followed by water quenching and a final tempering at 450°C for 1h.

The microstructure was investigated by light optical microscopy and the texture was analyzed to make sure that the initial anisotropy was removed. Then, Charpy tests and tensile tests were performed to evaluate the sensitivity to delamination of the heat-treated steel. Finally, the sensitivity to cleavage fracture was discussed in terms of critical cleavage stresses and size and spatial distributions of potential cleavage facets.

VI.2.1. Metallurgical characterization of the heat-treated steel

a) Microstructure

The (RD-ND) plane microstructure of the heat-treated steel was observed using light optical microscopy after Nital etching and compared to the as-received material (Figure VI-11). Ferrite grains that were initially elongated for the as-received steel became more equiaxed in the heat-treated steel. This suggested that the heat treatment was successful in making the steel more isotropic in terms of microstructure. A similar analysis was done on the average texture.

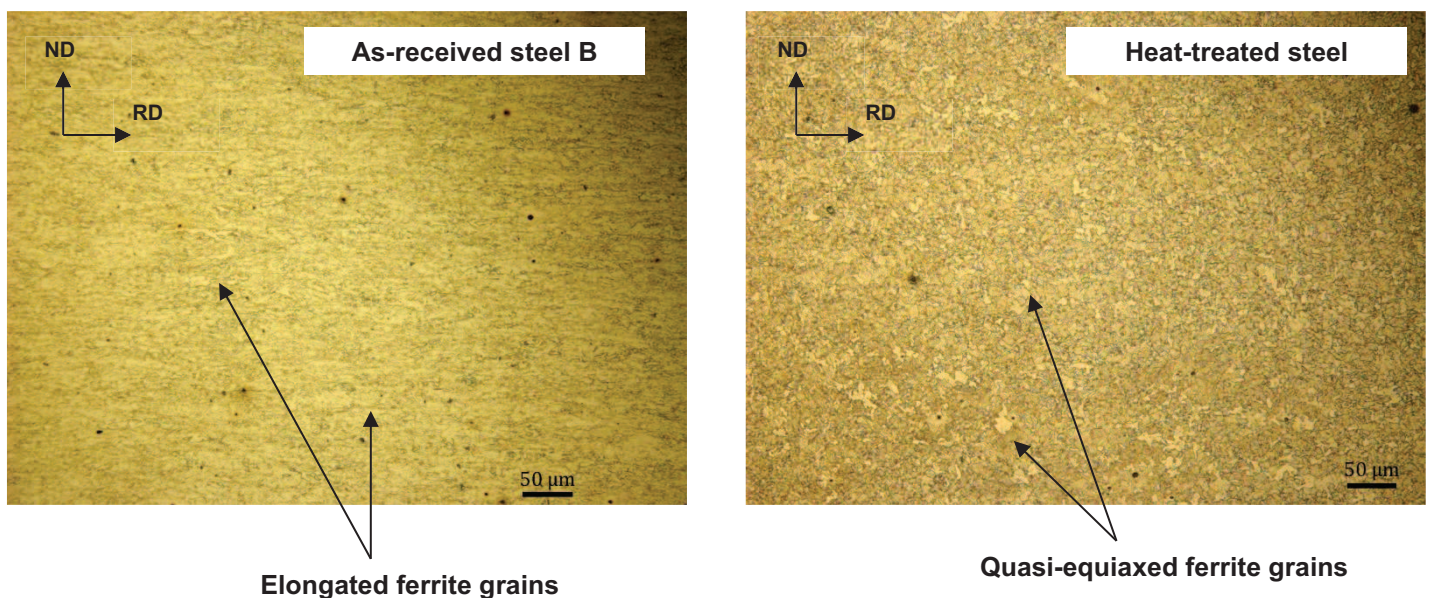


Figure VI-11: Optical micrographs of as-received and heat-treated Steel B in the (RD-ND) plane. The elongated shape of coarse ferrite grains was changed into an equiaxed shape after the heat treatment

b) Average texture

The ODF section at $\varphi_2 = 45^\circ$ was determined by X-ray diffraction for the heat-treated steel as was done for the as-received steel. The result is presented in Figure VI-12. The heat-treatment significantly reduced the average texture of the steel. The γ fibre is more uniform after the heat treatment. More obviously, the rotated cube component (which contributes to PCFs) has disappeared in the heat-treated steel; a slight Goss component, which does not contribute to the sensitivity of the rolling plane to cleavage fracture, has appeared, instead (see the maximum value in corresponding ODF section).

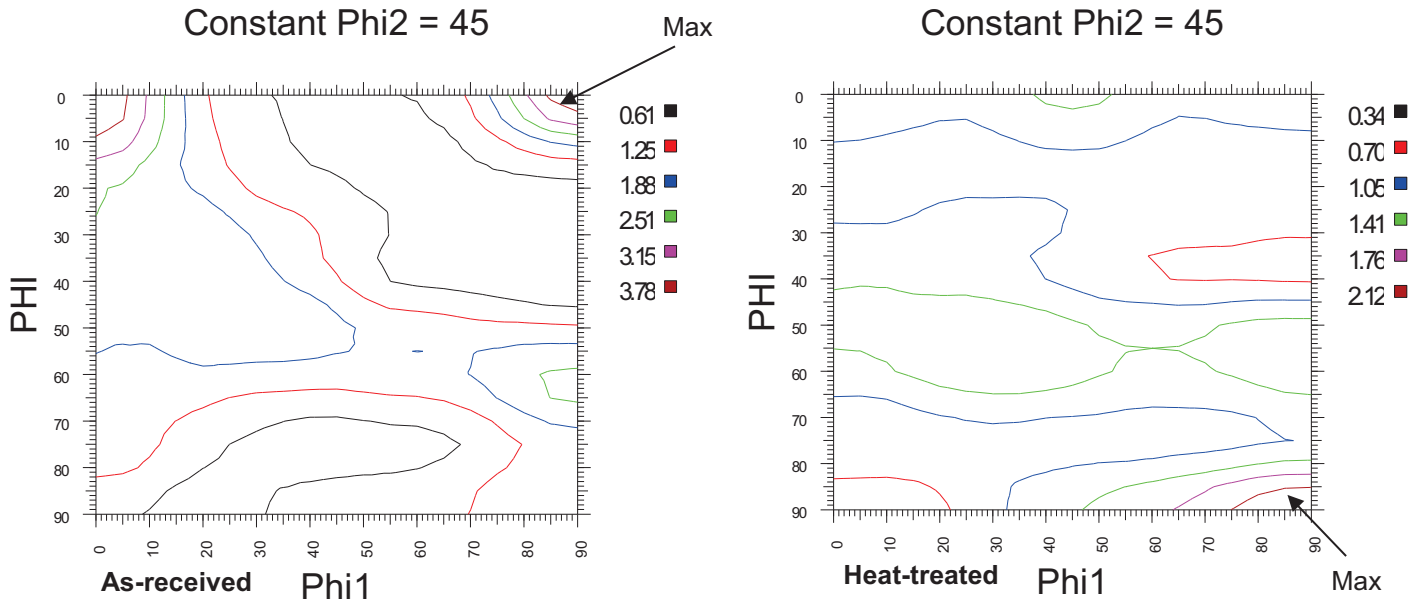


Figure VI-12: ODF section ($\varphi_2 = 45^\circ$) of as-received (left) and heat-treated (right) steels

c) Hardness

The hardness homogeneity across the thickness of the steel plates has been measured in the (TD-ND) plane (Figure VI-13). The hardness is homogenous across the thickness for both steels except near the skins of the heat-treated steel. This might not cause problems since all metallographic and mechanical analyses were done far from the skins. The average values of hardness are respectively $HV_{0.3} = 220 \pm 10$ and $HV_{0.3} = 190 \pm 10$ for the as-received and heat-treated steels. As a consequence, heat-treated Steel B is expected to be slightly softer than as-received Steel B.

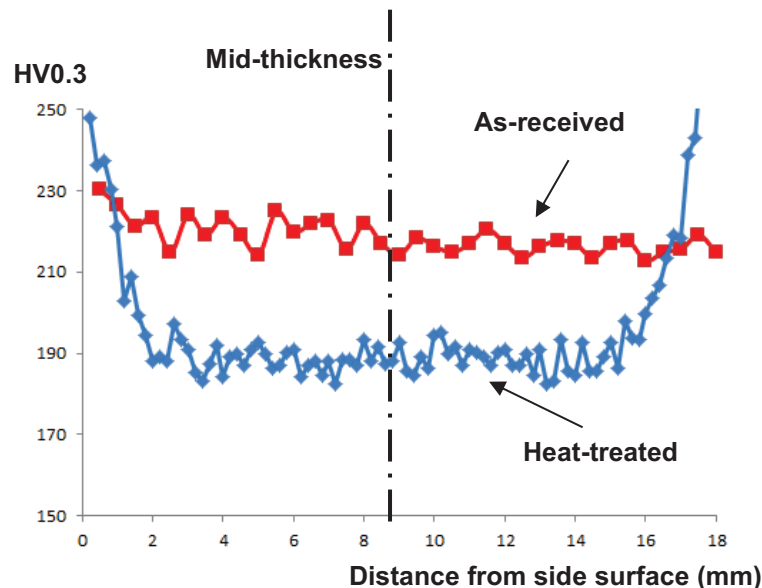


Figure VI-13: Homogenous evolution of hardness across the thickness of as-received and heat-treated steels.

VI.2.2. Charpy impact behavior of the heat-treated steel

Charpy tests were performed on (TD-RD) specimens at -100°C , -120°C and -140°C which were the temperatures where delamination was observed on the as-received steel (Figure VI-14). The lower shelf energy is similar for both steels, i.e., around 20J. The upper shelf energy of the as-received steel is lower by around 50J than that of the heat-treated steel. This result was not expected since the heat treated specimen was supposed to be softer than the as-received material according to hardness measurements. The most important result is that no delamination was observed on the heat-treated specimens, even in their ductile-to-brittle transition domain.

Even if the heat treatment removed the initial texture anisotropy, it also decreased the steel strength and therefore the stress state required to initiate delamination might not be reached before the onset of ductile failure. Complementary analyses were thus done on tensile specimens in the ductile to brittle transition domain, to assess the sensitivity of the heat-treated steel to cleavage cracking along the (RD-TD) plane.

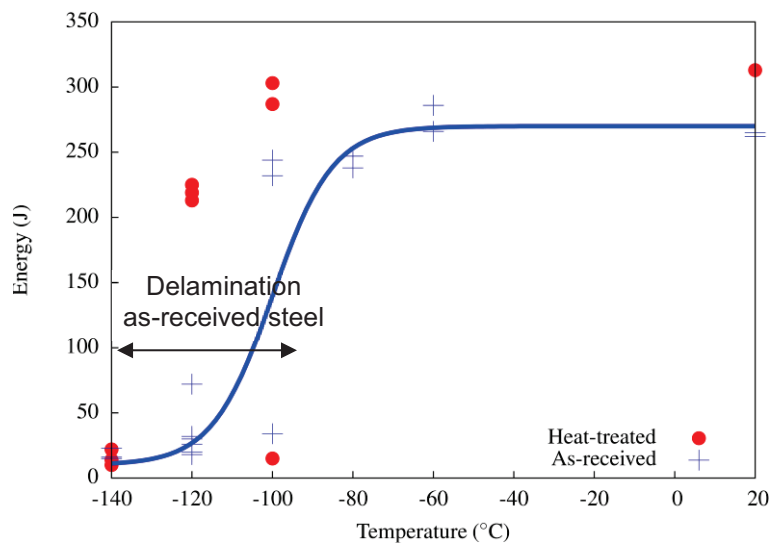


Figure VI-14: Results of Charpy tests on heat-treated Steel B, compared to the transition curve of the as-received material

VI.2.3. Tensile behavior in the ductile to brittle transition domain

Tensile tests on the heat-treated steel were performed in the ductile-to-brittle transition to investigate the occurrence of delamination. On the opposite of Charpy tests where delamination was only observed between -100°C and -140°C in the as-received steel, notched tensile specimens showed a larger range of temperatures where delamination was observed in the as-received steel (-40°C to -140°C). Therefore, the sensitivity of the heat-treated steel to delamination could be investigated within a larger range of temperatures in that case. A first series of tensile tests was performed at -140°C , where pronounced delamination cracks were observed on the as-received steel, so that the sensitivity to delamination could be investigated on the heat-treated steel at this critical temperature. A second series was done at -196°C to determine critical cleavage stresses.

Analysis of tensile tests on smooth specimens showed that the elastic-plastic behavior of the heat-treated steel at -140°C is the same as that of the as-received steel at -100°C (Figure VI-15). As expected from hardness measurements, the as-received steel is thus stronger than the heat-treated steel. This does not explain the increase in upper shelf energy after the heat treatment. The fracture surfaces of NT2 specimens of heat-treated Steel B tested at -140°C along ND, RD and TD are presented in Figure VI-16, Figure VI-17 and Figure VI-18 respectively. For all directions, flat cleavage fracture initiated from a circular ductile crack at the center of the specimen. This fracture mode was also observed on the as-received steel for tests along ND between -100°C and -140°C , but not along

RD and TD. Therefore, planes perpendicular to RD and TD are more sensitive to cleavage in the heat-treated steel than in the as-received steel. Moreover, very small splits were observed along some radii of the NT2 specimen tested along TD. These splits could not be called delamination because they did not propagate preferentially along the rolling plane. This suggested that critical cleavage stress might not vary a lot from one radial direction to another one, so that there is no preferential radial plane for cleavage crack propagation.

Given these differences in cleavage fracture between as-received and heat-treated Steel B, the intrinsic sensitivity to cleavage of planes perpendicular to ND, RD and TD was further studied in the heat-treated steel via tensile tests at -196°C and PCF analyses.

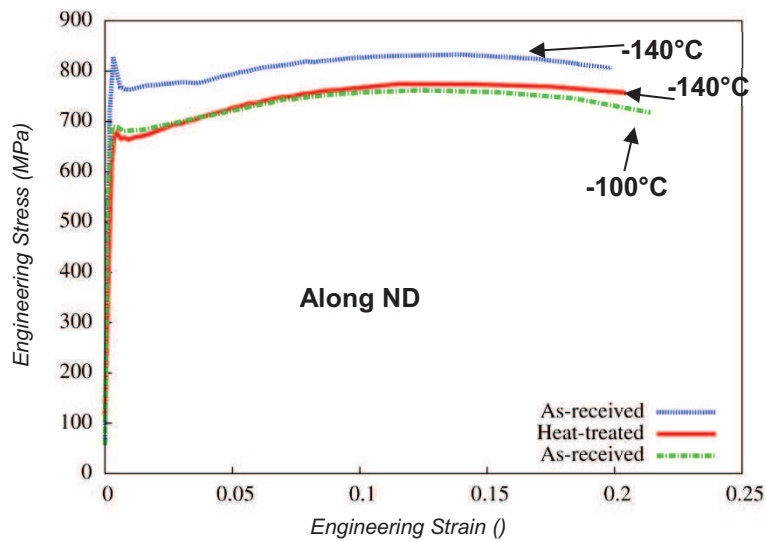


Figure VI-15: Tensile tests along ND on as-received and heat-treated steels. The elastic-plastic behavior of the heat-treated steel at -140°C is similar to that of the as-received steel at -100°C .

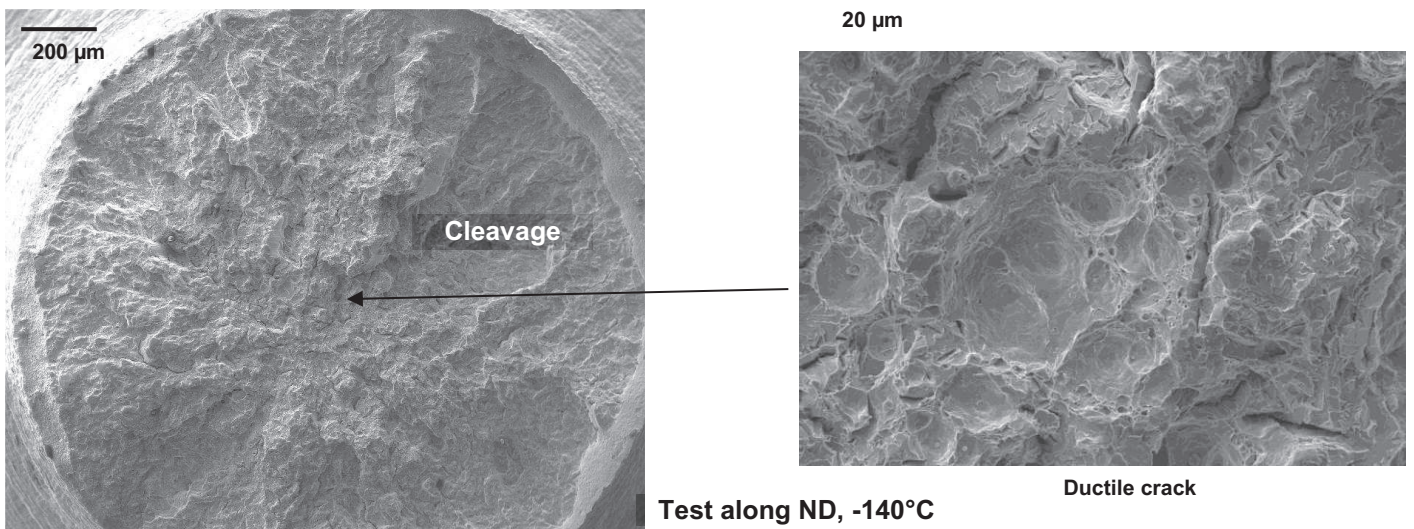


Figure VI-16: Fracture surface of tensile NT2 specimens along ND at -140°C . Heat treated steel.

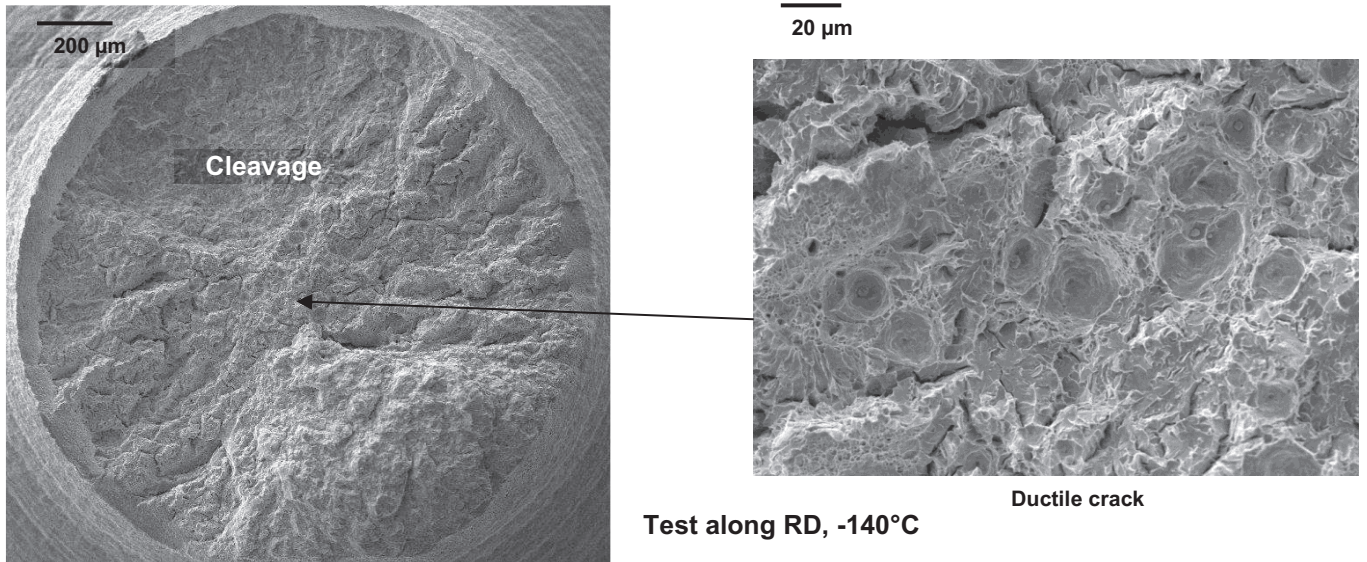


Figure VI-17: Fracture surface of tensile NT2 specimen along RD at -140°C. Heat treated steel.

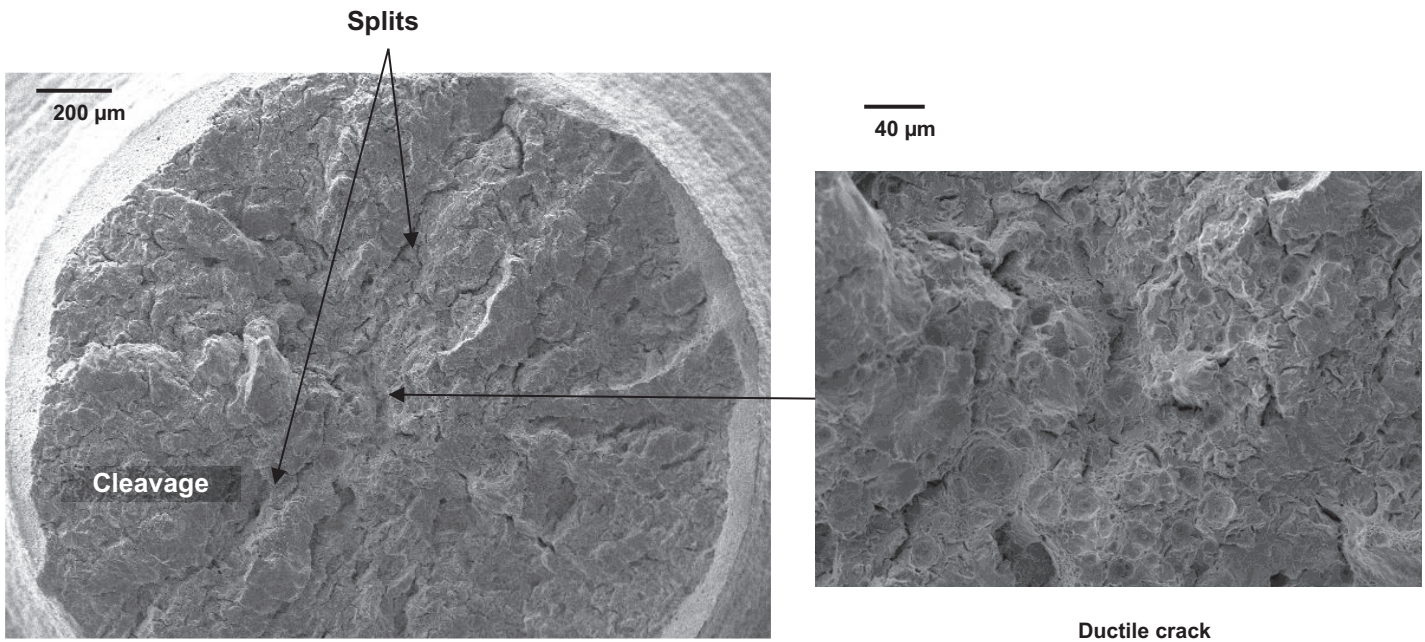


Figure VI-18: Fracture surface of tensile NT2 specimen along TD at -140°C. Heat treated steel.

VI.2.4. Cleavage fracture behavior of the heat-treated steel

a) Tensile tests at -196°C

Tensile tests were performed at -196°C in order to study cleavage fracture. Tensile curves on smooth and notched specimens are presented in Figure VI-19. To facilitate experimental tests on heat-treated steel specimens, a longitudinal extensometer was used instead of the radial extensometer that was used for the as-received material. Some problems were encountered with this longitudinal extensometer for tensile tests on notched specimens, which might explain the discrepancy between tensile curves observed in Figure VI-19. The tensile test on the smooth specimen was only done along ND, since the heat treatment was assumed to have made Steel B more isotropic. The deformation range of the extensometer saturated before fracture of the smooth specimen.

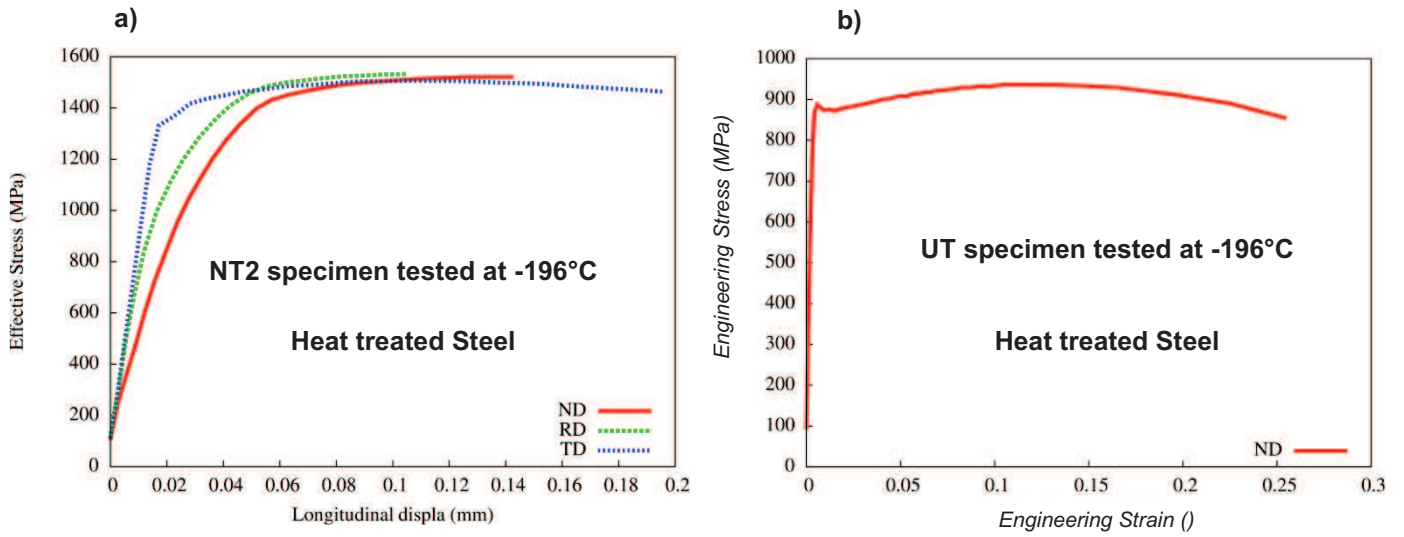


Figure VI-19: (a) Tensile curves of NT2 specimens tested at -196°C along ND, RD and TD; (b) Tensile curve of smooth specimen tested at -196°C along ND

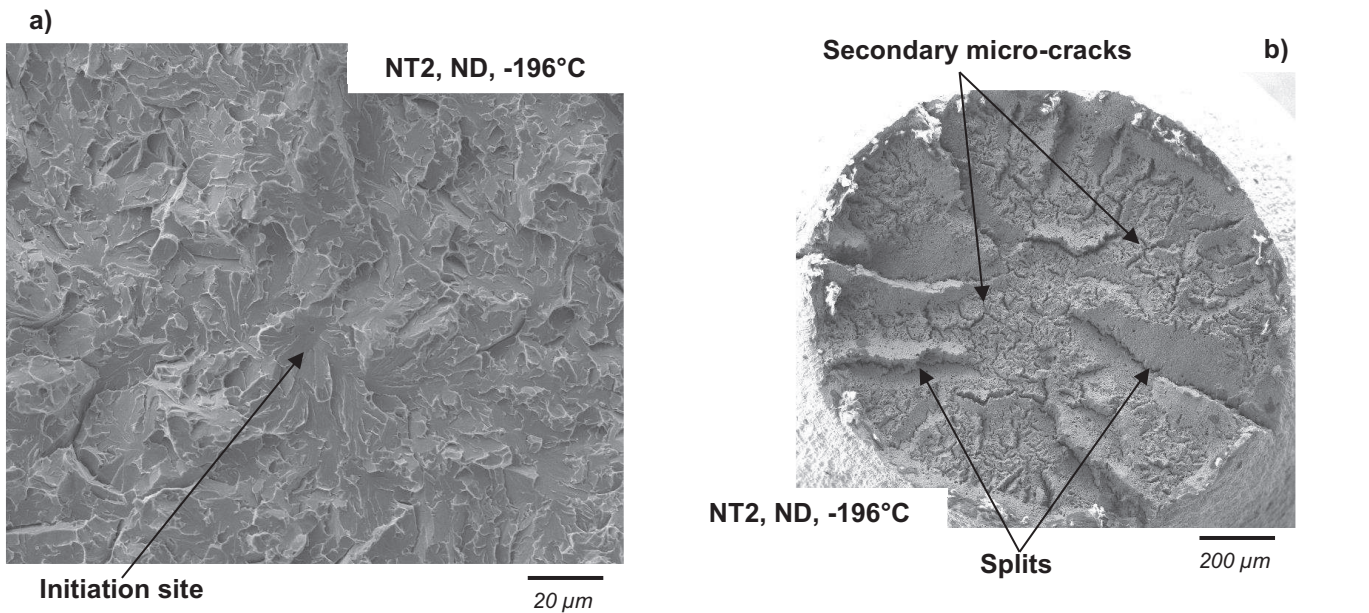


Figure VI-20: (a) Fracture surface of NT2 tested at -196°C along ND; (b) Fracture surface of smooth specimen tested at -196°C along ND

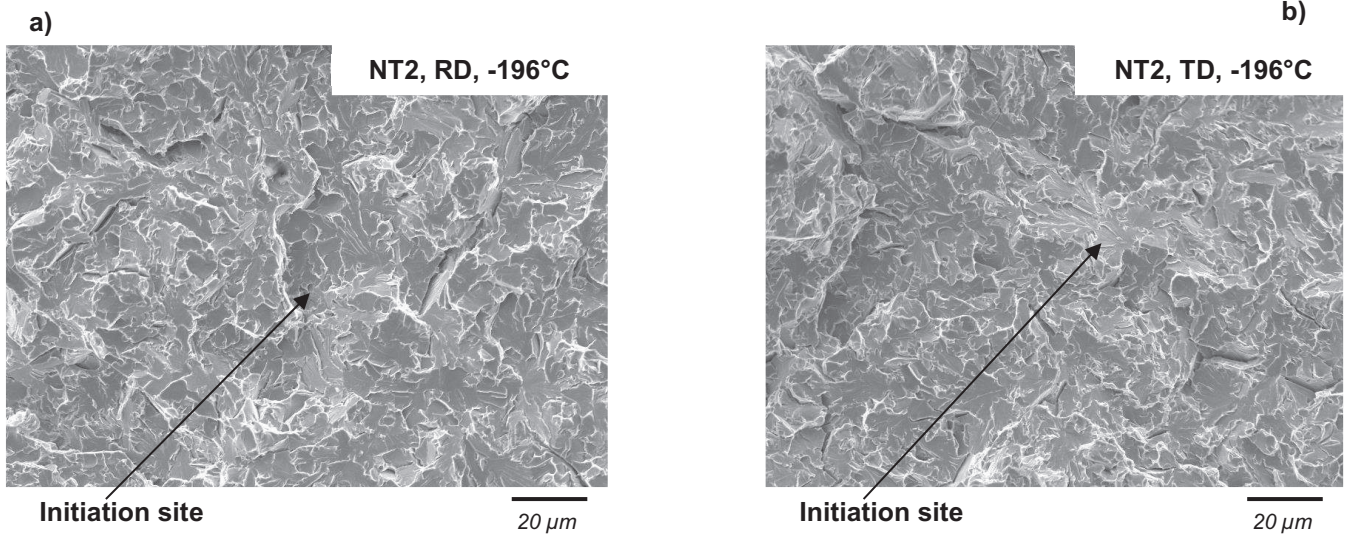


Figure VI-21: (a) Fracture surface of NT2 tested at -196°C along RD; (b) Fracture surface of NT2 tested at -196°C along TD

Fracture surfaces of heat-treated Steel B are presented in Figure VI-20 and Figure VI-21. Figure VI-20 shows the fracture surface of notched and smooth specimens tested at -196°C along ND. Full cleavage fracture was observed on the notched specimen as was the case for the as-received material. Micro-cracks and radial splits were observed in the smooth specimen. Figure VI-21 shows the fracture surface of notched specimens tested at -196°C along RD and TD. In contrast to the as-received steel where pronounced delamination cracks were observed, only flat cleavage fracture was observed for the heat-treated steel.

b) Identification of a critical cleavage fracture stress along ND, RD and TD

Critical cleavage stresses along ND, RD and TD were determined at -196°C . Tensile tests on notched specimens were simulated as for the as-received steel. A Barlat criterion was considered for the constitutive modelling, but in that case anisotropic parameters of the plastic yield were all set to 1 (leading in fact to a Hosford criterion), because the plastic flow behavior of the heat-treated material was assumed to be isotropic and the experimental database was not as large as for the as-received material. Strain hardening parameters and parameter “a” which controls the shape of the yield surface are presented in Table VI-2.

The values of critical cleavage stress estimated along ND, RD and TD were respectively, 2200 ± 50 MPa, 2300 ± 50 MPa and 2400 ± 50 MPa. Critical cleavage stress along ND was not changed compared to the as-received steel. On the contrary, critical cleavage stresses along RD and TD were lower than for the as-received material (2400 MPa for RD and > 2500 MPa for TD). Therefore, the initial anisotropy in critical cleavage stress was reduced by the heat treatment.

	σ_0	H	b	Q	a
T= -196°C	810	1000	36	108	14

Table VI-2: Parameters of the model identified on heat-treated steel at -196°C . All anisotropic yield parameters were set to 1.

c) Analysis of potential cleavage facets

The size and spatial distributions of potential cleavage facets of the heat-treated steel have only been investigated in the (RD-TD) plane. Results are compared in Figure VI-22 and Figure VI-23 for the as-received and heat-treated steels respectively. Potential cleavage facets were slightly smaller after the heat treatment. According to the PCF size observed in the heat treated steel, critical cleavage stress might be expected to reach 2350 MPa using the correlation established in chapter IV (Figure VI-24).

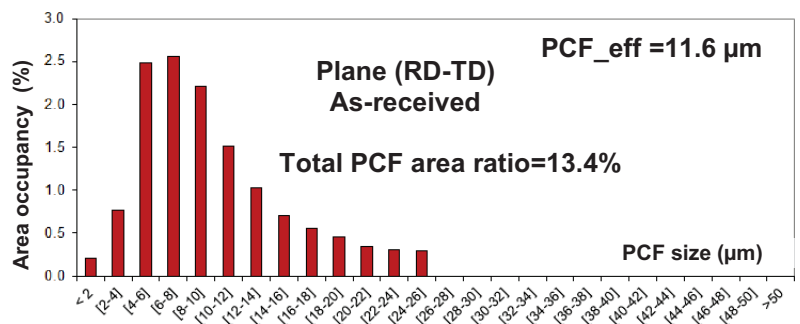
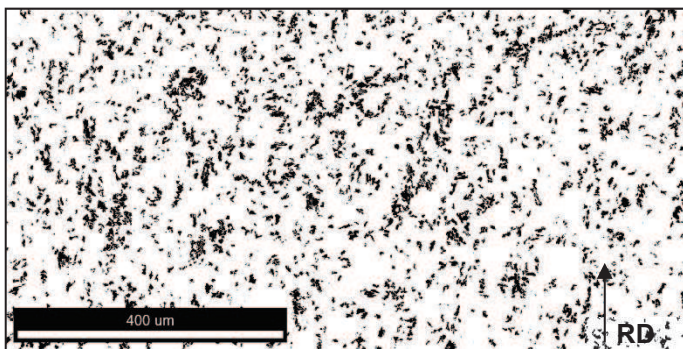


Figure VI-22: Distribution of potential cleavage facets within (RD-TD) plane for the as-received steel.

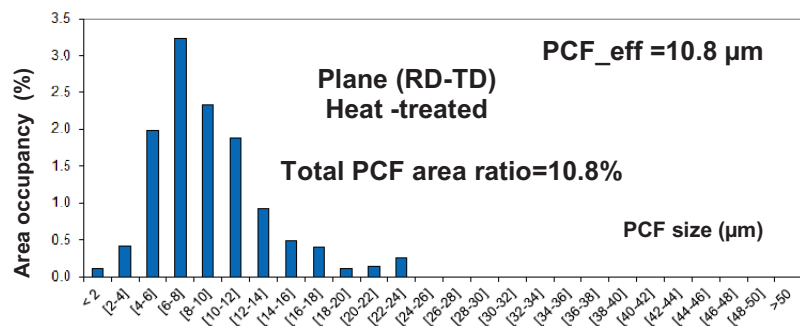
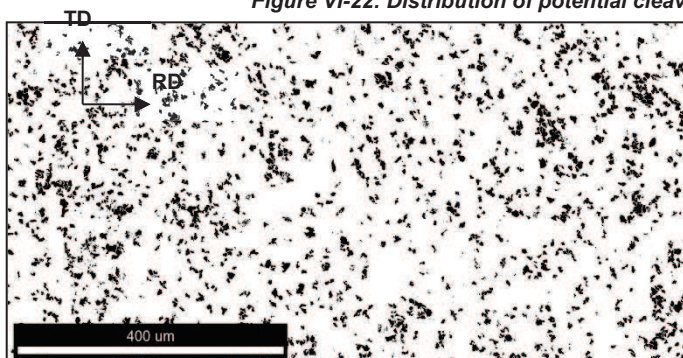


Figure VI-23: Distribution of potential cleavage facets within (RD-TD) plane for 20pct-steel.

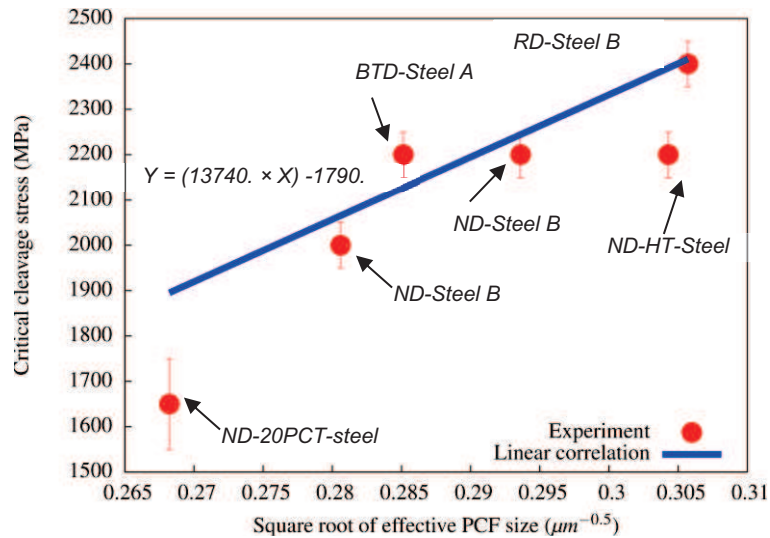


Figure VI-24: Correlation between critical cleavage stress and inverse square root of effective PCF size. Predicted critical cleavage stress of the heat treated (HT) steel is overestimated by the correlation model.

d) Discussion

After the heat-treating process, Steel B presents a microstructure and an average texture that are more isotropic and so, the initial anisotropy in critical cleavage stress is reduced. However, from tests performed on 20pct-steel, it was found that critical cleavage stress evolved with plastic strain. Therefore, during loading, the almost isotropic steel could become anisotropic because of the plastic strain which affects critical cleavage stresses. On smooth round bar specimens tested at -196°C where high plastic strain was observed after necking, the anisotropy of critical cleavage fracture stress, induced by plastic strain, led to radial splits on the fracture surface. In fact, there was no preferential direction for secondary cleavage fracture among all radial planes. This might be due to transverse symmetry conditions imposed by straining the circumferentially notched specimen.

VI.3. Conclusions

The sensitivity of Steel B to delamination has been investigated after prestraining and after a heat treatment (austenitization and tempering).

- After prestraining the as-received steel along TD by 20% by cold rolling, the microtexture of the rolling plane was modified and in particular PCFs became larger. Charpy tests performed on the prestrained material showed more pronounced delamination cracking. From tensile tests performed on notched specimens along ND, critical cleavage stress was found to have lower by 30% compared to the as-received material. This decrease was larger than the value expected from the correlation between critical cleavage stress and the effective PCF size determined in chapter IV. Therefore, dislocations induced by work hardening might play a complementary role in decreasing critical cleavage stress.
- The application of a heat treatment made Steel B more isotropic. No delamination was observed after Charpy tests. Tensile tests showed that the initial anisotropy in critical cleavage stress was reduced after the heat treatment. Nevertheless radial splits were observed during tensile tests, suggesting that there is no preferential direction for secondary crack propagation. The critical cleavage stress determined along ND was lower than the one predicted by the correlation between critical cleavage stress and the effective PCF size determined in chapter IV.

This analysis was done with a very light experimental campaign compared to that for the as-received material. Some uncertainty in plastic flow behavior was due to the use of longitudinal extensometer for notched specimens. Therefore, the results of this chapter aim at giving the general trend; more tests are necessary to make a reliable quantitative investigation.

To separately study the effect of crystal rotation (change in microtexture) and that of work-hardening after initial prestraining, tests should be performed after tempering of the pre-strained steel to deduce the effect of the dislocations induced by the cold hardening on critical cleavage stress.

Conclusions and Outlooks

Conclusions

Finding a correlation between DWTT and Charpy tests on modern pipeline steels within the brittle to ductile transition domain is an important goal in pipeline industry. This might pass through a better understanding of fracture modes and especially of brittle-out-of-plane cracking which occurs during these impact tests. Focusing on these issues, the main results of this study are as follows. Two pipeline steels were considered in this study: Steel A and Steel B, both obtained by thermomechanically controlled process.

- Brittle out-of-plane cracking during impact tests:

Delamination and brittle tilted fracture (BTF) are the main brittle out-of-plane cracking modes observed within the ductile to brittle transition domain. Delamination cracking propagates along the rolling plane and BTF propagates along so-called θ -planes. The shear area percentage which is associated to the impact toughness of DWTT specimens was decreased by the occurrence of BTF. A ductile crack advance with a triangle shape, followed by delamination cracks, was observed behind BTF for DWTT specimens. On the contrary, in Charpy specimens, BTF was found to initiate from the notch root. Moreover, in Charpy specimens, BTF was observed at very low temperatures compared to DWTT specimens. The larger ligament length of DWTT specimens facilitates BTF which could initiate from ductile crack even at higher temperatures (-30°C).

- Anisotropy in fracture mode:

Tensile tests performed along ND, BT, RD and TD showed that the rolling plane and the θ -plane were more sensitive to cleavage fracture than the (TD-ND) and (RD-ND) planes. A central delamination crack associated to an abrupt load drop was observed for specimens pulled along RD and TD. This delamination initiated from a ductile micro-crack located at the center of the specimen and elongated cleavage facets were observed. Specimens pulled along ND show a ductile to brittle transition in terms of fracture surface. The cleavage crack initiated from circular ductile cracks at the center of the specimen. The lower the temperature is, the higher the size of the ductile crack is. At -196°C full cleavage fracture was observed. Specimens pulled along BT also showed this ductile to brittle transition behavior in terms of fracture surface, even if delamination micro-cracks were observed for Steel A.

- Potential cleavage facets (PCFs) and anisotropy of critical cleavage stresses:

Potential cleavage facets were quantitatively defined as possible unit crack path for a particular loading direction. In the rolling plane, they correspond to apparently larger grains of the microstructure. The PCF size distribution was investigated on the rolling plane, the θ -plane, the (TD-ND) and (RD-ND) planes. The size of these PCFs was found to be well correlated of the sensitivity to cleavage fracture. Indeed, the rolling plane and the θ -plane which had larger PCFs were more sensitive to cleavage fracture. For each PCF size distribution, an effective PCF size was determined as the average PCF size over the distribution tail. Critical cleavage fracture stresses along ND, BT, RD and TD directions

were determined from numerical simulations performed on notched specimens at -196°C , where full cleavage fracture was observed. A constitutive model including a Barlat plastic yield criterion was chosen to estimate the stress state in the specimen at the fracture event. A good correlation between critical cleavage stress and the size of PCFs was found with a Griffith-like approach. Lower critical cleavage stresses were associated to larger effective PCF sizes.

- Numerical prediction of brittle out-of-plane cracking:

A critical cleavage stress criterion was used to numerically predict delamination occurrence. The stress along ND at the onset of delamination was compared to critical cleavage stress along ND. The ductile micro-crack observed at delamination initiation sites was modeled as an internal notch at the center of the NT specimen. Thus, the local increase in stress along ND induced by the presence of this micro-crack could be taken into account. Moreover, it was found that taking into account the evolution of critical cleavage stress with plastic strain was necessary to get a relevant cleavage fracture criterion. As a result, critical cleavage stress, and even its anisotropy, is not an intrinsic material characteristic. They depend on the actual microtexture of the material, which may be affected by plastic strain prior to cleavage fracture.

- Effect of prestraining and heat treatment on sensitivity to delamination:

After prestraining of Steel B by multiple passes cold rolling (20%), a critical cleavage stress along ND was decreased by around 30%. PCF sizes were also increased and pronounced delamination cracks were observed during Charpy tests. After an austenitization + temper heat treatment, the steel microstructure became more isotropic. The initial anisotropy on critical cleavage stress was less pronounced. As a consequence, delamination cracks were not observed during Charpy tests.

Outlooks

- The small ligament length of Charpy specimens is thought to inhibit propagation of the BTF after ductile crack initiation as it was observed at higher temperature for DWTT specimens. Performing tests on Charpy specimens with larger ligaments could be a good way to check the role of the ligament length on the occurrence of BTF, and might also partially explain why DWTTs are more conservative than Charpy tests with respect to fracture surface crystallinity.
- Critical cleavage stress along BTD was lower than that along ND for Steel B at very low temperature. There is no data on the evolution of the fracture mode within the ductile to brittle transition domain for tensile tests along BTD. Tensile tests on Steel B along BTD for temperatures between 20°C and -196°C should be performed to check that there is no delamination crack at the origin of brittle cleavage cracking.
- A first correlation between PCF size and critical cleavage stress was done via a Griffith like approach. The database used for this correlation is not very rich. Tensile tests at -196°C on different directions and materials should be done to enrich this database. A statistical local approach to fracture directly based on the distribution of PCF sizes could also be considered to investigate cleavage fracture.
- The prediction of brittle out-of-plane cracking, especially of delamination was validated on NT specimens after taking effects of the ductile micro-crack and of the plastic strain into account. The simulation of Charpy specimens was done with a von Mises yield criterion without adiabatic effect. The stress state inside the specimen was not accurately estimated and therefore delamination could not be predicted on Charpy specimens. More accurate simulation of Charpy specimens is necessary in order to numerically investigate brittle out-of-plane cracking.

- Prestraining of Steel B by multiple passes cold rolling led to significant evolution in critical cleavage stress. To get free from any contribution of dislocations introduced by cold rolling, a tempering treatment could be done before investigation of critical cleavage stress. In that case, attention should be paid to preserve as far as possible the microtexture before tempering. Other ways of prestraining the material could be tested with different deformation paths and different plastic strain levels to complete the database and more accurately assess the effect of prior plastic strain on the sensitivity to cleavage fracture. Better understanding of this phenomenon is required to improve physical knowledge of the brittle-to-ductile transition behavior in steels.

A- Interrupted DWTT and results of impact tests

A.1. Interrupted Battelle drop weight tear tests

These tests have been performed on specimens taken along TD from Steel B, to get better understanding of the competition between fracture modes in a given BWTT specimen. Crack propagation within DWTT specimens was interrupted using a ballistic method, i.e., by providing a total energy lower than the energy required for complete failure of the specimen. Since the height of the hammer above the specimen was fixed, the impact energy was reduced by decreasing the weight of the hammer. Consequently, the original weight of the hammer (985 kg) was reduced to around 430 kg. Three specimens have been tested at -60°C , which was the DWTT ductile to brittle transition temperature for Steel B according to a crystallinity criterion (FATT temperature).

After the test, two specimens were heated for one hour at 300°C to obtain color tinting of the fracture surface. Non-destructive evaluations (NDE) with ultrasonic waves and magnetoscopy have been performed to determine the dimensions of the cracks inside the specimen (Figure A-1).

CT-like specimens were then machined from interrupted DWTT samples (Figure A-2). Fatigue post cracking has been performed so that the fatigue crack could be easily distinguished from the cracks generated during DWTT. Post cracking has been done at room temperature on the same Instron equipment as that described in Chapter II. Load cycles between 40 kN and 4 kN have been applied with a frequency of 40 Hz.

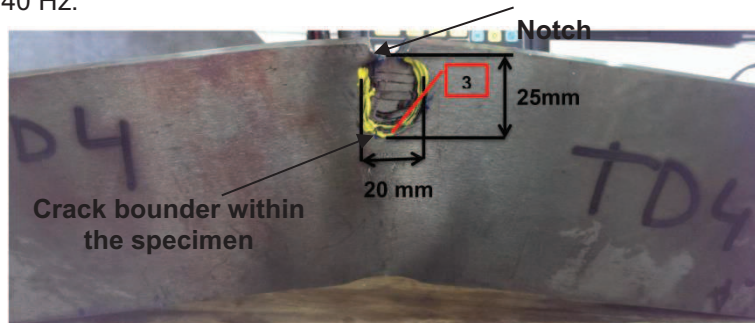


Figure A-1: Analysis of the cracks limit (in yellow) from non destructive evaluation technics

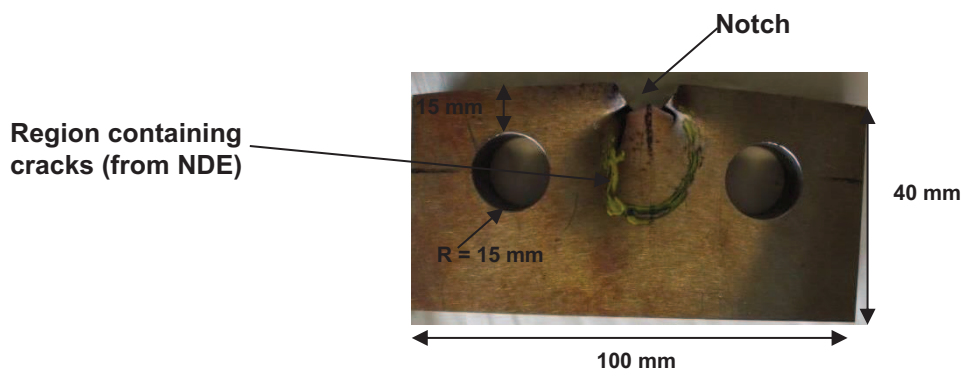


Figure A-2: Specimen geometry used for fatigue post-cracking. Same specimen as in the previous figure.

A typical fracture surface after fatigue post-cracking is presented in figure A-3. The tinted zone corresponds to ductile slant and contains delamination cracks. Far from the ductile slant, one delamination crack at mid thickness could be observed. This delamination crack might have not occurred during fatigue post-cracking, since the test was performed at room temperature and

according to observations carried out on different specimens, delamination did not appear for room temperature. This delamination crack observed should have been formed during the DWTT test.

The interaction between the delamination crack and the ductile slant could therefore be the following:

- A first delamination crack is formed at mid-thickness from ductile crack advance
- The delamination propagates until the stress state inside the specimen does not allow the condition for its further propagation
- Ductile slant then propagates on both sides of the delamination crack
- The propagation of this ductile slant modifies the stress state inside the specimen
- Delamination crack can initiate and propagate again

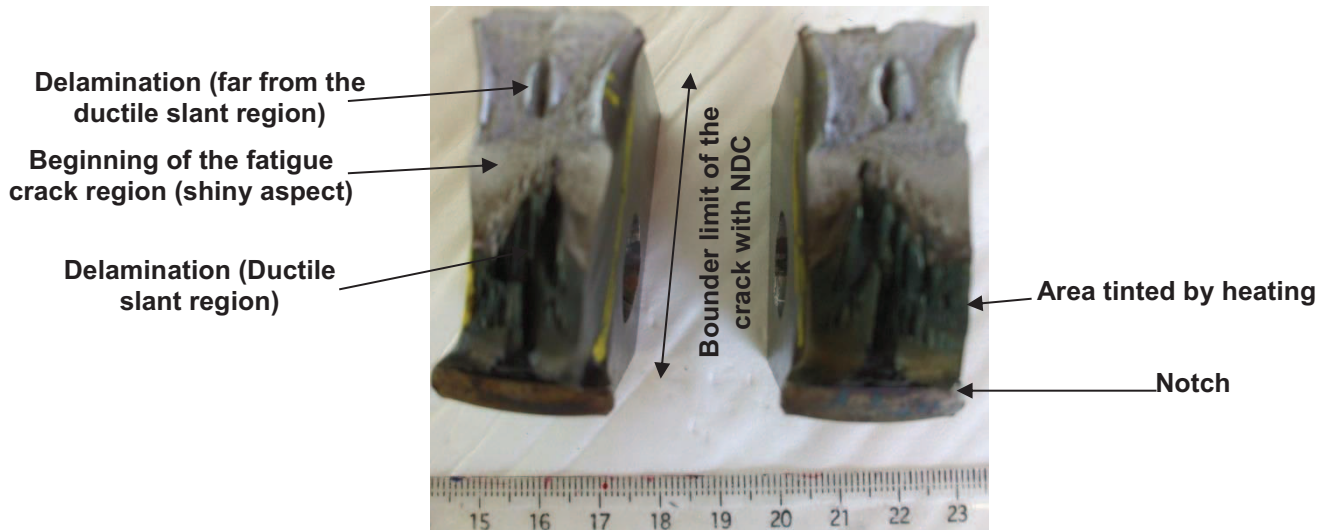


Figure A-3: Fracture surface of the specimen after fatigue post-cracking

A.2. Detailed results of drop weight tear tests

A.2.1. Tests along TD on as-received Steel A

DWTT on Steel A along TD			
Temperature	Specimen	Energy (kJ)	Ductile area (%)
-100°C	BDWTT_13	1.3	0
	BDWTT_14	0.7	0
-70°C	BDWTT_7	2.3	22
	BDWTT_8	2.8	22
-60°C	BDWTT_5	11.5	67
	BDWTT_6	11.2	50
-40°C	BDWTT_9	10.5	70
	BDWTT_10		84
-30°C	BDWTT_11	7.9	65
	BDWTT_12	13.7	67
-20°C	BDWTT_3	15.8	100
	BDWTT_4		97
0°C	BDWTT_1	17.4	100
	BDWTT_2		100

Some DWTT impact energies was not available because acquisition issues.

A.2.2. Tests along TD on Steel B

DWTT on Steel B along TD			
Temperature	Specimen	Energy (kJ)	Ductile area (%)
-100°C	BDWTT_9	1.1	0
	BDWTT_10	0.6	0
-80°C	BDWTT_7	9.0	16
	BDWTT_8	9.1	16
-60°C	BDWTT_1	9.7	38
	BDWTT_2	10.7	42
-40°C	BDWTT_3	14.1	90
	BDWTT_4		87
-20°C	BDWTT_5	13.3	75
	BDWTT_6	15.3	86

A.2.3. Tests along RD on Steel B

DWTT on Steel B along RD			
Temperature	Specimen	Energy (kJ)	Ductile area (%)
-100°C	BDWTT_7	1.2	0
	BDWTT_8	1.0	0
-80°C	BDWTT_3	2.5	7
	BDWTT_4	1.4	14
-60°C	BDWTT_1	13.9	72
	BDWTT_2	14.3	82
-40°C	BDWTT_5	6.1	87
	BDWTT_6	15.1	93
-20°C	BDWTT_9	18.7	95
	BDWTT_10	18.5	95

A.3. Charpy tests on as-received Steel A

A.3.1. RD-TD Charpy specimens

Charpy RD-TD, Steel A		
Temperature	Specimen	Energy (J)
-140°C	charpy_RD-TD_14	16
	charpy_RD-TD_15	9
	charpy_RD-TD_20	10

-120°C	charpy_RD-TD_7	152
	charpy_RD-TD_8	109
	charpy_RD-TD_12	41
	charpy_RD-TD_13	34
	charpy_RD-TD_18	10
	charpy_RD-TD_19	22
-100°C	charpy_RD-TD_5	44
	charpy_RD-TD_6	38
	charpy_RD-TD_10	144
	charpy_RD-TD_11	156
	charpy_RD-TD_16	232
	charpy_RD-TD_17	65
-80°C	charpy_RD-TD_3	181
	charpy_RD-TD_4	241
	charpy_RD-TD_9	184
20°C	charpy_RD-TD_1	263
	charpy_RD-TD_2	282

A.3.2. TD-RD Charpy specimens

Charpy TD-RD steel A		
Temperature	Specimen	Energy (J)
-120°C	charpy_TD-RD_19	26
	charpy_TD-RD_20	29
	charpy_TD-RD_21	29
	charpy_TD-RD_22	2
	charpy_TD-RD_23	14
-100°C	charpy_TD-RD_10	29
	charpy_TD-RD_11	42
	charpy_TD-RD_12	72
	charpy_TD-RD_13	26
	charpy_TD-RD_14	168
	charpy_TD-RD_17	60
	charpy_TD-RD_18	42
	charpy_TD-RD_34	34
	charpy_TD-RD_35	202
	charpy_TD-RD_36	98
	charpy_TD-RD_37	29
	charpy_TD-RD_38	143
	charpy_TD-RD_39	21
	charpy_TD-RD_40	30
charpy_TD-RD_41	33	

-80°C	charpy_TD-RD_7	232
	charpy_TD-RD_8	84
	charpy_TD-RD_9	47
	charpy_TD-RD_15	218
	charpy_TD-RD_16	234
	charpy_TD-RD_24	188
	charpy_TD-RD_25	212
	charpy_TD-RD_26	222
	charpy_TD-RD_27	43
	charpy_TD-RD_28	137
	charpy_TD-RD_29	271
	charpy_TD-RD_30	238
	charpy_TD-RD_31	185
	charpy_TD-RD_32	108
	charpy_TD-RD_33	40
-60°C	charpy_TD-RD_4	250
	charpy_TD-RD_5	260
	charpy_TD-RD_6	262
20°C	charpy_TD-RD_1	269
	charpy_TD-RD_2	279
	charpy_TD-RD_3	255

A.3.3. RD-ND Charpy specimens

Charpy RD-ND, steel A		
Temperature	Specimen	Energy (J)
-120°C	charpy_RD-ND_14	32
	charpy_RD-ND_15	100
-100°C	charpy_RD-ND_11	219
	charpy_RD-ND_12	213
	charpy_RD-ND_13	252

A.3.4. TD-ND Charpy specimens

Charpy TD-ND, Steel A		
Temperature	Specimen	Energy (J)
-140°C	charpy_TD-ND_13	21
	charpy_TD-ND_14	13
-120°C	charpy_TD-ND_7	102
	charpy_TD-ND_8	150
	charpy_TD-ND_11	46
	charpy_TD-ND_12	93
	charpy_TD-ND_16	130

	charpy_TD-ND_5	109
	charpy_TD-ND_6	52
	charpy_TD-ND_9	143
	charpy_TD-ND_10	176
-100°C	charpy_TD-ND_15	126
-80°C	charpy_TD-ND_3	175
	charpy_TD-ND_4	119
20°C	charpy_TD-ND_1	229
	charpy_TD-ND_2	243

A.4. Charpy tests on as-received Steel B

A.4.1. RD-TD Charpy specimens

Charpy RD-TD, Steel B		
Temperature	Specimen	Energy (J)
-140°C	charpy_RD-TD_18	22
	charpy_RD-TD_19	14
	charpy_RD-TD_20	15
-120°C	charpy_RD-TD_9	28
	charpy_RD-TD_12	157
	charpy_RD-TD_16	106
	charpy_RD-TD_10	167
	charpy_RD-TD_11	191
	charpy_RD-TD_14	162
-100°C	charpy_RD-TD_13	234
	charpy_RD-TD_15	264
	charpy_RD-TD_17	192
-80°C	charpy_RD-TD_8	260
	charpy_RD-TD_4	262
	charpy_RD-TD_6	278
-60°C	charpy_RD-TD_1	276
	charpy_RD-TD_5	278
	charpy_RD-TD_7	282
20°C	charpy_RD-TD_2	286
	charpy_RD-TD_3	287

A.4.2. TD-RD Charpy specimens

Charpy TD-RD, Steel B		
Temperature	Specimen	Energy (J)
-140°C	charpy_TD-RD_18	23
	charpy_TD-RD_19	15
	charpy_TD-RD_20	16
-120°C	charpy_TD-RD_3	30
	charpy_TD-RD_6	26
	charpy_TD-RD_9	18
	charpy_TD-RD_5	72
	charpy_TD-RD_12	32
	charpy_TD-RD_14	20
-100°C	charpy_TD-RD_11	244
	charpy_TD-RD_13	34
	charpy_TD-RD_15	232
-80°C	charpy_TD-RD_7	238
	charpy_TD-RD_8	247
	charpy_TD-RD_17	247
-60°C	charpy_TD-RD_1	286
	charpy_TD-RD_10	266
	charpy_TD-RD_16	286
20°C	charpy_TD-RD_2	265
	charpy_TD-RD_4	262

A.4.3. RD-ND Charpy specimens

Charpy RD-ND, Steel B		
Temperature	Specimen	Energy (J)
-140°C	charpy_RD-ND_7	85
	charpy_RD-ND_8	216
	charpy_RD-ND_9	204
-120°C	charpy_RD-ND_4	206
	charpy_RD-ND_5	208
	charpy_RD-ND_6	288
-100°C	charpy_RD-ND_1	295
	charpy_RD-ND_2	215
	charpy_RD-ND_3	260

A.4.4. TD-ND Charpy specimens

Charpy TD-ND, Steel B		
Temperature	Specimen	Energy (J)
-140°C	11688_charpy_TD_ND_16	71
	11688_charpy_TD_ND_18	30
	11688_charpy_TD_ND_19	16
-120°C	11688_charpy_TD_ND_3	190
	11688_charpy_TD_ND_5	107
	11688_charpy_TD_ND_8	49
	11688_charpy_TD_ND_2	192
	11688_charpy_TD_ND_12	242
	11688_charpy_TD_ND_14	206
-100°C	11688_charpy_TD_ND_11	68
	11688_charpy_TD_ND_15	207
	11688_charpy_TD_ND_17	113
-80°C	11688_charpy_TD_ND_1	210
	11688_charpy_TD_ND_10	124
	11688_charpy_TD_ND_20	201
-60°C	11688_charpy_TD_ND_7	286
	11688_charpy_TD_ND_9	220
	11688_charpy_TD_ND_13	272
20°C	11688_charpy_TD_ND_4	262
	11688_charpy_TD_ND_6	274

B- Design of NT2 geometry and detailed results of tensile tests on smooth and notched specimens

This appendix is divided into two parts. The first part reports the design procedure of NT2 specimens used in chapter III, to perform tensile tests mainly along ND and BTD directions. The second part summarizes, via tables, the results of tensile tests for all tested temperatures and directions.

B.1. Design of NT2 specimen geometry

Delamination and brittle tilted fracture are two brittle out-of-plane fracture modes that have been observed after impact tests. In these fracture modes, the brittle crack propagates respectively along the rolling plane and along the θ -plane. This suggested a sensitivity of these planes to cleavage fracture. It seemed necessary to perform tests perpendicularly to the rolling plane and to the θ -plane respectively, so that the response of these planes under mode I loading could be investigated properly.

Because of the rather small thickness of the available steel plates (19 mm for Steel A), conventional notched specimens could not be used for these tests. This part presents the design procedure of the notched bar geometry used for tensile tests perpendicularly to the rolling plane and θ -plane.

B.1.1. Identification of the constitutive behavior

The design of the notched bar geometry involved some numerical calculations. Therefore, identification of the constitutive behavior was a preliminary step. This identification has been done on Steel A, which has the lowest thickness. Ideally, the identification should have been done using experimental data obtained from tests along the normal direction of the plate (ND). Since no specimen geometry was yet available to test along this direction, the identification has been done from the results of conventional tensile tests along the transverse direction (TD). An isotropic Von Mises yield criterion was then assumed for this design even if preliminary tests revealed an anisotropic behavior of the steel.

A nonlinear isotropic hardening rule with a double exponential term coupled with a linear term was chosen, as given by the following equation in the uniaxial case for the flow stress:

$$\sigma_Y = \sigma_0 + Hp + Q_1(1 - \exp(-b_1p)) + Q_2(1 - \exp(-b_2p)) \quad \text{Equation B-1}$$

Where p is the cumulative plastic strain, σ_0 the yield strength and H , Q_1 , b_1 , Q_2 , b_2 are parameters to be identified.

The set of parameters H , Q_1 , b_1 , Q_2 and b_2 has been identified using Z-set software from tensile tests on smooth specimens (Figure B-1). This identification was done on tensile tests along TD at -100°C because delamination cracking was found to occur on notched specimens with these conditions, so that tests along ND were planned at that temperature. The dynamic instability phenomenon at the start of yielding was not modeled, since focus was made on the part of the curve after the yield point. In fact, the strain level measured at fracture on NT specimens was always larger than 0.05.

The constitutive equations were used to perform FE simulations on a conventional notched bar geometry (NT1). A finite strain Newton-Raphson resolution for global convergence was chosen with an implicit integration scheme for constitutive equations. Quadratic axisymmetric elements (eight nodes)

with reduced integration points (four Gauss points per element) are used. Figure B-2 gives the boundary conditions applied on the specimen.

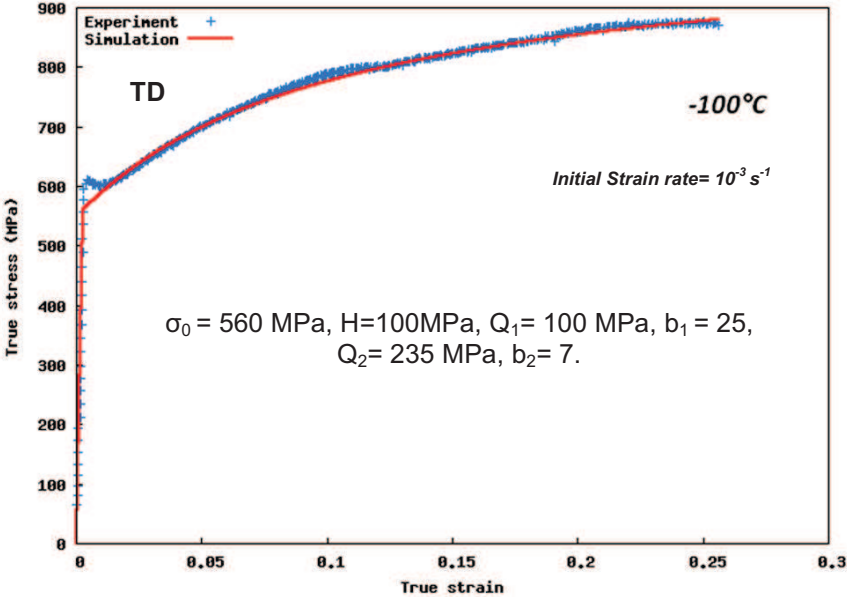


Figure B-1: Tensile test on smooth specimen of Steel A (TD, -100°C), model prediction (“simulation”) compared with experimental curve

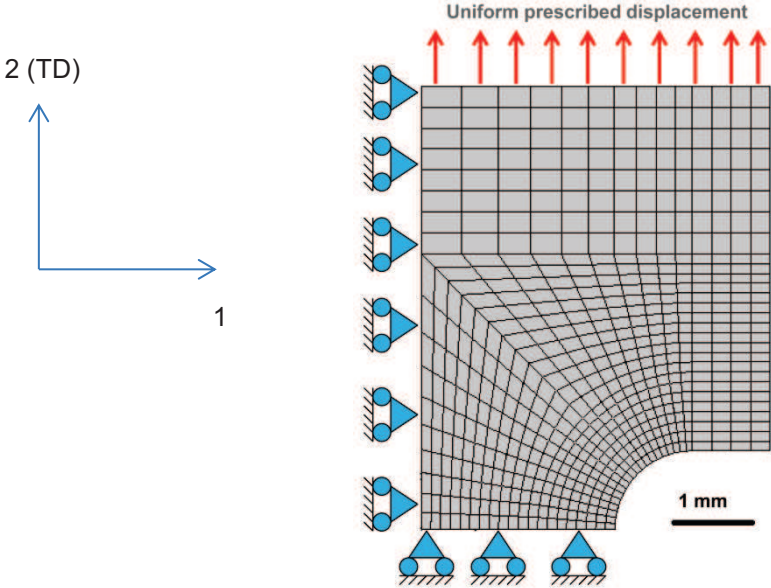


Figure B-2: Boundary conditions applied to the specimen

The load vs. average diameter reduction curve predicted by simulation was compared to experimental results along TD (Figure B-3). The loads predicted by simulation are overestimated by 5% compared to experiment. This might be caused by the yield criterion isotropy assumption used in the constitutive model. Even if the stress state within the specimen might be also overestimated by 5%, the constitutive equation identified has been used for the design of NT2 geometry.

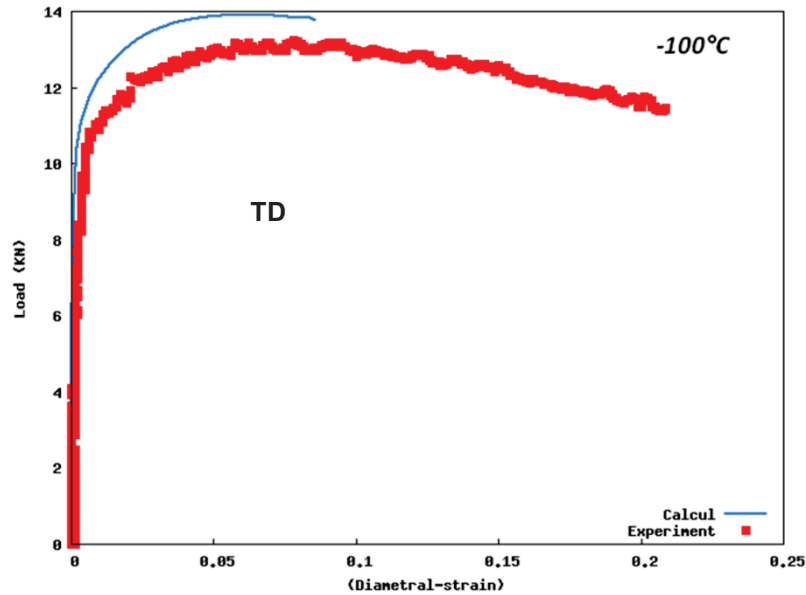


Figure B-3: Validation of the constitutive model on notched round bar along TD

B.1.2. Requirements for NT2 specimen geometry

The NT2 geometry should allow specimens to be taken along ND and should lead to cleavage fracture. These two requirements are explicitly defined above.

Geometry requirements

The specimen should have a round notched bar shape, with a total length of 18 mm so that it could be taken along the normal direction (Steel A plate thickness is 19 mm). The diameter value of specimen ends was fixed to 5 mm, so that they could suit the available grips. The minimal section diameter should be high enough so that continuum mechanics hypothesis remains valid, i.e., it should be much larger than the ferrite grain size (less than 50 μm). Therefore, a minimum value of 1 mm was fixed for the minimal section diameter. The initial value of the notch opening should be significantly higher than 0.5 mm so that the knives of the radial extensometer (thickness equal to 0.5 mm) could pass through it.

Required stress state within the specimen

Stress state prediction within the NT2 specimen has been done using the constitutive model previously identified along TD at -100°C . According to the classical Ritchie-Knott-Rice (RKR) approach, to get cleavage fracture, the maximum principal stress should exceed a critical value over a volume which contains more than one microstructural feature enable to trigger cleavage fracture. At that stage of the study, the features suspected for the triggering of cleavage fracture were the large elongated entities observed in both steels (chapter I). Baldi [16] found critical cleavage stresses along ND lower than 2000 MPa on high strength low alloy steels yet showing a pronounced banded microstructure. Lambert-Perlade [33] showed that cleavage fracture could be observed on broken notched specimens with a coarse bainitic microstructure for tensile tests with an average reduction in diameter up to 30%. By combining these two results, the condition of cleavage fracture occurrence chosen for the design of NT2 could be summarized like this: *The volume of the specimen scanned with a maximal principal stress of at least 2000 MPa at 30% of average radial strain should contain much more than one large cluster of large ferrite grains.*

B.1.3. Choice of the optimal NT2 geometry

Three round notched specimen geometries were studied for the design. These geometries were obtained by a length reduction of a notched specimen commonly used in the laboratory (Fig B-4). This conventional notched specimen geometry, in fact, the NT1 geometry reported in the main text, was used to investigate the mechanical behavior along RD and TD directions. First, the ends of this conventional notched specimen geometry were cut to shorten the specimen. Then, the rest of the specimen dimensions were proportionally reduced, so that the value of the final length of the specimen was equal to 18 mm as requested. The new geometry has been called NT2-a. Two other versions of NT2-a, with different values of notch radius were also considered. The first version with 0.25 mm in notch radius was called NT2-b and the second one with 0.4 mm in notch radius was called NT2-c. A general view of the mesh of the three studied geometries is reported in figure B-5.

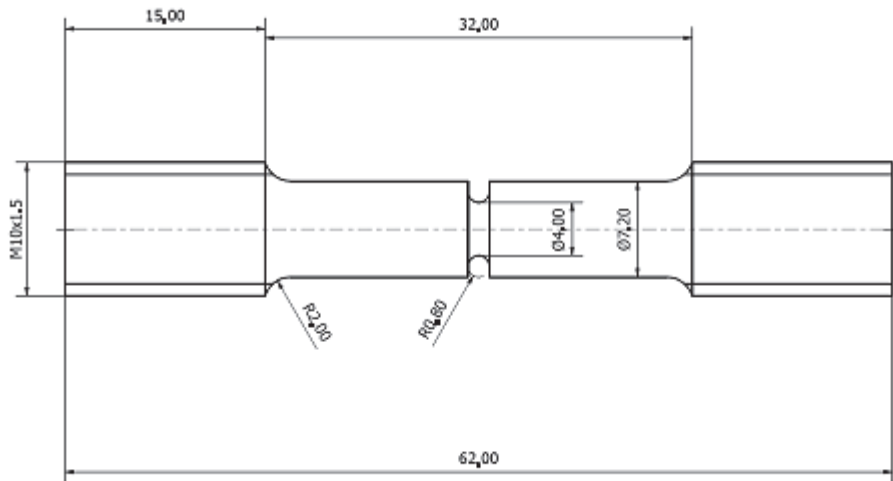


Figure B-4: Geometry of conventional (NT1) notched bar specimen used for loading along TD and RD directions

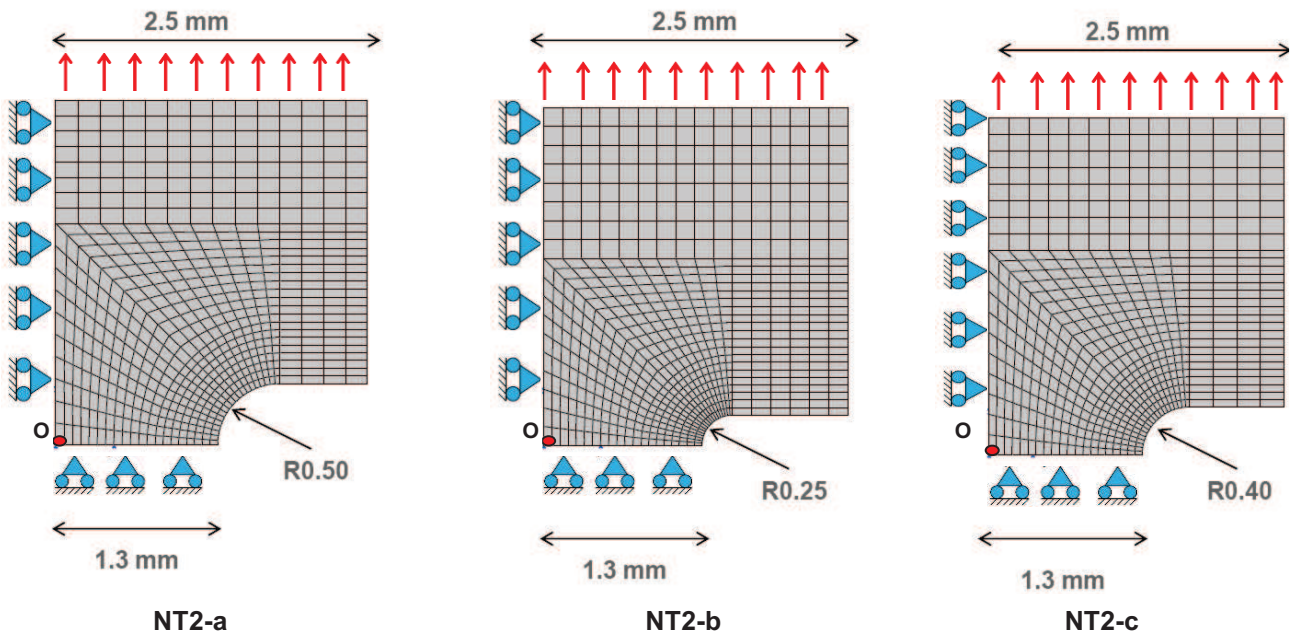


Figure B-5: Overview of the mesh of the three studied geometries

The comparison between geometries has been based on maximal axial stress values, since it is assumed to be an interesting preliminary cleavage fracture criterion. This maximal axial stress was expected to be located near the center of the specimen after general yielding and corresponding stress redistribution. That explains why the evolution of the axial stress at center of the specimen (point "O" in figure B-5) has been plotted for both geometries (figure B-6). The curve obtained for NT2-

b which had lower notch radius exhibited an unusual shape for diameter reductions lower than 0.15. Local examinations of the stress state within the three specimen geometries have been performed. The maximal axial stress was around the center of specimens, except for NT2-b for diameter reduction lower than 0.15. That might explain the unusual shape of the curve obtained for this specimen for lower diameter reductions. Nevertheless, from a global point of view, the maximal axial stress increased when the notch radius decreased, for a given value of diameter reduction.

According to the above mentioned design requirements, the volume of specimen scanned with a maximal principal stress higher than 2000 MPa at 30% of average diameter reduction was a key parameter. The maximal principal stress was found to be the axial stress for these geometries. Therefore, a first focus has been made on the axial stress distribution along the ligament at 30% of diameter reduction, since the axial stress is thought to be maximal within the ligament (section of minimum area). Figure B-7 shows this axial stress distribution. It appears that the maximal axial stress which was found near point "O" was higher for geometry NT2-b, as suggested by figure B-6 (for diameter reductions larger than 0.15). The ligament length scanned with a stress higher than 2000 MPa was respectively 0.35 mm, 0.45mm and 0.50 mm for geometries NT2-a, NT2-c and NT2-b. This result suggests that, for 30% in diameter reduction, the specimen area within the minimal section that is loaded with an axial stress of 2000 MPa increases when the notch radius decreases.

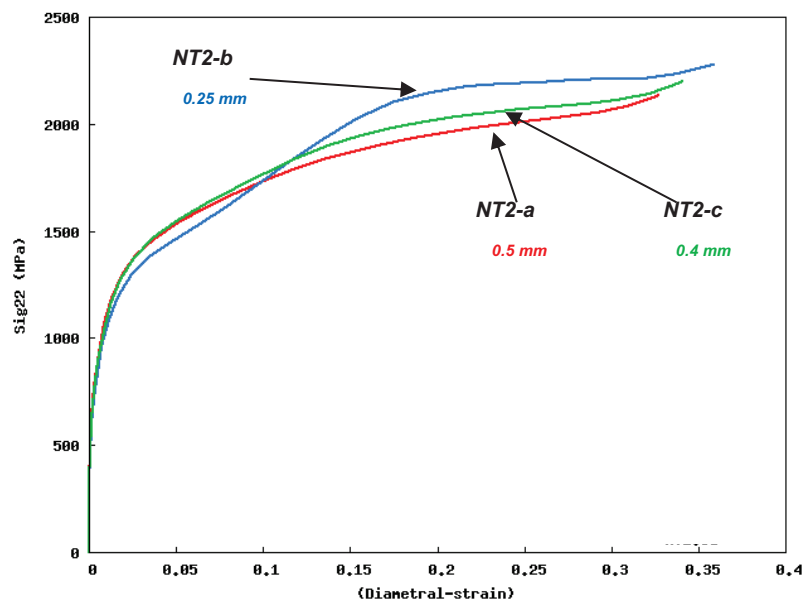


Figure B-6: Evolution of the axial stress at the center of specimens (Point "O"): NT2-a, NT2-b, NT2-c

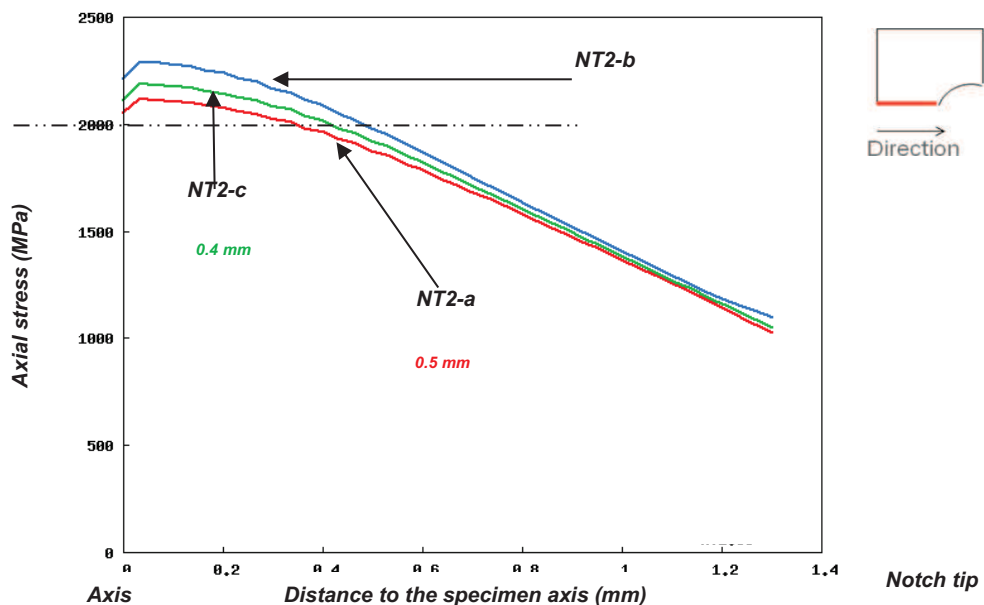


Figure B-7: Distribution of the axial stress along the ligament for various values of the notch radius at 30% of average diameter reduction

After having focussed on the distribution of axial stress along the ligament, an additional study was made on the volume in the whole specimen that was scanned with an axial stress of at least 2000 MPa at 30% of average diameter reduction. These volumes were approximated as spheres, so that the measurement could be simplified. Figure B-8 shows the regions in specimen where the axial stress exceeds 2000 MPa at 30% of diameter reduction for the three geometries, in the deformed configuration. This result supports the conclusion that, at 30% of diameter reduction, the volume of specimen scanned with a stress of 2000 MPa increases when the notch radius decreases.

The same studies were made to determine the volume of specimen scanned with a stress of at least 1700 MPa and 1500 MPa respectively, still at 30% of average diameter reduction. These regions are referred as “process zones” hereafter. The results are presented in figures B-9 and B-10. It was also found that the volume of the process zone increases with a decrease in the notch radius, but the difference between those volumes decreases when the threshold value of axial stress also decreases. For instance, for a targeted axial stress of 1500 MPa, the relative difference between these volumes for geometry NT2-b and NT2-c is only 10%.

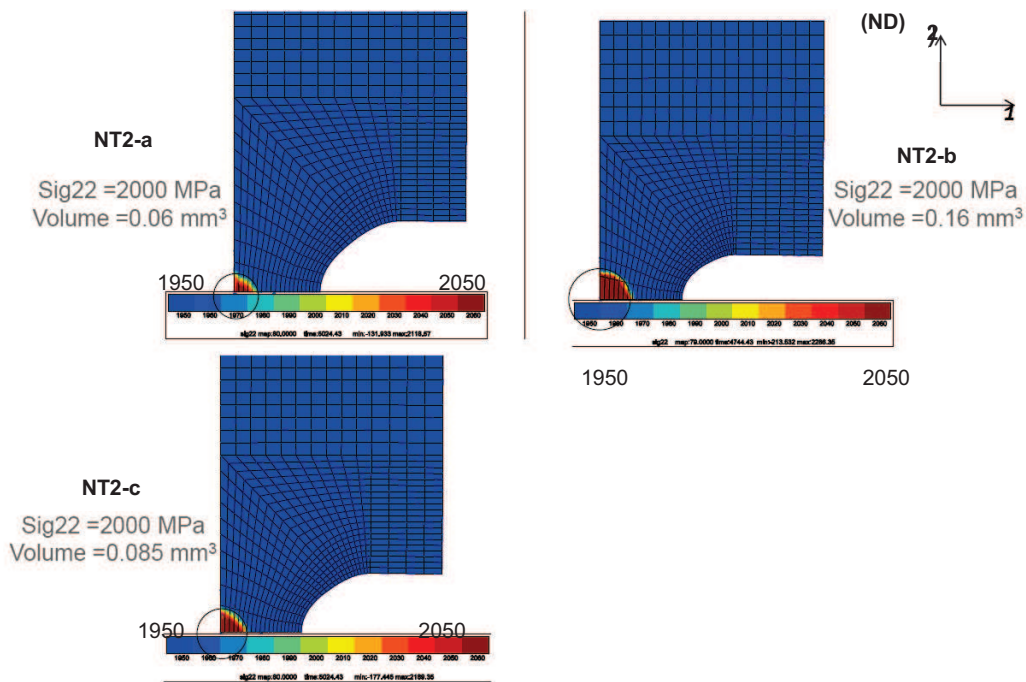


Figure B-8: Volume of specimen with an axial stress (σ_{22}) higher than 2000 MPa at 30% of diameter reduction (deformed configuration).

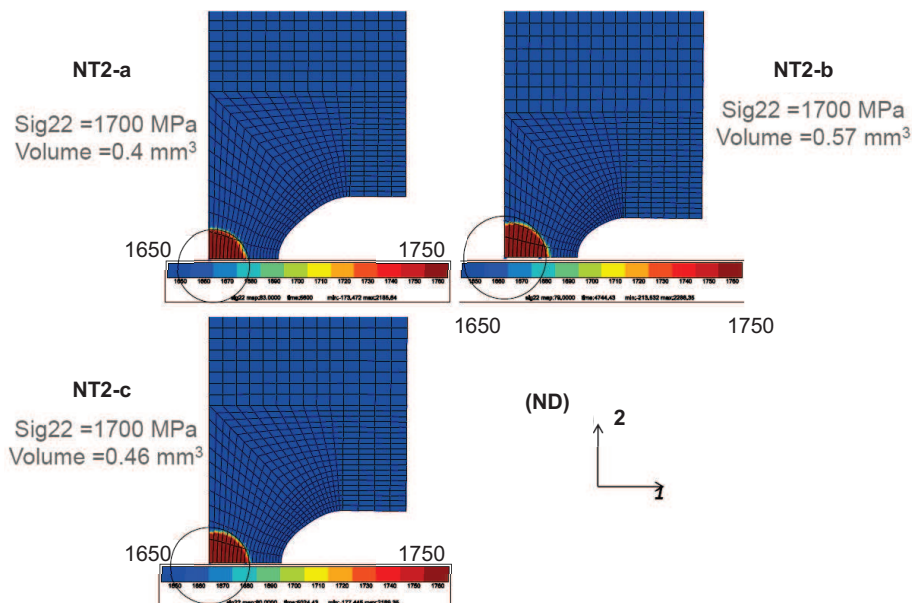


Figure B-9: Volume of specimen with an axial stress (σ_{22}) higher than 1700 MPa at 30% of diameter reduction (deformed configuration).

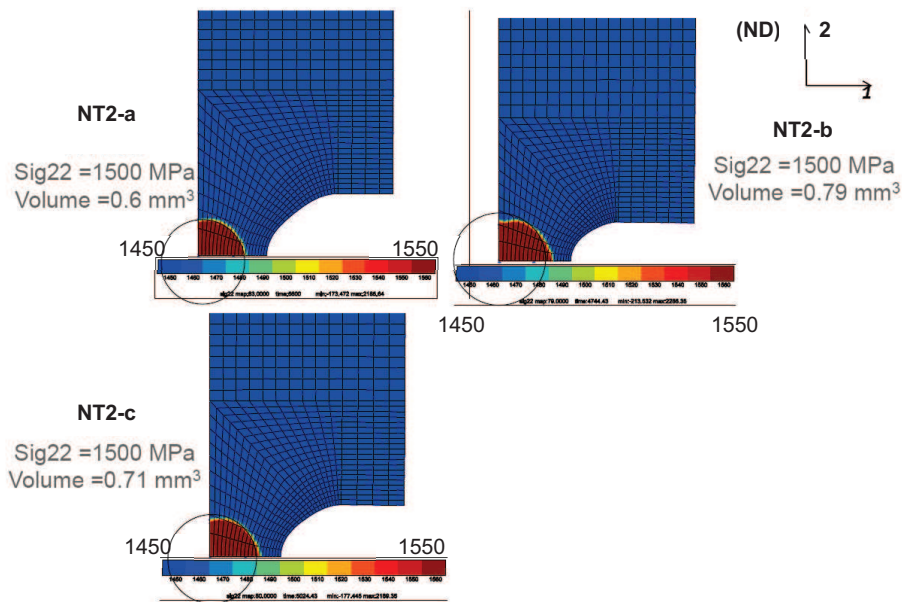


Figure B-10: Volume of specimen with an axial stress (σ_{22}) higher than 1500 MPa at 30% of diameter reduction (deformed configuration).

Preliminary conclusions:

Three geometries, namely, NT2-a, NT2-b and NT2-c with notch radius values respectively equal to 0.5 mm, 0.25 mm and 0.4 mm were studied for the design of notched specimens to be tested along the normal direction of the plates. For a diameter reduction of 30%, the volume of the specimen submitted to a maximum principal stress higher than 2000 MPa, 1700 MPa and 1500 MPa, respectively, was measured for each of those geometries (the results being summarized in table 1). This analysis shows that the measured volume increases when the notch radius decreases. Consequently, the cleavage fracture criterion is thought to be more readily satisfied when the value of the notch radius is lower.

According to this result, the geometry NT2.b with 0.25 mm was the most suitable one. But, this geometry is not appropriate in our particular case because of the small initial value of the notch opening (0.5 mm) which does not enable use of the available radial extensometer. Another problem with this geometry is the difficulty to machine such severe notches.

Finally, the geometry NT2-c with a notch radius of 0.4 mm has been chosen for the design of specimens along the normal direction. For this geometry, the stress triaxiality near the center of the specimen is approximately equal to 1.6 for a diameter reduction of 30%. It was also found that at this level of strain, the threshold plastic strain of 10^{-6} mentioned in literature [33] was reached all over the notched region.

	NT2-b (0.25 mm)	NT2-c (0.4 mm)	NT2-a (0.5 mm)
2000 MPa	0.16 mm ³	0.085 mm ³	0.06 mm ³
1700 MPa	0.57 mm ³	0.46 mm ³	0.4 mm ³
1500 MPa	0.79 mm ³	0.71 mm ³	0.6 mm ³

Table 1: Volume of specimen submitted to an axial stress higher than 2000 MPa, 1700 MPa and 1500 MPa, for the three geometries

B.1.4. Validation of the specimen geometry

Validation of geometry requirements

The main requirements concerning specimen geometry were the total length of the specimen and the diameter of specimen ends which were set to 18 mm and 5 mm respectively. These conditions were fulfilled with geometry NT2-c. Moreover, the minimal section diameter of this geometry is larger than 1 mm, which was the requested condition for the application of continuum mechanics.

Validation of condition for cleavage occurrence

This condition was based on the RKR model, it was summarized like this: “The volume of specimen scanned with a stress of at least 2000 MPa at 30% of radial strain should contain more than one large cluster of large grains”. In figure B-11, the projected volumes of material scanned with axial stresses of

at least 2000 MPa, 1700 MPa, 1500 MPa are represented on a micrograph of Steel A, along the rolling plane (delamination plane). According to this picture, geometry NT2-c fulfills the expected condition of cleavage occurrence, since large clusters of larger grains are readily found within the volume scanned with a stress greater than 2000 MPa.

Conclusion

NT2-c geometry fulfilled the design requirements. The experimental campaign of tensile tests along ND and BTd was performed using this geometry, denoted as NT2 in the remaining of this manuscript (including main text).

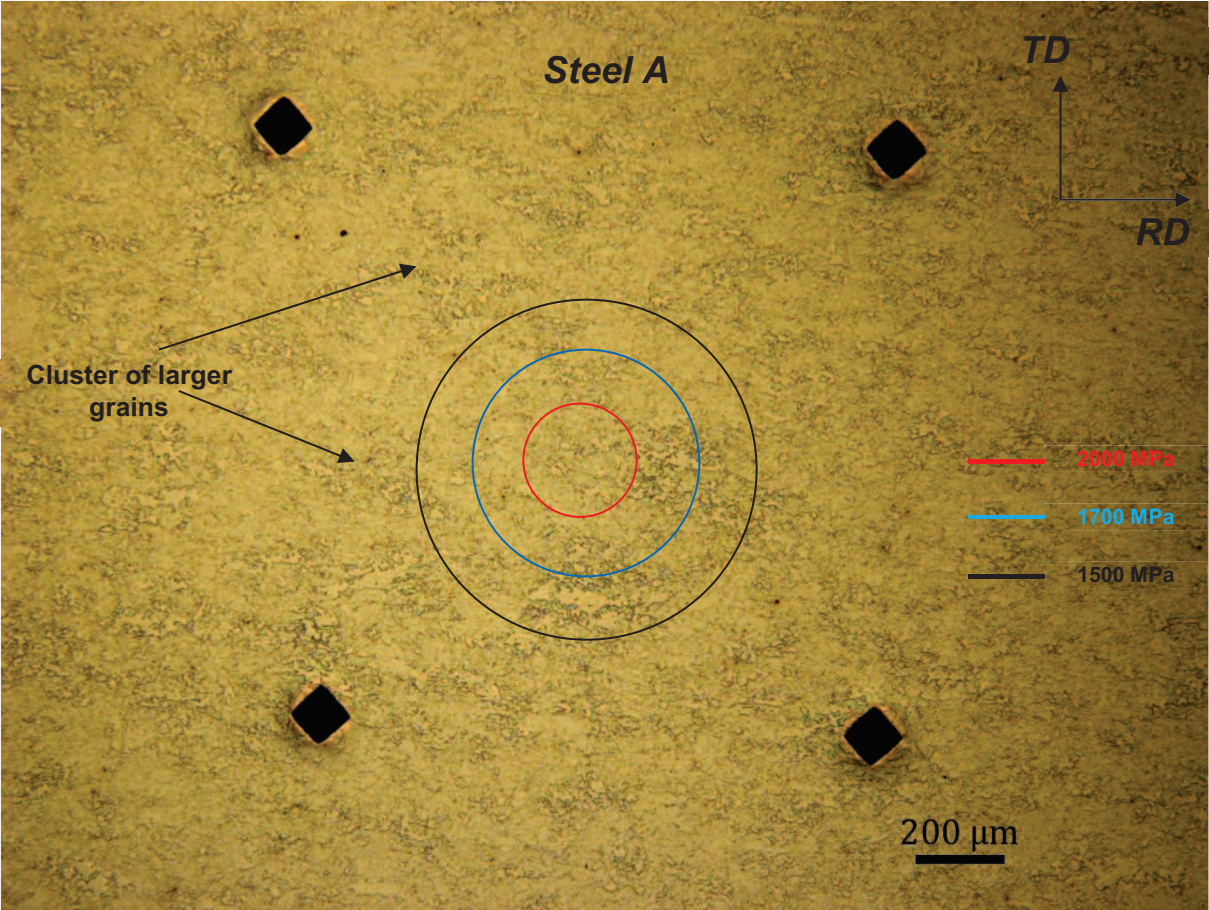


Figure B-11: Projection of the volume of specimen with axial stresses predicted to be larger than 2000 MPa, 1700 MPa, 1500 MPa, on Steel A micrograph

B.2. Results of tensile tests along ND

B.2.1. Tensile tests on smooth specimens

Temperature	Steel A (UT2 geometry)	
	0.2% proof stress (MPa)	Tensile strength (MPa)
-196°C	827	976
-140°C	715	796
-120°C	646	756
-100°C	610	722
-55°C	570	685
20°C	490	604

Steel B (UT2 geometry)		
Temperature	0.2% proof stress (MPa)	Tensile strength (MPa)
-196°C	955	978
-196°C	971	990
-196°C	940	1020
-140°C	780	835
-120°C	725	790
-120°C	720	790
-100°C	695	764
20°C	576	636
20°C	560	660

B.2.2. Tensile tests on notched specimens

Steel A (NT2 geometry)		
Temperature	Diameter reduction at fracture ()	Load line displacement rate (mm/s)
-100°C	0.13	5×10^{-3}
	0.19	5×10^{-3}
-90°C	0.19	10^{-3}
-80°C	0.29	10^{-3}
-70°C	0.29	5×10^{-3}
-60°C	0.33	5×10^{-3}
-55°C	0.33	10^{-3}
	0.31	5×10^{-3}
-50°C	0.31	5×10^{-3}
-40°C	0.33	5×10^{-3}
20°C	0.33	5×10^{-3}
	0.34	5×10^{-3}

Steel B (NT2 geometry)		
Temperature	Diameter reduction at fracture ()	Load line displacement rate (mm/s)
-196°C	0.003	5×10^{-3}
-140°C	0.13	5×10^{-3}
-130°C	0.15	5×10^{-3}
-120°C	0.17	5×10^{-3}
-110°C	0.14	5×10^{-3}
-100°C	0.26	5×10^{-3}
20°C	0.25	5×10^{-3}

B.3. Results of tensile tests along BTD

B.3.1. Tensile tests on smooth specimens

Steel A (UT2 geometry)		
Temperature	0.2% proof stress (MPa)	Tensile strength (MPa)
-196°C	970	976
-140°C	708	790
-120°C	660	760
-100°C	617	720
20°C	516	610

Steel B (UT2 geometry)		
Temperature	0.2% proof stress (MPa)	Tensile strength (MPa)
-196°C	945	980
20°C	540	640

B.3.2. Tensile tests on notched specimens

Steel A (NT2 geometry)		
Temperature	Diameter reduction at fracture()	Load line displacement rate (mm/s)
-196°C	0.06	5×10^{-3}
	0.02	5×10^{-3}
-150°C	0.02	5×10^{-3}
-140°C	0.17	5×10^{-3}
	0.18	5×10^{-3}
-120°C	0.2	5×10^{-3}
-100°C	0.23	5×10^{-3}
	0.09	5×10^{-3}
-90°C	0.33	5×10^{-3}
-80°C	0.22	5×10^{-3}
-55°C	0.35	5×10^{-3}
20°C	0.38	5×10^{-3}

Steel B (NT2 geometry)		
Temperature	Diameter reduction at fracture ()	Load line displacement rate (mm/s)
-196°C	0.02	5×10^{-3}
	0.02	5×10^{-3}
20°C	0.34	5×10^{-3}

B.4. Results of tensile tests along RD

B.4.1. Tensile tests on smooth specimens

Steel A (UT1 geometry)		
Temperature	0.2% proof stress (MPa)	Tensile strength (MPa)
20°C	518	613

Steel B (UT1 geometry)		
Temperature	0.2% proof stress (MPa)	Tensile strength (MPa)
20°C	523	630

B.4.2. Tensile tests on notched specimens

Steel A (NT1 geometry)			
Temperature	Final diam reduction ()	Final longi displacement (mm)	Load line displacement (mm/s)
-140°C	0.34	1.36	5×10^{-3}
-100°C	interrupted	interrupted	5×10^{-3}
	0.31	1.2	5×10^{-3}
-80°C	0.4	1.2	5×10^{-3}
-80°C	0.4	1.4	5×10^{-3}
20°C	interrupted	interrupted	5×10^{-3}

Steel A (NT2 modified geometry)		
Temperature	Final diam reduction ()	Load line displacement (mm/s)
-196°C	0.06	5×10^{-3}
	0.07	5×10^{-3}

Steel B (NT1 geometry)			
Temperature	Final diam reduction ()	Final longi displacement (mm)	Load line displacement (mm/s)
-120°C	0.29	1.4	5×10^{-3}
-100°C	0.28	1.1	5×10^{-3}
20°C	0.47	1.2	5×10^{-3}

Steel B (NT2 geometry)		
Temperature	Final diam reduction ()	Load line displacement (mm/s)
-196°C	0.04	5×10^{-3}
	0.04	5×10^{-3}

B.5. Results of tensile tests along TD

B.5.1. Tensile tests on smooth specimens

Steel A (UT1 geometry)		
Temperature	0.2% proof stress (MPa)	Tensile strength (MPa)
-196°C	977	995
-140°C	741	817
-120°C	672	785
-100°C	637	753
-100°C	636	744
-80°C	594	723
20°C	540	622

Steel B (UT1 geometry)		
Temperature	0.2% proof stress (MPa)	Tensile strength (MPa)
-196°C	970	996
-140°C	775	830
-120°C	700	790
-100°C	700	770
20°C	570	647

B.5.2. Tensile tests on notched specimens

Steel A (NT1 geometry)			
Temperature	Final diam reduction ()	Final longi displa (mm)	Load line displa (mm)
-140°C	0.3	1.5	5×10^{-3}
-100°C	0.3	1	5×10^{-3}
	0.32	1.36	5×10^{-3}
	interrupted	interrupted	5×10^{-3}
-60°C	0.38	1.1	5×10^{-3}
20°C	0.37	1.05	5×10^{-3}

Steel A (NT2 modified geometry)		
Temperature	Final diam reduction ()	Load line displacement (mm/s)
-196°C	0.02	5×10^{-3}
	0.05	5×10^{-3}

Steel B (NT1 geometry)			
Temperature	Final diam reduction ()	Final longi displa (mm)	Load line displa (mm)
-140°C	0.26	1	5×10^{-3}
-120°C	0.31	1.2	5×10^{-3}
-100°C	0.3	1.24	5×10^{-3}
-80°C	0.32	1.1	5×10^{-3}
-60°C	0.33	1.34	5×10^{-3}
-40°C	0.37	1.02	5×10^{-3}
20°C	0.4	Not measured	5×10^{-3}

Steel B (NT2 modified geometry)		
Temperature	Final diam reduction ()	Load line displacement (mm/s)
-196°C	0.06	5×10^{-3}
	0.04	5×10^{-3}

C- Elastic-plastic constitutive modelling for quasi-static tests

Tensile tests performed on notched specimens along ND, BT, RD and TD directions showed anisotropy in cleavage fracture behavior. To quantify the cleavage fracture sensitivity of specimens taken along the four considered directions, good knowledge of the stress state inside the notched specimen at the onset of cleavage fracture is required. Since this stress state could not be measured, numerical analysis was necessary to extract local stresses. The more accurate the numerical simulation, the more reliable the estimation of critical cleavage stresses.

In the first part of this appendix, the mesh size effect is reported and the results of simulation with linear and quadratic elements are compared. In the second part, elastic-plastic constitutive equations of Steel A and Steel B are determined with von Mises, Hill and Barlat plastic yield criteria. The results obtained with these plastic yield criteria are then compared, in terms of local stresses and global responses.

C.1. Choice of the mesh size and element type

The effects of mesh sizes and element types were analyzed on both NT1 and NT2 geometries which had different notch root radii. Figure C-1 illustrates the mesh design of both geometries for calculation. One eighth of specimens was simulated because of symmetry conditions. The initial height “h” of the element at the center of the specimen was chosen as the variable parameter for the mesh size dependence study. In fact, a linear relation between “h” and the smaller element length at the notch root was kept. The value of “h” was varied between 150 μm and 8 μm to analyze the mesh size effect. This effect was firstly studied from a global point of view by comparing the effective stress vs. longitudinal displacement, and effective stress vs. diameter reduction curves (Figure C-2). According to these curves, within the range of element size considered, global responses were not affected for any of both geometries. This result was obtained both for linear elements (full integration) and for quadratic elements (reduced integration).

The local distribution of axial stress and of radial stress was then studied for both geometries. The distribution of these stresses has been plotted along the symmetry axis and along two perpendicular radii. Since both results were comparable, only the distribution along the axis of symmetry is reported here. The analysis was done for the loading condition experimentally observed at fracture.

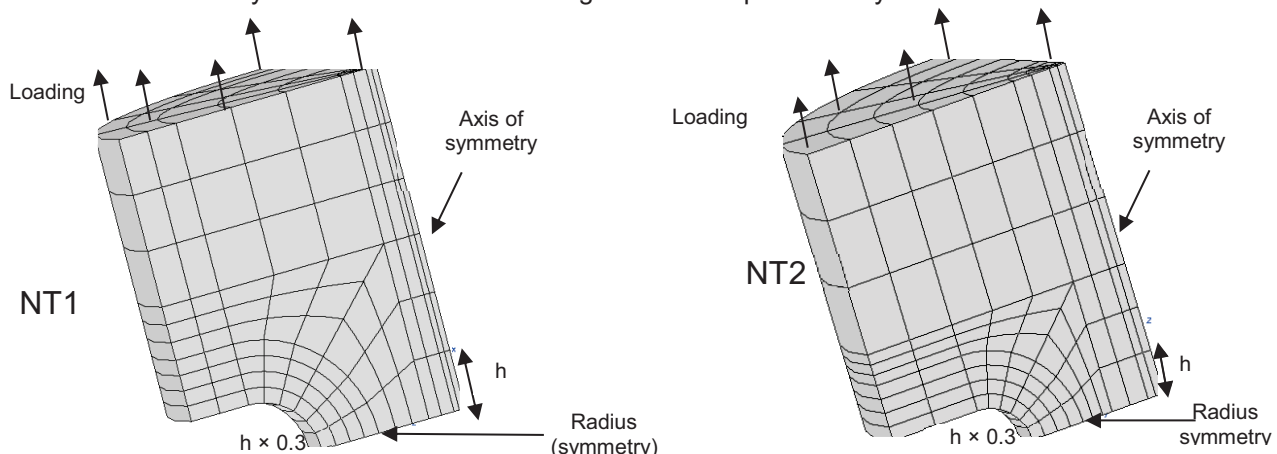


Figure C-1: Mesh design of NT1 and NT2 geometries for numerical calculations

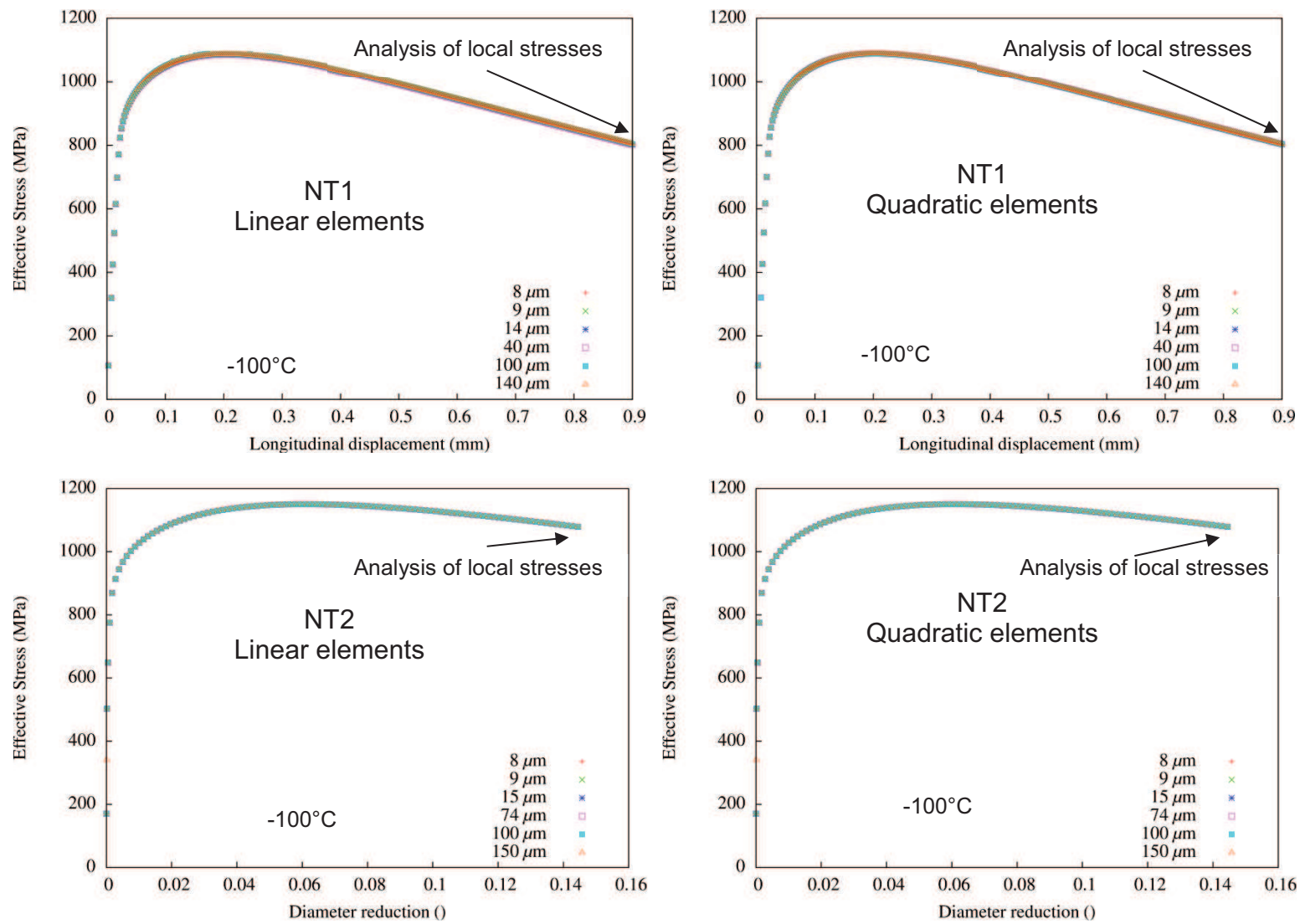


Figure C-2: Effect of mesh size and element type on the global response of NT1 and NT2 geometries: Linear and quadratic elements. Simulation of tensile tests at -100°C; stress distributions are analyzed at the stage indicated by arrows

C.1.1. Mesh size effect on local stress distribution with linear elements

Figures C-3 and C-4 show the distribution of axial and radial stresses along the axis of symmetry on the initial configuration. As observed for the global response, there is no significant mesh size effect. The ratio between axial and radial stresses is higher than 2.

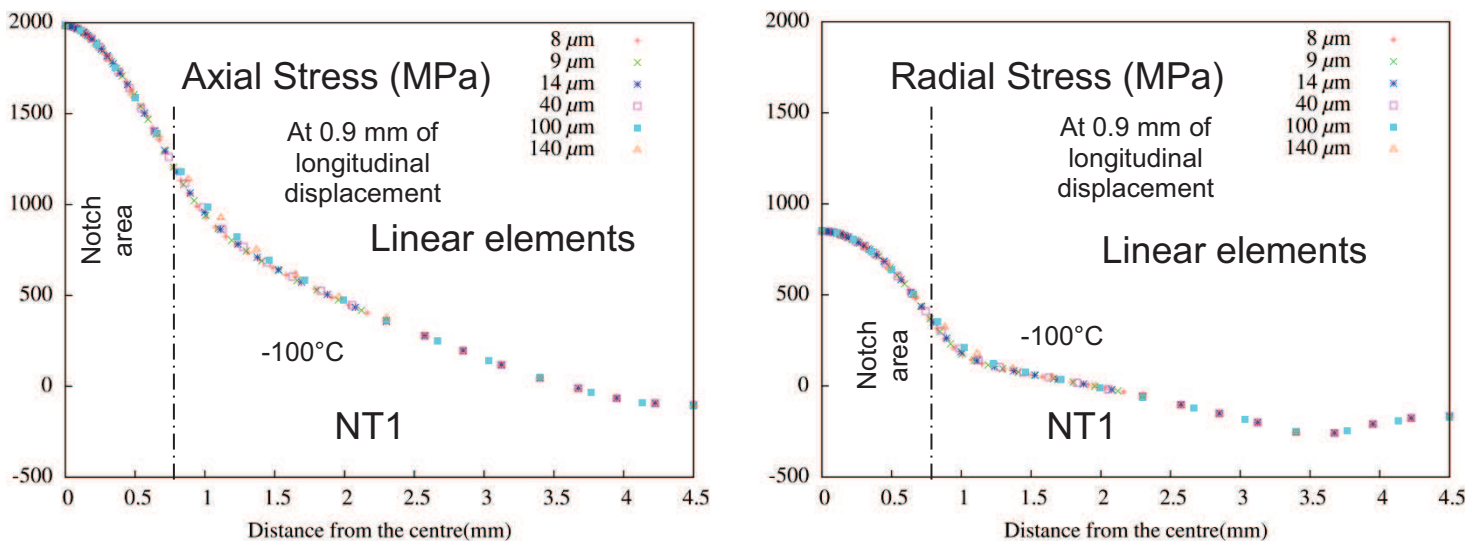


Figure C-3: Effect of mesh size on axial and radial stress distributions along the symmetry axis (NT1 geometry)

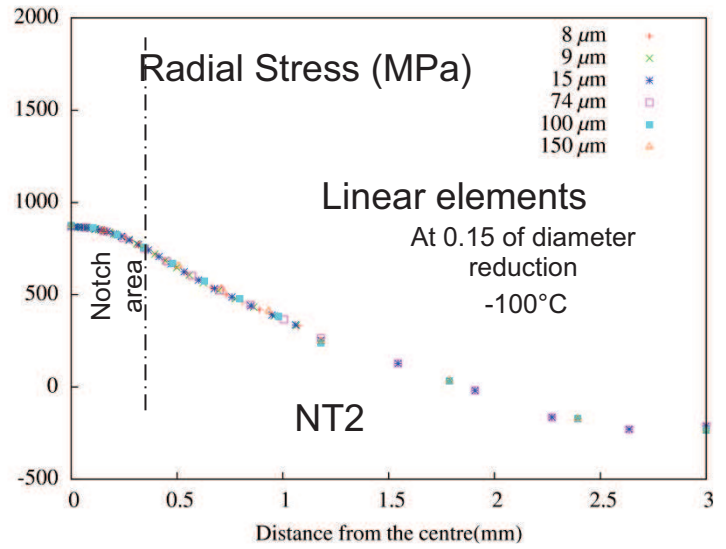
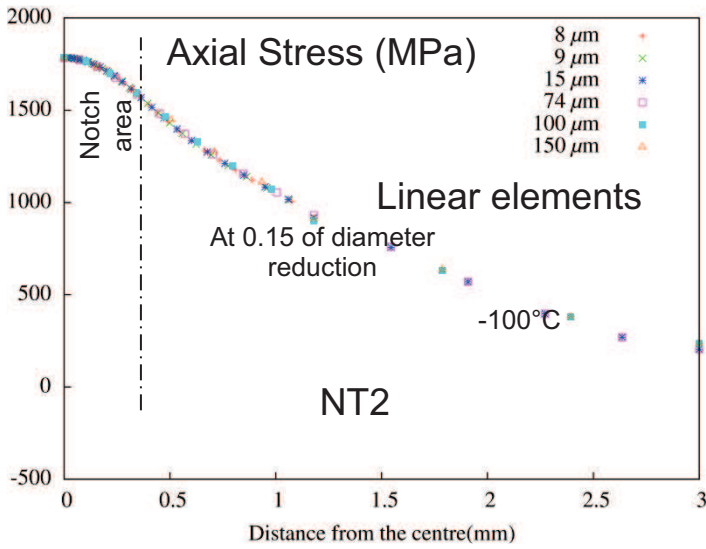


Figure C-4: Effect of mesh size on axial and radial stress distributions along the symmetry axis (NT2 geometry)

C.1.2. Mesh size effect on local stress distribution with quadratic elements

Figures C-5 and C-6 show the distribution of axial and radial stresses along the symmetry axis. No significant mesh size effect has been observed.

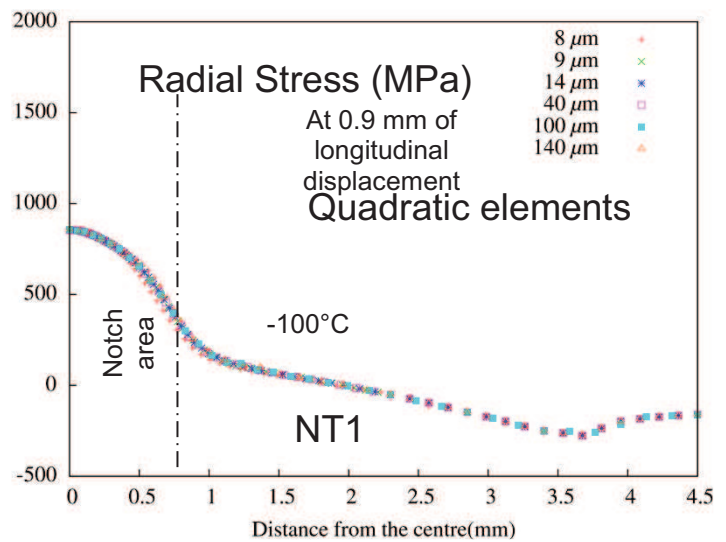
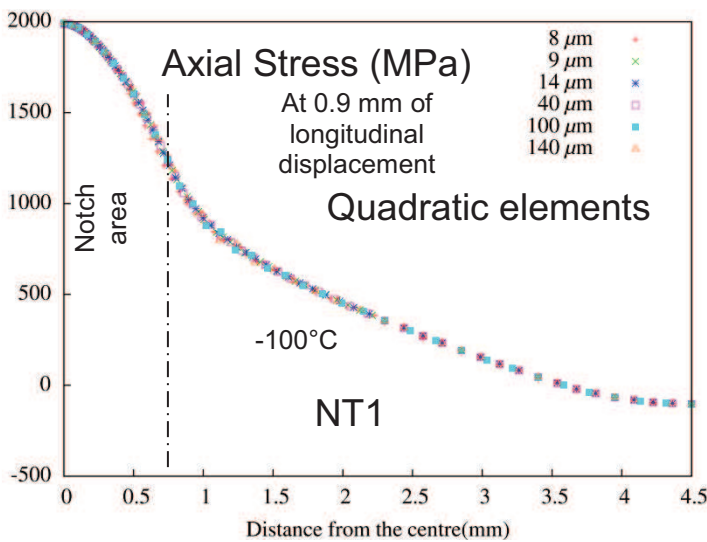


Figure C-5: Effect of mesh size on axial and radial stress distributions along the symmetry axis (NT1 geometry)

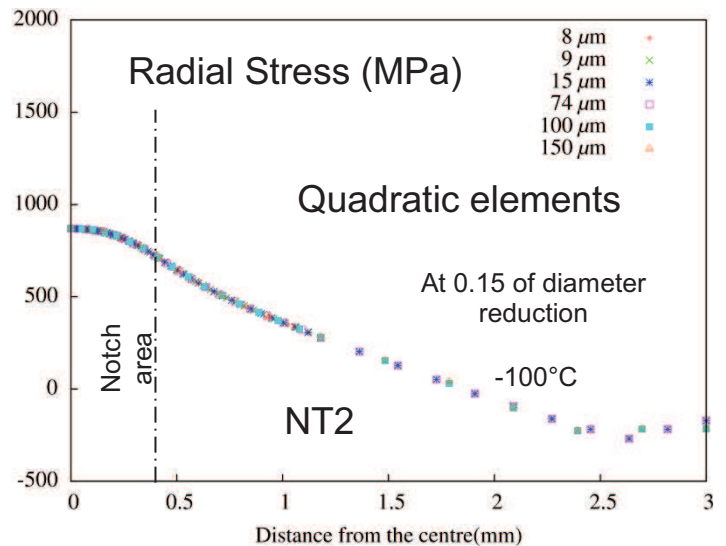
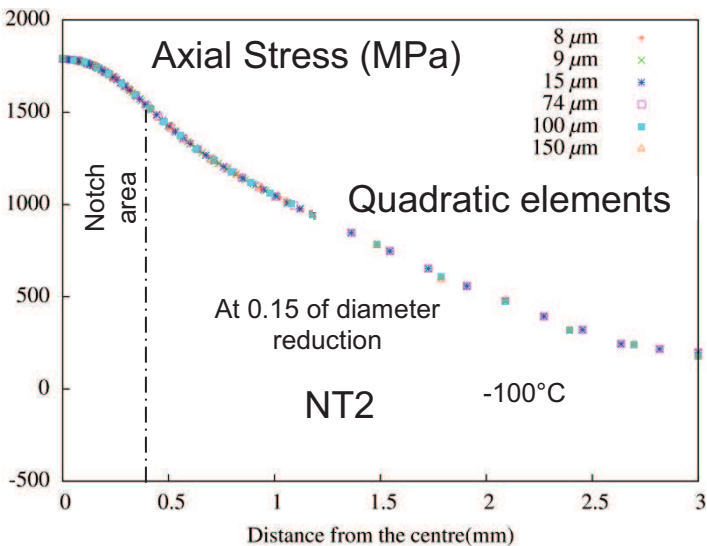


Figure C-6: Effect of mesh size on axial and radial stress distributions along the symmetry axis (NT2 geometry)

C.1.3. Comparison of local stress distributions for linear and quadratic elements

For a mesh size of 150 μm , axial and radial stress distributions have been compared with linear and quadratic elements (Figure C-7). The results with linear and quadratic elements are similar.

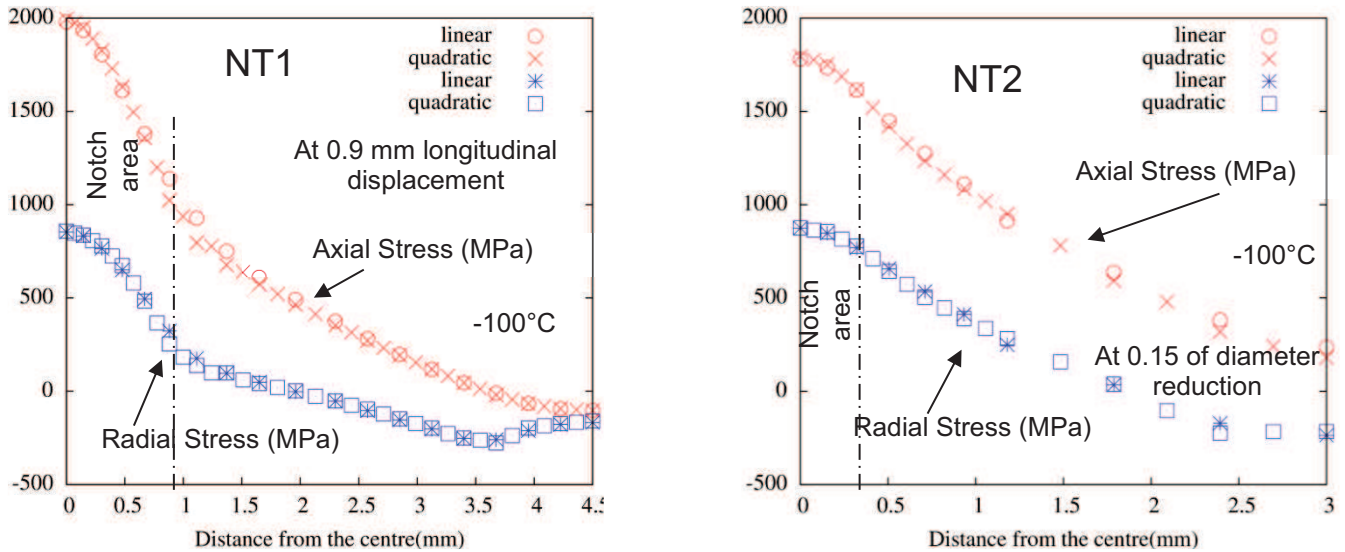


Figure C-7: Comparison of the stress distribution with linear and quadratic elements

C.1.4. Choice of mesh size and element type

For elastic-plastic calculations, reduced quadratic elements with a mesh size of 15 μm at the center of the specimen have been chosen, to get precise values of local stresses and accurately estimate critical cleavage stress.

C.2. Modeling of the elastic-plastic constitutive behavior

All calculations were carried out using a finite strain framework but for the sake of simplicity, model equations presented below are expressed using small strain formalism. Even if 15 μm quadratic elements used at the center were necessary for a proper description on the local stress state, such a fine mesh did not enable an iterative procedure for the identification of parameters of the constitutive equations. Therefore, the fine mesh has been kept for local stress analysis and a coarser mesh was used for the parameter identifications. This coarse mesh was chosen so that the global load vs. displacement curve obtained with this mesh should be similar to the one obtained with the fine mesh. The mesh sizes used for parameters identification were therefore fixed at 700 μm for NT1 and 400 μm for NT2.

The following assumptions have been assumed for the calibration of an optimal elastic-plastic model:

- Plastic flow anisotropy is independent of temperature, so that the anisotropy parameters identified at room temperature could be used for other temperatures. In term of stress anisotropy this assumption is plausible, since the stress anisotropy was negligible for all the temperature (chapter III). Concerning the strain anisotropy, Lankford coefficients were measured at only one temperature per tested direction.
- For temperatures lower than -100°C , strain hardening is independent of temperature. Only the yield stress increases with an exponential manner when temperature decreases. This assumption was supported by experimental results of chapter III. Therefore, the hardening parameters have

been determined at 20°C and -100°C. The hardening parameters determined at -100°C have also been used for temperatures lower than -100°C.

C.2.1. Elastic-plastic constitutive model

Isotropic elastic properties were assumed (Young's modulus of 210 GPa and Poisson ratio of 0.3). Three yield criteria were considered, namely, a von Mises yield criterion, the quadratic anisotropic Hill criterion [47] and the anisotropic criterion developed by Barlat et al. [48].

The yield surface was defined as:

$$f(\underline{\sigma}, p) = (\underline{\sigma})_{eq} - R(p) \quad (\text{Equation C-1})$$

where $R(p)$ which defines the isotropic hardening, follows a Voce equation:

$$R(p) = R_0 + H p + Q(1 - \exp(-bp)) \quad (\text{Equation C-2})$$

The definition of $(\underline{\sigma})_{eq}$ depend on the chosen yield criterion.

For the von Mises yield criterion:

$$(\underline{\sigma})_{eq} = \sqrt{\frac{3}{2} \underline{\sigma}^d : \underline{\sigma}^d} \quad (\text{Equation C-3})$$

$$\underline{\sigma}^d = \underline{\sigma} - \frac{1}{3} \text{Trace}(\underline{\sigma}) \underline{I} \quad (\text{Equation C-4})$$

For the Hill yield criterion:

$$(\underline{\sigma})_{eq} = \sqrt{\frac{3}{2} \underline{\sigma}^d : \underline{H} : \underline{\sigma}^d} \quad (\text{Equation C-5})$$

$$\underline{\sigma}^d = \underline{\sigma} - \frac{1}{3} \text{Trace}(\underline{\sigma}) \times \underline{I} \quad (\text{Equation C-6})$$

Where the Hill tensor \underline{H} is represented by a 6×6 diagonal matrix in Voigt's notation, with coefficients h_i , and describes the plastic anisotropy.

For the Barlat yield criterion:

$$(\underline{\sigma})_{eq} = \frac{1}{2} \left(\left| \sigma^{dev}_1 - \sigma^{dev}_2 \right|^a + \left| \sigma^{dev}_2 - \sigma^{dev}_3 \right|^a + \left| \sigma^{dev}_3 - \sigma^{dev}_1 \right|^a \right)^{1/a} \quad (\text{Equation C-7})$$

Where $\sigma^{dev}_1 \geq \sigma^{dev}_2 \geq \sigma^{dev}_3$ are the eigenvalues of tensor $\underline{\sigma}^{dev}$

$$\underline{\sigma}^{dev} = \underline{S} : \underline{\sigma}, \text{ with } \underline{S} = \begin{pmatrix} \frac{c_2 + c_3}{3} & -\frac{c_3}{3} & -\frac{c_2}{3} & 0 & 0 & 0 \\ -\frac{c_3}{3} & \frac{c_1 + c_3}{3} & -\frac{c_1}{3} & 0 & 0 & 0 \\ -\frac{c_2}{3} & -\frac{c_1}{3} & \frac{c_1 + c_2}{3} & 0 & 0 & 0 \\ 0 & 0 & 0 & c_4 & 0 & 0 \\ 0 & 0 & 0 & 0 & c_5 & 0 \\ 0 & 0 & 0 & 0 & 0 & c_6 \end{pmatrix} \quad (\text{Equation C-8})$$

Therefore the parameters to be identified are:

- For the model with the von Mises yield criterion: R_0 , H , b and Q
- For the model with the Hill yield criterion: R_0 , H , b , Q , h_1 , h_2 , h_3 , h_4 , h_5 and h_6
- For the model with the Barlat yield criterion: R_0 , H , b , Q , a , c_1 , c_2 , c_3 , c_4 , c_5 and c_6

C.2.2. Procedure for the identification of constitutive parameters

The parameters of the constitutive equations have been identified using the tensile curves obtained with smooth and notched specimens, and the Lankford coefficients determined on smooth specimens (chapter III). In order to complete the experimental database for a better description of the strain anisotropy, a coefficient similar to Lankford coefficient was determined on notched specimens as the ratio of the minimal to the maximal diameter reductions. The various values of strain anisotropy ratio of notched specimens are presented in table C-1.

Identification was first performed at 20°C, then at -100°C. The parameters identified at -100°C were also been used for temperature lower than -100°C, except for the yield strength R_0 which was considered to evolve with temperature in an exponential manner already presented in chapter III:

$$R_0(T) = \sigma_a + d \times \exp(-c \times (T+273.15)) \quad (T \text{ in } ^\circ\text{C}) \text{ Equation C.9}$$

	ND	BTD	RD	TD
Steel A	0.89	0.78	0.75	0.83
Steel B	1.00	0.86	0.80	0.89

Table C-1: Strain anisotropy ratios of notched specimens for Steel A and Steel B

a- Identification of parameters at 20°C

In that study, it was decided to perform the identification of parameters from the more complex to the less complex model. Therefore, the first model considered for the identification of parameters was that with the Barlat yield criterion. A Levenberg-Marcquardt optimization algorithm was used to minimize differences between numerical prediction and experimental database containing tensile curves, Lankford ratio on smooth specimens and strain anisotropy ratio on notched specimens. In order to limit the number of parameter to be identified and thus computation time, parameter a of the Barlat criterion was set to 12, so that the yield surface could be similar to Tresca which was adapted for the investigated steels.

The next step of identification was performed for the model using the Hill criterion. Despite a number of trials, the model was not able to predict both stress and strain anisotropy. For this study, the priority was put on stress anisotropy, so that tensile curves could be well predicted.

Finally, parameters of the model with the von Mises yield criterion were set by assigning a value of 1 to all anisotropic Hill parameters.

By assuming the independence of anisotropy parameters with respect to test temperature, the anisotropic parameters identified at 20°C have been used for other temperatures.

b- Identification of parameters at -100°C

At -100°C, only hardening parameters H, Q, b have been determined for each of the three models.

c- For temperature lowers than -100°C

All parameters determined at -100°C have been used except for the yield strength. The effect of temperature has been included on the yield strength value (Equation C-9).

C.2.3. Results of constitutive parameter identification for Steel A

The hardening-related parameters H, b, Q were the same for both three plastic yield criteria: von Mises, Hill and Barlat (Table C-2). The yield strength R_0 was estimated from equation C-9, with $\sigma_a = 478 \text{ MPa}$; $d=1036 \text{ MPa}$; $c=0.013$ for Steel A.

The complementary parameters necessary for the description of Hill and Barlat plastic yield criteria are presented in table C-3 and table C-4 respectively. The parameters determined for Hill yield

criteria are further to one compared to parameters of Barlat yield criterion. Nevertheless both criteria suggest a noticeable anisotropy of plastic behavior.

	H (MPa)	b	Q (MPa)
T=20°C	435	28	165
T≤-100°C	430	17	220

Table C-2: Strain hardening parameters of Steel A

a	C ₁	C ₂	C ₃	C ₄	C ₅	C ₆
12	1.038	1.057	0.952	1.041	1.034	1.032

Table C-3: Parameters of Barlat yield criterion for Steel A, independent of temperature

h ₁	h ₂	h ₃	h ₄	h ₅	h ₆
0.955	0.980	1.125	1.204	1.059	1.353

Table C-4: Parameters of Hill yield criterion for Steel A, independent of temperature

Experimental and predicted tensile curves are presented in Figures C-8 to C-20. For each considered temperature, the numerical curves respectively predicted using von Mises, Hill and Barlat criteria are compared to experiment. Concerning tensile tests on smooth specimens, the model does not aim at accurately describing the yield point which was commonly observed for plastic strain lower than 0.02. In fact, cleavage cracking was found to occur for plastic strains higher than 0.05 even at -196°C. For notched specimens, effective stress vs. longitudinal displacement and effective stress vs. diameter reduction curves were used for parameter identification. The color code is the same for all the following curves, which explains why some graphs have less contrasted colors.

For all considered temperatures, tensile curves obtained with Barlat and Hill criteria are in good agreement with experiments. The maximal error between simulations and experiments is less than 5%. The error between simulations and experiments using the von Mises criterion is around 10 %.

Temperature = 20°C

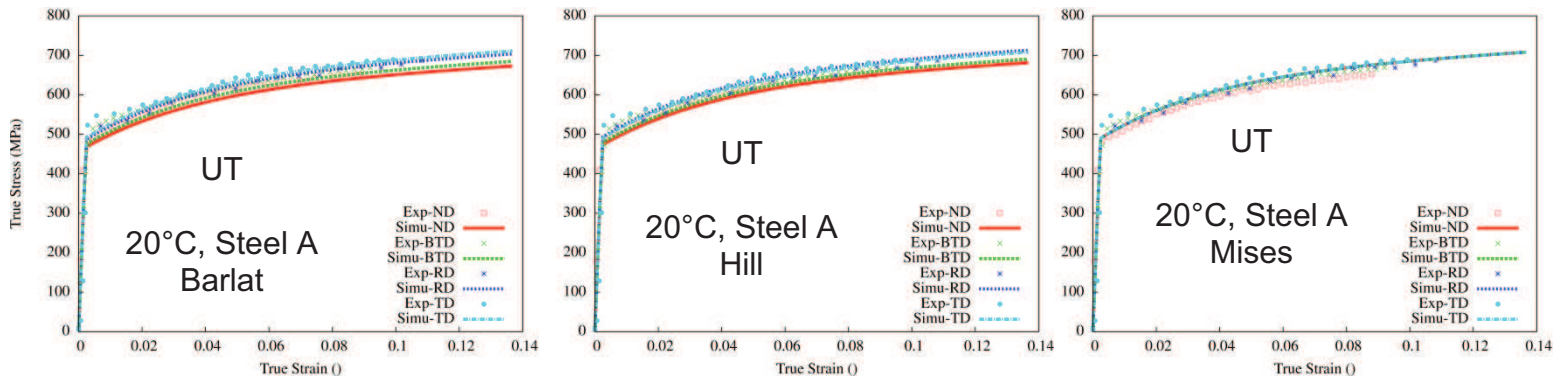
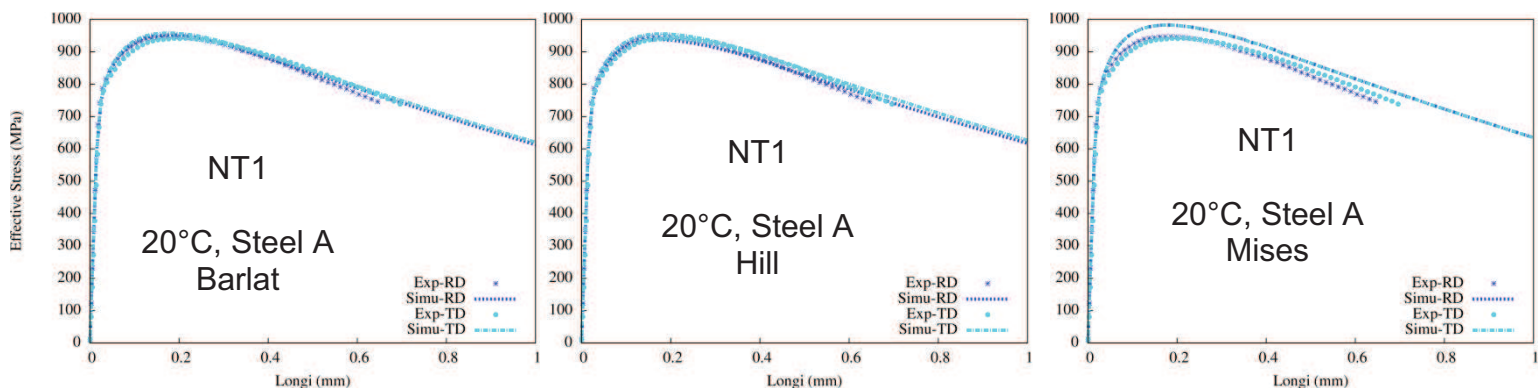


Figure C-8: Comparison between experimental curves and predictions from the three models. Tensile tests on smooth specimens. Steel A, 20°C.



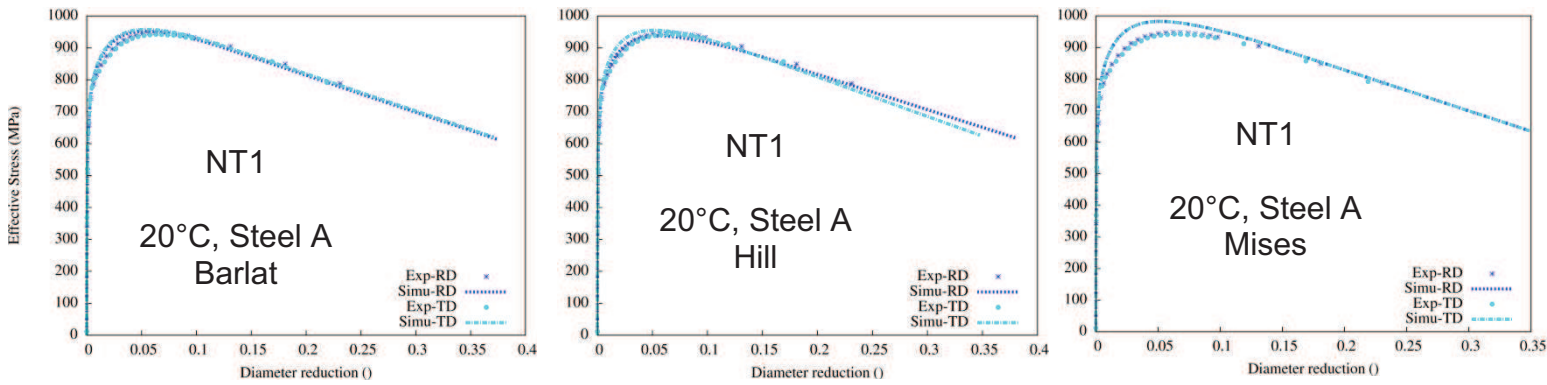


Figure C-9: Comparison between experimental and predictions from the three models. Tensile tests on NT1 specimens. Steel A, 20°C.

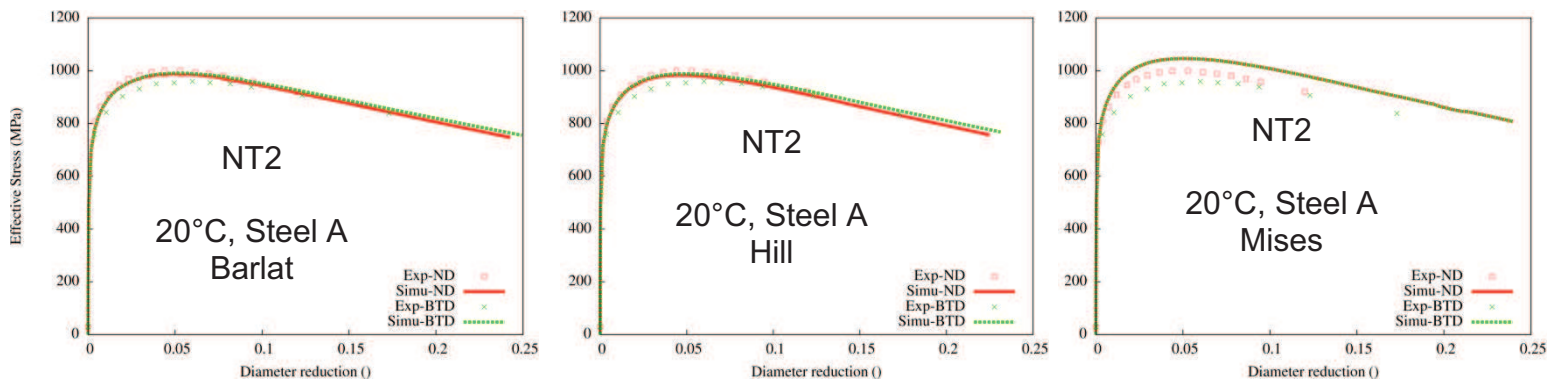


Figure C-10: Comparison between experimental curves and predictions from the three models. Tensile tests on NT2 specimens. Steel A, 20°C.

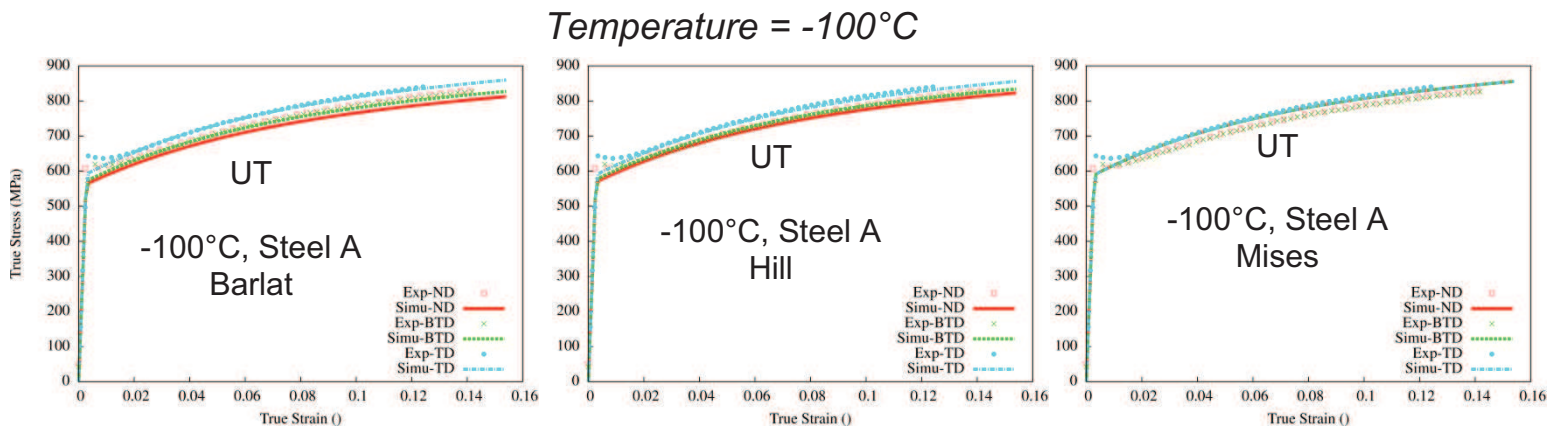
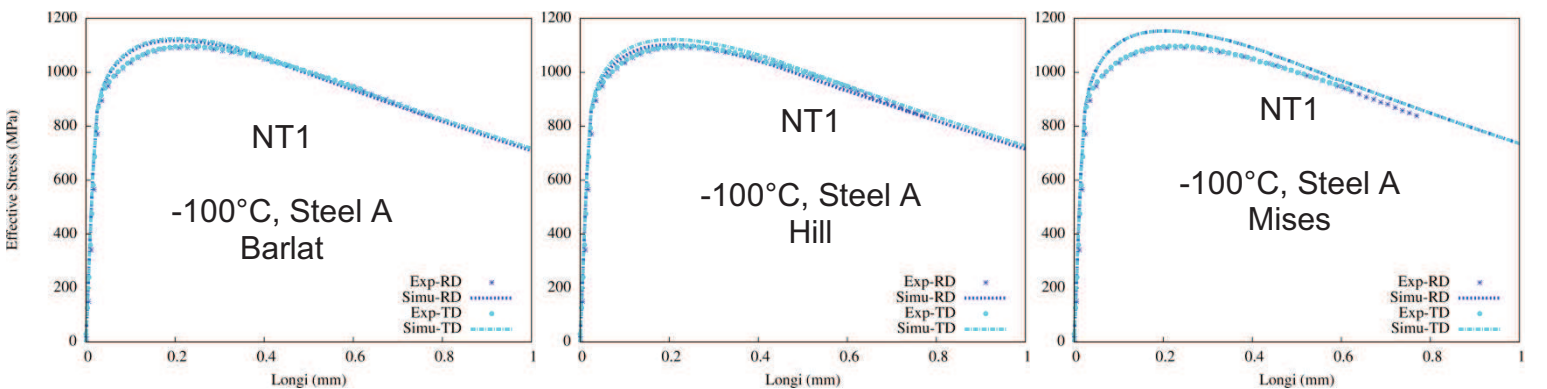


Figure C-11: Comparison between experimental curves and predictions from the three models. Tensile tests on smooth specimens. Steel A, -100°C.



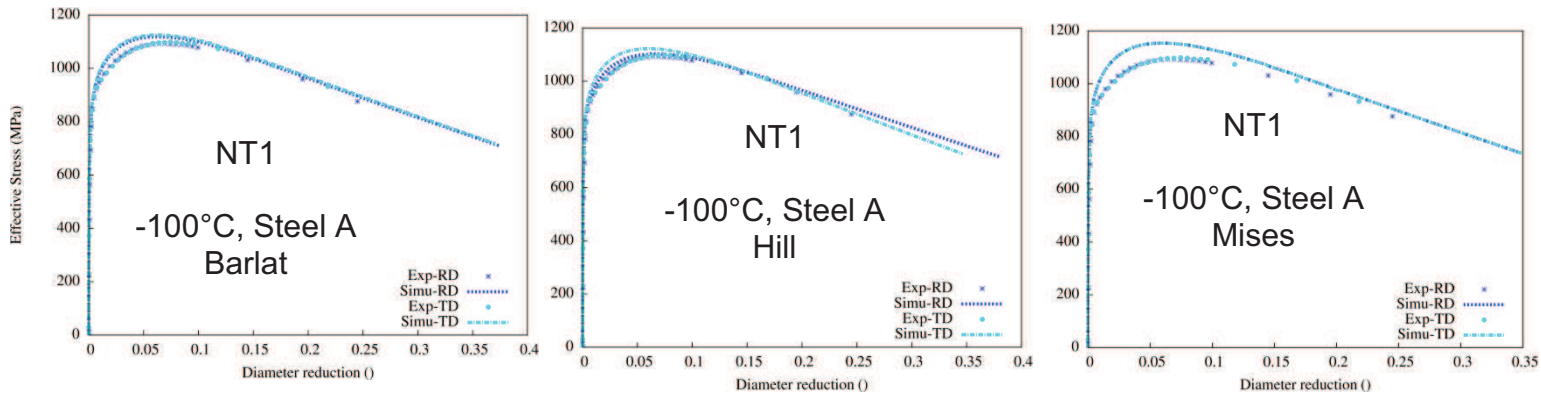


Figure C-12: Comparison between experimental curves and predictions from the three models. Tensile tests on NT1 specimens. Steel A, -100°C.

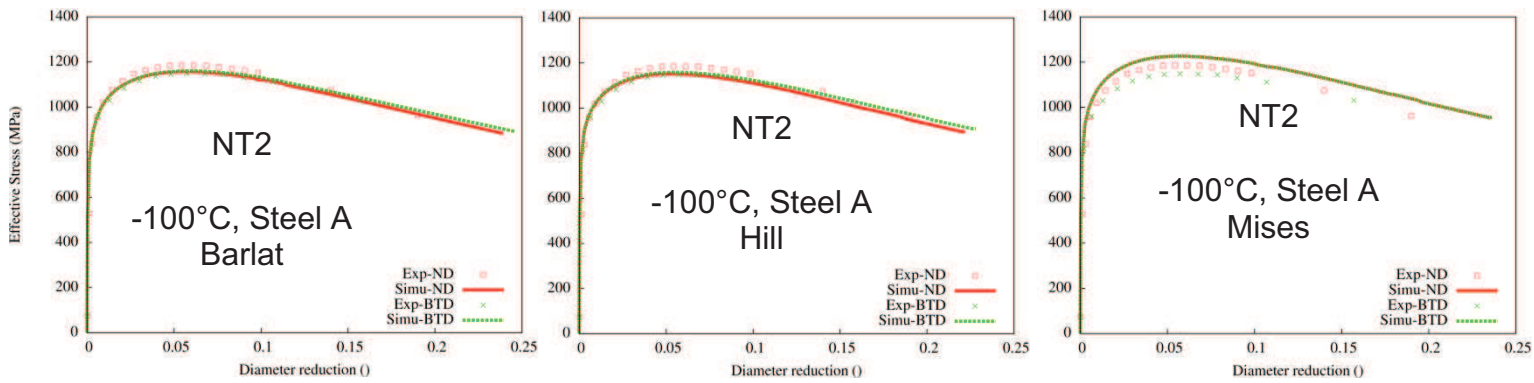


Figure C-13: Comparison between experimental curves and predictions from the three models. Tensile tests on NT2 specimens. Steel A, -100°C.

Temperature = -120°C

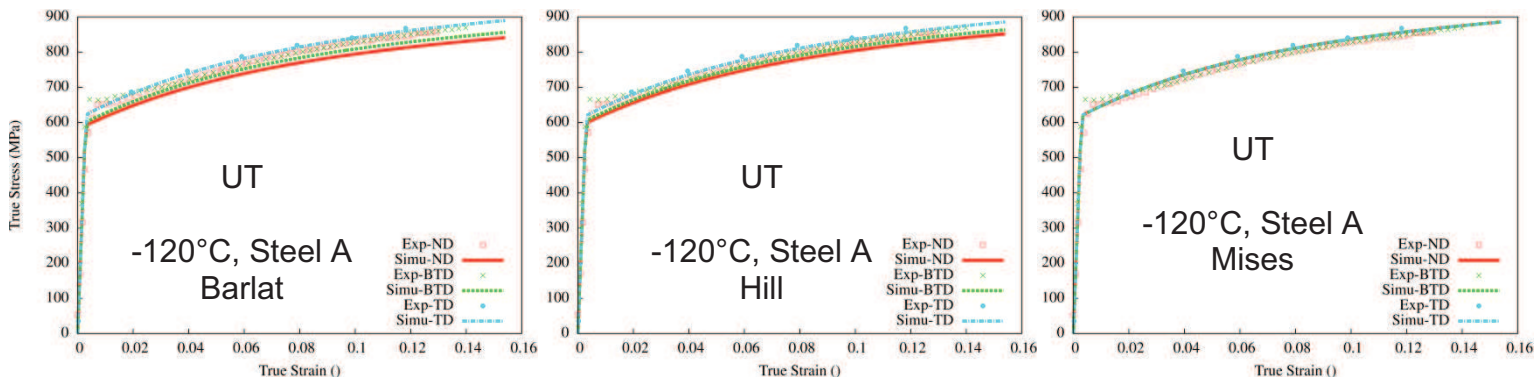


Figure C-14: Comparison between experimental curves and predictions from the three models. Tensile tests on smooth specimens. Steel A, -120°C.

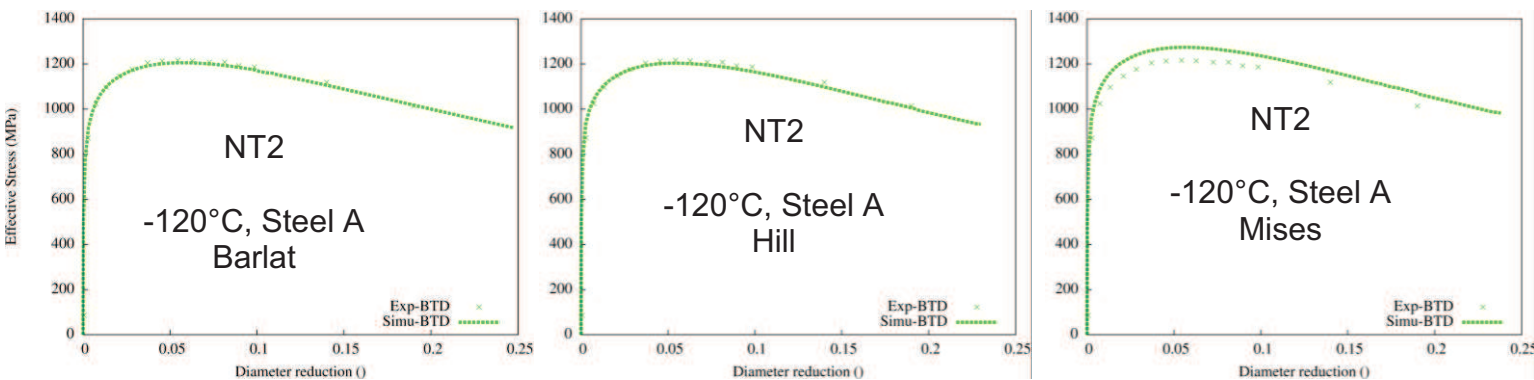


Figure C-15: Comparison between experimental curves and predictions from the three models. Tensile tests on NT2 specimens. Steel A, -120°C.

Temperature = -140°C

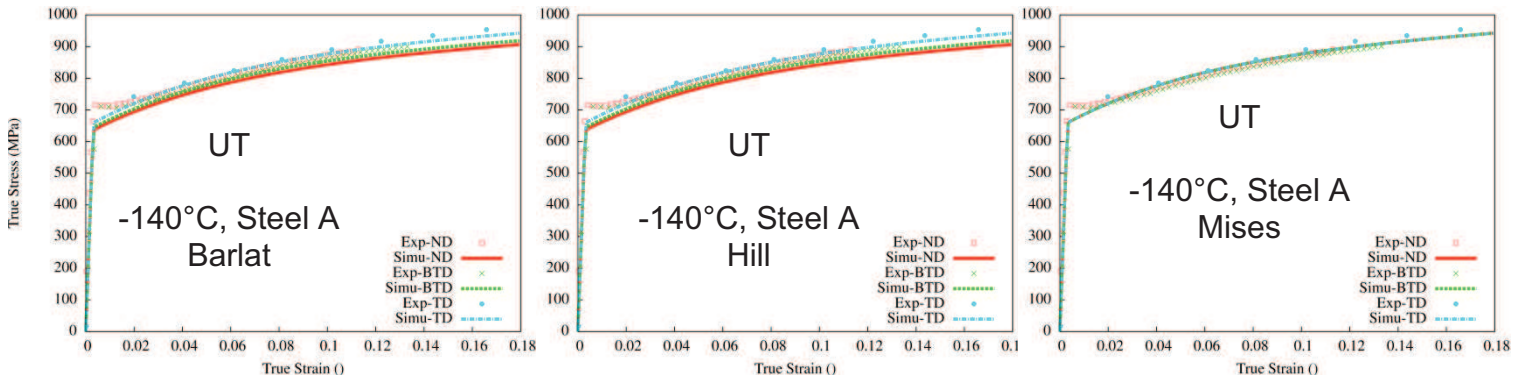


Figure C-16: Comparison between experimental curves and predictions from the three models. Tensile tests on smooth specimens. Steel A, -140°C.

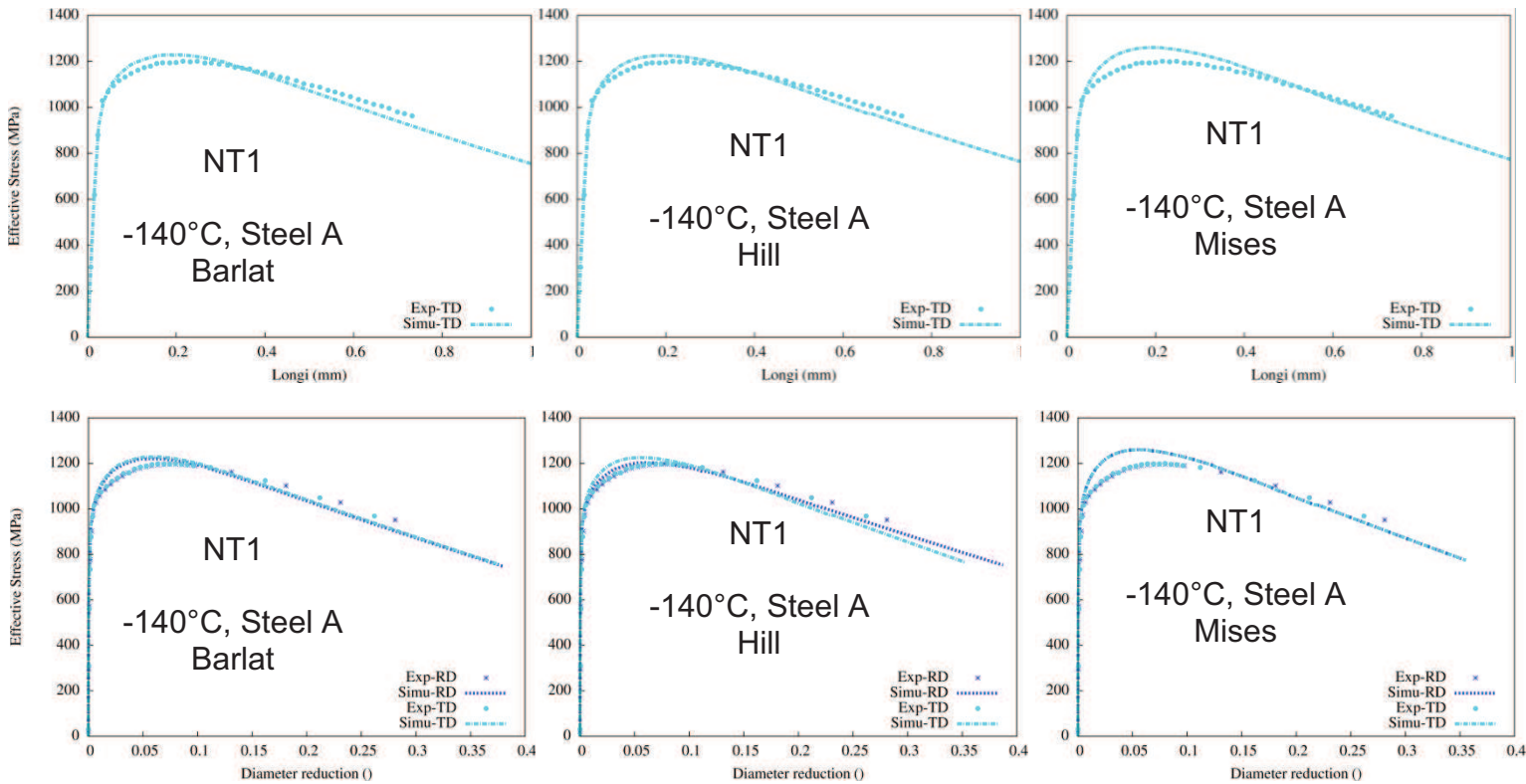


Figure C-17: Comparison between experimental curves and predictions from the three models. Tensile tests on NT1 specimens. Steel A, -140°C.

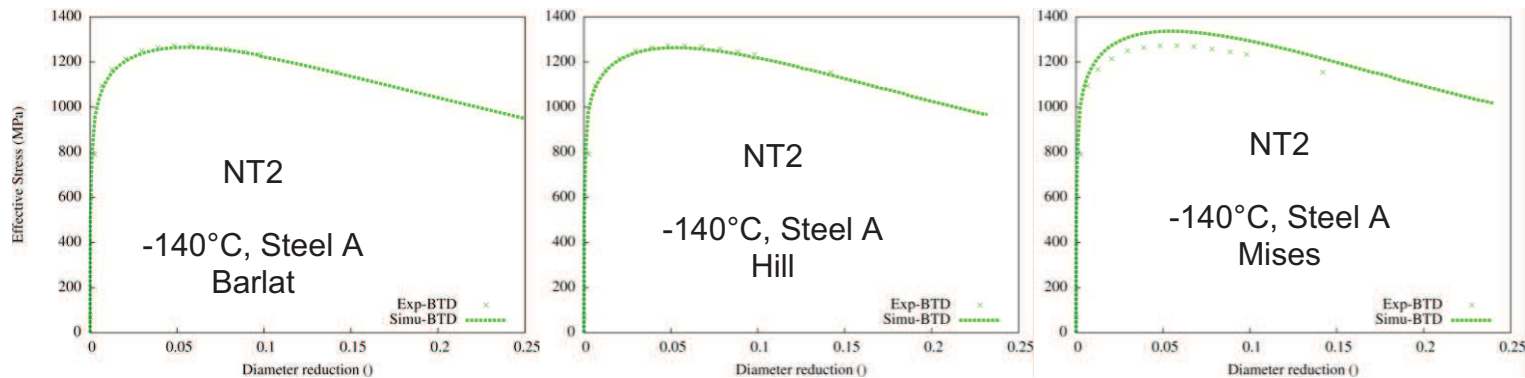


Figure C-18: Comparison between experimental curves and predictions from the three models. Tensile tests on NT2

Temperature = -196°C

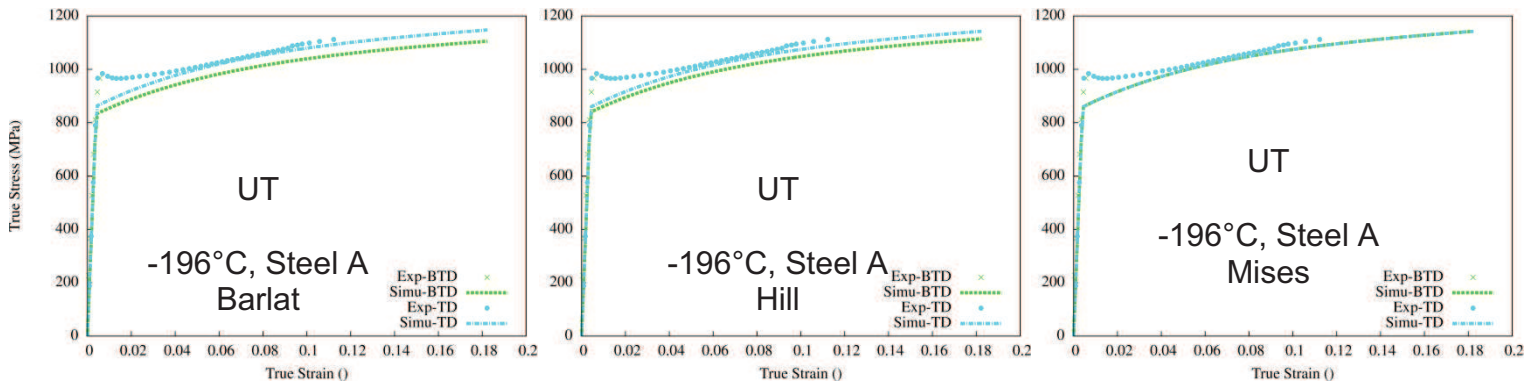


Figure C-19: Comparison between experimental curves and predictions from the three models. Tensile tests on smooth specimens. Steel A, -196°C.

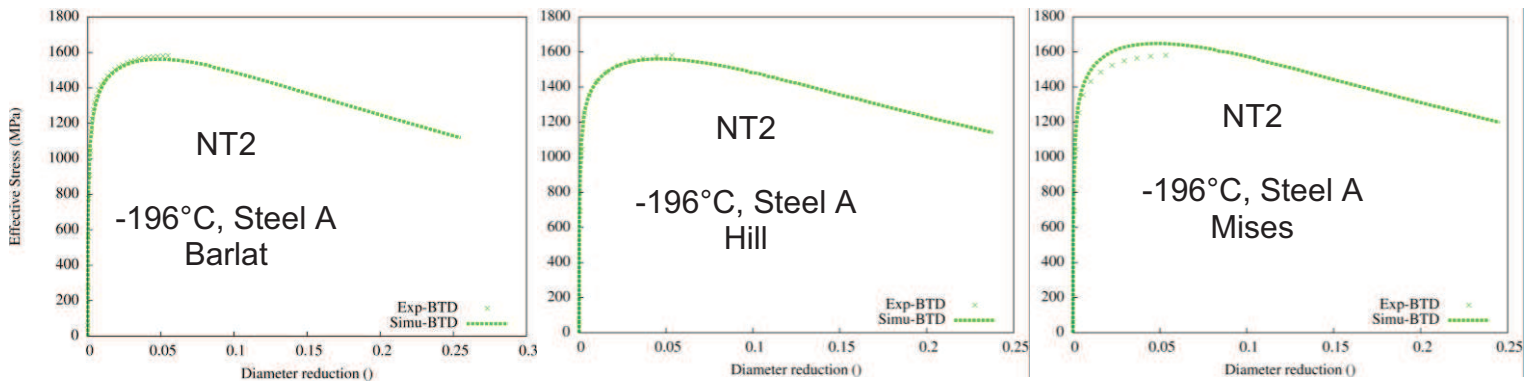


Figure C-20: Comparison between experimental and predictions from the three models. Tensile tests on NT2 specimens. Steel A, -196°C.

Finally, strain anisotropy prediction has been analyzed for the three criteria. Table C-5 and C-6 give the measured and predicted Lankford coefficients for smooth and strain anisotropy ratios for notched specimens. The predicted Lankford coefficients and strain anisotropy ratios were determined with the same procedure as that used for experimental data processing to get a reliable comparison. For each model, the errors between simulation and experiment were calculated for all directions and the average between these errors was calculated to propose an “average model error” for model evaluation.

The Barlat yield criterion leads to the best agreement with experiment. Hill model parameters fail in predicting strain anisotropy, since for some directions, predictions with the von Mises criterion were even better than those with the Hill criterion.

	ND	BTD	RD	TD	
Experiment	0.80	0.77	n.a	0.73	Average model error
Barlat	0.93	0.86	n.a	0.70	9%
Hill	1.02	0.93	n.a	0.86	18%
Mises	1.00	1.00	n.a	1.00	23%

Table C-5: Comparison between experimental and numerical Lankford coefficients on smooth specimens. Steel A. n.a.: data not available

	ND	BTD	RD	TD	
Experiment	0.89	0.78	0.75	0.83	Average model error
Barlat	0.98	0.91	0.89	0.9	11%
Hill	0.86	1.08	0.88	1.01	16%
Mises	1.00	1.00	1.00	1.00	19%

Table C-6: Comparison between experimental and numerical strain anisotropy ratios on notched specimens. Steel A

C.2.4. Results of constitutive parameter identification for Steel B

As for Steel A, hardening-related parameters were the same for both three plastic yield criteria: von Mises, Hill and Barlat. A unique set of parameters H , b , Q was determined for tests at 20°C and another set for temperatures lower than or equal to -100°C (Table C-7). The yield strength R_0 was estimated from equation C-9, where: $\sigma_a = 540 \text{ MPa}$; $d=1020 \text{ MPa}$; $c=0.014$ for Steel B.

The complementary parameters necessary for the description of Hill and Barlat plastic yield criteria are presented in table C-8 and table C-9 respectively. The Barlat yield criterion parameters determined for Steel B are close to the ones previously determined for Steel A. Concerning Hill criterion parameters of Steel B, they are noticeably different (by more than 10%) from the ones determined for Steel A.

	H (MPa)	b	Q (MPa)
T=20°C	340	16	160
T≤-100°C	682	26	180

Table C-7: Strain hardening parameters of Steel B

a	c ₁	c ₂	c ₃	c ₄	c ₅	c ₆
12	1.028	1.034	0.982	0.999	1.032	1.062

Table C-8: Parameters of Barlat yield criterion for Steel B, independent of temperature

h ₁	h ₂	h ₃	h ₄	h ₅	h ₆
1.022	0.986	1.125	1.033	1.037	1.577

Table C-9: Parameters of Hill yield criterion for Steel B, independent of temperature

Experimental and numerical tensile curves are presented in Figures C-21 to C-34. For each considered temperature, curves predicted using von Mises, Hill and Barlat criteria are compared to experimental data. As for Steel A, it was chosen to not accurately describe the yield point observed on tensile curves of smooth specimens.

For all considered temperatures, tensile curves obtained with the Barlat yield criterion are in good agreement with experiments. The maximum difference between simulations and experiments remains lower than 3%. Model predictions using the Hill criterion are also in good agreement with experiments, except for NT1 geometry where this maximal difference could be higher than 5%. The error between simulations and experiments for Mises criterion is around 10 %.

Temperature = 20°C

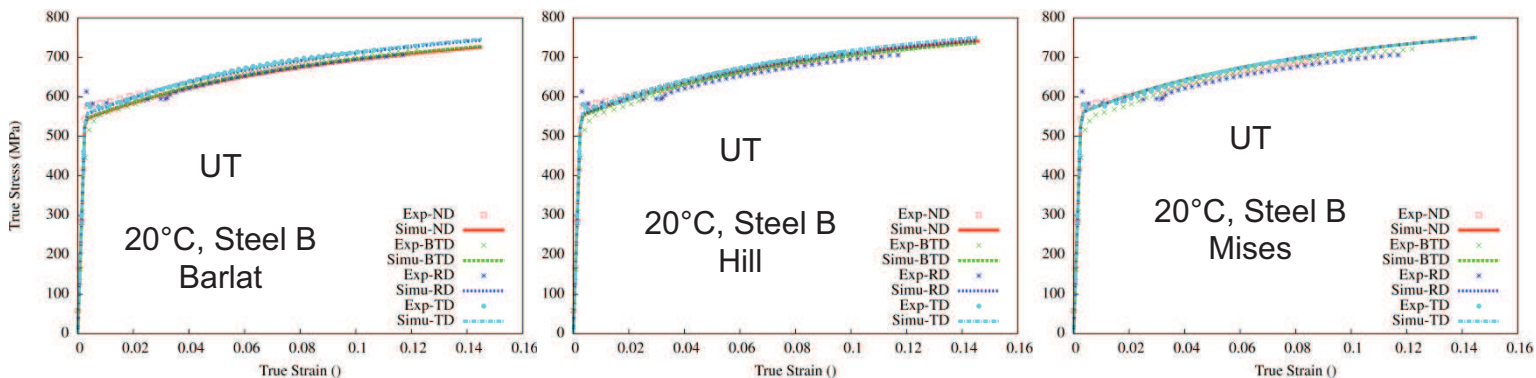


Figure C-21: Comparison between experimental curves and predictions from the three models. Tensile tests on smooth specimens. Steel B, 20°C.

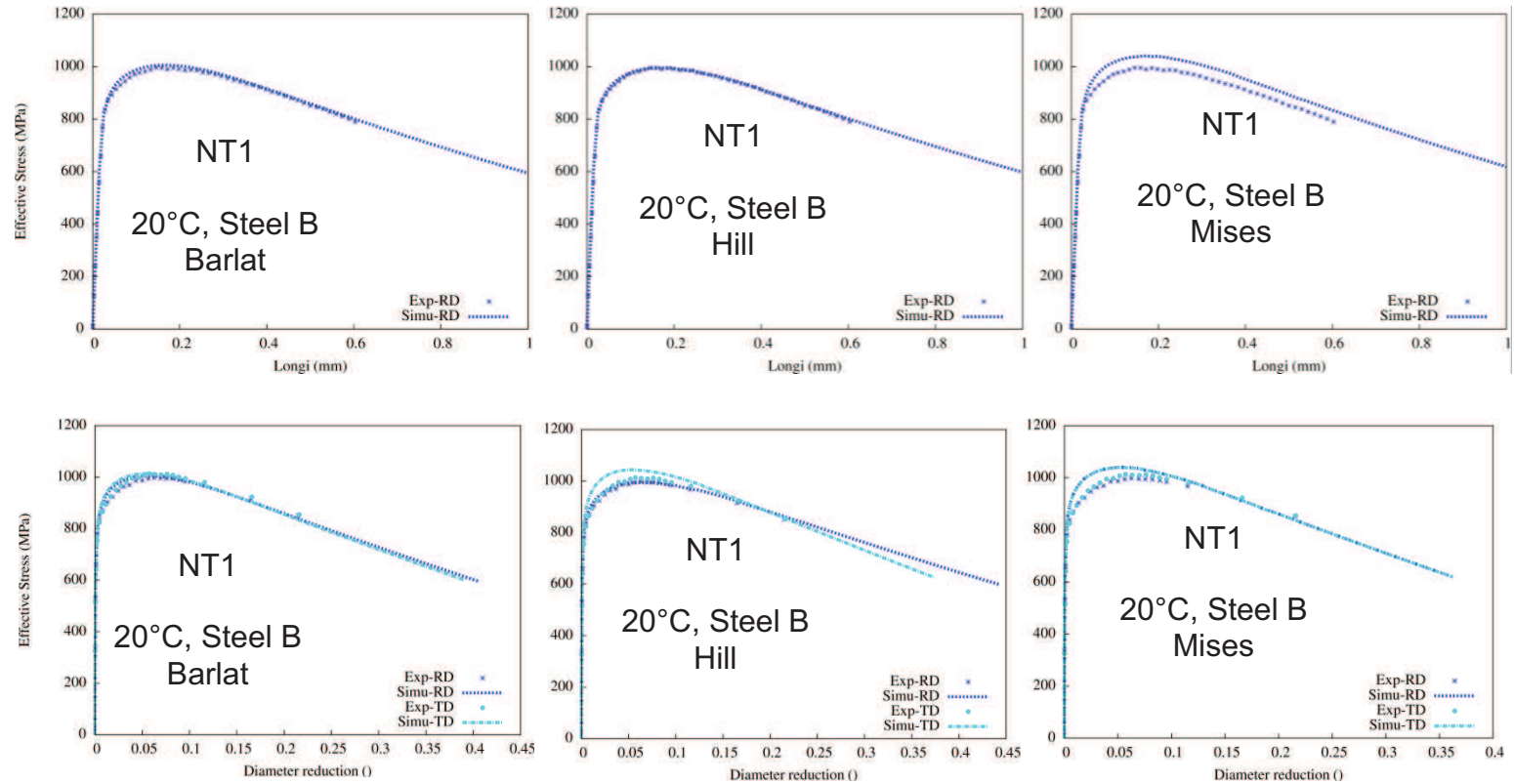


Figure C-22: Comparison between experimental curves and predictions from the three models. Tensile tests on NT1 specimens. Steel B, 20°C.

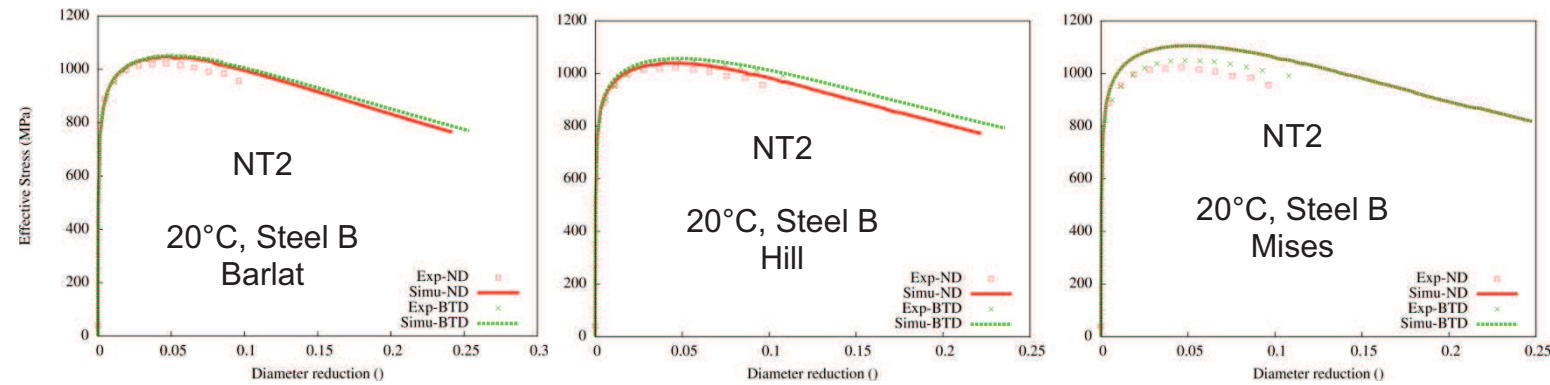


Figure C-23: Comparison between experimental curves and predictions from the three models. Tensile tests on NT2 specimens. Steel B, 20°C.

Temperature = -100°C

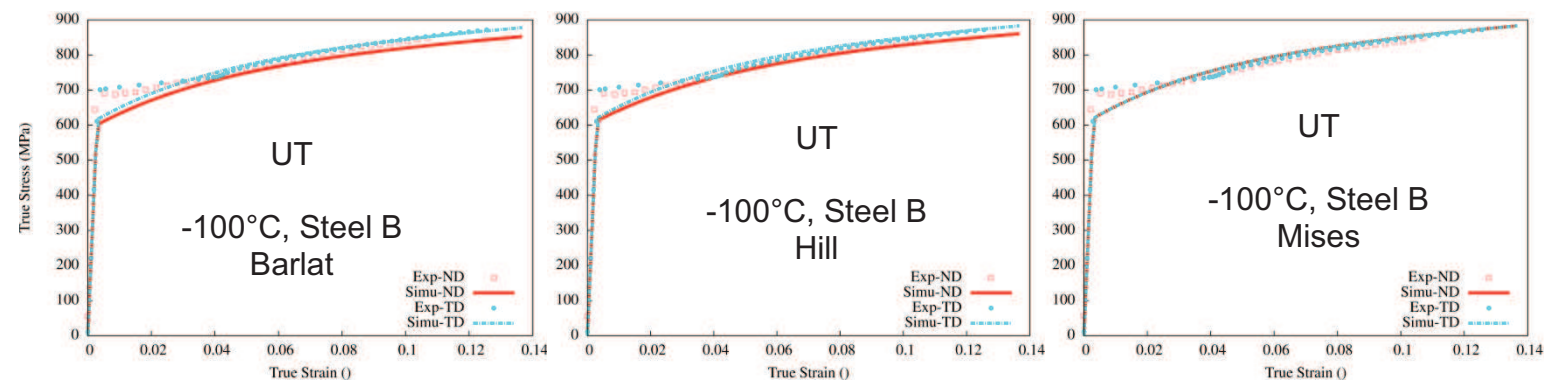


Figure C-24: Comparison between experimental curves and predictions from the three models. Tensile tests on smooth specimens. Steel B, -100°C.

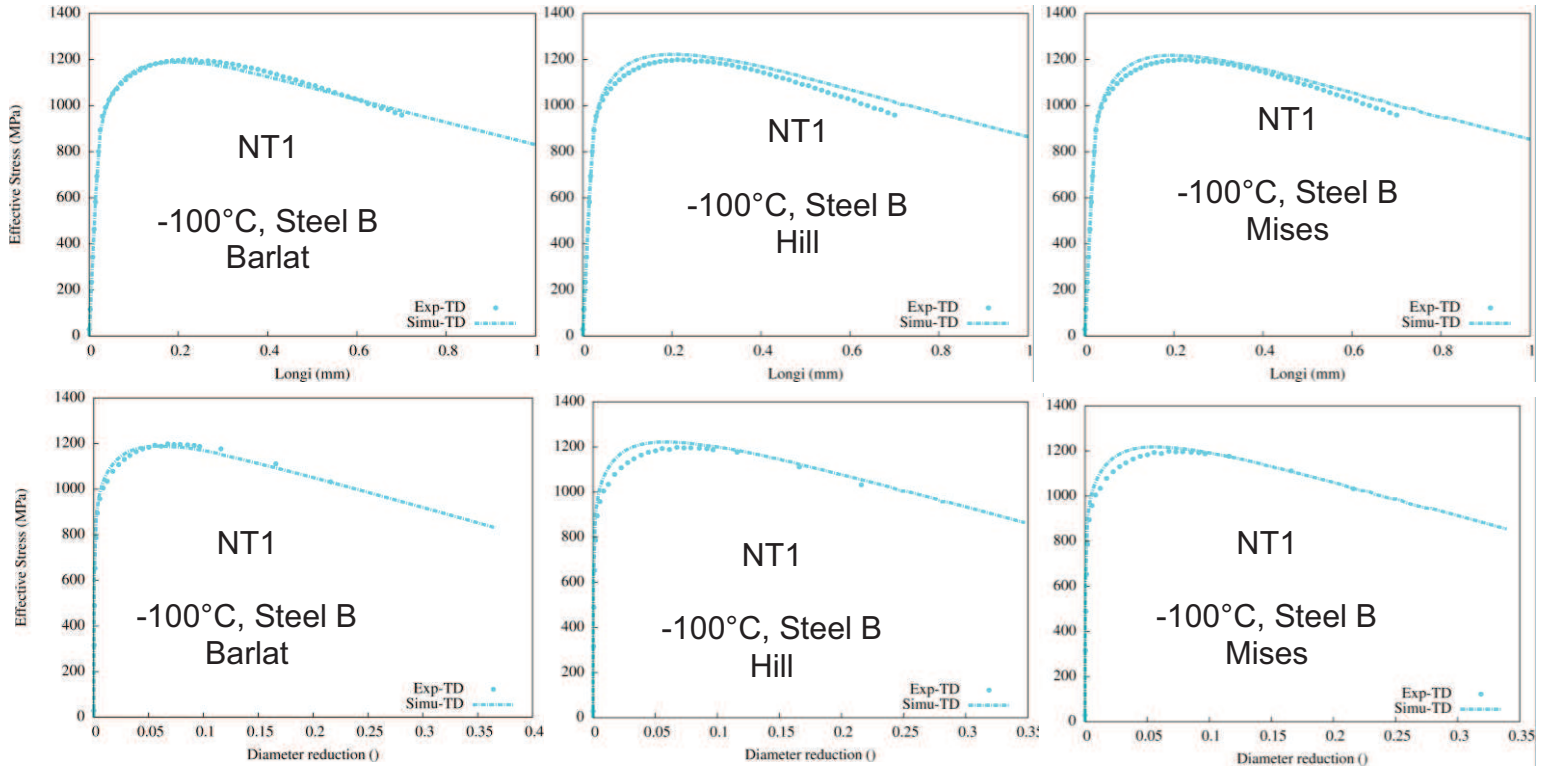


Figure C-25: Comparison between experimental and predictions from the three models. Tensile tests on NT1 specimens. Steel B, -100°C

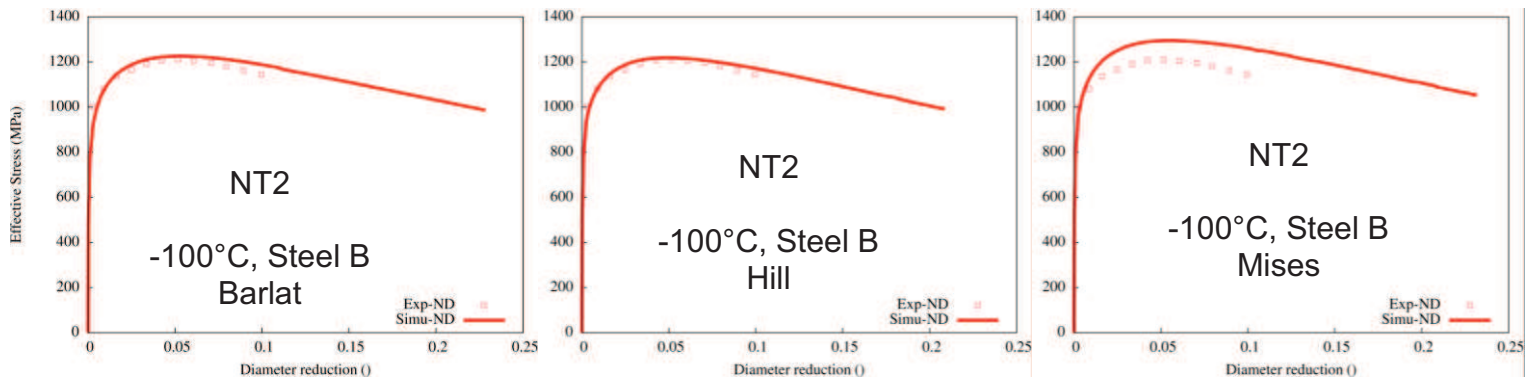


Figure C-26: Comparison between experimental and predictions from the three models. Tensile tests on NT2 specimens. Steel B, -100°C.

Temperature = -120°C

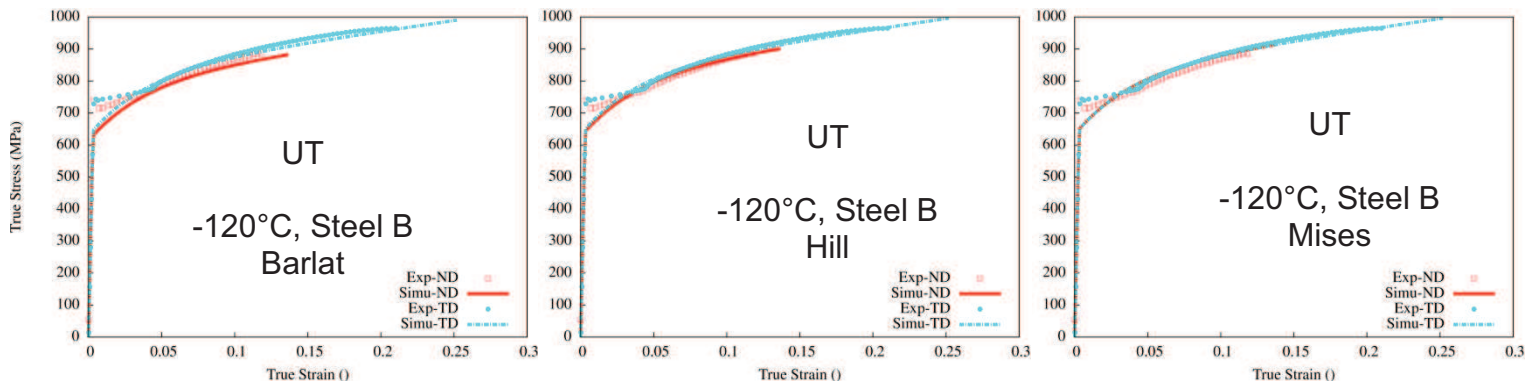


Figure C-27: Comparison between experimental curves and predictions from the three models. Tensile tests on smooth specimens. Steel B, -120°C.

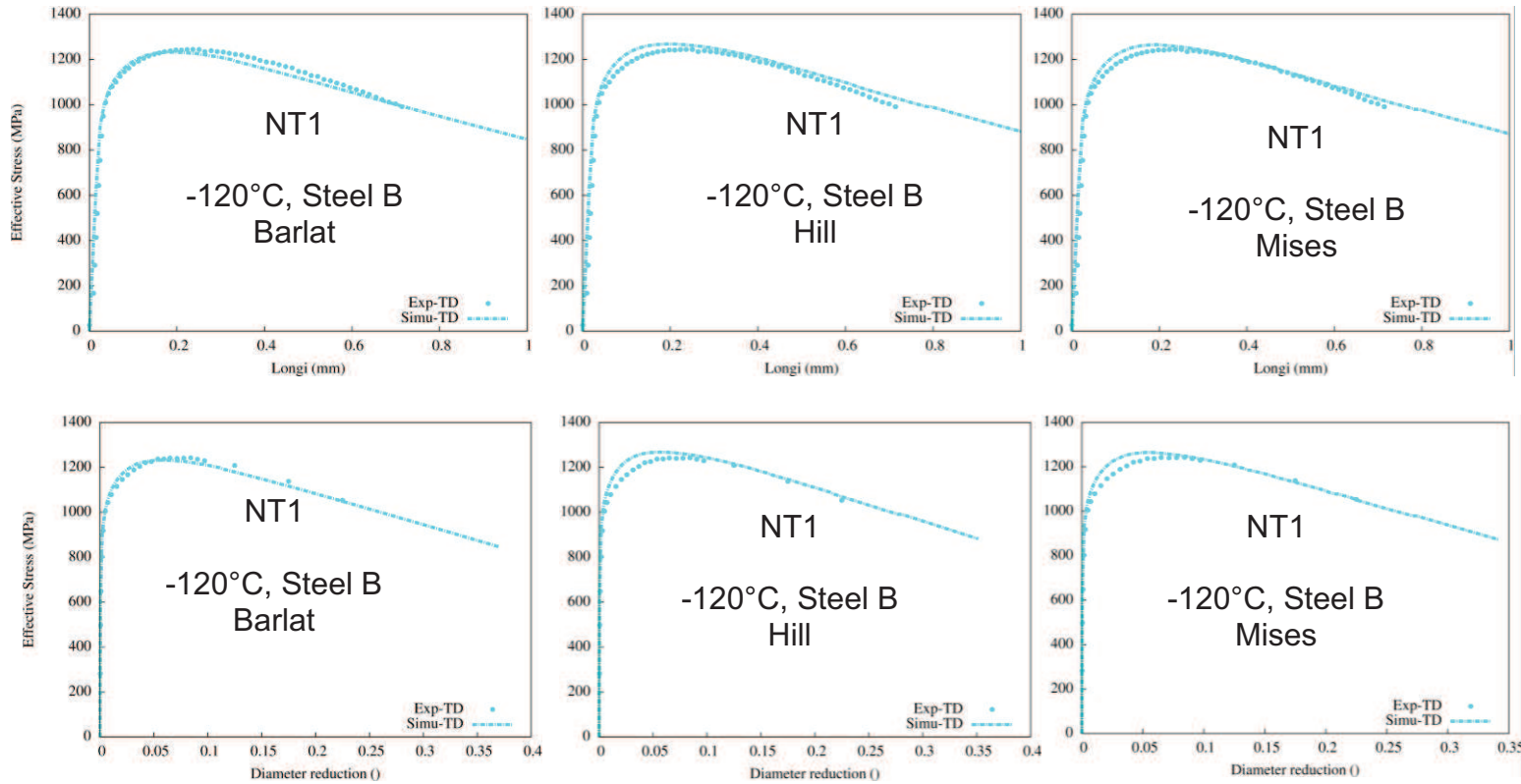


Figure C-28: Comparison between experimental curves and predictions from the three models. Tensile tests on NT1 specimens. Steel B, -120°C

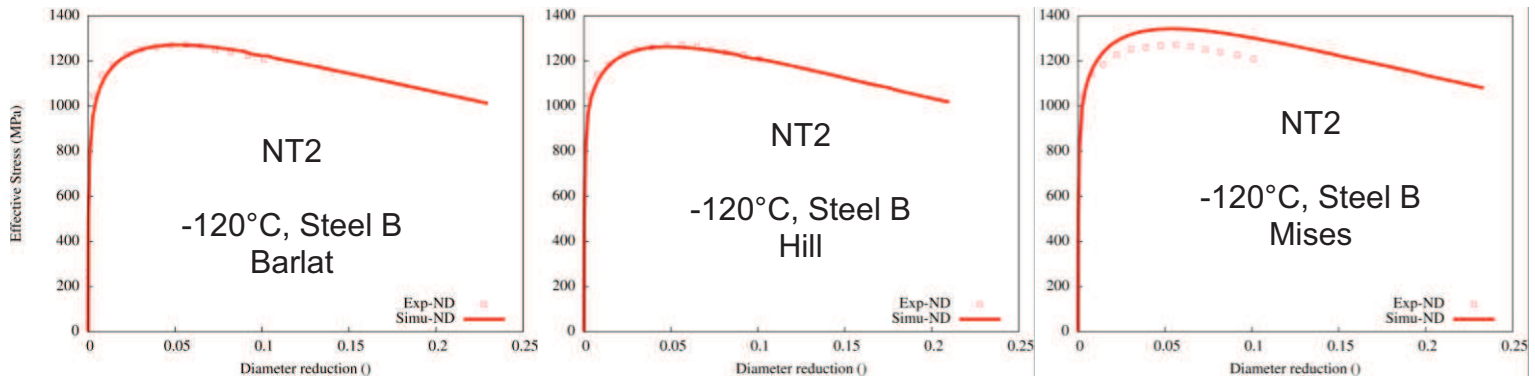


Figure C-29: Comparison between experimental curves and predictions from the three models. Tensile tests on NT2 specimens. Steel B, -120°C.

Temperature = -140°C

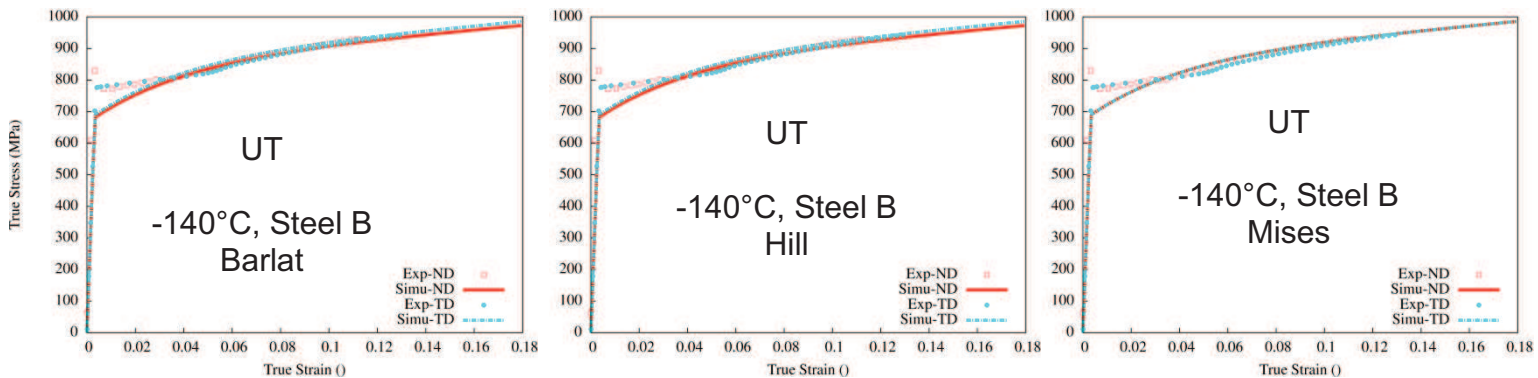


Figure C-30: Comparison between experimental curves and predictions from the three models. Tensile tests on smooth specimens. Steel B, -140°C.

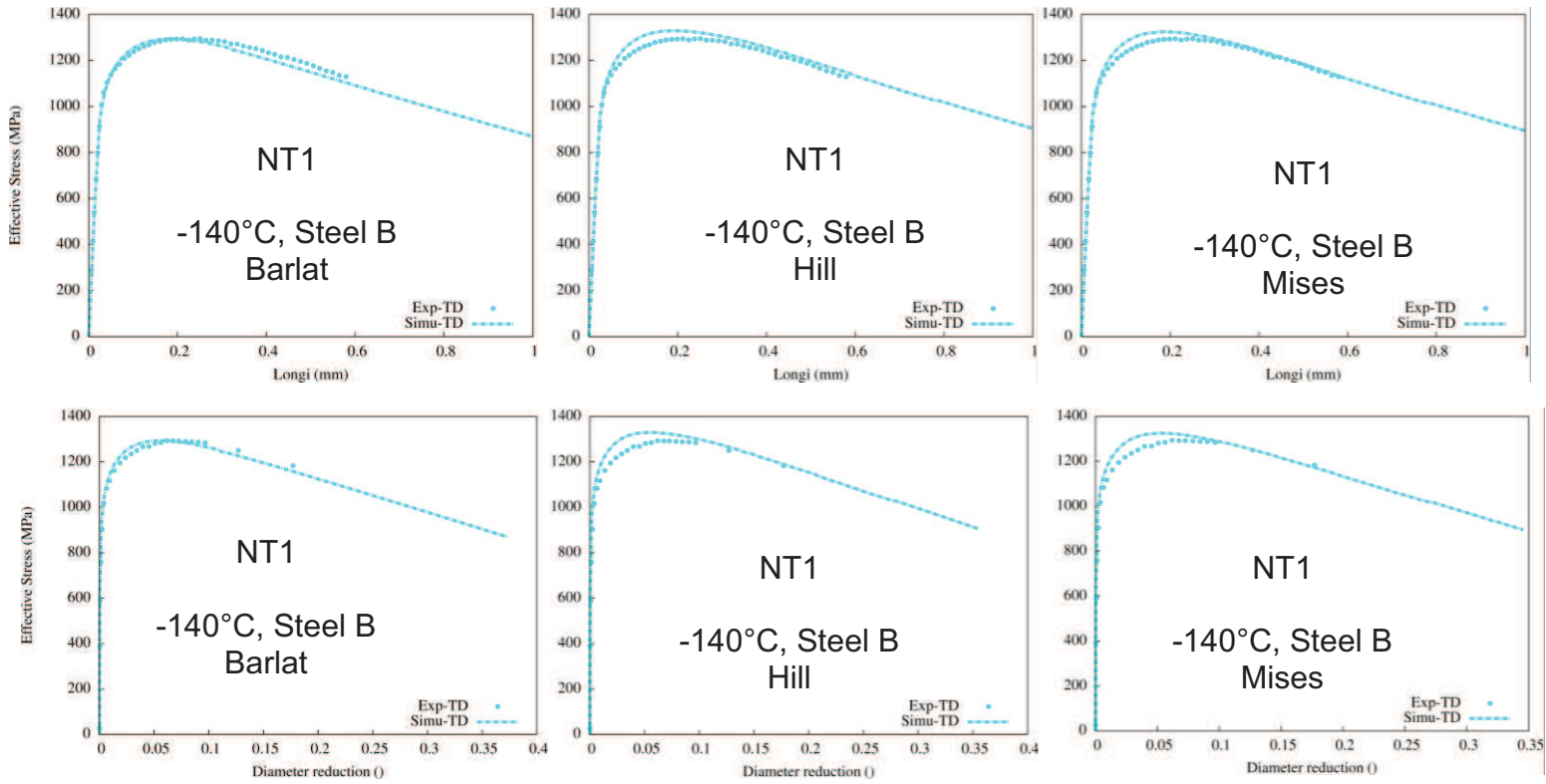


Figure C-31: Comparison between experimental curves and predictions from the three models. Tensile tests on NT1 specimens. Steel B, -140°C

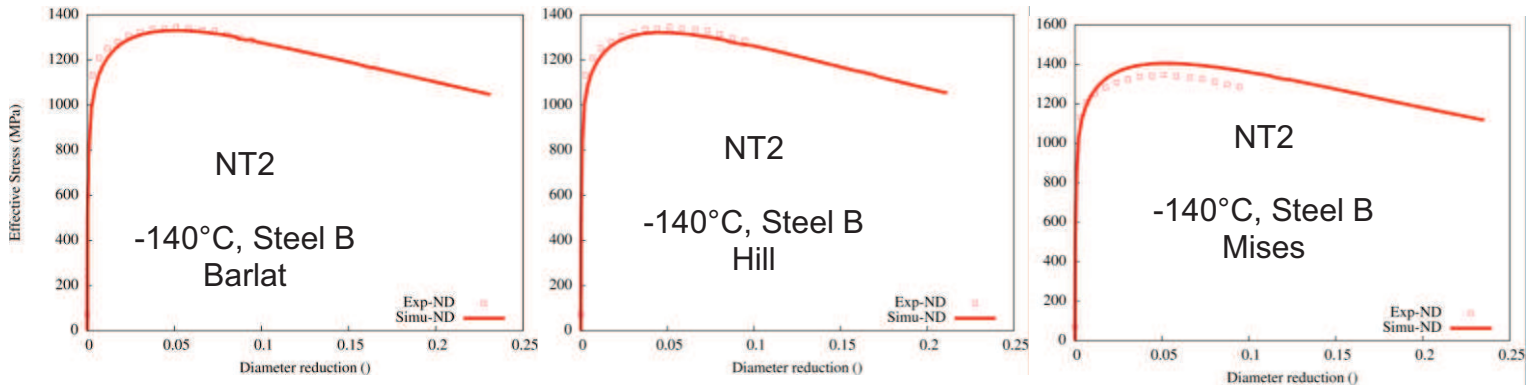


Figure C-32: Comparison between experimental curves and predictions from the three models. Tensile tests on NT2 specimens. Steel B, -140°C.

Temperature = -196°C

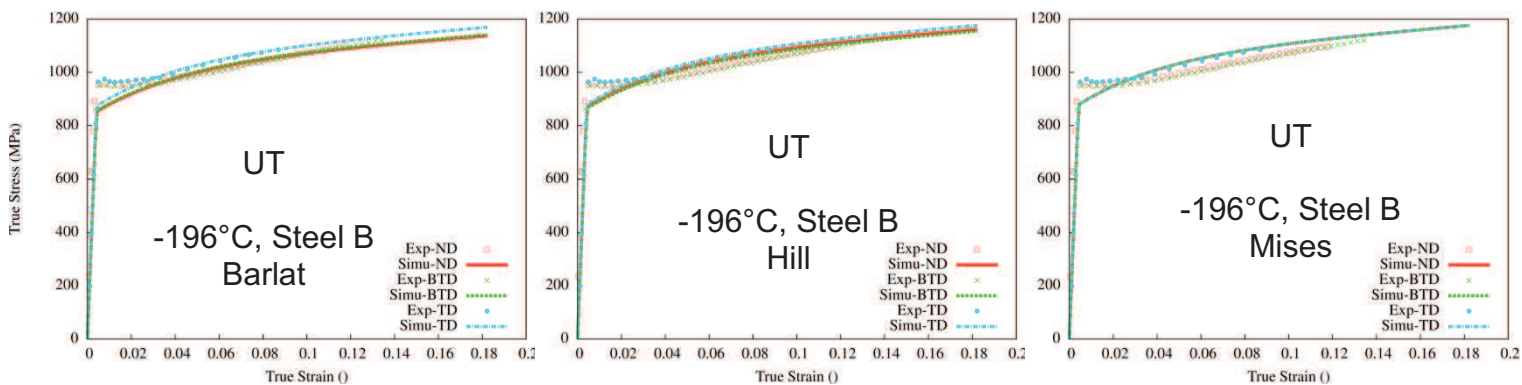


Figure C-33: Comparison between experimental curves and predictions from the three models. Tensile tests on smooth specimens. Steel B, -196°C.

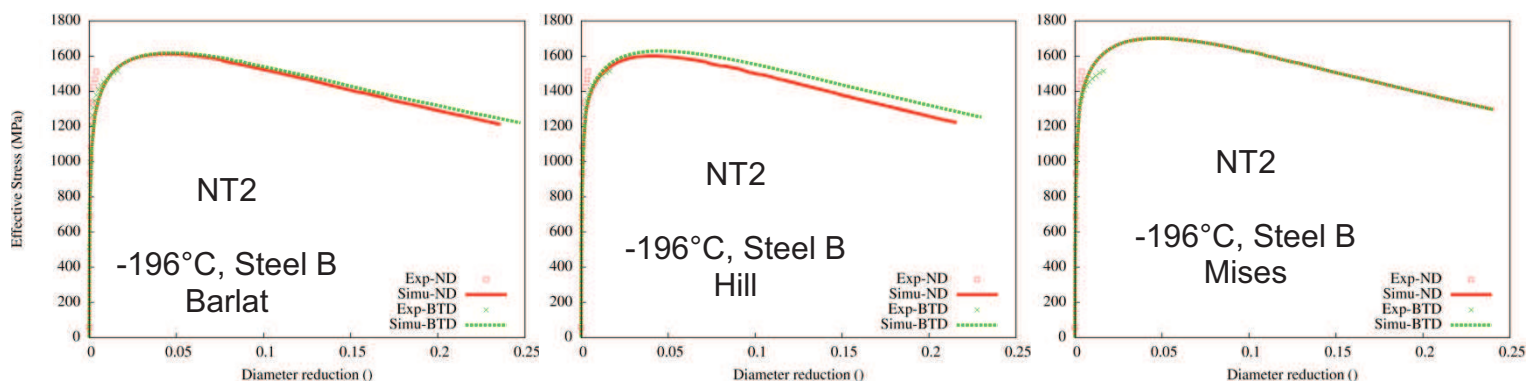


Figure C-34: Comparison between experimental curves and predictions from the three models. Tensile tests on NT2 specimens. Steel B, -196°C.

The model with the Barlat yield criterion shows the best agreement with experiment. The Hill criterion does not accurately predict strain anisotropy, since for some directions, predictions were even better with the von Mises criterion than with the Hill criterion.

As for Steel A, strain anisotropy prediction has been analyzed for the three criteria. Table C-10 and C-11 give the measured and simulated Lankford coefficients for smooth specimens and strain anisotropy ratios for notched specimens. The average difference between numerical predictions and experimental measurements for each model was evaluated as for Steel A. The model using the Barlat criterion yields very good agreement with experiment, comparing to Mises and Hill criteria. For notched specimens, the Hill yield criterion leads to less good agreement than the von Mises criterion.

	ND	BTD	RD	TD		
Experiment	0.86	0.80	0.71	0.83	Average model error	
Barlat	0.97	0.88	0.80	0.99		8%
Hill	0.97	1.00	0.96	0.99		18%
Mises	1.00	1.00	1.00	1.00		20%

Table C-10: Comparison between experimental and numerical Lankford coefficients on smooth specimens. Steel B

	ND	BTD	RD	TD		
Experiment	1.00	0.86	0.80	0.89	Average model error	
Barlat	0.94	1.00	0.80	0.89		5%
Hill	0.76	1.16	0.68	0.89		16%
Mises	1.00	1.00	1.00	1.00		12%

Table C-11: Comparison between experimental and numerical strain anisotropy ratios on notched specimens. Steel B

C.2.5. Analysis of the local stress and strain state for the three models, final choice of the elastoplastic model used to calculate critical cleavage stresses

Tensile tests at -100°C on notched specimens have been simulated in more detail with von Mises, Hill and Barlat yield criteria. NT1 specimens of Steel A pulled along RD have been considered, because the strain anisotropy was highest for that steel and along that direction, and therefore the three model predictions could be compared for this extreme case. Quadratic elements, with 15 μm mesh size at the center of specimen have been chosen as already mentioned for the analysis of local stress state.

a- Comparison of local stress states for tensile tests on notched specimens

The stress state distribution has been investigated within the minimal section, where flat cleavage fracture commonly occurred. Evolution of the axial stress (along RD) and of the radial stress (along

ND) has been studied along one radius. These analyses have been done for a longitudinal displacement of 0.75 mm, which corresponds to the value measured at the onset of delamination. Figure C-35 shows distributions of axial stress and of radial stress predicted by the three models. Independently of the model, the maximal axial and radial stress were reached at the center of specimens for the considered longitudinal displacements. Around the specimen center, where cleavage generally initiated from, the axial stress predicted with von Mises and Barlat criteria are very close to each other (differing by less than 3%). On the contrary, the axial stress predicted with the Hill criterion was around 10% lower than that predicted using the other two models. Concerning radial stress, Mises and Barlat criteria predicted similar values around the center (difference lower than 1%), contrarily to Hill criterion which predicted a value lower by 20%. To summarize, the stress state predicted at the center is similar for Barlat and von Mises yield criteria. The Hill criterion, which has a higher number of parameters comparing to the von Mises criterion, is not efficient enough for the local stress state estimate.

b- Comparison of local strain states for tensile tests on notched specimens

The previous section showed that von Mises and Barlat yield criteria lead to similar estimates of the stress state at the center of the specimen. This result is important because reliable determination of critical cleavage stresses is related to reliable estimation of the stress state around the center of specimens. Moreover, since delamination cracking always started from the center of specimens, a criterion based on critical cleavage stress along ND could be used either with a Barlat or a von Mises yield criterion. Nevertheless, if we assume an impact of plastic strain on the cleavage fracture stress as presented in chapter VI, a reliable estimation of plastic strain at the center of specimens is also necessary. The evolution of the equivalent plastic strain at the center of the specimen during the loading has thus been analyzed for von Mises, Hill and Barlat yield criteria (Figure C-36).

Predictions using von Mises and Hill criteria are similar in terms of equivalent plastic strain. The equivalent plastic strains estimated with both criteria are lower than those obtained from using the Barlat criterion. For a longitudinal displacement of 0.75mm, which corresponds to the onset of delamination, the equivalent plastic strain estimated with the Mises criterion is 20% higher than that estimated using the Barlat criterion. Therefore, despite the fact that the von Mises criterion predicted a proper stress state at the center of the specimen, the strain state is considerably underestimated with respect to the Barlat yield criterion.

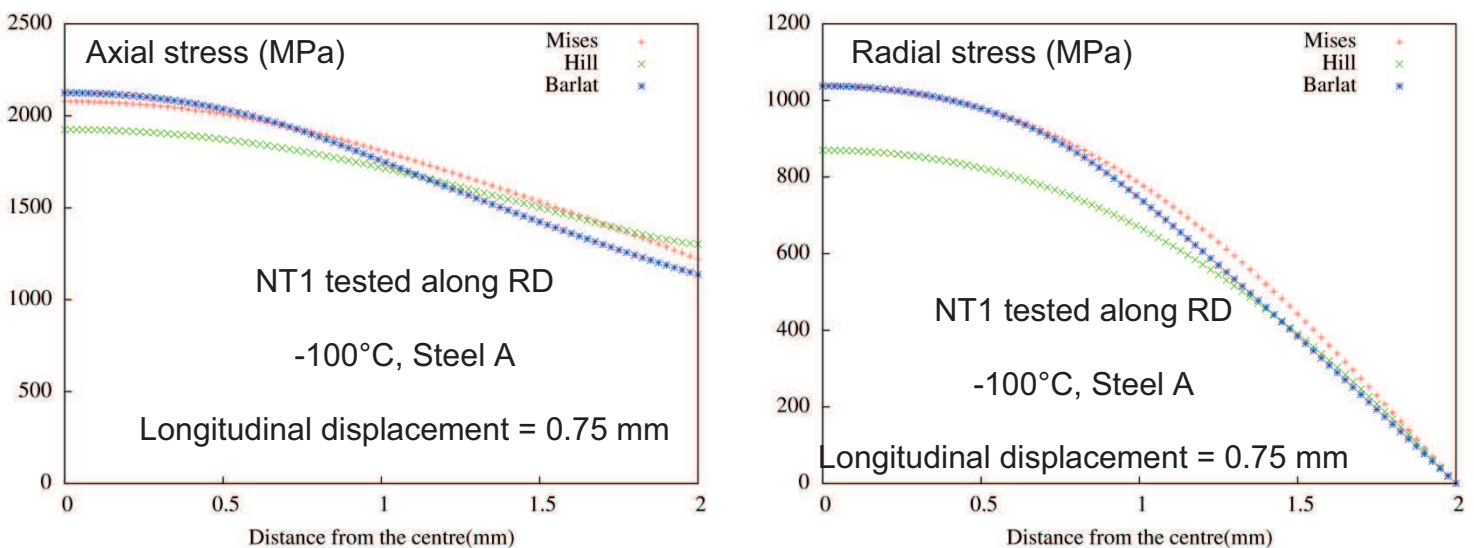


Figure C-35: Comparison of the local axial and radial stress distributions obtained using Barlat, Hill and von Mises yield criteria.

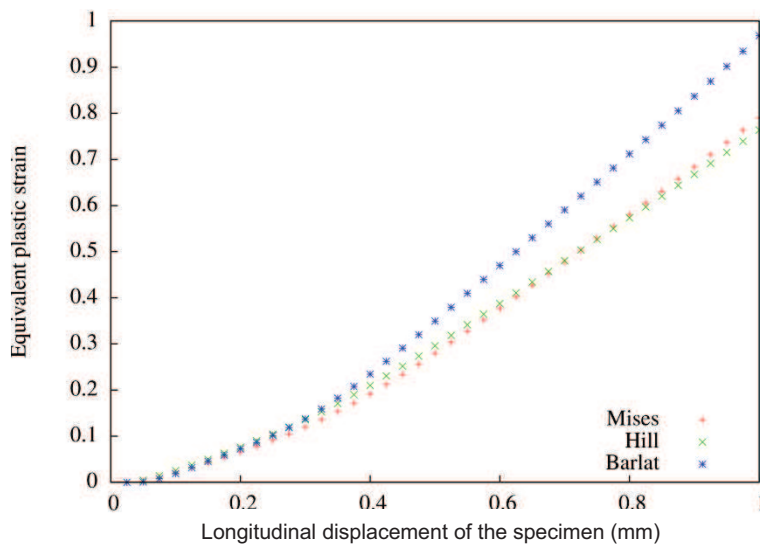


Figure C-36: Evolution of the cumulative plastic strain at the center during the loading, obtained using Barlat, Hill and von Mises yield criteria

c- Choice of the elastic-plastic model for mechanical analysis of quasi-static tensile tests

Two kinds of models should be chosen: a robust model which could provide precise results necessary for an accurate mechanical analysis, and a simplified model which is helpful in industry for preliminary analyses. This simplified model could also be used to perform complete analyses after consideration of errors generated by the model with respect to the reference (robust) model predictions.

The Barlat model has been chosen for mechanical analyses of tensile tests on notched specimens.

For readily industrial use, a von Mises yield criterion identified on tests along the TD direction could be chosen. Only the three parameters of the strain hardening evolution have to be identified and calculation of round bars could be done on 2D axisymmetric meshes. In fact, since the axial stress around the center is predicted to be similar using von Mises and Barlat criteria, critical cleavage stress could be well and easily estimated using a von Mises criterion. Nevertheless, tensile tests have to be performed at very low temperature (-196°C for instance), so that only small amounts of plastic strain could be involved and the poor prediction of local strain with the von Mises criterion does not affect the results significantly.

The model using the Mises criterion might not be used for ductile damage modeling, where plastic strain plays an important role. Therefore, ductile damage development was only modeled with the Barlat yield criterion.

D- Simulation of Charpy tests: Ductile crack advance modeling up to the onset of delamination

This appendix focuses on the modelling of Charpy tests. The first part addresses the modeling of the elastic-plastic response. The three anisotropic yield criteria (namely, those of von Mises, Hill [47] and Barlat [48]) used for the analysis of quasi-static tests were successively considered for modelling of Charpy tests. The sensitivity to strain rate (i.e., low temperature viscoplastic behavior) was modeled using a Norton power-law. The second part presents ductile damage modeling. To take the ductile crack advance observed before cleavage fracture of Charpy specimens into account, a Gurson-Tvergaard-Needleman (GTN) model [49] was used.

D.1. Meshing of the specimens and boundary conditions

One quarter of the specimen was used with usual symmetry conditions. The loading was applied using prescribed hammer displacement. Sliding with a Coulomb friction coefficient equal to 0.1 was assumed for the specimen vs. anvil contact and specimen vs. hammer contact. The initial speed of the hammer was taken as 5 m/s for Steel A and 5.5 m/s for Steel B according to experimental setups. Charpy tests along TD were considered for simulation.

Reduced linear 3D elements were chosen for the mesh. Regular elements of 100 μm in size covered all the ligament region (Figure D-1).

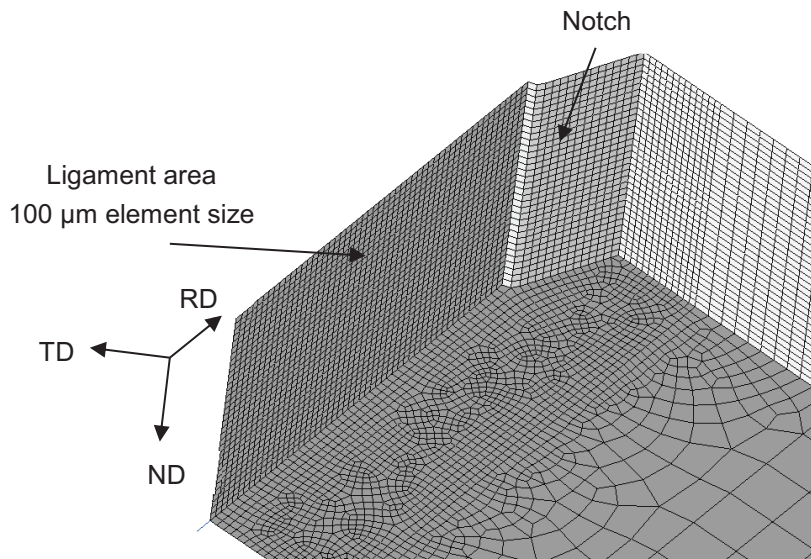


Figure D-1: 3D mesh used for numerical modeling of Charpy tests

D.2. Elastic-plastic constitutive model for mechanical analysis of Charpy tests

The three elastoplastic models (with von Mises, Hill and Barlat yield criteria) identified in chapter IV and appendix C from quasi-static tests were modified to take into account the rate dependence that is

necessary for impact test modeling. In that case, the (visco)plastic multiplier \dot{p} was computed using a Norton flow rule, which introduced two additional material parameters (K and n) as follows:

Equation D.1

$$\dot{p} = \left\langle \frac{\sigma}{K} \right\rangle^n$$

In eq. D.1, σ represents the viscoplastic potential. Parameters K and n were set to 55 MPas^{1/n} and 5 respectively, according to the results of [50] who also worked on pipeline steels.

Results of simulations with von Mises, Hill and Barlat yield criteria were compared both from a global and from a local point of view, for Steel A at 20°C. Explicit Zmat calculations were done with isothermal conditions, since the effects of adiabatic heating could be neglected at 20°C. Figure D-2 compares predicted load vs. displacement curves with experimental results. Simulations curves were cut at the maximal load, for which the effect of any ductile crack advance was considered to be negligible. Predictions using Barlat and Hill criteria are close to the experimental curve compared to predictions using a von Mises criterion which overestimates the load.

The maximum values of stress along ND, RD and TD were compared for a hammer displacement of 0.25 mm (that is to say, within the elastoplastic domain) for von Mises, Hill and Barlat yield criteria. The results are presented in table D-1. Local stresses along RD and TD obtained with the Hill criterion are similar to the ones obtained with the Barlat criterion (relative difference of around 5%). The stress along ND is 14% greater with a Hill criterion compared to that estimated with a Barlat criterion. Concerning estimates with a von Mises criterion, stresses along RD and TD are 11% higher and stress along ND is 22% higher comparing to values obtained with a Barlat yield criterion.

Using a von Mises yield criterion, thus leads to an overestimation of the local stress levels. On the other hand, only this model could be coupled with ductile damage in the available version of Abaqus software. As a consequence, a von Mises yield criterion was selected to model Charpy tests, bearing in mind the expected relative errors in local stress estimates.

To end this part of the study, similar analyses were done on Steel B. The load vs. displacement curve obtained with a von Mises criterion is presented in figure D-3. The load obtained by simulation is higher than experimental results even from the start of yielding (relative error: more than 20%). This overestimate could not be only associated to the model, since complementary simulations with a Barlat criterion (not presented here) confirmed this tendency. The difference between model predictions and experimental results could likely come from either the modelling of strain rate dependence or from experimental artifacts. The first origin is not plausible since Steel A and Steel B microstructures are close to each other, so that their strain rate sensitivities were expected to be similar. The last option is a possible artifact on load measured during Charpy tests on Steel B, which were carried out in another laboratory (RWTH Aachen). This origin is plausible, but no additional Charpy specimen of Steel B was available yet for testing at OCAS to confirm this artifact.

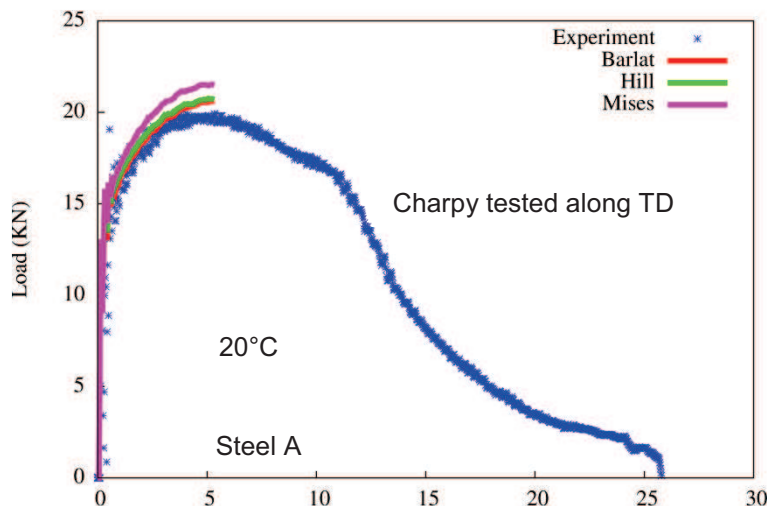


Figure D-2: Load vs. hammer displacement curves of a Charpy specimen of Steel A tested at 20°C. Experimental result and numerical prediction with von Mises, Hill and Barlat yield criteria

	σ_{ND} (max)	σ_{RD} (max)	σ_{TD} (max)
Barlat	820 MPa	720 MPa	1510 MPa
Hill	950 MPa	700 MPa	1610 MPa
Comparison to Barlat	+14%	-3%	+6%
Mises	1050 MPa	810 MPa	1700 MPa
Comparison to Barlat	+22%	+11%	+11%

Table D-1: Local maximum stresses along ND, RD and TD for Mises, Hill and Barlat yield criteria. Charpy test at 20°C on Steel A. Analysis for hammer displacement of 0.25 mm.

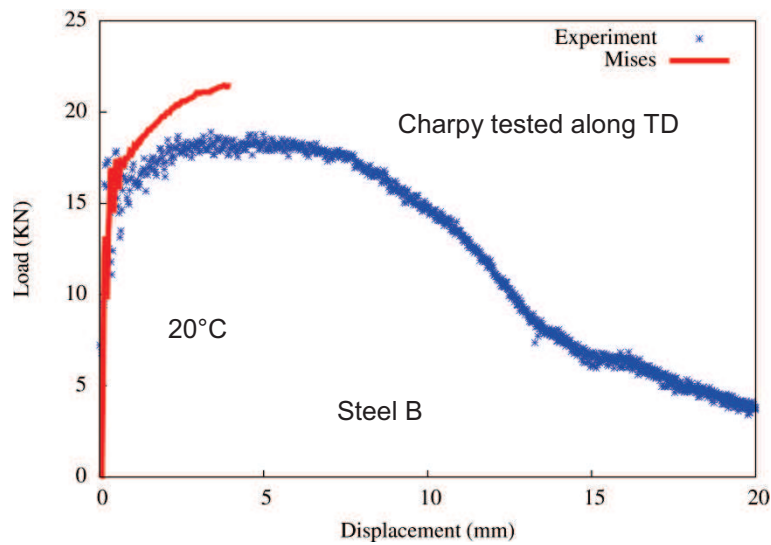


Figure D-3: Load vs. hammer displacement curves of a Charpy specimen of Steel B tested at 20°C

Figure D-4 shows the response of Steel A and Steel B along TD, during tensile tests and Charpy tests at 20°C. According to tensile tests, Steel B is around 10% stronger than Steel A, but according to Charpy tests, Steel A is stronger by around 10% than Steel B. Since other tests such as hardness measurements further support the fact that Steel B is stronger than Steel A, the error might come from Charpy results. The Charpy results of Steel B could therefore show lower strength than “real” values.

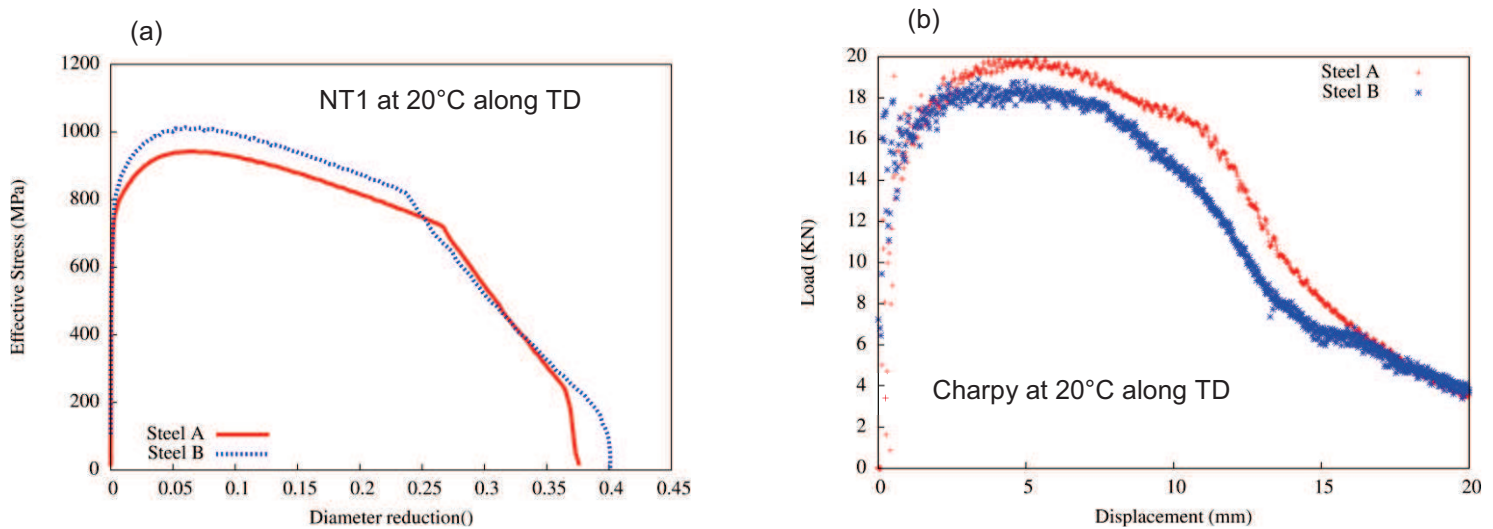


Figure D-4: (a) Tensile curves of Steel A and Steel B along TD at 20°C. (b) Charpy curves of Steel A and Steel B along TD at 20°C.

D.3. Evidence for anisotropy in ductile fracture behavior

D.3.1. Experimental study

The ductile fracture behavior of NT specimens was investigated for ND, BT, RD and TD directions at room temperature. Tensile curves and fracture surfaces were analyzed and compared to study any source and effect of anisotropy. Finally, fracture surfaces of notched specimens and Charpy specimens were compared.

- Analysis of tensile curves

From tensile curves, the diameter reduction at the onset of stable ductile crack propagation was assumed to correspond to an acceleration in the stress decrease which leads to a change in slope of the curve (marked with arrows). The resulting value is lower for ND compared to BT (Figure D-5). Even for RD and TD directions which look similar in the elastic-plastic domain, this value of diameter reduction is not the same. Therefore, the ductile damage process seems to differ from one direction to the other for both Steels A and B.

- Analysis of fracture surfaces

The dimple size distributions were compared for ND, BT and TD directions and correlated to the differences between the macroscopic curves (Figure D-6 and Figure D-7). For both steels, specimens tested along ND had the lower fraction of small dimples. Even if the size of large dimples is similar for both fracture surfaces, specimens tested along ND showed a greater proportion of these large dimples. Therefore, primary void nucleation is expected to be easier for specimen tested along ND, which enables these primary voids to grow significantly during the test. The coalescence by internal necking might lead to the sooner stable ductile crack propagation observed as the mechanical response along ND.

- Charpy tests vs. tensile tests

In this section, the ductile fracture behavior observed after Charpy tests is compared to the ones observed during tensile tests. The fracture surfaces of Charpy specimens tested at 20 °C along TD were observed (Figure D-8). At the notch root, fine dimples cover a great part of the fracture surface. The proportion of large dimples is considerably lower compared to that observed for tensile specimens. Behind this first region, large elongated dimples (more than 100µm in size) are observed. This second region is closer to the results of tensile tests along ND, except that the size of large dimples is even larger and fine dimples are hardly found in Charpy specimens. Moreover, the elongated shape of dimples was not observed for tensile specimens.

- Summary on ductile behavior

Some anisotropy in ductile fracture mechanism was observed after tensile tests along ND, BT, RD and TD. Voids seem to nucleate and grow earlier for NT specimens pulled along the ND direction, leading to earlier ductile fracture. Therefore, an isotropic ductile damage model should not be appropriate to describe the ductile behavior of these steels. Moreover, the dimple population observed on Charpy specimens was different from those observed on tensile specimens. Very fine dimples covered the notch root region and large elongated dimples were observed behind the notch root region. Consequently, a ductile damage model identified in notched tensile specimens could not be directly used for Charpy specimens, at least for Steel B for which fracture surfaces of Charpy specimens were available. It is not possible to conclude on Steel A for this point.

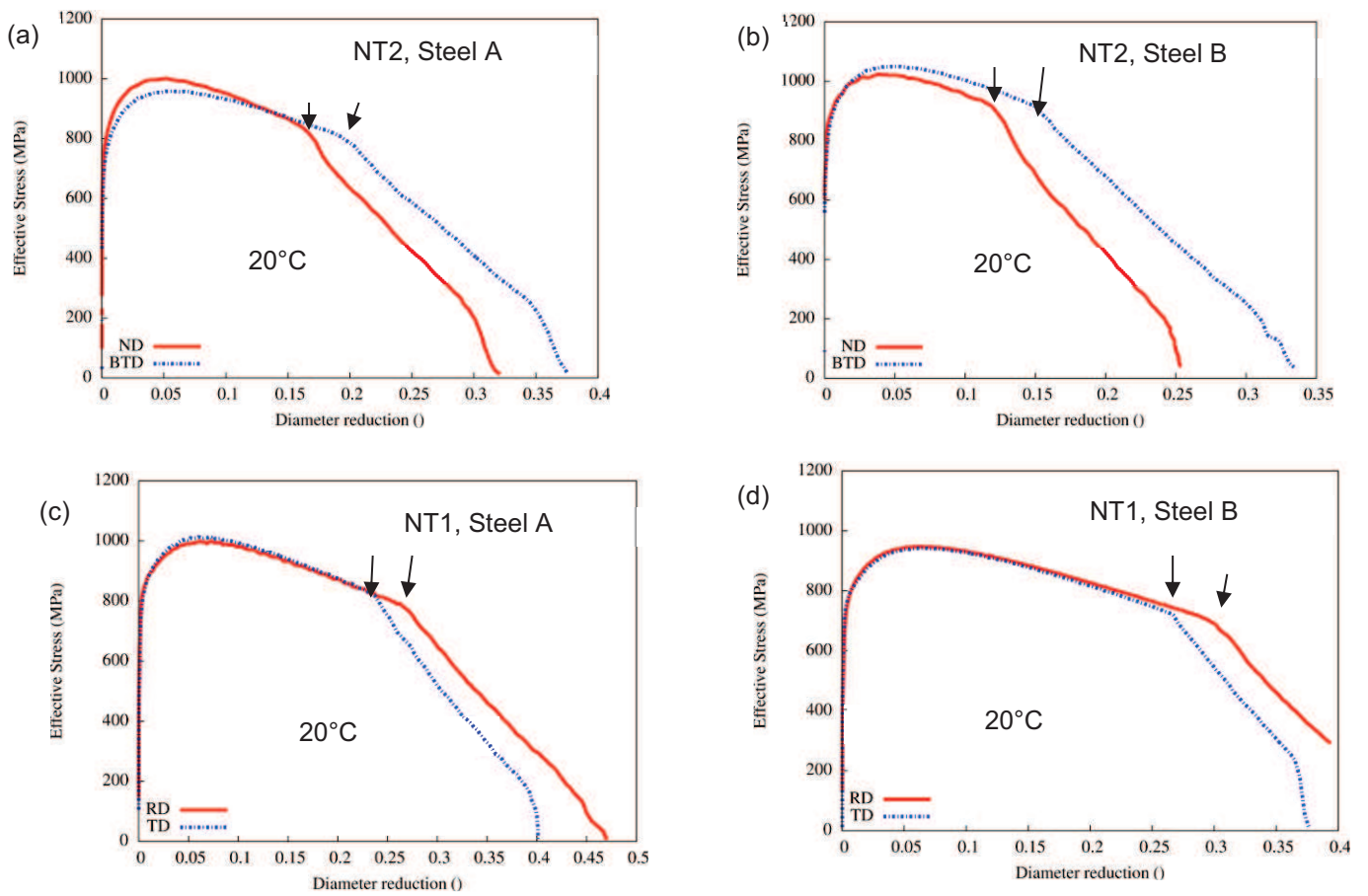


Figure D-5: Tensile curves at 20°C of notched specimens taken along ND, BTD, RD, TD for Steel A and Steel B

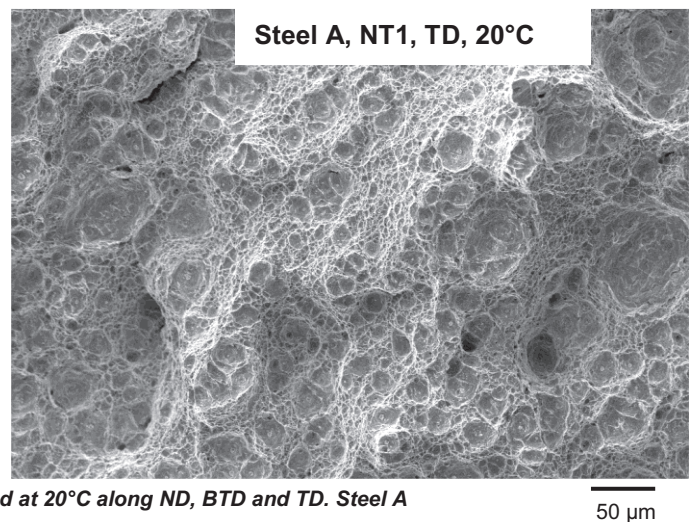
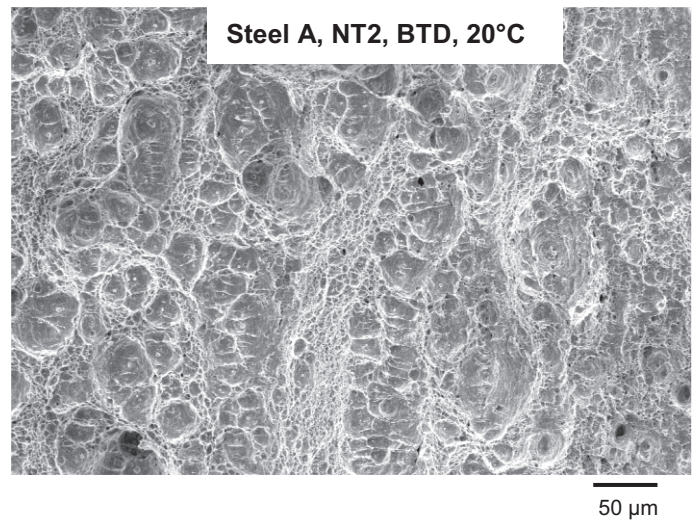
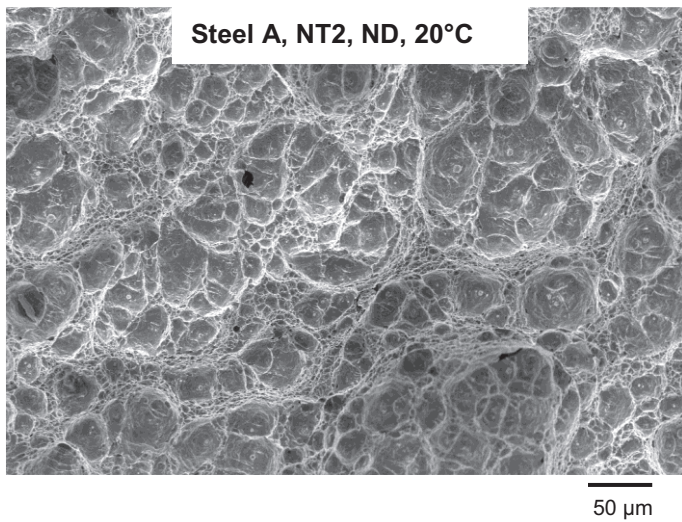


Figure D-6: Fracture surface of tensile specimens tested at 20°C along ND, BTD and TD. Steel A

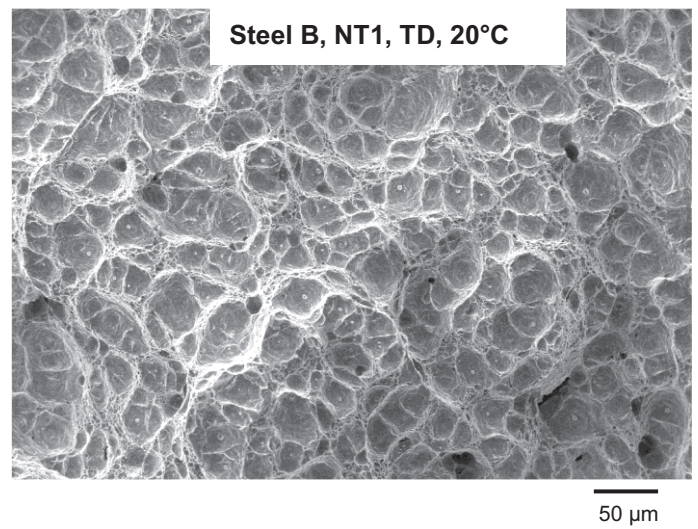
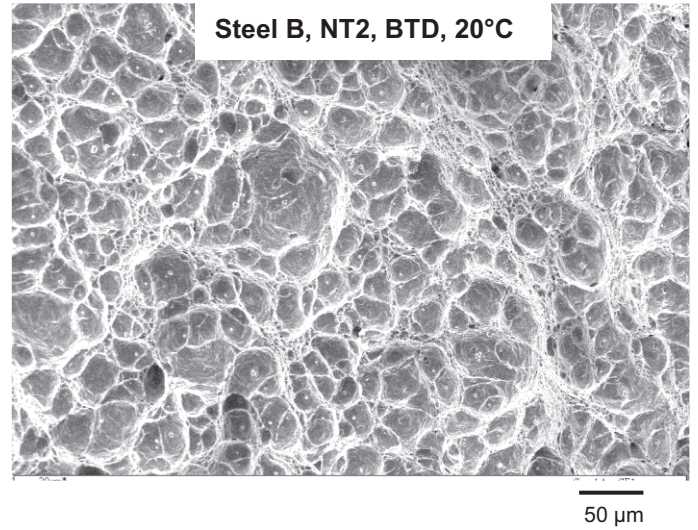
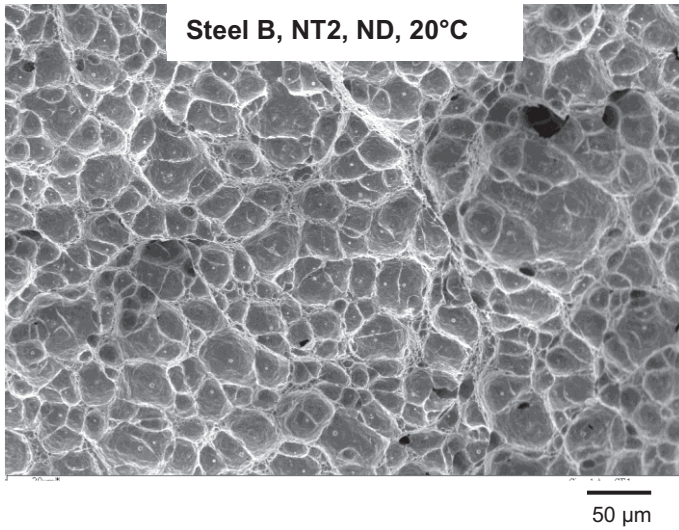


Figure D-7: Fracture surface of tensile specimens tested at 20°C along ND, BT and TD. Steel B

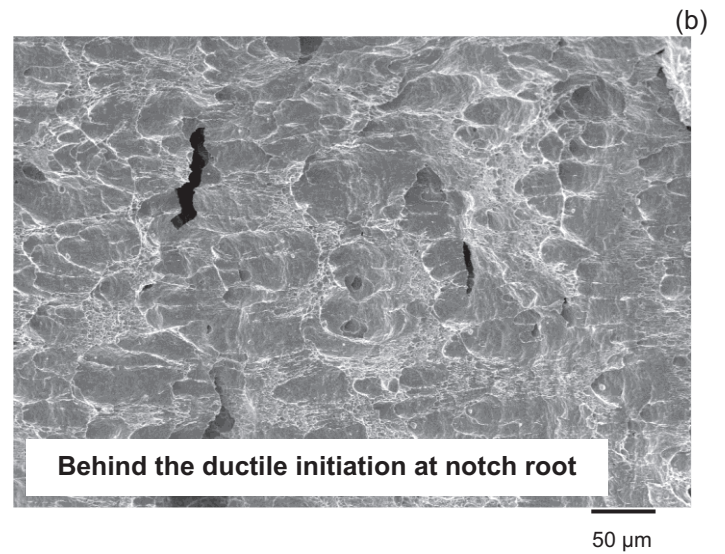
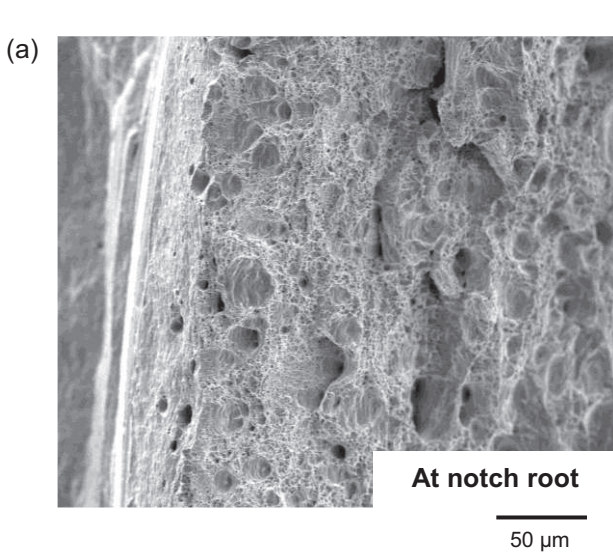


Figure D-8: Fracture surface of Steel B Charpy TD-ND specimen tested at 20°C. Detailed view at the notch root (a), and of the region behind the notch root (b). The notch is on the left, the crack propagates from the left to the right

D.3.2. Modeling of ductile damage and fracture

The aim of ductile damage modeling was to introduce a ductile crack (representative of that experimentally observed) in the Charpy specimen, which was expected to modify the stress state as it was the case in notched tensile specimens. Therefore, the numerical study of ductile fracture was only a tool for brittle out-of-plane cracking analysis.

- Model and model parameters

The Gurson-Tvergaard-Needleman (GTN) model was used. Damage represented by a single scalar variable f representing void volume fraction, was assumed to be isotropic, even if experiments showed the anisotropy of ductile failure. A complete presentation of the model is proposed in [50].

The effective stress σ_* obeys the following implicit equation:

$$\frac{\bar{\sigma}^2}{\sigma_*^2} + 2q_1 f_* \cosh\left(\frac{q_2 \sigma_{kk}}{2 \sigma_*}\right) - 1 - q_1^2 f_*^2 = 0 \quad \text{Equation D.2}$$

Where σ_{kk} is the trace of the stress tensor $\bar{\sigma}$, q_1 and q_2 are material parameters. The equivalent stress f is a function of the porosity. f_* is introduced to represent the final failure by coalescence.

$$f_* = \begin{cases} f & \text{if } f \leq f_c \\ f_c + \frac{1/q_1 - f_c}{f_F - f_c} (f - f_c) & \text{otherwise} \end{cases}$$

Equation D.3

In this equation, f_c is the critical porosity for the onset of coalescence and f_F is the porosity at failure.

The evolution of porosity is given by the following equation accounting for both void nucleation (right term) and void growth by plastic strain and mass balance (left term):

$$\dot{f} = (1 - \dot{f}) \text{trace}(\dot{\underline{\epsilon}}_p) + \frac{f_n}{\sqrt{2\pi} s_n} \exp\left(-\frac{1}{2} \left(\frac{p - \epsilon_n}{s_n}\right)^2\right) \dot{p} \quad \text{Equation D.4}$$

where f_n , ϵ_n and s_n are parameters controlling void nucleation.

The mesh size has been fixed to 100 μm which was the element size along the Charpy ligament. The initial porosity f_0 was taken as 2.2×10^{-4} for Steel A and 2.2×10^{-4} for Steel B, according to results of inclusion analysis (Chapter I).

- Identification of GTN model parameters

To be really representative of ductile fracture mechanisms in Charpy tests, the GTN model parameters should be directly identified from Charpy curves. Since Charpy calculations cost a lot of time, it was yet decided to use parameters identified from notched tensile specimens, even if fractography analyses showed differences in dimple populations. Numerical simulations of Charpy tests were then validated by comparison between experimental load-displacement curves and ductile crack advance at the onset of delamination, which was the stage of the test that had to be correctly represented by numerical simulation using the model.

• **Steel A:**

The GTN model parameters identified on NT2 specimens along ND at 20°C were used for numerical simulation of Charpy tests because they lead to the best estimate in terms of load vs. displacement curves. Table D-2 gives corresponding parameters, which correspond to classical value for pipeline steels. Predicted tensile curves are in good agreement with experiments as presented in figure D-9. The GTN model identified on the tests along ND could also simulate the ductile damage for the

specimen along BTD. The relatively inaccurate modeling of the elastic-plastic domain for BTD might yet affect the ductile damage simulation result.

Concerning Charpy tests, except for the slight overestimate of the load induced by using a von Mises yield criterion, there is good agreement between experimental and predicted curves (Figure D-10). The GTN model parameters identified at 20°C have then also been used for Charpy tests at -100°C. Isothermal conditions were still considered even if at such low temperature, effects of adiabatic self-heating might not be negligible. Figure D-11 shows the experimental and predicted load-displacement curves of Charpy TD-ND specimen. The values of load are overestimated by around 10%.

The last point is to compare the predicted geometry of the ductile crack to the experimental one. The simulation of Charpy TD-ND specimen tested at -100°C was stopped at the abrupt load drop associated with brittle crack propagation. The ductile crack advance predicted by the model is compared to the (rare) fracture surface of Charpy specimens of Steel A in figure D-12. There is good agreement between the experimental and simulated geometries of the ductile crack.

q_1	q_2	f_c	f_F	f_n	ϵ_n	s_n
1.5	1	0.025	0.19	0.005	0.45	0.2

Table D-2: GTN parameters of Steel A identified at 20°C on NT2 specimens tested along ND and BTD

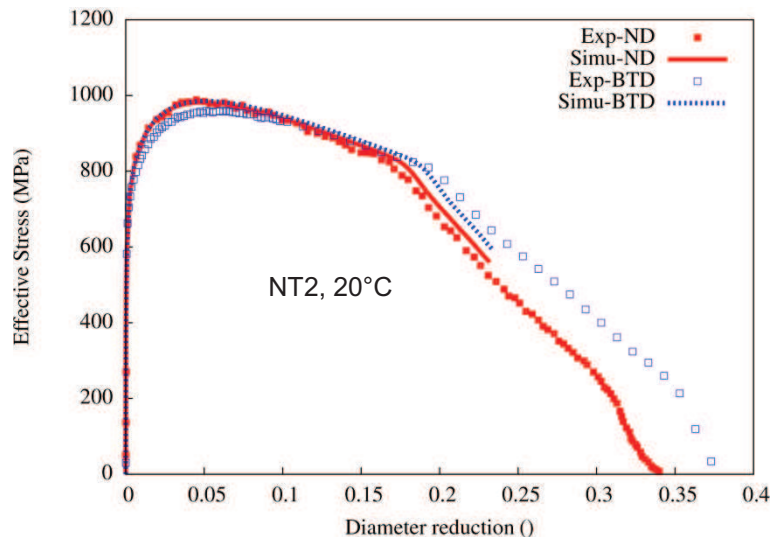


Figure D-9: Tensile curves on NT2 specimens of Steel A tested at 20°C along ND and BTD. Good agreement between experiment and simulation

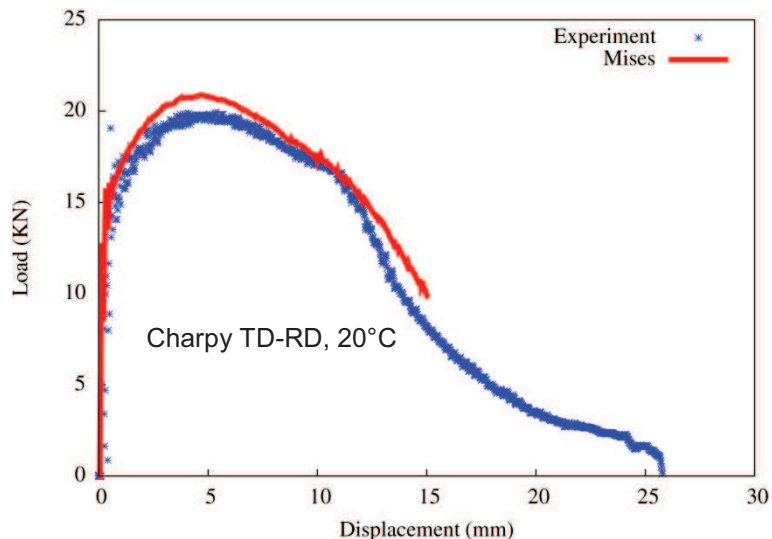


Figure D-10: Experimental and predicted Charpy curves of Steel A along TD at 20°C. Good agreement between experiment and simulation

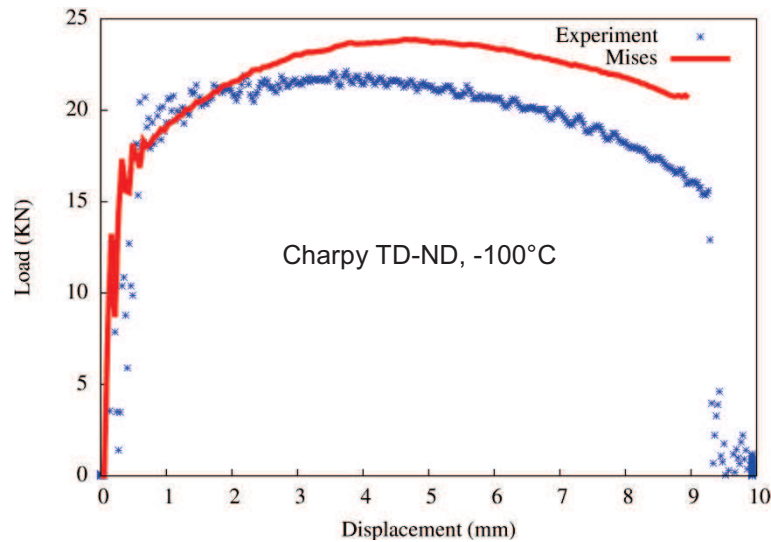


Figure D-11: Experimental and predicted curves for Charpy TD-ND test on Steel A at -100°C. The numerical simulation overestimates the load.

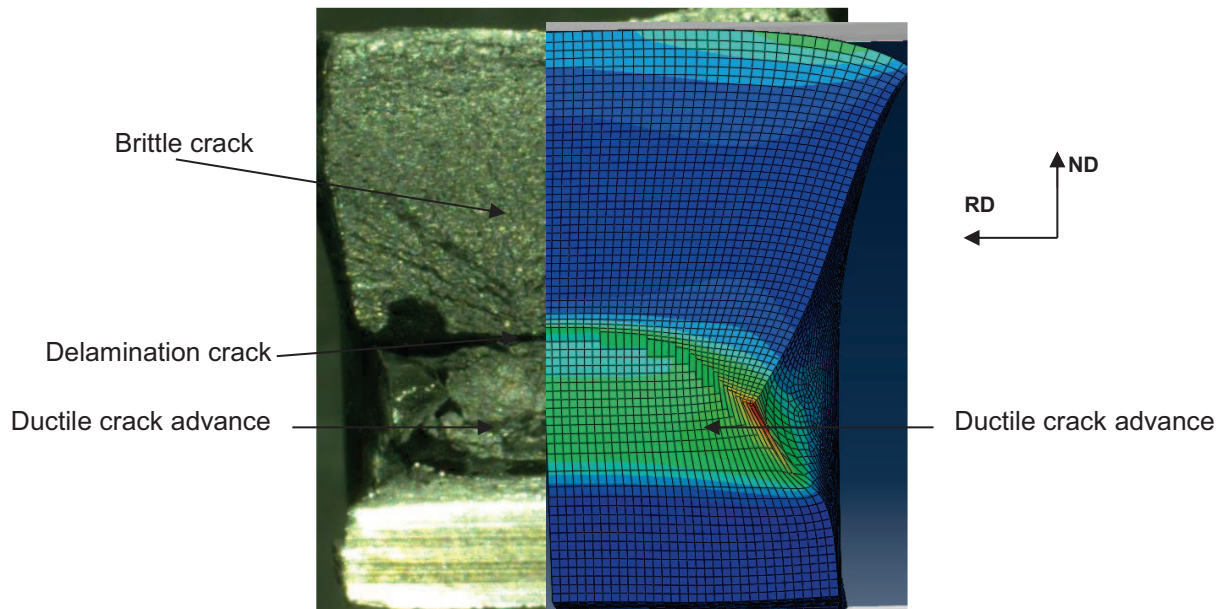


Figure D-12: Charpy TD-ND specimen of Steel A at -100°C. Good agreement between predicted and experimental ductile crack advance at the onset of delamination

- **Steel B:**

In a first step, GTN model parameters were identified on NT2 specimens at 20°C, as for Steel A. Because of the high anisotropy on tensile curves in terms of ductile cracking, it was not possible to obtain good agreement along ND and BTD with the same set of damage parameters for this steel. After a separate identification of GTN parameters for both directions, BTD was found to lead to a better description of ductile damage for Charpy tests compared to ND. Identified GTN parameters are presented in table D-3.

Tensile curves predicted by the model are presented in figure D-13. Concerning Charpy tests, the first simulation done using the GTN parameters of Steel B showed a load decrease occurring much earlier than in the experiment. By using the GTN parameters previously determined for Steel A, there was better agreement between experiment and simulation, out of the elastic-plastic domain (Figure D-14).

The GTN parameters determined for Steel A were therefore used for Charpy simulation at -100°C on Steel B. Figure D-15 shows the experimental and predicted load-displacement curves of Charpy TD-ND tests. The load levels are overestimated by around 20%.

The last point is to compare the predicted size of the ductile crack advance to the experimental one. The simulation of Charpy TD-ND specimen tested at -100°C was stopped at the load drop associated to brittle crack propagation. The ductile crack advance predicted by simulation is compared to experiment in figure D-16. There is good agreement between the experimental and simulated geometries of the ductile crack at this stage of the test.

q_1	q_2	f_c	f_F	f_n	ϵ_n	s_n
1.5	1	0.015	0.25	0.007	0.3	0.1

Table D-3: GTN parameters of Steel B identified at 20°C on NT2 specimens tested along ND and BTD

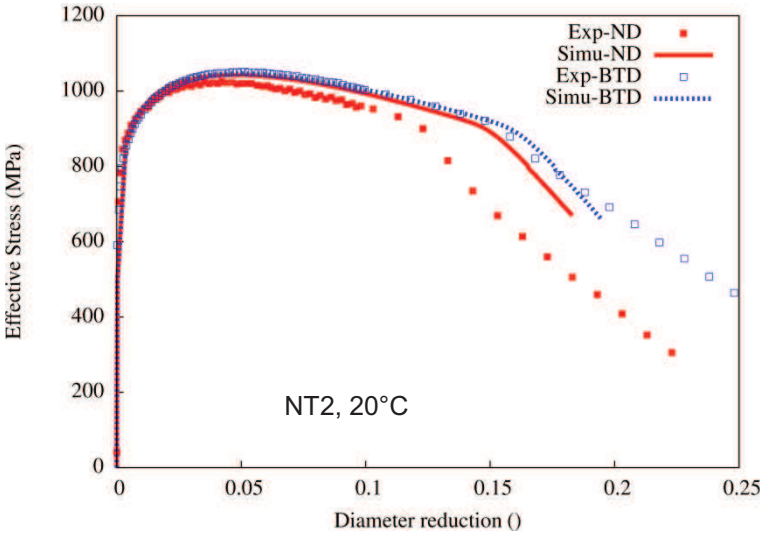


Figure D-13: Tensile curves on NT2 specimens of Steel B tested at 20°C along ND and BTD. Good agreement between experiment and simulation for BTB.

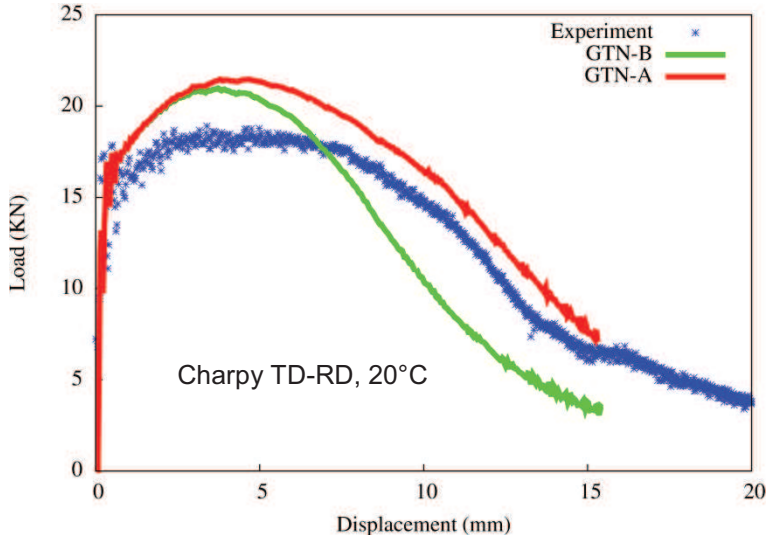


Figure D-14: Charpy specimen of Steel B along TD at 20°C. Calculations were carried out with both Steel A and Steel B GTN model parameters

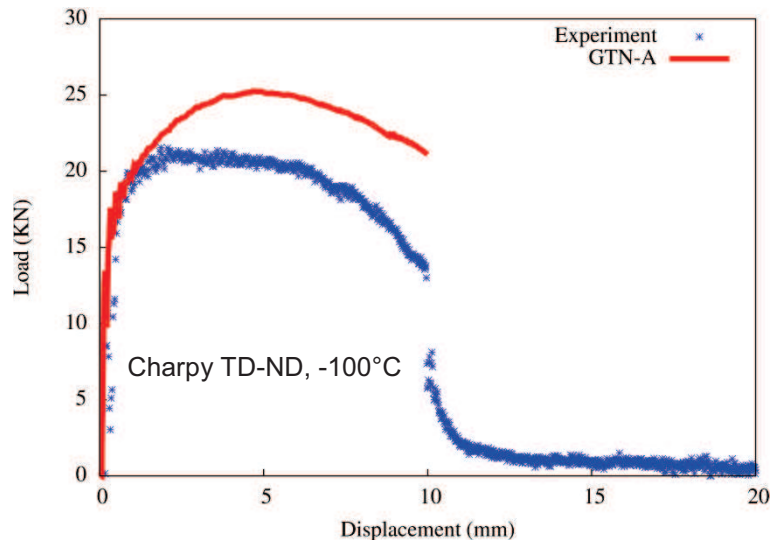


Figure D-15: Charpy TD-ND of Steel B at -100°C. Model predictions uses damage parameters identified for Steel A. The numerical simulation overestimates the load.

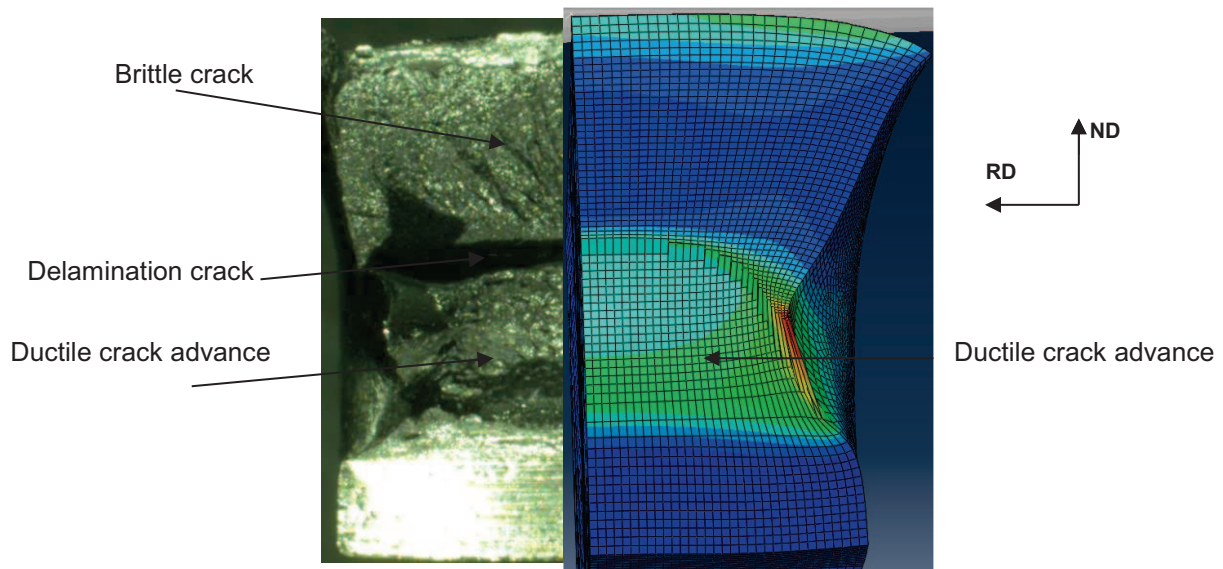


Figure D-16: Charpy TD-ND specimen of Steel B fractured at -100°C. Good agreement between predicted and experimental ductile crack advance

Conclusion

The conditions for the numerical simulation of Charpy tests have been set up. A 3D mesh with linear elements of 100 μm in size was chosen, to simulate one quarter of Charpy specimens. A von Mises yield criterion was chosen to model the elastoplastic domain of Charpy curve, even if an overestimate of the local stress was observed compared to that estimated with a Barlat yield criterion. This hypothesis was necessary to enable one to investigate the ductile fracture using a GTN model on the available Abaqus software.

Experimental analyses showed anisotropy in ductile damage development and also some differences between the ductile fracture on tensile specimens and Charpy specimens. Therefore, a unique GTN model could not be used to analyze the ductile fracture along ND, BT, RD and TD at the same time. Moreover the GTN model identified on NT specimens could not directly be used for Charpy specimens. The GTN model identified for Steel A led to good agreement between the experimental results and the numerical simulation of Charpy tests. The predicted geometry of the ductile crack by numerical simulation was very close to the one experimentally observed. Concerning Steel B, even if

the predicted ductile crack was also in good agreement with the experimental one, the global Charpy curve obtained with numerical simulation was around 20% overestimated in terms of strength.

References

- [1] TANGUY B., Modélisation de l'essai Charpy par l'approche locale de la rupture. Application au cas de l'acier 16MND5 dans le domaine de transition. PhD Thesis: Ecole des Mines de Paris, 2001. 516 p. (in French)
- [2] FUJISHIRO T., and HARA T., Effect of separation on ductile crack propagation behavior during drop weight tear test. In : Proceedings of the Twenty-first (2011) International Offshore and Polar Engineering Conference, ISOPE, 2011, June 2011, Hawaii, p. 237-242
- [3] COSHAM A., JONES D.G., EIBER R., and HOPKINS P., Don't drop the drop weight tear test. In : Pipeline Technology Conference, October 2009, Ostend
- [4] NF EN10274 Standard, Matériaux métalliques - essai de chute de masse, Norme, Juillet 1999, 20 p.
- [5] ANSI/API RP 5L3 Standard, Recommended practice for conducting drop-weight tear tests on line pipe, Norme, April 1996, 9 p.
- [6] OSBORNE N. Instrumented drop weight tear testing. Advanced materials and processes, 2009, vol.167, p. 26-27
- [7] SHIM D-J, WILKOWSKI G., BRUST F. W, and RUDLAND D.L., DUAN D.M., Evaluation of fracture speed on ductile fracture resistance. In : Pipeline Technology Conference, October 2009, Ostend
- [8] HWANG B., LEE S., KIM Y.M., KIM N.J., YOO J.W., and WOO C.S., Analysis of abnormal fracture occurring during drop-weight tear test of high-toughness line-pipe steel, Materials Science and Engineering A, 2004, 368, p. 18 -27
- [9] YANG Z., KIM C-B., FENG Y., and CHO C., Abnormal fracture appearance in drop-weight tear test specimens of pipeline steel, Materials Science and Engineering A, 2008, 483-484, p. 239-241
- [10] RUDLAND D.L., WANG Y-Y, WILKOWSKI G., and HORSLEY D.J., Characterizing dynamic fracture toughness of line pipe steels using the pressed-notch drop-weight-tear test specimen, Engineering Fracture Mechanics, 2004, 71, p. 2533-2549
- [11] HWANG B., SHIN S. Y., LEE S., and KIM N.J. et al., Correlation of crack-tip opening angle for stable crack propagation with Charpy and drop-weight tear test properties in high-toughness API X70 pipeline steels, Metallurgical and Materials Transactions A, 2006, 37, p. 371-380
- [12] O'DONOGHUE P.E., KANNINEN M.F., LEUNG C.P., DEMOFONTI G., and VENZI S., The development and validation of a dynamic fracture propagation model for gas transmission pipelines, International Journal of Pressure Vessels and Piping, 1997, 70, p. 11-25
- [13] HARA T., SHINOHARA Y., ASAHI H., and TERADA Y., Effects of microstructure and texture on DWTT properties for high strength line pipe steels. In : Proceedings of IPC, International Pipeline conference, September 2006, Calgary, Paper IPC2006-10255, p. 245-250
- [14] SHIN Y.S., HONG S., BAE J-H., KIM K., and LEE S., Separation phenomenon occurring during the Charpy impact test of API X80 pipeline steels, Metallurgical and Materials Transactions A, 2009, 40, p. 2333-2349

- [15] PISARSKI H.G., HAMMOND R., and WATT K. Significance of splits and pop-ins observed during fracture toughness testing of line pipe steel, in : Proceedings of IPC2008, 7th International Pipeline conference, October 2008, Canada, Paper IPC2008-64676, p. 473-482
- [16] BALDI G., and BUZZICHELLI G., Critical stress for delamination fracture in HSLA steels, Metal Science, 1978, 12, p. 459-472
- [17] YANG Z., HUO C., and GUO. W., The Charpy notch impact test of X70 pipeline steel with delamination cracks, Key Engineering Materials, 2005, 297-300, p. 2391-2396
- [18] YANG Z., GUO. W., HUO C., and WANG Y., Fracture appearance evaluation of high performance pipeline steel DWTT specimen with delamination cracks, Key Engineering Materials, 2006, 324-325, p. 59-62
- [19] AHN S.S., CHO W.Y., YOON T-Y., and YOO J-H., Mechanical properties and bending behaviors of low temperature toughness linepipe steels, in : Proceedings of the 26th International Pipeline conference on Offshore Mechanics and Arctic Engineering, June 2007, San Diego, p. 465-474
- [20] BRAMFITT B.L. and MARDER A.R., A study of the delamination behavior of a very low-carbon steel, Metallurgical Transactions A, 1977, 8, p.1263-1273
- [21] ZOK F. and EMBURY J.D., On the analysis of delamination fractures in high strength steels, Metallurgical Transactions A, 1990, 21, p. 2565-2575
- [22] YAN W., SHA W., ZHU L., WANG W., SHAN Y-Y., and YANG K., Delamination fracture related to tempering in a high-strength low-alloy steel, Metallurgical and Materials Transactions A, 2010, 41, p. 159-171
- [23] JOO M.S., SUH D-W., BAE J.H., and BHADSHIA H.K.D.H., Role of delamination and crystallography on anisotropy of Charpy toughness in API-X80 steel, Materials Science and Engineering A, 2012, 546, p. 314-322
- [24] HARA T., SHINOHARA Y., TERADA Y., and ASAHI H., DWTT properties for high strength line pipe steels. In : Proceedings of the Eighteenth (2008) International Offshore and Polar Engineering Conference, Vancouver July 2008, ISOPE, p. 189-193
- [25] FRANCOIS D., Essais de mesure de la ténacité – Mécanique de la rupture. Techniques de l'ingénieur, M4166, Juillet 2007
- [26] SUN J., BOYD J.D., Effect of thermomechanical processing on anisotropy of cleavage fracture stress in microalloyed linepipe steel. International Journal of Pressure vessels and piping, 2000, 77, p. 369-377
- [27] PINEAU, A., PARDOEN, T., Failure of metals, in : Comprehensive Structural Integrity, 2, Elsevier, Chapter 2.06, p. 684-783, 2008.
- [28] BOWEN P., DRUCE S.G., KNOTT J.F., Effects of microstructure on cleavage fracture in pressure vessel steel. Acta Metallurgica, 1986, 34, p. 1121-1131
- [29] PINEAU, A., Practical application of local approach methods, in : Comprehensive Structural Integrity, 7, Elsevier, Chapter 7.05, p. 177-225, 2004.
- [30] CHEN J.H., LI G., CAO R., FANG X.Y., Micromechanism of cleavage fracture at the lower shelf transition temperatures of a C–Mn steel. Materials Science and Engineering A, 2010, 527, p. 5044-5054

- [31] McROBIE D.E., KNOTT J.F., Effects of strain and strain aging on fracture toughness of C-Mn weld metal. Material Science and Technology, 1985, 1, p. 357-365
- [32] ROSENFELD A.R., SHETTY D.K., SKIDMORE A.J., Fractographic observations of cleavage initiation in the ductile-brittle transition region of a reactor-pressure-vessel steel. Metallurgical Transactions A, 1983, 14, p. 1934-1937
- [33] LAMBERT-PERLADE A., GOURGUES A.F, BESSON J., STUREL T., PINEAU A., Mechanisms and modeling of cleavage fracture in simulated heat-affected zone microstructures of a high-strength low alloy steel. Metallurgical and Materials Transaction A, 2004, 35, p. 1039-1053
- [34] KOTRECHKO S., STETSENKO N., SHEVCHENKO S., Effect of texture smearing on the anisotropy of cleavage-stress of metals and alloys. Theoretical and Applied Fracture Mechanics, 2004, 42, p. 89-98
- [35] BOZZO P., BUZZECHELLI G., MASCANZONI A., MIRABILE M., Microstructure and cleavage resistance of low-carbon bainitic steels. Metal Science, 1977, 17, p. 123-130
- [36] DI SHINO A., GUARNASCHELLI C., Microstructure and cleavage resistance of high strength steels. Materials Science forum, 2010, 638-642, p. 3188-3193
- [37] ZENER C., Fracturing of metals. In : 29th National Metal Congress and Exposition, American Society for Metals. 1948, p. 3–31.
- [38] STROH A.N., The formation of cracks as a result of plastic flow. Proceedings of the royal society London A, 223, 1954, p. 404–414.
- [39] COTTRELL A.H., Theory of brittle fracture in steel and similar metals. Transactions of the Metallurgical Society of AIME, 211, 1958, p. 192–203.
- [40] SMITH E., The nucleation and growth of cleavage microcracks in mild-steels. In : Proceedings Conference on “Physical basis of yield and fracture”, Institute of Physics and Physical Society, 1966, p. 36–46
- [41] CURRY D.A., Cleavage micromechanisms of crack extension in steels. Metal science, 14, 1980, p. 319–326.
- [42] RITCHIE R.O., KNOTT J.F., RICE J.R., On the relationship between critical tensile stress and fracture and toughness in mild steel. Journal of the mechanics and physics of solids, 1973, 21, p. 395-410
- [43] CHEN J.H., WANG G.Z., Study of mechanism of cleavage fracture at low temperature. Metallurgical Transactions A, 1992, 23A, p. 509-517
- [44] MARTIN-MEIZOSO A., OCANA-ARIZCORRETA I., J. GIL-SEVILLANO, and FUNTES-PEREZ M., Modelling cleavage fracture of bainitic steels. Acta Metallurgica et Materialia, 1994, 42, p. 2057-2068.
- [45] PINEAU A., TANGUY B., Advance in cleavage fracture modeling in steels: Micromechanical, numerical and multiscale aspects. Compte Rendu Physique, 2010, 11, p. 316-325.
- [46] CARASSOU S. Déclenchement du clivage dans un acier faiblement allié : Rôle de l'endommagement ductile localisé autour des inclusions. Phd Thesis: Ecole des Mines de Paris, 2000. 198 p. (In French)

- [47] HILL R., A theory of the yielding and the plastic flow of anisotropic solids. Proceedings of the Royal Society of London A, 1948, 193, p. 281-297
- [48] BARLAT F., LEGE D., BREM J., A six-component yield function for anisotropic materials. International Journal of Plasticity, 1991, 7, p. 693-712
- [49] Tvergaard V., Material failure by void growth to coalescence. Advanced Applied Mechanics, 1990, 27, p. 83-151
- [50] TANGUY B., LUU T.T., PERRIN G., PINEAU A., and BESSON J., Plastic and damage behavior of a high strength X100 pipeline steel: Experiments and modelling, International Journal of Pressure Vessel and Piping, 2008, 85, p. 322-335

Transition ductile-fragile des aciers pour gazoducs: Etude quantitative des ruptures fragiles hors plan et corrélation à l'anisotropie de microtexture

RESUME : La bonne ténacité des aciers pour gazoducs aux basses températures est nécessaire pour éviter la propagation de fissures de manière catastrophique. Cette étude vise à améliorer la compréhension physique et l'évaluation quantitative du comportement à rupture des aciers pour gazoducs laminés à chaud, en nous intéressant plus particulièrement aux températures au pied de la transition ductile-fragile. La résilience de ces aciers est généralement validée à l'aide d'essais dits *drop weight tear tests* (DWTT), pour lesquels le faciès de rupture doit contenir moins de 15% de zone fragile. Pour les aciers mis en forme par laminage thermomécanique (TMCP), des ruptures fragiles hors plan, comme le délaminage (qui se propage dans le plan de laminage de la tôle), et la rupture fragile en biseau le long des plans dits θ (inclinés de 40° autour de la direction de laminage par rapport au plan de laminage) apparaissent dans la transition ductile-fragile. Ces modes de rupture, observés lors des essais de résilience (DWTT, Charpy) et de ténacité (CT), affectent la résistance à la rupture de ces aciers. L'anisotropie de l'écoulement plastique, puis celle de la sensibilité à la rupture par clivage ont été caractérisées en fonction de la température, à l'aide d'essais de traction sur des éprouvettes lisses et entaillées conçues pour cette étude. L'analyse mécanique de ces essais effectuée à l'aide de calculs par éléments finis a permis de déterminer des contraintes critiques de clivage dans les directions perpendiculaires au plan de laminage et aux plans θ . Les valeurs obtenues dans ces directions sont de 25% inférieures à celles correspondant aux directions de laminage et travers long. L'anisotropie de la contrainte critique de clivage a été quantitativement corrélée à l'anisotropie de microtexture du matériau. Des entités appelées « facettes de clivage potentielles » ont été définies et mesurées dans cette étude, comme des régions contenant un plan {100} défavorablement orienté et dans lesquelles les fissures de clivage se propagent sans être arrêtées. Par exemple, un plan contenant 20% de facettes de clivage potentielles présenterait une contrainte critique de clivage 20% moins élevée qu'un plan présentant seulement 10% de facettes de clivage potentielles. La taille et la forme de ces facettes de clivage potentielles évoluent avec la déformation plastique. Par conséquent, la contrainte critique de clivage est affectée par l'historique de déformation. Dans le cas du délaminage, les facettes de clivage potentielles s'allongent au cours d'un chargement dans la direction travers long, conduisant à une augmentation de leur taille effective et par conséquent à une diminution (qui peut atteindre 30%) de la contrainte critique de clivage dans le plan de la tôle. Cette diminution facilite *in fine* l'apparition du délaminage. De plus, la présence de micro-fissures ductiles facilite la rupture par délaminage en modifiant l'état de contrainte local. Un critère a ainsi été proposé pour prédire numériquement l'amorçage du délaminage dans des éprouvettes de traction et/ou de résilience Charpy. L'application de cette approche à des échantillons traités thermiquement et à des échantillons pré-déformés a montré que la sensibilité au délaminage pouvait être contrôlée en modifiant la texture locale initiale du matériau.

Mots clés : Aciers pour gazoducs, Transition ductile-fragile, Délaminage, Rupture fragile en biseau, Anisotropie, Microtexture

Ductile to brittle transition in pipeline steels: Quantitative investigation of brittle out-of-plane cracking and correlation to microtexture anisotropy

ABSTRACT: High toughness of pipeline steels at low temperature is required to avoid catastrophic propagation of brittle crack. The aim of the study is to improve physical understanding and quantitative assessment of the toughness behavior of hot-rolled pipeline steels, focusing on the lower part of the ductile to brittle transition temperature range. The impact toughness of these steels is commonly validated using drop weight tear tests (DWTT), on the basis of fracture surfaces that must exhibit less than 15% of brittle fracture appearance. In thermomechanical control processed steels, brittle out-of-plane cracks such as delamination (which propagates along the rolling plane), and brittle tilted fracture (BTF) along θ -planes (tilted around RD by 40° with respect to rolling plane), have been characterized in the ductile to brittle transition temperature range, for both industrial (DWTT) and laboratory Charpy impact tests. In both cases, as well as in fracture toughness tests, such brittle out-of-plane cracking has been shown to impair the impact toughness. The anisotropies in plastic flow and sensitivity to cleavage fracture have been characterized as a function of temperature, by using tensile tests on specifically designed smooth and notched specimens. From finite element mechanical analysis of these tests, critical cleavage stresses normal to the rolling plane and the θ -plane are considerably lower (around 25%) than for planes normal to the rolling and transverse directions. The anisotropy in critical cleavage stress has been quantitatively correlated to microtexture anisotropy. So-called "potential cleavage facets" have been defined and measured in this study, as regions with unfavorably oriented {100} planes, which are taken as unit crack paths for cleavage propagation. A sample containing 20% of potential cleavage facets had a critical cleavage stress 20% lower than a sample with only 10% of potential cleavage facets. The size and shape of these potential cleavage facets evolve during plastic deformation. Therefore, the critical cleavage stress was found to be affected by plastic strain history. In the case of delamination, potential cleavage facets along the rolling plane were elongated during loading, their area was increased and the corresponding critical cleavage stress decreased by around 30% with respect to the undeformed case. This made delamination cracking easier. Moreover, the presence of a ductile crack at the initiation site of delamination locally modified the stress state and also facilitated delamination occurrence. A criterion has been developed to numerically predict the onset of delamination in tensile and Charpy specimens. Application of this approach to heat-treated and to prestrained specimens eventually showed that it was possible to modify the sensitivity to delamination by strongly modifying the initial microtexture anisotropy.

Keywords : Pipeline steels, Ductile to brittle transition, Delamination, Brittle tilted fracture Anisotropy, Microtexture

